Department of Physics and Astronomy

University of Heidelberg

Master thesis

in Physics

submitted by

Bogdan - Mihail BLIDARU

born in Buzău, Romania

2019

Discharge propagation

in double-GEM detectors

This Master thesis has been carried out by

Bogdan - Mihail BLIDARU at the

Physikalisches Institut of the University of Heidelberg and

GSI Helmholtzzentrum für Schwerionenforschung, Darmstadt

under the supervision of

Prof. Dr. Silvia Masciocchi

Abstract:

The Large Hadron Collider will provide Pb-Pb collisions at an interaction rate of 50 kHz starting from 2021 on, following its Long Shutdown 2.

The ALICE Time Projection Chamber Upgrade project developed a readout based on a stack of four Gas Electron Multiplier (GEM) foils at the amplification stage in order to be able to operate continuously. After their installation in the ALICE cavern, the GEM chambers will be inaccessible. Thus, long-term stability and reliable readout over a time span of about 10 years is mandatory.

GEMs are sensitive structures and one major challenge they must overcome are electrical discharges. High charge density, resulting from gas ionization accumulating near the GEM holes, can produce primary discharges. Some of the more powerful events are the secondary discharges occurring in the gaps between GEMs. They threaten to short-circuit the GEM foil and render it inactive, as well as damage the readout electronics.

A small $10 \times 10\,\mathrm{cm}^2$ detector with two GEM foils is used in this thesis to study the occurrence of secondary discharges. It was found that they are heavily influenced by the propagation in between GEMs of the primary discharge. Results show that the propagation can be mitigated by the use of decoupling resistors.

The propagating behavior was believed to be caused by photons traveling to the upper GEM, since its occurrence was immediate. However, occasional events in which the propagation has a delay have sparked curiosity and are subject to further investigation.

Zusammenfassung:

Nach dem Long Shutdown 2 liefert der Large Hadron Collider ab 2021 Pb-Pb-Kollisionen mit einer Interaktionsrate von 50 kHz.

Für das ALICE Time Projection Chamber (TPC) Upgrade Projekt wurden neue Auslesekammern entwickelt, die auf vier gestapelten GEMs (Gas Electron Multiplier) basieren. Somit ist es möglich die TPC kontinuierlich auszulesen. Nach Ihrer Installation in der ALICE-Kaverne, sind die GEM-Kammern nicht mehr zugänglich. Langzeitstabilität und zuverlässige Funktion über einen Zeitraum von ca. 10 Jahren sind daher unabdingbar.

Da GEMs empfindliche Strukturen sind, ist es eine große Herausforderung elektrischen Entladungen standzuhalten. Eine hohe Ladungsdichte, die sich aus der Gasionisation in der Nähe der GEM-Löcher ergibt, kann zu primären Entladungen führen. Einige der stärkeren Ereignisse sind die Sekundärentladungen, die in den Lücken zwischen den GEMs auftreten. Diese können, die GEM-Folie kurzzuschließen und deshalb inaktiv machen, sowie die Ausleseelektronik beschädigen.

Für diese Arbeit wurde ein kleiner Detektor mit einer Größe von $10 \times 10\,\mathrm{cm}^2$ und zwei GEM-Folien verwendet, um das Auftreten von Sekundärentladungen zu untersuchen. Es wurde festgestellt, dass diese stark von der Ausbreitung der Primärentladungen zwischen den GEM-Foilen beeinflusst werden. Die Ergebnisse zeigen, dass die Ausbreitung durch den Einsatz von Entkopplungswiderständen gemindert werden kann.

Da die Ausbreitung unmittelbar auftrat, wurde bisher angenommen, dass sie durch Photonen verursacht wird, die zur oberen GEM wandern. Gelegentliche Ereignisse, bei denen die Ausbreitung verzögert ist, haben jedoch die Neugier geweckt und sind Gegenstand weiterer Untersuchungen.

Acknowledgements

This thesis has been prepared based on research done at GSI Helmholtzzentrum für Schwerionenforschung in Darmstadt.

I would like to above all express my heartfelt gratitude to Prof. Dr. Silvia Masciocchi for allowing me the unique opportunity to carry this study under her supervision. Your dynamism, generosity and motivation have inspired me to believe in myself and push a little harder each time in order to learn something new. I appreciate the confidence you showed in me and I look forward to engaging in future projects guided by you!

My deepest consideration goes to Dr. Alexander Deisting. You nurtured my need to constantly learn and you have always found those "few minutes for some questions". You have dedicated yourself time and time again to shape me as a future researcher by patiently answering my most naive questions. I highly value the insights and guidance you provided!

My most sincere appreciation goes to Dr. Chilo Garabatos Cuadrado and Mr. Daniel Baitinger for their valuable and constructive suggestions during the planning and development of this research work, as well as for the great insight and recommendations during measurements. Thank you for such a wonderful and fruitful collaboration!

I am particularly grateful for the assistance given by Prof. Dr. André Schöning throughout my years in Heidelberg, for the opportunity to learn more about the pixel detectors in his group and for his amenability to be the second examiner of this thesis!

I further extend my profound recognition to Dr. Dariusz Miskowiec, Dr. Kai Schweda, Mr. Pascal Becht and Mr. Vlad Cristescu who have provided me extensive personal and professional guidance. I appreciate the information and advice you have shared!

I am grateful to all my GSI colleagues which offered their support and advice when I was in need. I appreciate your assistance and look forward to continuing working alongside you for the next years!

Nobody has been more important to me in this journey than the members of my family. Although this period of my life was filled with many ups and downs, there is no one that supported and motivated me more than the two most wonderful persons in the world: my mother, Marilena and my partner in life, Maria. My father has been in my thoughts and heart every step of the way and I know he is delighted and at peace to see how I set my path in life. I miss you dad!

Their love, kindness and support have helped me overcome each and every obstacle in my pursuit to be a better person. They believe in me, in my dream to become a scientist, never lessening. I hope that I make you all proud!

Contents

1 A brief history of time

Aristotle said a bunch of stuff that was wrong.
Galileo and Newton fixed things up.
Then Einstein broke everything again.
Now, we've basically got it all worked out...
except for small stuff, big stuff, hot stuff, cold stuff,
fast stuff, heavy stuff, dark stuff, turbulence and the concept of time. [1]

Progress towards an analytical understanding of Nature is believed by many to have been started with the expositions of Aristotle's doctrines. He is credited as the most recognizable figure of classical antiquity that advanced a systematic set of ideas about the physical world. He was among the first to have a feeling about how the natural world works and the first to test his observations by making use of his senses.

Aristotle's casual everyday observations strongly influenced human thought until the early modern period, pointing to the importance of empirical evidence in human understanding.

Although Aristotle managed to make contributions to every field, from biology and physics to logic and politics, he also managed to be wrong about a great deal of ideas. He is not to be blamed, since ancient Greeks were ultimately philosophers, not scientists. As such he would approach an idea with some common truth gained through observation and then deduct specifics from this.

Aristotelian physics remained the prevailing scientific paradigm in Europe until the times of Galileo Galilei, Isaac Newton and many others who, collectively, during the Scientific Revolution era, argued that Aristotle's general principles are ill suited, his methods flawed and sought to satisfy the scientific method into what we now know as Classical Mechanics.

The physicists of that era made inspired guesses about how nature works, but unlike the ancient Greeks, they put their ideas to the test employing mathematical tools and simple experiments to determine the truth behind different concepts.

Most notable of all, Newton brought together all the ideas set forth during the Scientific Revolution, effectively establishing the foundation for modern society in mathematics and science. His ideas were groundbreaking, mathematically substantiated and are still applied in our day by day experience, having stood the test of time. There is perhaps no better example to justify the importance of classical physics than the fact that the first manned mission on the surface of the Moon in 1969 was computed using nothing else than the classical equations of motion derived by Newton more than 300 years ago.

The ordinary, unexceptional manifestations of Physics explained by classical mechanics are experienced (and described) by objects that are close to ambient temperature, that experience speeds a tiny fraction of the speed of light, entities that are larger than atoms and molecules, but smaller than a planet and that are studied in an inertial frame

of reference. For nearly two hundred years, classical physics' dominance was absolute, unquestionable, although some parts of it required clarification.

So, it is acknowledged... but how does it actually work? That is a question that bugged Albert Einstein and its answer was radical and shook the foundations of physics. When Einstein introduced his theories of relativity, he showed that Newton's laws were but a mere approximation of the way Nature works, that his equations broke down at speeds that approached that of light or when encountering very strong gravitational fields.

After Eddington conducted an experiment during a total solar eclipse, the ordered universe of Newton was replaced with an entirely new philosophy. It's not that classical physics was wrong. It was just superseded by the newer relativistic theory. It was the second time in humankind's history that a well established foundation was shattered and needed rebuilding. And up to this point in time, this new theory has withstood every test thrown at it.

Although presenting a picture of the universe that persists to this day, Einstein's quest generated a lot more puzzles. It was noted at the time that classical mechanics provided no means to explain the existence of subatomic particles and their properties. In order to do that, scientists needed a way to probe inside matter.

The pioneering work in this field has generated an abundance of physical theories about the fundamental particles the universe is made of and their weird interaction. Since Einstein proved that matter and energy are different, but closely related features of the same idea, physicists have come up with the idea of converting the energy of ordinary particles into new and difficult to find ones.

To get consistently higher energies for the particles they are using, scientists began to boost them in large accelerators and observed that by smashing them into each other or into stationary targets, they would produce a wealth of new particles, some short lived, some behaving in strange ways, and they began studying them. What happens in a split second during these high-energetic collisions can reveal to us the fundamental secrets of nature.

Today, the largest of these circular accelerating structures is the Large Hadron Collider, located at the border between Switzerland and France. Along 27 kilometers, particles are accelerated at nearly the speed of light and are hurled at each other in four areas where detectors are built to observe the impact. Most of these collisions produce new particles that travel outward of the collision point and are recorded using state-of-the-art detectors that infer their trajectory and extrapolate their identity and properties. This way, physicists have a good understanding of what has happened at the instant of the collision.

ALICE is one of those detector assemblies that tries to understand one of the puzzles still left in physics - the hot and dense stuff. This in turn will help us understand how the universe formed and why it looks the way it does today.

There is just one caveat - the price for precision is complexity. In this thesis I tumble down the rabbit hole and I will detail about pitfalls that arise when dealing with these intricate media, as well as the technical challenges needed to characterize it.

2 At the heart of matter

Humankind's knowledge on the structure of reality and the inner workings of the Universe can mathematically be explained through the theoretical framework of Physics. Although a "theory of everything" has not yet been formulated, almost all we know about the laws of physics falls into one of two cornerstone theories which operate on monumentally different hierarchies - the Standard Model of particle physics and General Relativity.

The first one is a quantum field theory that dwells into the realm of the very small and is based on the curious intricacies of quantum mechanics and the special theory of relativity. It describes with great accuracy all of the fundamental particles we've observed and the forces that make them interact - electromagnetism, the weak force and the strong nuclear force.

The latter is based on Einstein's theory of General Relativity, which describes the fourth force, gravity, and its influence on regions of large scale and big mass. It tells us how planets orbit stars, how the universe expands and it gives us black holes!

The quest is still ongoing to reconcile the two theories and attempt to link together all physical aspects of the universe under one all-encompassing formula.

2.1 Standard Model

What is matter made of? - is the fundamental question elementary particle physics addresses. The discoveries of the last hundred or so years have resulted in a stunning perception into the elementary constituents of matter. Everything around us is made from just a few fundamental particles that are pieced together like in a puzzle by fundamental forces. The sum of our understanding of how this is accomplished is condensed into the Standard Model of particle physics. This theoretical feat has successfully and with great accuracy predicted and explained various phenomena, grounding itself as one the greatest achievements of high-energy physics.

A thorough definition of the Standard Model is that it is a renormalizable gauge quantum field theory encompassing the internal symmetries of the unitary product group $\mathrm{SU}(3) \times \mathrm{SU}(2) \times \mathrm{U}(1)$ [2].

The Standard Model is a gauge theory, which means that the Lagrangian is invariant under certain local group transformations. Renormalization can be regarded as the process of effectively establishing the relationship between parameters at different scales and is seen as a tool which is used to treat infinite divergences arising in calculating finite quantities.

Groups are extremely useful for describing both continuous and discrete symmetries. The gauge transformations form a symmetry group of the theory. The three factors of the gauge symmetry of the Standard Model give rise to three fundamental interactions.

Finally, Standard Model is a quantum field theory because it treats particles as excited states of their underlying quantum field. Particle interactions (depicted in Fig. 2.1) are described by means of interaction terms in the Lagrangian involving their respective fields. The fields of the Standard Model are:

- Ψ - the fermion fields that describe matter particles
- W_1, W_2, W_3, B - electroweak sector boson fields
- G_a - the eight gluon fields
- φ - the Higgs field

U(1) acts on B and φ, SU(2) acts on W_i and Ψ, while SU(3) acts on G_a.

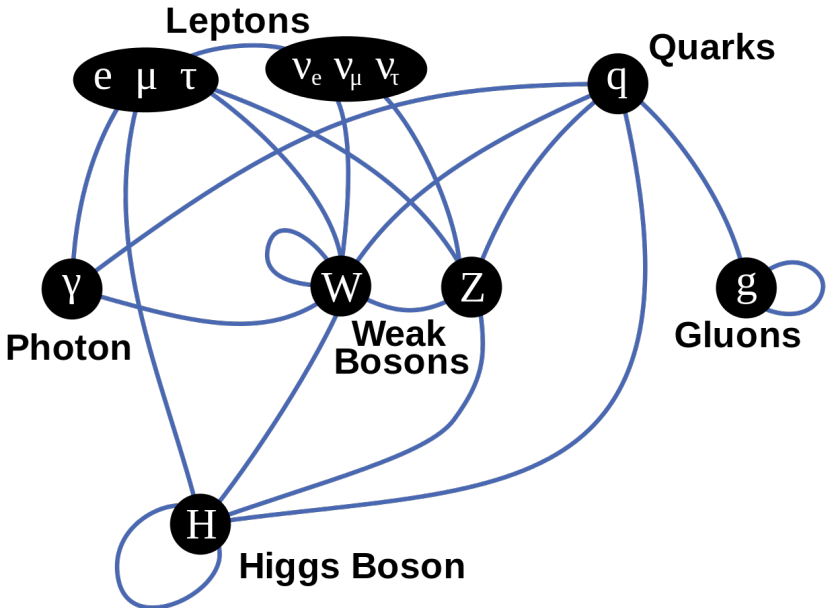

Figure 2.1: Interactions between elementary particles [3].

One of the easiest and most compact ways of expressing the theory is by means of the Lagrangian density, which is a function of the fields in the system and their derivatives. Fundamental interactions are represented as changes in this Lagrangian function of quantum fields.

$$\mathcal{L}_{\mathcal{SM}} = -\frac{1}{4}F_{\mu\nu}F^{\mu\nu} \quad + \quad i\bar{\psi}\not{D}\psi + h.c. \quad + \quad \bar{\psi}_i y_{ij}\psi_j\phi + h.c. \quad + \quad |D_\mu\phi|^2 - V(\phi)$$

The Lagrangian controls the dynamics and the kinematics of the theory.

The first term is the scalar product of the field strength tensor $F_{\mu\nu}$ and encompasses the U(1), SU(2) and SU(3) gauge terms. It is a gauge invariant kinetic term constructed from the commutator of two covariant derivatives and contains the information for all interaction particles (except the Higgs boson) to exist and interact.

The second term describes what happens when those interaction particles meet matter particles. This summand contains the description of the three fundamental interactions the Standard Model can account for - electromagnetic, weak and strong. The gravitational force between two particles is extremely small at subatomic scales and can be neglected when dealing with particle interactions.

The third term in the Lagrangian resolves the coupling of matter particles to the Higgs field and describes their mass generation mechanism.

The last entry reveals how the weak interacting bosons couple to the Higgs field and how they obtain their mass. It also illustrates the potential of the Higgs field and leads to the mechanism of spontaneous symmetry breaking.

Elementary particles are divided into two categories, based on their spin, an intrinsic property they possess.

The fundamental matter particles are the fermions, half-integer spin particles that obey the Fermi-Dirac statistics. There are 12 particles and 12 respective antiparticles, which have the same mass, but possess opposite electric charge. Half of the particles are quarks - up (u), down (d), charm (c), strange (s), top (t), bottom (b) - which have a color charge and take part in the strong interactions, and the other half is made of leptons - electron (e), electron neutrino (ν_e), muon (μ), muon neutrino (ν_μ), tau (τ), tau neutrino (ν_τ) - that have no color charge; both types participate in electroweak interactions. The matter particles and some of their properties are listed in Table 2.1.

Lepton	Charge [e]	Mass [c^{-2}]	Quark	Charge [e]	Mass [c^{-2}]
e	-1	0.511 MeV	u	+2/3	2.2 MeV
ν_e	0	< 2.2 eV	d	−1/3	4.7 MeV
μ	-1	105.66 MeV	c	+2/3	1.28 GeV
ν_μ	0	< 0.17 MeV	s	−1/3	96 MeV
τ	-1	1.777 GeV	t	+2/3	173.1 GeV
ν_τ	0	< 18.2 MeV	b	−1/3	4.18 MeV

Table 2.1: The fermions of the Standard Model. The mass is taken from [4].

In the other category are the force carrier particles, the bosons, which have integer spin values. They obey the Bose-Einstein statistics, meaning they can overlap and coexist with other bosons, unlike fermions that follow the Pauli exclusion principle. The gauge bosons (spin 1) incorporate the massless photon (γ) – the mediator of the electromagnetic interactions between charged particles, the eight massless gluons (g) – which mediate the strong interaction between quarks and other gluons, and the three massive weak bosons (W^+, W^- and Z^0). Joining them is the Higgs boson (H^0), a massive scalar (spin 0), which is responsible for the mass generation of the weak bosons, but leaves the photon massless. It is equally liable for generating mass for the charged leptons and the quarks. The mediators and some of their properties are listed in Table 2.2.

Boson	Charge [e]	Mass [c^{-2}]	Spin	Mediator of
Gluon g_{1-8}	0	0	1	Strong interaction (QCD)
Photon γ	0	0	0	Electromagnetic (QED)
$W^{\pm}$	$\pm$ 1	80.39 GeV	1	Weak interaction
Z^0	0	91.19 GeV	1	Weak interaction
Higgs H^0	0	124.97 GeV	0	Higgs field

Table 2.2: The bosons of the Standard Model. The mass is taken from [4].

In total, there are 61 elementary particles (accounting for the color charge of quarks) described by the Standard Model, all of them having been experimentally detected.

2.2 Elementary particle production

To be able to study the elementary particles and their interaction, one possibility is to generate a high energy beam. The basis of this reasoning lies with the de Broglie wavelength associated with a particle $\lambda = h/p$, relating its momentum and mass. To resolve small structures, like particles, a comparably short wavelength, and therefore a high momentum needs to be provided. As such, the higher the energy, the more penetrating distance it can achieve and the better it can resolve structures. In turn, the more energy available in the collision, the higher the energy available to create the more massive particles.

Experiments in particle physics are primarily designed to benefit the following purposes:

- To verify existing theories and the particles deriving from them, as well as their postulated behavior
- To possibly discover new particles
- To measure particle properties, like mass, charge, spin and interaction type (strong, weak or even new interactions) via their production and decay channels

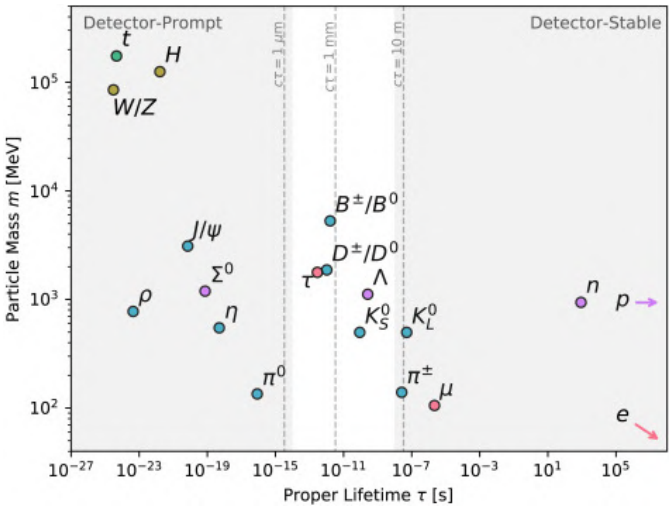

Figure 2.2: A selection of Standard Model particles as a function of mass and lifetime. Taken from [5].

In order to prove that a theory is right and to be able to see the multitude of particles, scientists need to be able to detect them. But even before that, particles need to first be produced.

With the exception of the photon, the electron, the proton and the lightest of the three types of neutrinos, the rest of the particles decay very rapidly. Furthermore, they can't be probed with just our human senses.

2.2.1 Producing elementary particles

Photons are in abundance around us, zipping through air at any given time on a spectrum of different frequencies depending on how they are created. Focusing them is extremely easy and is routinely done in lasers by stimulated emission.

Electrons are also easily produced by thermal emission. In order to get a beam of electrons, a positively charged piece of metal with a hole, acting as anode, is placed some distance away from the emitter.

Protons are processed from hydrogen, which is the most abundant element in the Universe. A hydrogen atom has a single positively charged proton in the nucleus and a single electron bound to the nucleus by the Coulomb force. An electric field can be applied to the system to strip hydrogen atoms of their electrons, leaving only the protons behind.

Neutrinos are the hardest to artificially produce and observe. They are sometimes called "ghost particles". They are naturally produced by various radioactive decays, by our Sun through nuclear fusion or by distant supernovae. Neutrinos can also be created artificially with nuclear reactors and particle accelerators.

For more exotic particles there are three main means of production:

- Nuclear reactors - radioactive decays result in alpha particles, electrons, gamma rays, neutrons and neutrinos.
- Particle accelerators - by smashing together particles one can generate every particle in the standard model.
- Cosmic rays - multi-TeV extra-galactic particles bombard earth daily, albeit at a very small rate [4]. Their energies are bigger than what is technologically achievable on earth at this time. At the atmosphere interface, these fragments produce showers of secondary particles which are then detected on the ground.

The heavier the particle to be produced is, the higher the energy of the collision must be and the higher the energy for a collision, the bigger the accelerator complex. The biggest accelerator complex is the Large Hadron Collider (LHC) at CERN. Further details about the accelerator complex and the detectors therein are given in Sec. 3.1.1.

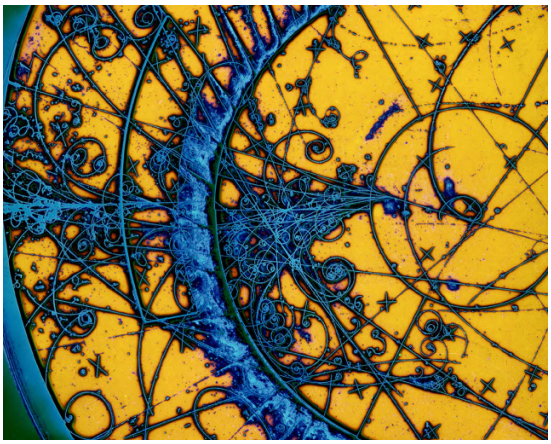

Figure 2.3: Event from the Big European Bubble Chamber (BEBC) at CERN. [6] Particles create an ionization track around which the liquid in the vessel vaporizes, forming microscopic bubbles.

2.2.2 Particle detection

We are told to *trust* the idea put forward by ancient Greeks, that atoms are out there, too tiny to see and they are the fundamental bricks that make up our world. The word *trust* does not exist in the world of science. It is instead replaced by *proof*. And there is a lot of work involved for just that purpose!

The traditional way of looking at small things has been by the use of microscopes and the light waves deflected by objects. Until very recently, microscope technology was unable to see even individual atoms. In a strict sense, this is still true. Atoms are *invisible* to light waves, because they are smaller than the visible wavelengths.

Moreover, atoms are huge in comparison with elementary particles! As such, some other means to *see* them are needed. The main idea behind particle detection is that instead of searching for the particle itself, its presence is inferred and the path that it traveled is reconstructed based on a unique signature track created in its wake, as it passes through matter. It can be compared to a police reconstruction at a crime scene.

After a collision, the resulting charged particles (or recoil particle) usually travel in straight lines, unless bent by some externally applied magnetic field. Given that different particles have different mass, a subtle separation can be made by the curvature of a particle in a known magnetic field. Not only that, but the sign of their charge can be deducted from the direction of the curve, due to the difference in the electric charge.

Following the Lorentz force formula, a particle of charge q traveling perpendicular to a magnetic field B will have a momentum p proportional to the radius of curvature r. In SI units [1], this reads:

$$p\,[\mathrm{GeV}/c] \;=\; 0.3 \cdot q\,[e] \cdot B\,[\mathrm{T}] \cdot r\,[\mathrm{m}]$$

On top of that, particles lose energy in a medium due to collisions and bremsstrahlung[2]. Accordingly, particles can be identified by where they stop in the detector.

Last, but not least, for particles with relatively long proper lifetime, a time-of-flight measurement can yield information about the particle's velocity. To this end, two detectors that record the time at which a particle traverse their sensitive medium are used, and the time difference computed.

Combining these different sources, it is possible to reconstruct the properties - momentum, mass, charge, energy - of particles interacting with the detectors, and ultimately the identity of the particles themselves.

"Given how small the atom is it's amazing how much physics we can get out of it. We haven't just worked out what atoms are, we've realised that they are marvellously complex structures." (Laura J. Harkness-Brennan) [7].

[1] The International System of Units (SI), commonly known as the metric system, is the international standard for measurement. It comprises a coherent system of units of measurement built on seven base units.

[2] Bremsstrahlung is electromagnetic radiation produced by the deceleration of a charged particle when deflected by another charged particle, typically an electron by an atomic nucleus

3 Down the rabbit hole

3.1 A modern type of architecture

Major advances in particle physics have been, in part, achieved by building complex accelerator systems of ever increasing energies. This progress is complemented by disciplines that go beyond the limits set by current accelerator technology. They can either point to the direction of neutrinos, nucleon decay, dark matter searches or to astrophysics and cosmology where the Universe is used as a source of high energetic particles that cannot be produced on Earth.

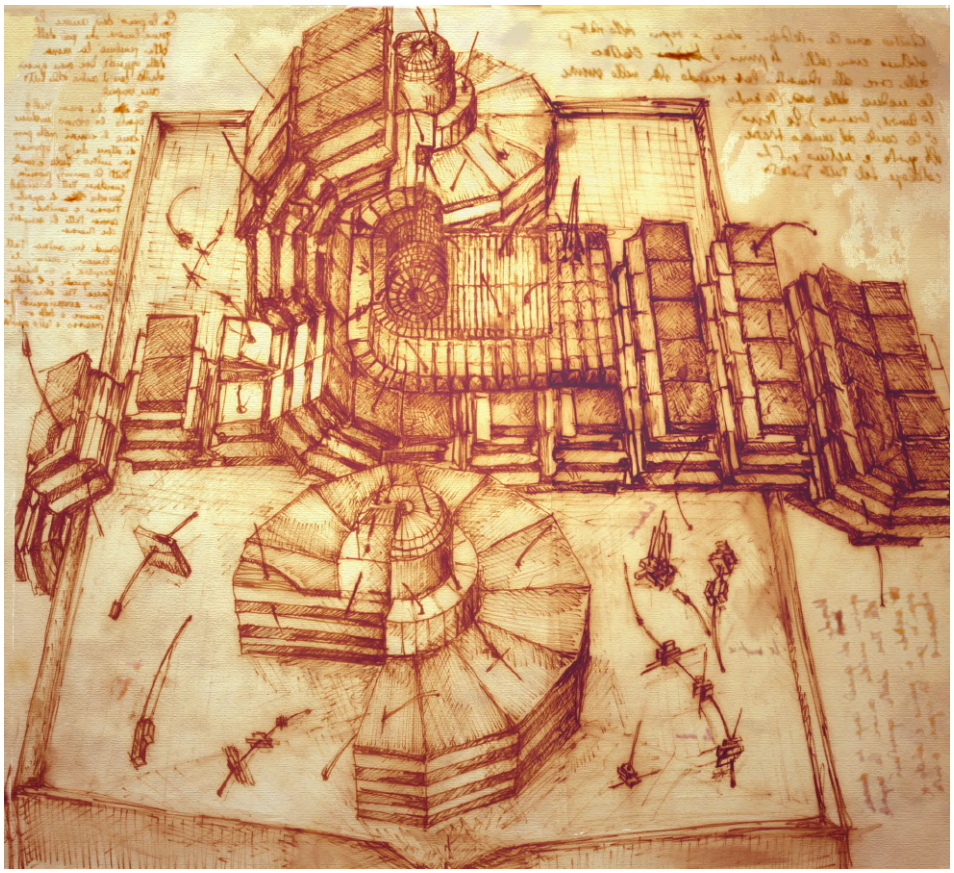

Figure 3.1: Drawing of a detector by S. Cittolin in the style of Leonardo da Vinci [8].

In the years following the discovery of the electron, particle accelerators emerged into an extensive array of devices, from the cathode rays used in the television picture tubes to the gargantuan colliders of particle physics. They remain a crucial tool to tackle a multitude of exciting questions about the world we live in.

3.1.1 Accelerators at the Terascale

"The act of colliding subatomic particles at very high energy is not merely a destructive act; it is, more profoundly, a creative one." — Matt Strassler [9]

Ever since scientists understood that exceedingly rare particles can be created by having sufficient energy packed in a small space, a quest to attain higher and higher energy regimes has begun.

The most convenient way of making use of the fact that matter is a form of energy is to get any particle and hurl it at a target. Even better, one can get double the amount of energy if two of those particles are fired at each other. The higher the energy of the colliding particles, the more energy is available to be transformed into mass.

A particle accelerator is a complex machinery that uses electromagnetic fields to force charged particles into a narrow beam, at velocities up to the speed of light. Then, the particles are either smashed onto stationary targets or against other particles circulating in the opposite direction.

At present, CERN's Large Hadron Collider (LHC) is the largest and most powerful accelerator. Laying below ground, in the tunnel of the former Large Electron–Positron Collider (LEP) and stretching 27 km in circumference, it was designed to accelerate protons (pp) and heavy-ions up to a maximum energy of $\sqrt{s} = 14\,\text{TeV}$ (7 TeV per beam), probing the high energy frontier of particle physics.

Alongside the center of mass energy, one of the main parameters describing the accelerator system is the instantaneous luminosity ($\mathcal{L}$). This is the parameter that quantifies the ability of a particle accelerator to produce the required number of interactions. It is expressed in units of $\text{cm}^{-2}\,\text{s}^{-1}$. The bigger the value of $\mathcal{L}$, the bigger the number of collisions.

The LHC houses two high energy particle beams that travel close to the speed of light. The accelerator guides the particles along two tubes called beam pipes that are kept in ultra-high vacuum. The beams travel in opposite directions and are steered along the accelerator ring by powerful electromagnets.

Such a complex has two stringent requirements [10]. In a high energy collision with composite particles (like hadrons), only the constituents, which carry just a fraction of the total momentum, interact with each other. As such, less than the center-of-mass energy of the accelerated particle is available for the collision. Therefore, it is desirable to have high energy proton/ion beams. On the other side, it needs to have a high collision rate to acquire enough data for extremely rare events associated with new particles.

Protons start from a hydrogen bottle located at the beginning of the Linear Accelerator (LINAC) 2 (see Fig. 3.2). Here, the hydrogen is stripped off its electron by an electric field and only protons enter the linear accelerator. Inside, radio-frequency (RF) cavities alternate between positive and negative polarity, producing an initial boost by accelerating or decelerating protons of different energies, constraining them at a desired energy.

To ensure that the particle beam does not spread, quadrupole magnets are used, while dipole magnets define a fixed orbit and keep the protons on track. At the end of LINAC 2, the protons have gained an energy of 50 MeV and are ready for the next stage.

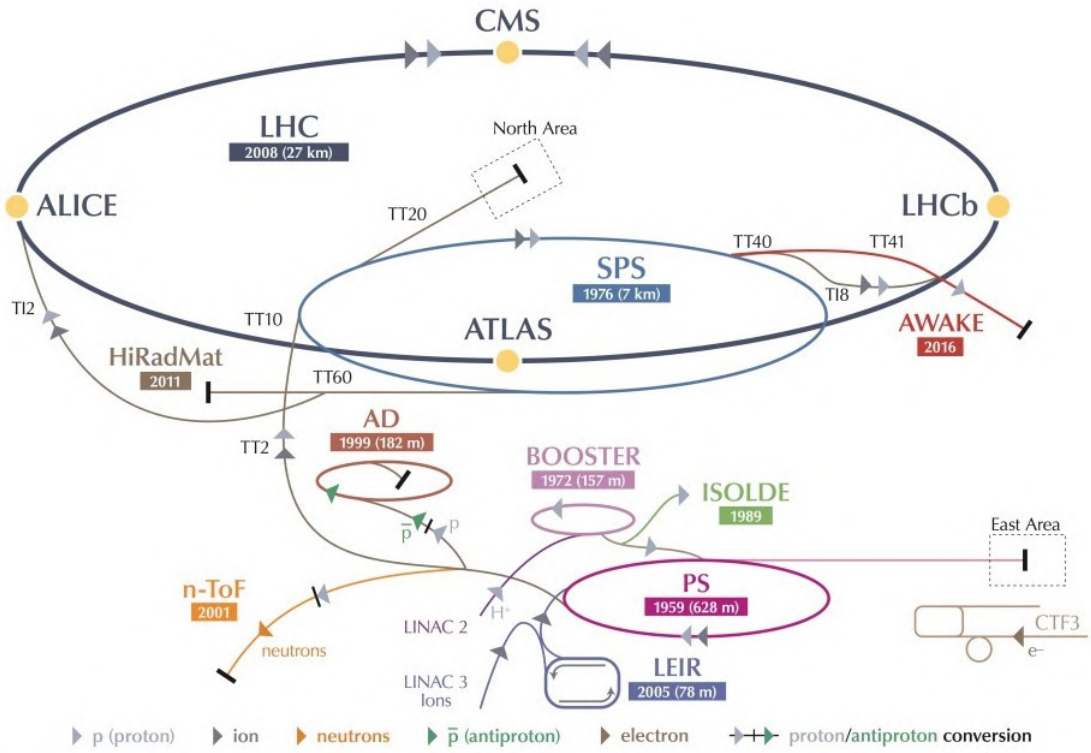

Figure 3.2: Schematic of the LHC accelerator complex (dark grey ring), the last in a complex chain of particle accelerators. The smaller machines in the chain help boost the particles from rest to their final energies while also providing beams to smaller experiments [11].

They are then injected into the Synchrotron Booster, a device featuring four superimposed synchrotron rings, that accelerate the protons from 50 MeV to 1.4 GeV. From here, they are fed to the Proton Synchrotron (PS) and pushed to 25 GeV.

Alternatively, the PS can be fed with heavy ions, albeit with a smaller bunch density. LHC currently accelerates mainly the ^{208}Pb isotope as part of its heavy-ion programme (a run was also done with ^{129}Xe) since it has a spherical nucleus, the ground state configuration is well known and the collision geometry is simple. A piece of pure Pb is heated and vaporizes a small number of atoms. Throughout their acceleration in an electric field the Pb atoms are stripped of their electrons and remain as positively charged ions. The Pb atoms are pre-accelerated in the LINAC 3 and injected into the Low Energy Ion Ring (LEIR), before they are delivered to the PS.

The particles in the few tens of GeV range exiting the PS are supplied to the Super Proton Synchrotron (SPS) ring. This is the last step particles have to take to be ready for injection in the LHC ring. The SPS increases the energy of the particles up to 450 GeV, which, by now, are split into bunches.

Inside the LHC, a number of accelerating structures continue to boost the energy of the particles up to a maximum of 7 TeV $\times$ (Z/A) (for Pb the atomic number –Z– and the mass number –A– are 82 and 208, respectively; for protons, the ratio is unity).

Irregardless of the particles being accelerated, the particle beams cross at interaction points, which are surrounded by detectors. At the LHC four such interaction points exist, housing four detectors ALICE, ATLAS, CMS, and LHCb. These detectors are showered with particles produced when the two beams cross each other.

3.2 ALICE

A **L**arge **I**on **C**ollider **E**xperiment (ALICE) is a detector at the LHC that focuses on products of heavy-ion collisions. It was designed to address the physics of strongly interacting matter and the quark-gluon plasma (QGP), the amalgamate of hot and dense particles mentioned in the introduction.

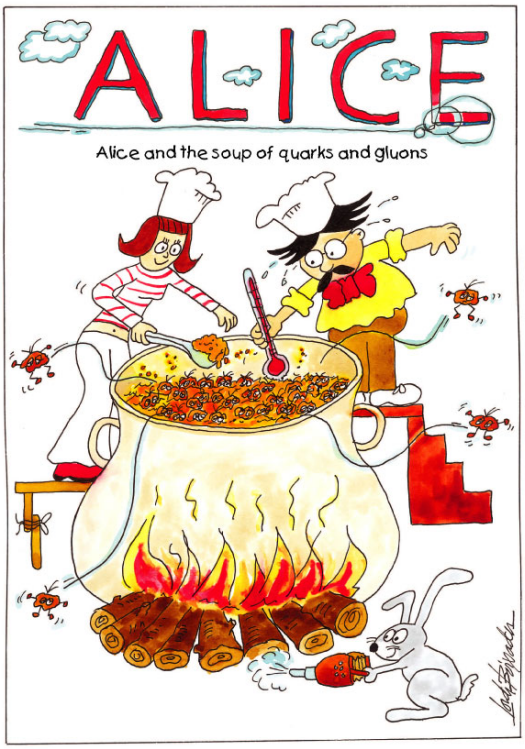

Figure 3.3: The quark-gluon plasma, a soup of hot and dense stuff [12].

3.2.1 Quantum ChromoDynamics

The exotic medium created in heavy-ion collisions exists only transiently, undergoing a phase transition while it cools down. The physics governing the QGP, its transition and its properties are the physics of the strong interaction, which is included in the Standard Model.

The quantum field theory of the strong interactions is Quantum Chromodynamics (QCD). It is a non-abelian gauge field theory that has as basic dynamical degrees of freedom the quarks and gluons. Its Lagrangian density is invariant under local SU(3) symmetry transformations and can be written as [13]:

$$\mathcal{L}_{\mathcal{QCD}} = -\frac{1}{4} G^a_{\mu\nu} G^{\mu\nu}_a + \sum_f^{N_f} \bar{q}_f \left(i\gamma^\mu \partial_\mu - g_s \gamma^\mu \sum_a \mathcal{A}^a_\mu \frac{\lambda^a}{2} - m_f \right) q_f$$

where q_f represents the quark Dirac spinor with the index f being the respective quark flavor and $g_s = \sqrt{4\pi\alpha_s}$ the strong coupling constant.

Gluons are physical degrees of freedom and therefore must carry energy and momentum themselves. As such, a term must be added in the Lagrangian to account for these physical features. This is the gauge invariant gluon field strength tensor $G^a_{\mu\nu}$ defined as:

$$G^a_{\mu\nu} = \partial_\mu \mathcal{A}^a_\nu - \partial_\nu \mathcal{A}^a_\mu + g_s f^{abc} \mathcal{A}^b_\mu \mathcal{A}^c_\nu$$

$\mathcal{A}^a_\mu$ are the 8 gluon fields ($a = 1, ..., 8$) introduced to restore local SU(3) gauge invariance, one for each of the generators, f^{abc} are the structure constants of the SU(3) group.

QCD interactions are able to exchange the quark color charge (the analog of the electric charge in QED) through gluons, while conserving the quark flavor. There are no explicit mass terms for the gluons in the initial QCD Lagrangian; there is just a parameter for the mass of a quark, obeying the Dirac equation and is not directly observable. The masses of the quarks are generated through a symmetry breaking phase transition of the electroweak interactions, by the coupling to the Higgs field.

The electromagnetic interaction proceeds due to photon exchanges. Analogously, the partons interact exchanging the gluons. As quarks separate, the force between the quarks takes the form of a color field mediated by gluons. When enough energy is stored in these so called flux tubes [14], colorless $q\bar{q}$ pairs are formed out of the vacuum. This is what makes it impossible to isolate individual quarks.

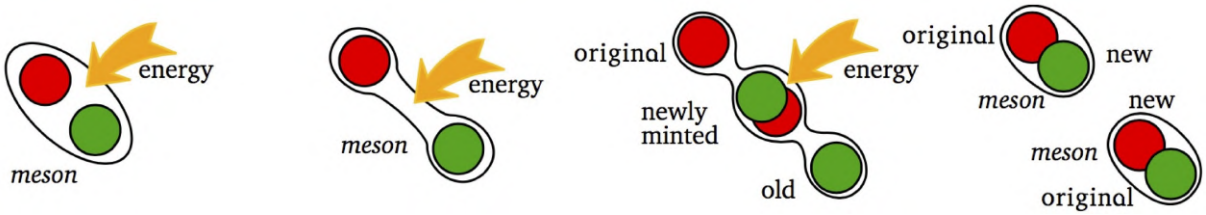

Figure 3.4: Color confinement. At a certain range it is more energetically favorable to create a $q\bar{q}$ new pair than to continue to elongate the color flux tube [15].

Colored objects are always confined to color singlets; objects with non-zero color charge cannot propagate as free particles. Due to the fact that gluons carry color charge, they are able to interact with each other. This fact can be seen in the presence of the last term of the gluon field strength tensor.

These gluon self-interactions are the reason why the strong interaction is fundamentally different from QED and are responsible for many of the unique and salient features of the QCD, like asymptotic freedom and color confinement, the last of which, although analytically unproved, is a well established fact from decades of experiments. In terms of Feynman diagrams, the analogy to QED works so far.

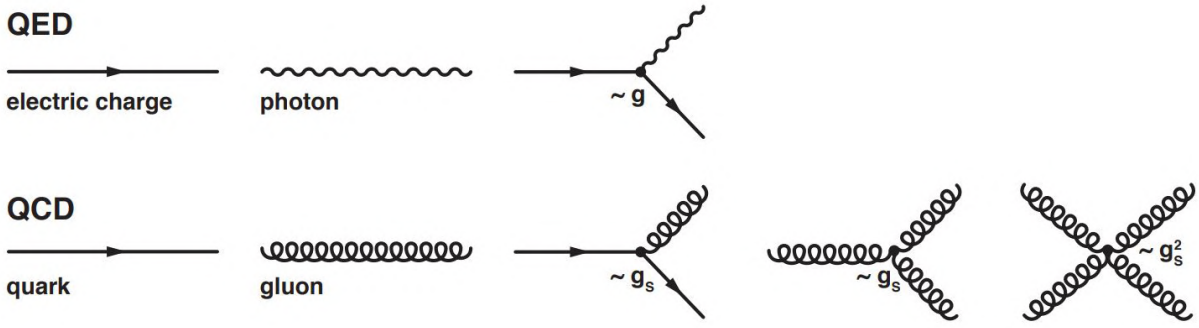

Figure 3.5: QED and QCD fundamental vertices. The extra term in the gluon field strength tensor gives rise to gg self-interactions [16].

The quantity that describes these interactions is the strong coupling constant α_s. Given the different physics processes encountered as the renormalization[1] scale changes, it is said that the coupling constant is *running* [17].

In perturbative QCD, it can be shown that the coupling constant, in first order, after renormalization is given by [4]:

$$\alpha_s(Q^2) = \frac{\alpha_s(\mu^2)}{1 + \beta\alpha_s(\mu^2)\ln\left(\frac{Q^2}{\mu^2}\right)}$$

The renormalization of the strong coupling constant [18] to a scale μ allows α_s to take values corresponding to measurements done at different energy regimes. At a momentum transfer of Q^2 comparable to the renormalization scale, the equation gives a measure of the strength of the strong interaction.

The peculiar aspect of this equation is the β term:

$$\beta = \frac{11N_c - 2n_f}{12\pi}$$

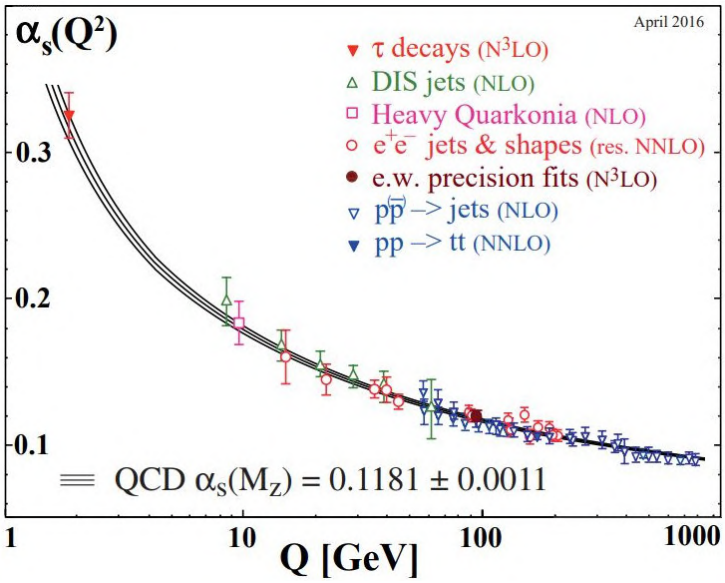

Figure 3.6: The running of α_s [4].

Computing for $n_f = 6$ for the number of quark flavors and $N_c = 3$ for the number of quark colors, it can be seen that $\beta > 0$. This is due to the positive contribution from the gluon loops (last two Feynman diagrams from the bottom line in Fig. 3.5).

At high momentum transfers ($Q^2 \to \infty$), an immediate consequence of the running coupling constant is that $\alpha_s \to 0$. This is known as asymptotic freedom [19]. Basically, quarks and gluons will no longer be tightly bound by the strong force when the energy density is high, but will behave as if they are quasi-free particles.

QCD has been successful in predicting phenomena involving large momentum transfers, but its perturbative methods fail at the scale of the hadronic world, where α_s increases. Lattice QCD [20] provides a non-perturbative numerical approach to the strong force for determining the low energy properties of QCD.

When heavy ions collide at high energies they form a soup of partons, labeled the quark-gluon plasma, a fireball of hot and dense matter. It is believed that some 10 ps after the Big Bang and lasting for 10 µs [21] the Universe was in a quark-gluon plasma state. After the Universe expanded and cooled down, the QGP coalesced into hadrons - neutrons and protons, in particular - which made the formation of atomic nuclei possible.

[1] Renormalization is a procedure in quantum field theory by which divergent parts of a calculation, leading to nonsensical infinite results, are absorbed by redefinition into a few measurable quantities, thus yielding finite answers.

This plasma is not observed directly in nature, but distant astrophysical objects - like the neutron stars - might conceal this form of matter in their dense center [22]. By studying it, scientists hope to have a better understanding of what happened after the Big Bang and to disentangle the nature of matter at extreme conditions of temperature and density.

QCD leads to a prediction of a deconfined state of partons [23] at energy densities exceeding $1\,\mathrm{GeV/fm^3}$. The confinement/deconfinement phase transition is accompanied by the breaking/restoration of the chiral symmetry, which means that quarks will assume their current mass (the Higgs mechanism generates the few MeV current mass of the u and d quarks; when the quarks condense in the vacuum, by means of the chiral symmetry breaking, they gain an *effective* (constituent), dynamically generated mass of some 300 MeV; constituent masses are only defined in the context of a particular hadronic model).

As there is a transition from the normal hadronic matter to this high-temperature QGP, there has to be a sort of boundary separating the two states, as can be seen in Fig. 3.7.

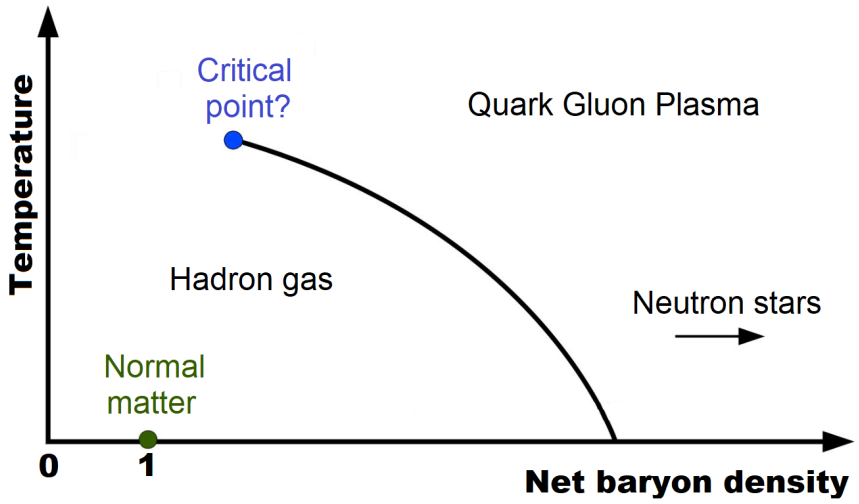

Figure 3.7: A sketch of the phase diagram of QCD matter.
The QGP can be achieved by either having a very dense or a very hot environment. In the case of heavy-ion collisions, a very hot environment is created.

While the ordinate will be expressed in all representations of the phase diagram as the temperature, a measure of how much energy is put in the system, the abscissa can either be represented by the net baryon density (ρ) or by the baryon chemical potential (μ_B). In Fig. 3.7 the net baryonic density is chosen, a measure of the difference between baryon and antibaryon densities.

The point at $T = \rho = 0$ is where the vacuum of QCD is situated at. Temperature ($T = E/k_B$) is expressed in units of MeV, where 100 MeV corresponds to approximately $10^{12}\,\mathrm{K}$. The boundary constrained by the black line on the lower left side is where the ordinary hadronic matter is situated.

At low net baryon densities, the transition between hadronic matter and a QGP is believed to be a smooth cross-over [23], while at large densities, the transition is of first order [24]. A critical point separates these two regions and lattice QCD calculations indicate that it should happen at a critical temperature of $T_C = (154 \pm 9)$ MeV [25].

Experimentally, the phase diagram can be explored in relativistic heavy-ion collisions, which were envisaged to be an ideal way to probe the harsh conditions of extremely high temperature and density.

If two heavy ions are collided with sufficiently high energy, they might just create a *fireball* of quarks and gluons above the temperatures and densities needed for deconfinement. Once a QGP has been formed in a collision, it will expand rapidly and cool off in about $10\,\mathrm{fm}/c$ [26] due to a very high density gradient compared to the surrounding medium.

The collision between two ultra-relativistic nuclei is an event characterized by a complex space-time evolution (see Fig. 3.8).

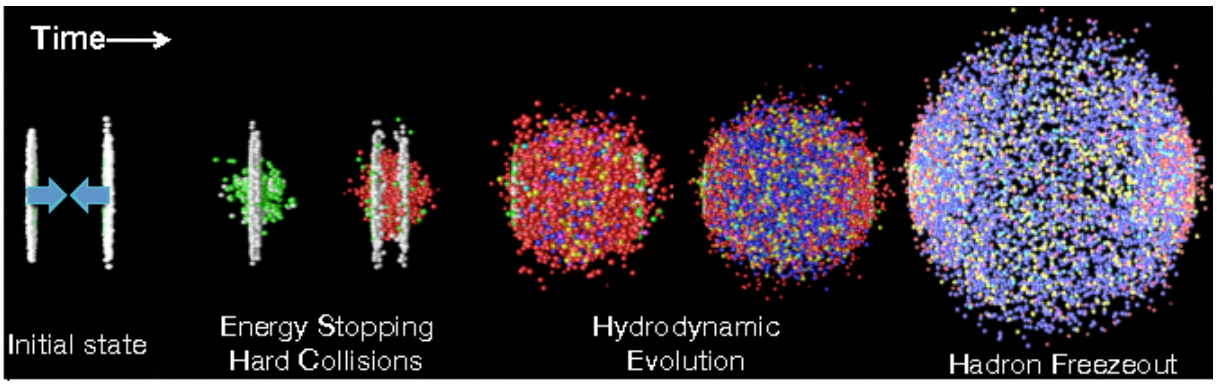

Figure 3.8: Evolution of the system formed after the collision of two nuclei at high energies [27].

The nuclei travelling in the accelerator ring at energies of a few TeV are Lorentz contracted. The disks approach each other until they collide.

The partons will scatter on one another, leading to an exchange of energy and momentum. In case of hard inelastic scattering processes, large momentum transfers allow the production of heavy quarks (c or b quarks) and electroweak gauge bosons ($W^{\pm}$, Z and γ). The heavy quarks are powerful probes to study the QGP since they will suffer multiple scattering in the medium during their propagation, leading to radiative and collisional energy loss and transverse momentum broadening, therefore being sensitive to the medium properties.

Within about $0.1 - 1$ fm/c [28] (roughly few 10^{-24} s) a system of quarks and gluons will form. The size and geometry of the medium is highly dependent on the overlap region of the two nuclei. The more central the collision, the higher the number of participating nucleons.

Although not initially in thermal equilibrium, the system will thermalize quickly and will evolve according to the equations of hydrodynamics. The plasma will expand and its temperature will start decreasing until it reaches the critical transition temperature T_C and undergoes the transition from a QGP to a hadronic medium (hadronization). In Pb-Pb collisions at LHC, this is estimated to happen after a time of $\tau \sim 10\,\mathrm{fm}/c$ [29].

After the hadronization, a stage called (*chemical freezeout*) is reached, where inelastic collisions will no longer occur and the particles species will be fixed.

At a time $\tau \sim 20\,\mathrm{fm}/c$, the density will become so low that it will be improbable for constituents to interact elastically. After the temperature drops below this *kinetic freezeout*

point, the momentum of the particles will be fixed. Finally, the hadrons will emerge from the collision region and can be detected.

Typical values for thermal and chemical freezeout at LHC in central Pb-Pb collisions at 2.76 TeV are $T_{\mathrm{chem}} = (156.5 \pm 1.5)$ MeV [25] and $T_{\mathrm{kin}} \sim 100$ MeV [30].

Bearing in mind that the time scales involved for the creation and evolution of the QGP are in the order of fm/c, the direct measurement of any variables from the system is impossible. Accordingly, quantities involving the QGP have to be obtained indirectly by studying those particles created in the first stages of the collision, before the QGP formed, which were able to experience its full evolution.

One observable used to quantify the effect of the nuclear medium on particle production is the nuclear modification factor (R_{AA}). It is defined as the p_{T}-differential particle yield measured in nucleus-nucleus collisions divided by the particle yield in proton-proton collisions:

$$R_{\mathrm{AA}}(p_{\mathrm{T}}) = \frac{1}{\langle N_{\mathrm{coll}} \rangle} \frac{\mathrm{d}N^{\mathrm{AA}}/\mathrm{d}p_{\mathrm{T}}}{\mathrm{d}N^{\mathrm{PP}}/\mathrm{d}p_{\mathrm{T}}}$$

Nucleus-nucleus (A–A) collisions have to be scaled by the number of elementary nucleon-nucleon collisions (N_{coll}), considering that particles can undergo more than one interaction.

If an A–A collision would be the same as N_{coll} independent, simultaneously occuring pp collisions (see Fig. 3.9), then the nuclear modification factor would be equal to unity. However, variation of R_{AA} from unity signals a change of physics during the A–A collisions and provides input to quantify medium induced effects.

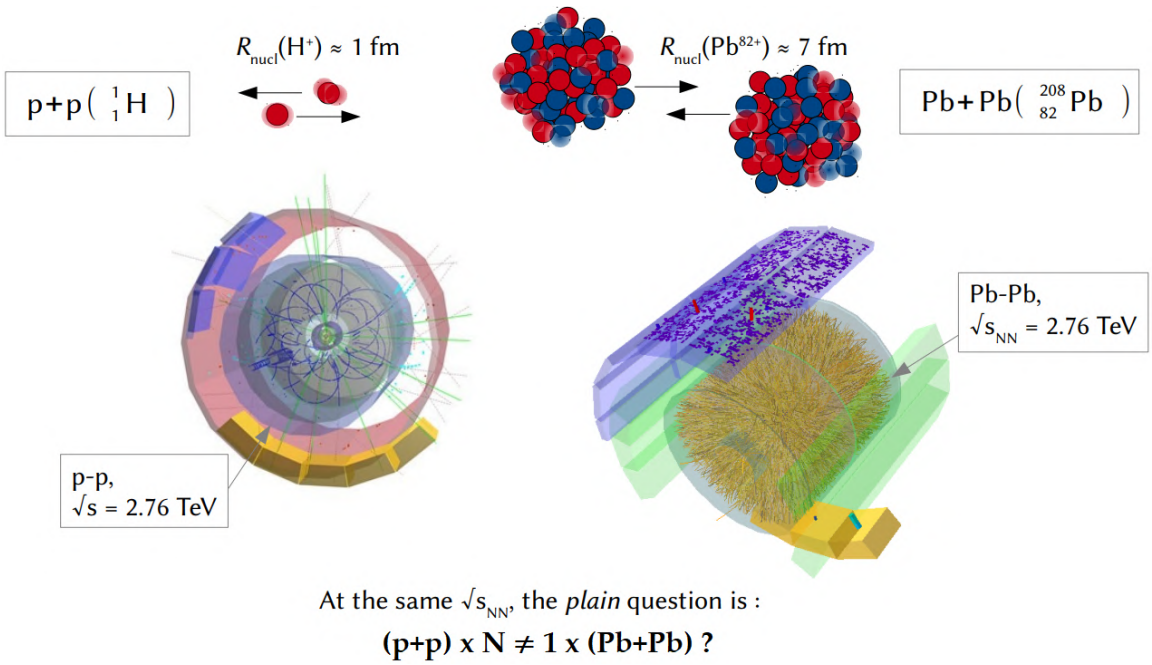

Figure 3.9: Comparison between a pp collision and a Pb-Pb collision at the same $\sqrt{s_{\mathrm{NN}}} = 2.76$ TeV. Plot taken from [31].

To investigate this effect, A–A, pp and p–A collisions have to be measured and compared. An example is shown in Fig. 3.10.

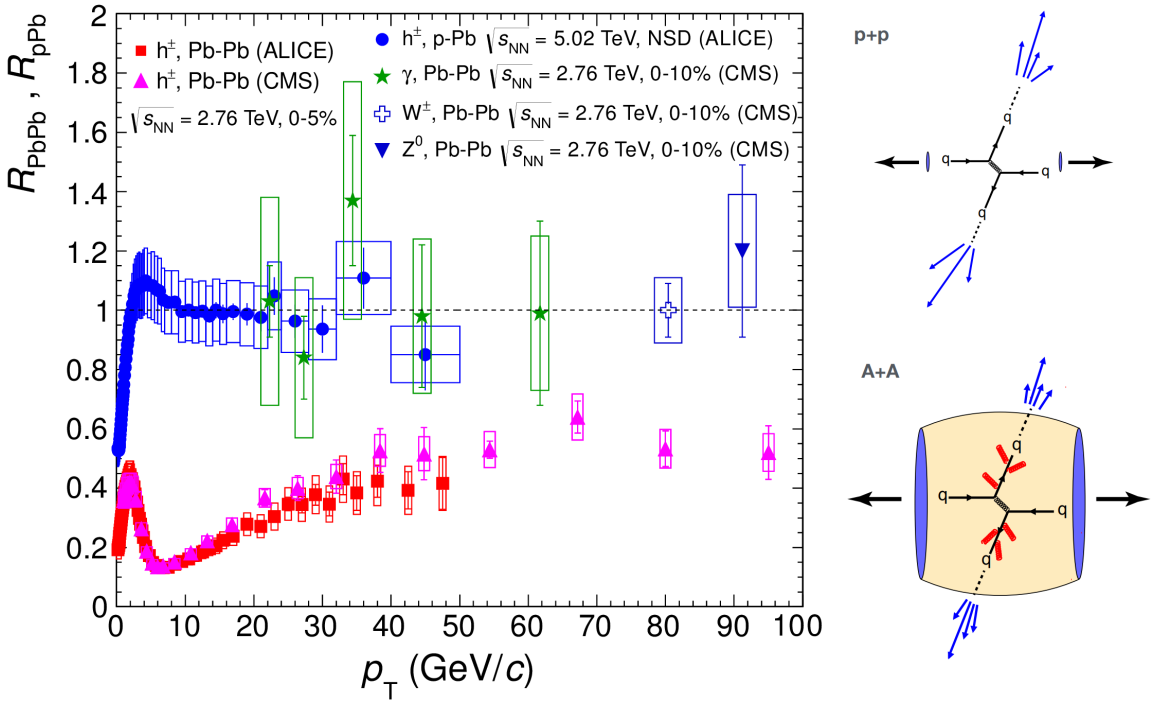

Figure 3.10: The p_T differential nuclear modification factor R_{AA} in central Pb–Pb and p–Pb collisions for charged hadrons and electroweak bosons [32] [33].

The p–Pb results are primarily used to differentiate signatures of the QGP from the effects already present in the interaction with the cold nuclear matter. These effects appear due to the fact that the nucleons are bound in the target nucleus. As such, p–Pb collisions at the same energy as Pb-Pb help disentangle initial from final state effects. The ALICE R_{pPb} measurement at high p_T is comparable with unity and shows no indication of nuclear matter modification of hadron production and is consistent with binary collision scaling.

As expected, the medium is nearly transparent to electroweak probes, like $W^{\pm}$, Z and γ, which are insensitive to the strong interaction dynamics and decay before the QGP is formed, are left unaffected and their nuclear modification factor is close to unity in Pb–Pb collisions, confirming the N_{coll} scaling.

The striking feature however is the fact that in Pb–Pb collisions the $R_{AA} < 1$. There is a big suppression by a factor of up to 7 for high p_T ($> 5\,\text{GeV}$) hadrons in Pb–Pb relative to the binary scaling expectations. This implies the creation of strongly interacting matter.

The shape of the R_{AA} in Pb–Pb collisions influenced by effects such as collective flow and energy loss, in addition to the cold nuclear matter effects. There is an interplay between these effects and different models are trying to explain the different behaviors. Nevertheless, a significant deviation from unity is seen in all energy regimes. This suppression is proof that in nucleus-nucleus collisions a new medium is formed.

3.2.2 The ALICE detector

There are plenty of reasons for why this hot and dense phase called the Quark-Gluon Plasma can be artificially created. But how can the properties of this exotic state of matter that prevailed in the first instants of the Universe be detected?

A dedicated heavy-ion experiment, ALICE, was proposed to be operated at the LHC. Its design was primarily driven by the physics requirements and the experimental conditions assumed in heavy-ion collisions at multi-TeV energy regimes.

The most demanding requirement of the experiment was the ability to cope with extreme particle densities expected in central Pb–Pb collisions. For this, data taken at lower energies in previous experiments has been extrapolated and suggested a factor of two to five increase in particle multiplicity is to be expected. Similarly, compared to the normal pp collisions at the nominal energy at LHC, this would mean an increase by three orders of magnitude of the number of ejected particles from the interaction [34].

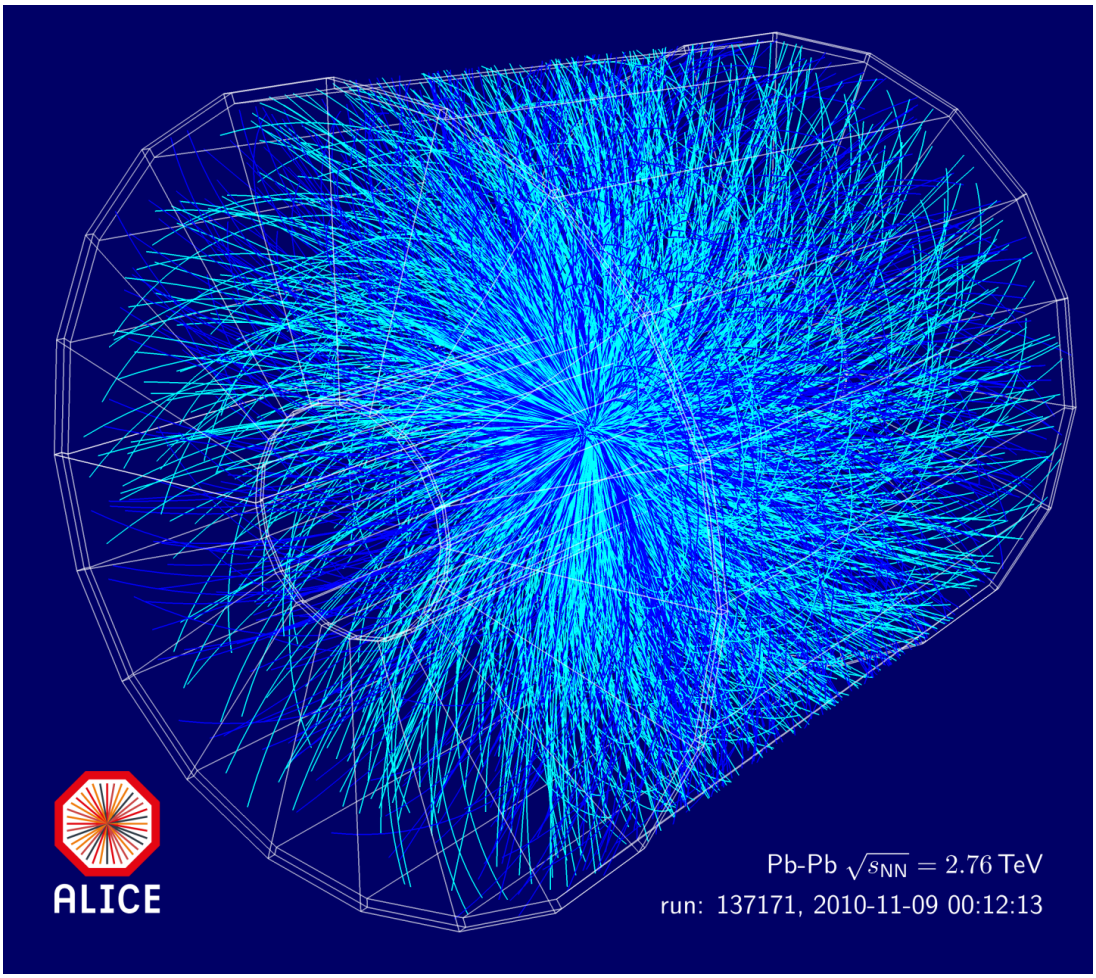

Figure 3.11: A high multiplicity Pb–Pb event recorded with ALICE at $\sqrt{s_{\mathrm{NN}}} = 2.76\,\mathrm{TeV}$ [35].

The main goal of ALICE is to record sensitive signatures from QGP observables. This is achieved by probing particles created inside the QGP that live long enough to experience the medium's evolution and are able to reach the sensitive detector layers. Assessing properties of this state requires a precise understanding of the underlying collision dynamics.

ALICE is also able to provide unique information on low-p_{T} pp physics (thanks to the low material budget and low magnetic field), which makes the experiment complementary to CMS and ATLAS.

Owing to the high multiplicity in the heavy-ion collisions, tracking of the particle trajectories is problematic. The detectors require fine granularity to be able to disentangle each track on an event-by-event basis out of several thousand reconstructed particles.

In ALICE this is done using three-dimensional hit information in a moderate magnetic field of 0.5 T. This ensures a large enough lever arm of the detector for tracking high momentum particles, while also safeguarding charged low-momentum particles from spiraling before reaching the tracking stations. By virtue of the mild magnetic field, it is possible to track particles over a large dynamic range, spanning more than three orders of magnitude, from about 150 MeV/c to well over 100 GeV/c [36].

The bulk of the particles are thermally produced, so low p_{T} tracking is mandatory. This is the case for low-mass dileptons, as well as collective effects at large length scales and resonance decays encountered in the aggregate of QGP observables. Nonetheless, there are also jet physics events for which the energies exceed several tens of GeV that need to be unambiguously identified.

Since most of the observables in the heavy flavor sector are mass or flavor dependent, ALICE is required to have good particle identification (PID) capabilities over much of the momentum range. Therefore, ALICE employs almost all of the PID technologies in its volume - specific ionization energy loss, time-of-flight, transition radiation and Cherenkov detectors, calorimetry and muon stations. This is motivated by the fact that devices for PID usually operate well in relatively small momentum ranges, whereas ALICE has a wide range of particle momenta to cover (see Fig. 3.12); therefore, so different technologies need to be combined to amass reliable and precise PID.

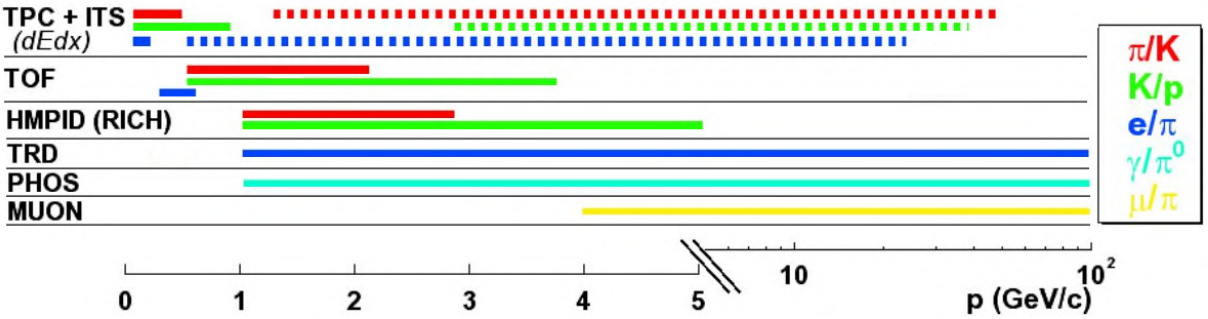

Figure 3.12: ALICE PID performance as a function of momentum in terms of particle ratios. Solid lines represent a separation of $\geq 3\sigma$ and dashed lines $\geq 2\sigma$ [37].

All the constraints summed before lead to the final design of ALICE, a low mass detector complex, encompassing 18 subdetector systems, each with its own specific detection technology and design constraints. The experimental setup of ALICE is shown in Fig. 3.13.

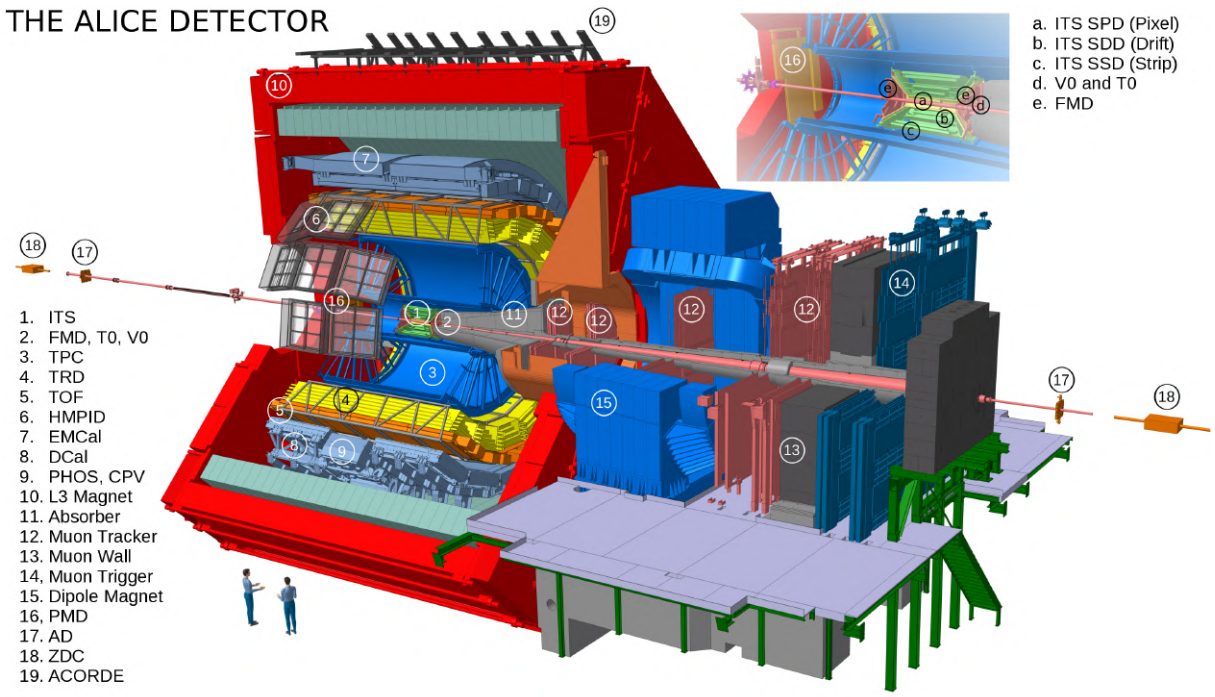

Figure 3.13: The ALICE experiment and its subdetectors [38].

Although referred to as one of the small detectors, the meaning of *small* in the LHC's context means a detector that stands 16 m tall, 16 m wide and 26 m long, weighing approximately 10000 tons.

The ALICE ensemble is divided into a central barrel part that mainly measures hadrons, electrons and photons and a forward single arm spectrometer that specializes in measuring muons.

The ALICE global coordinate system is used to describe the positions of detectors; on top of that, the parameters of reconstructed tracks are also given in the global coordinate frame. It is a right-handed Cartesian coordinate system with the origin at the interaction point. The longitudinal direction (z-axis) is following the beam axis (positive z points along towards the access shaft to the ALICE cavern), the x-axis points towards the accelerator center, in the local horizontal plane and the y-axis points in the direction perpendicular to the x-axis, with positive y facing upwards.

The rapidity y of a particle is defined as

$$y = \frac{1}{2} \ln \left(\frac{E + p_z}{E - p_z} \right)$$

where E is the energy of the particle and p_z the longitudinal momentum relative to the beam axis. In high energy collisions, the rapidity is often replaced by the pseudo-rapidity η in the limit where $p \gg m$:

$$\eta = -\ln\left[\tan\left(\frac{\theta}{2}\right)\right] = \frac{1}{2}\ln\left(\frac{|\overrightarrow{p}| + p_z}{\overrightarrow{p} - p_z}\right) \approx y$$

where θ is the polar angle relative to the beam axis.

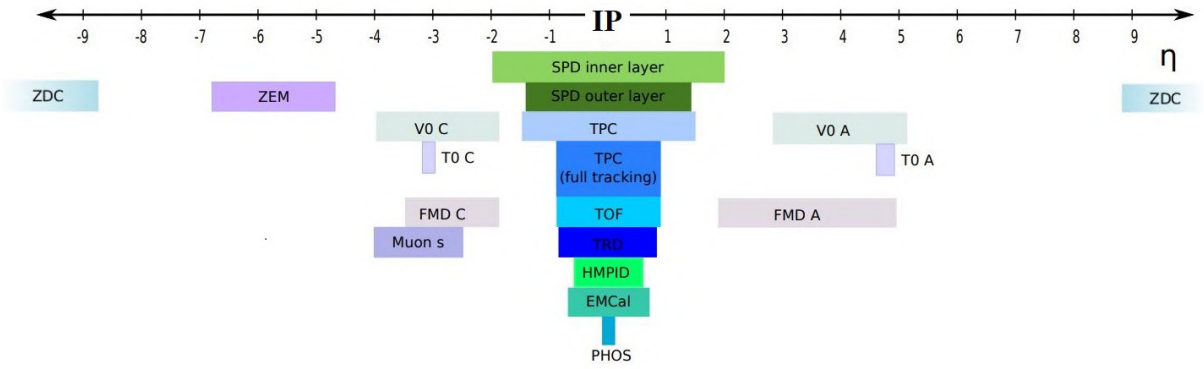

Figure 3.14: Pseudo-rapidity and azimuthal coverage of the ALICE detector system. [39].

In spite of the rather modest intensity of heavy-ion beams in the LHC (i.e. interaction rates of the order of 10 kHz) and the small up-time (1 month/year of Pb-Pb data), one event can generate upwards of 100 Mb (Pb–Pb), so the data acquisition system has a very high bandwidth with speeds of more than 1Gb/s to permanent storage, which is able to collect hundreds of millions of events.

The central barrel is bathed in the uniform magnetic field of the L3 solenoid magnet and consists of a set of tracking detectors designed to measure the curvature of the particles and thus relay information about their momentum. It covers the direction perpendicular to the beam, from 45° to 135°, approximately the pseudorapidity region $|\eta| < 1$. The forward arm complements the measurements at low angles (2° to 9°) and consists of a pattern of absorbers, a large dipole magnet and a large number of tracking chambers.

The central barrel contains the main tracking and PID detectors. The closest sub-detector to the interaction point is the **Inner Tracking System (ITS)**, a silicon detector located at radii between 4 and 43 cm. Its main purpose is to locate with a resolution better than 100 µm [34] the collision point (i.e. the primary vertex), to disentangle and reconstruct secondary vertices from decays of heavy flavored hadrons (e.g., $D^0 \to K^-\pi^+$), as well as to track and identify particles with momenta smaller than 200 MeV.

To be able to accurately measure the low p_{T} particles, they must not be completely stopped before they are charaterized. Hence, the combined material budget of this mechanical structure has to be minimized. To this end, ITS employs six cylindrical layers, which in total amount to 7.2% [34] of a radiation length. This also reduces the decline of the momentum resolution by multiple scattering, the dominant deterioration factor at low momenta.

Owing to the high particle densities close to the interaction point, the first two layers consist of Silicon Pixel Detectors (SPD), followed by two more layers of Silicon Drift Detectors (SDD). The particle densities will drop further away from the vertex, so for the last two layers, double-sided Silicon micro-Strip Detectors (SSD) are employed.

Altogether, they cover an area of $7\,\mathrm{m}^2$ and include close to 13 million electronic channels [34]. The outer four layers, the SDD and SSD, can be used for particle identification via energy loss, since they have analog readout.

Surrounding the ITS is the **Time Projection Chamber (TPC)**, a gaseous detector, the main tracking and particle identification detector of the ALICE complex. Particles ionize the gas molecules in this vessel, losing energy and their output is read out by Multi-Wire Proportional Chambers (MWPC) with pad readout at the two end-caps. The continuous tracking makes the TPC unequivocally a must-have in the high-multiplicity environments of the heavy-ion collisions. A detailed explanation is given in Sec. 3.2.3.

Further away from the interaction point lies the **Transition Radiation Detector (TRD)**, a device tailored to identify electrons for momenta larger than $1\,\mathrm{GeV}/c$. It consists of six detector modules radially stacked on top of the TPC, each of them containing 48 mm [34] of radiator material and a drift region filled with Xe-CO_2 about 37 mm [34] across.

Inside such a radiator material, fast enough charged particles (those with a Lorentz factor $\gamma = 1/\sqrt{1-(v/c)^2} > 1000$) cross successive boundaries between polarized materials with different dielectric constants, leading (with some probability) to the emission of photons with a narrow energy range. These transition radiation photons are recorded in the MWPC chambers at the end of each module.

The intensity of the radiation depends linearly on the γ factor; for a fixed momentum, the electrons produce about $m_\pi/m_e \approx 280$ times more transition radiation than pions. As such, it is possible to distinguish the two particles in terms of the different signal shapes they liberate in the detector.

In addition, the TRD provides further momentum resolution at high p_T as a result of extending the measured track length by the longer level arm of the detector. Complementary, it manages to correct space-point distortions in the TPC and acts as a fast trigger for particles with high momentum [40].

Charged hadrons in the intermediate momentum range (up to a few GeV/c) are identified by the **Time Of Flight (TOF)** detector, in conjunction with the momentum and track length measured by the tracking detectors. It exhibits a cylindrical symmetry, consisting of a large area array of Multi-gap Resistive Plate Chambers (MRPC).

This detector measures the velocity of charged particles by virtue of the time they need to travel from the interaction point to the detector's sensitive medium. The initial time (t_0) of the interaction is given by the T0 detector, located close to the ITS. Inside the detector, the charged particles ionizes the gas, creating an avalanche of electrons, which are collected by electrodes.

The intrinsic time resolution of the TOF is better than 40 ps (RMS) [34], good enough to also separate particles produced in pile-up events (the interactions of different bunch

crossings). On top of that, it operates at 100% efficiency. Using the track information provided by the ITS and TPC, and linking them with the timing information supplied by the TOF detector, the particles can be unambiguously identified.

The TOF detector, being limited to low energy particles ($\gamma \leq 5$), is complemented by the **High Momentum Particle Identification Detector (HMPID)**, which, as the name implies, targets the highly energetic particles. Specifically, it aims at discriminating π/K and K/p above what the main detectors of the central barrel can achieve.

The identification is done by means of Cherenkov radiation. The device embodies seven Ring Imaging Cherenkov (RICH) counters [34] mounted between the TOF and the L3 magnet. As the charged particles pass through the dielectric medium of the detector at speeds greater than the phase velocity of light in that medium, Cherenkov rings are produced. The velocity of particles is calculated from the opening angle ($\cos\theta = 1/(n\beta)$) of the Cherenkov photons thus emitted.

Furthest away radially from the interaction point are the calorimeters of ALICE - the **Electromagnetic Calorimeter (EMCal)** and the **Photon Spectrometer (PHOS)**. The first is a lead and plastic-scintillator sampling calorimeter designed to measure the energy of photons and electrons coming from π_0 and η decays, as well as improve jet measurement capabilities (interaction of energetic partons with dense matter). The latter is a homogeneous high-density lead-tungstate calorimeter primarily designed to measure photons that contain thermal and dynamical properties of the initial phase of the collision.

Apart from the main detectors mentioned above, a number of small and specialized systems are embedded in the ALICE experiment. Their combined data is used to study heavy-ion, pp and p–Pb collisions as well as cosmics and extract information about the medium created at the instant of the interaction. Further information about the detector ensemble can be found in [36].

3.2.3 TPC

The **Time Projection Chamber (TPC)** is the main tracking detector of the central barrel of ALICE. It fulfills three important tasks in the experiment — the three-dimensional reconstruction of particle tracks, momentum measurement, alongside particle identification via their specific energy loss ($\mathrm{d}E/\mathrm{d}x$).

From central Pb–Pb collisions at LHC's design luminosity in Run 2, an interaction rate of 8 kHz is expected. Taken into account the charged particle multiplicity, the TPC was designed to cope with up to 20000 charged tracks, so a high granularity detector is desired.

It covers a large p_T range, from about 0.1 GeV/c up to 100 GeV/c with good momentum resolution. It is shaped as a hollow cylinder wrapped around the ITS module, bathed in a uniform magnetic field of 0.5 T and is filled with a counting gas mixture, to keep the material budget as small as possible. The following subsection contains technical details taken from [41] and specifics from LHC's Run 2.

The TPC cylinder measures 5 m along the beam direction, has an inner radius of about 85 cm, an outer radius of about 250 cm and contains 88 m^3 of gas in which the electrons that result from ionized tracks of charged particles are transported. It is divided into two drift regions by a central electrode charged to 100 kV that, alongside a voltage divider network at the inner and outer surface of the cylinder, provides a precise axial electric field of 400 V/cm pointing toward the central electrode. Readout chambers are installed at the two end-plates of the cylinder, recording the electrons and transforming them into electric signal.

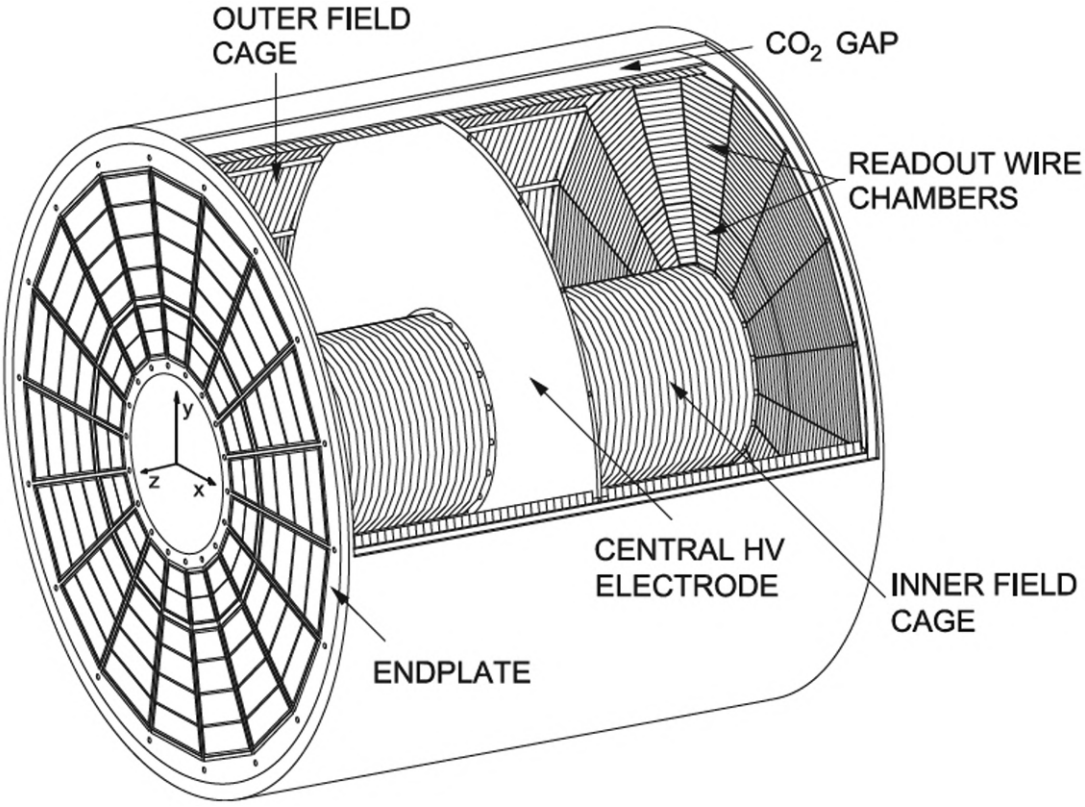

Figure 3.15: A schematic of the ALICE Time Projection Chamber [42].

Charged particles that emerge from the interaction will enter the vessel and will suffer random collisions with the gas molecules, losing energy along their trajectory in the process and leaving behind a trail of electron-ion pairs, which serve as the basic constituents of electrical signal. The electric field present in the chamber, oriented along the beam-pipe direction, will separate these primary electrons and ions and they will start drifting to opposite directions, following the electric field lines.

The electrons will start drifting toward the endcap on the side they were created in, where they will be amplified and then read-out, while the ions will travel in the opposite direction, toward the main central high-voltage (HV) electrode. The readout is sectorized to preserve spatial information of the electrons in the plane perpendicular to the drift field.

Although the particles lose energy from a number of discrete events with each event having a random result (e.g. the electrons from ionization can receive an arbitrary amount of energy), the process can be approximated as a continuous loss of energy. The average specific energy loss of particles through ionization or excitation is described by the Bethe-Bloch formula [4]:

$$-\left\langle \frac{\mathrm{d}E}{\mathrm{d}x} \right\rangle = Kz^2 \frac{Z}{A} \frac{1}{\beta^2} \left(\ln \frac{C\gamma^2\beta^2}{I} - \beta^2 - \frac{\delta}{2} \right)$$

The energy loss per *density-scaled distance* (since it depends on the absorber) has units of $\mathrm{MeV\,g^{-1}\,cm^2}$ and is only valid for energetic, massive charged particles in the range $0.1 \lesssim \beta\gamma \lesssim 1000$. It cannot be used for particles that are slow (i.e., whose velocities are similar or lower than orbiting atomic electrons) or particles that are light, like electrons.

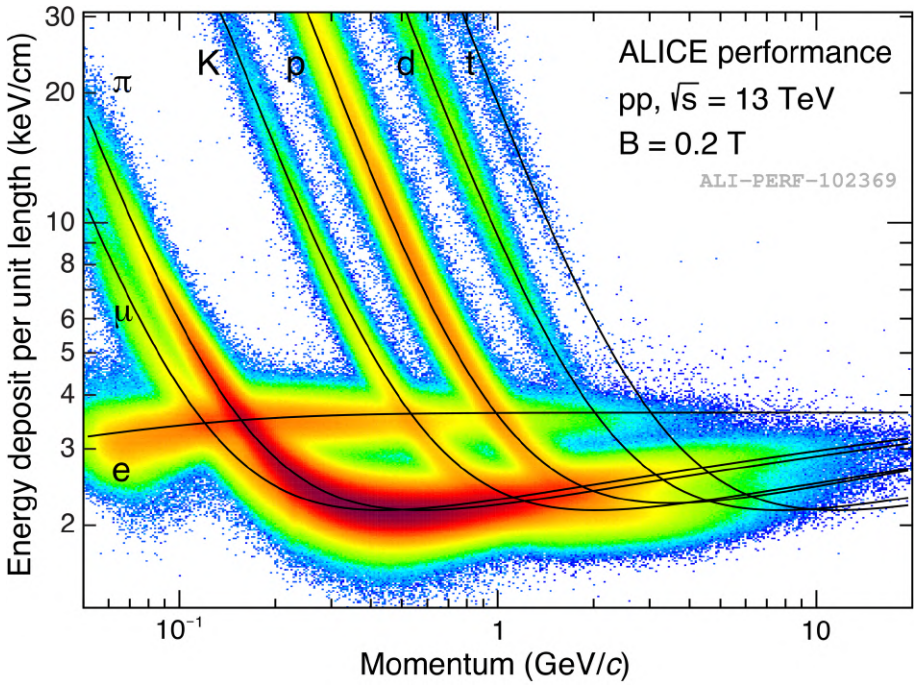

Figure 3.16: Specific energy loss ($\mathrm{d}E/\mathrm{d}x$) versus particle momentum in the TPC. The lines show the parametrizations of the expected mean energy loss. [43].

$K = 0.307\,\mathrm{MeV\,cm^2\,mol^{-1}}$ and $C = 1.022\,\mathrm{MeV}$ are constants. z represents the projectile charge (measured in units of e). Z and A are the atomic number and atomic mass of the absorber, respectively. β and γ are the Lorentz factors and are a representation of the velocity of the projectile, with $\beta\gamma = p/mc$. I is the absorber's mean excitation energy (averaged over all its electrons), which has a value for most chemical elements between 5 and 20 eV. Finally, δ is a correction due to how much the extended transverse electric field of the incident particle is screened by the charge density of the atomic electrons.

At low momenta, the energy loss is dominated by the $1/\beta^2$ term, since momentum transfer increases with the effective interaction time (i.e., slower particles feel the electric

force of the atomic electrons for a longer time). For momenta corresponding to three to four times the mass of the particle, a minimum is reached. Most relativistic particles have energy loss rates close to this minimum ($\sim 2\,\mathrm{keV/cm}$) and are termed *minimum ionizing particles*.

At higher particle momenta, the logarithmic term in the Bethe-Bloch equation becomes dominant (an asymptotic increase of the maximal energy transfer and of the transverse component of the electric field with γ). Owing to the density effect (δ term), the logarithmic rise saturates at high energies, reaching the so called *Fermi plateau*.

As can be seen, the energy loss as a function of the particle momentum is dependent on the particle mass. Thus, by measuring the particle momentum (from the deflection in the magnetic field), alongside the energy loss, the mass of the particle and thus its identity is found. The low momentum region and the relativistic rise are the regions where PID is possible. Especially in the high momentum sector, where the separation is proximal, the intrinsic resolution of the $\mathrm{d}E/\mathrm{d}x$ is 5% due to fluctuations in the Bethe Bloch curve.

After the particle's passage through the medium of the TPC, it will have ionized and released a number of n_p primary electrons along its path, with random distributed energies. If the energy transferred to the released electron is larger than the average energy required to produce an electron-ion pair (the ionization energy W_i - for gases it has a value of $\sim 30\,\mathrm{eV}$), those electrons will be able to further ionize atoms in secondary inelastic collisions with the gas molecules.

The total number of ionization electrons will be given by the ratio of the total energy deposited and the ionization energy of the gas:

$$n_\mathrm{tot} = \frac{\triangle E}{W_\mathrm{i}}$$

Predominantly, W_i is larger than I thanks to a good part of the energy being converted into excitation of gas atoms and into kinetic energy of the electron-ion pair. For a few of the gases usually used in a TPC, the values for the ionization potential, the ionization energy, alongside the mean number of primary electrons and the mean number of total electrons is given in Table 3.1.

Gas Molecule	Z	I(eV)	W_i(eV)	$n_\mathrm{p}(\mathrm{cm}^{-2})$	$n_\mathrm{tot}(\mathrm{cm}^{-2})$
Ar	18	15.8	26	24.3	94
CO_2	22	13.7	33	36.5	91
Ne	10	21.6	36	12	43
Xe	54	12.1	22	44	307

Table 3.1: Parameters for typical TPC gases [44].

The detector performance depends inherently on the choice of gas, since this influences the charge transport in the drift volume, alongside the amplification process at the readout stage. Few requirements of the detector which can be achieved with a good gas are: low charge loss, stable operation, high ionization density, low diffusion, suitable drift velocity, alongside low space charge and dead time.

Noble gases, on account of their electropositivity (the tendency to lose electrons to form positive ions), are a good starting point, since for them gas multiplication takes place at lower electric fields than for complex molecular gases. This being the case, it is obvious that the noble gases with bigger atomic numbers (i.e., krypton, xenon) are better at achieving this. Moreover, the multiple scattering - which is a function of the atomic number - is kept low. The caveat is that they are very expensive and hard to refine and purify, given the overall capacity of the TPC and the fact that the gas has to be recirculated, cleaned and new gas injected continuously into the system.

Argon was disfavored in Run 1, the main reason being that it is denser ($\rho_{Ar} = 1.784\,\mathrm{g/L} > \rho_{Ne} = 0.9\,\mathrm{g/L}$) and multiple scattering was bigger [45]. Moreover, it has a slower ion reduced mobility (K_0); taking into account temperature and pressure effects, $K_0(Ar) = (1.94 \pm 0.01)\ \mathrm{cm}^2/\mathrm{V\,s}$ and $K_0(Ne) = (4.06 \pm 0.07)\ \mathrm{cm}^2/\mathrm{V\,s}$ [46]. For the second run of LHC, the main noble gas was chosen to be Argon to allow for a more stable response to high particle fluxes generated during Pb-Pb collisions, without a significant degradation of the momentum resolution at low p_{T}.

A pure noble gas is not suitable for such a system. For example, Ar ions arriving at the cathode will form neutral Ar atoms by extracting an electron from the cathode. Furthermore, vacuum-ultraviolet photons formed by electron-ion recombination are able to extract electrons from the cathode. To prevent this from happening, a *quencher* that is able to absorb those photons is added.

Tests have been performed with many such admixtures; most notably, hydrocarbons were excluded due to ageing effects (depositions on the anode wires, which degrades resolution). The best choice was CO_2 ($K_0 = (1.10 \pm 0.01)\ \mathrm{cm}^2/\mathrm{V\,s}$). Given that the requirement for the TPC was to have a field cage operating at $400\,\mathrm{V/cm}$, with a drift time below $100\,\mu\mathrm{s}$, an addition of 12 parts of CO_2 for 88 parts of Ar was made for the TPC in Run 2.

As such, in Run 2 for Ar-CO_2 (88-12), at a value of W_{i} of $28.8\,\mathrm{eV}$, there are $n_{\mathrm{p}} = 26.4$ primary electrons/cm and $n_{\mathrm{tot}} = 74.9$ total electrons/cm [47].

The electrons released during ionization processes will start drifting towards the readout chambers influenced by both electric and magnetic fields. The time variable (i.e., the time it takes for them to drift and record a signal) is related to their position along the TPC, so understanding drift and diffusion processes that appear in gas and how they can affect the spatial resolution is important.

The velocity $\overrightarrow{v}$ of an electron of mass m under the influence of both an electric and a magnetic field can be interpreted by the Langevin equation [47]:

$$m\frac{d\overrightarrow{v}}{dt} = e(\overrightarrow{E} + \overrightarrow{v} \times \overrightarrow{B}) + \overrightarrow{F}(t)$$

where $\overrightarrow{F}(t)$ is a time-dependent noise term appearing due to collisions with gas molecules.

A stationary solution for a vanishing $\overrightarrow{B}$ field can be written in terms of mobility μ:

$$\overrightarrow{v_{\mathrm{D}}} = \mu\overrightarrow{E} = \frac{e\tau}{m}\overrightarrow{E}$$

where τ is the time between collisions.

The general solution for the drift velocity in the case of a non vanishing $\overrightarrow{B}$ is:

$$\overrightarrow{v_{\mathrm{D}}} = \frac{\mu E}{1+\omega^2\tau^2}\left[\hat{E} + \omega\tau\hat{E}\times\hat{B} + \omega^2\tau^2(\hat{E}\cdot\hat{B})\hat{B}\right]$$

Here, the Larmor frequency ω is taken into account as are the unit vectors $\hat{E}$ and $\hat{B}$. Since in the TPC, the electric field is nearly parallel to the magnetic field, and the propagation of particles is helix-like, the second term vanishes and we get a simplified term (allowing for $\hat{E}\cdot\hat{B} = 1$ for $E \parallel B$):

$$\overrightarrow{v_{\mathrm{D}}} = \frac{\mu E}{1+\omega^2\tau^2}\hat{E}(1+\omega^2\tau^2) = \mu\overrightarrow{E} = \overrightarrow{v_{\mathrm{D}}}(\overrightarrow{B}=0)$$

This shows that a parallel alignment of the fields is equivalent to the absence of the magnetic force in terms of drift speed. A good alignment of the two fields is therefore important to keep the corrections low.

For a slow gas, typical values for the drift velocities at 400 V/cm are $\overrightarrow{v_{\mathrm{D}}} \sim 2\mathrm{cm/\mu s}$ for electrons and $\overrightarrow{v_{\mathrm{D}}} \sim 2\cdot 10^{-4}\,\mathrm{cm/\mu s}$ for ions, given that their mobilities are so different as a consequence of the mass difference.

During the drift to the readout chambers, ions and electrons created within the gas have a tendency to diffuse away from regions of high density; they are subject to transverse and longitudinal diffusion caused by collisions with gas molecules. This can, in turn, enhance the spatial resolution because the charge will be spread over several pads. Determining the center of gravity of the charge distribution therefore allows for a position resolution much better then the actual pad size.

An initial point-like cloud of electrons will spread isotropically (i.e., *diffuse*) and will assume a Gaussian density distribution after some time t:

$$n(t) = \frac{1}{\sqrt{4\pi D_{\mathrm{L}}\,t}}\left(\frac{1}{\sqrt{4\pi D_{\mathrm{T}}\,t}}\right)^2 \exp\left[-\frac{x^2+y^2}{4D_{\mathrm{T}}\,t} - \frac{(z-v_{\mathrm{D}}t)^2}{4D_{\mathrm{L}}\,t}\right]$$

where D_{L} and D_{T} are the longitudinal and transverse diffusion coefficients. It can be seen that the mean squared deviation of the electrons is $\sigma_{\mathrm{L}} = \sqrt{2D_{\mathrm{L}}\,t}$ for the longitudinal spread and $\sigma_{\mathrm{T}} = \sqrt{2D_{\mathrm{T}}\,t}$ for the transverse one.

Magnetic fields will decrease the diffusion perpendicular to the field direction, since the electrons will *curl up* between collisions. The transverse diffusion will be reduced:

$$\frac{D_{\mathrm{T}}(B)}{D_{\mathrm{T}}(0)} = \frac{1}{1+\omega^2\tau^2}$$

This is essential for the TPC where long drift distances are involved and is one of the main reasons for making the magnetic field parallel to the electric field. The lateral diffusion is unchanged by the presence of a magnetic field $D_{\mathrm{L}}(B) = D_{\mathrm{L}}(0)$.

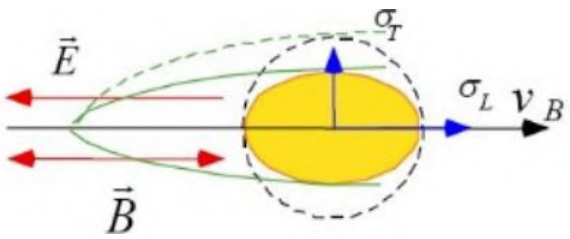

Figure 3.17: The B field reduces diffusion in the transverse direction [48].

The values for the gas choice in Run 2 of Ar-CO_2 (88-12) for the diffusion and drift of electrons are: $D_{\mathrm{T}} = 199\,\mu\mathrm{m}/\sqrt{\mathrm{cm}}$, $D_{\mathrm{L}} = 246\,\mu\mathrm{m}/\sqrt{\mathrm{cm}}$, $v_{\mathrm{D}} = 2.74\,\mathrm{cm}/\mu\mathrm{s}$ for a magnetic field of 0.5 T and an electric field of 400 V/cm at standard pressure and temperature [47].

Given the values for the gas used in Run 2, the electrons will need about 92 µs to travel the full distance from the central HV electrode to the readout chambers.

The electrons from the tracks will bear different time information, considering the track proximity to the detector readout plane. With the time information that the TPC records and with knowledge of the gas properties, the z-coordinate can be calculated from the *time projection*:

$$z = v_{\mathrm{drift}} \cdot (t_{\mathrm{arrival}} - t_{\mathrm{collision}})$$

The $xy-$plane coordinate, given by the position of deposited charge on the pad plane, is determined at the readout chambers situated at the two end-cap wheels of the TPC.

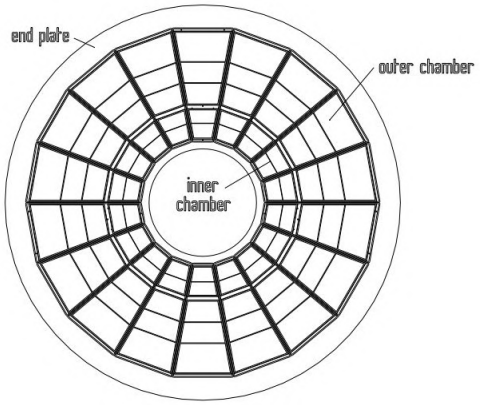

Figure 3.18: Segmentation of the readout plane [41].

In the interest of optimizing the momentum and $\mathrm{d}E/\mathrm{d}x$ resolution for the full azimuthal coverage, the design of the readout chambers has to maximize the total area of the endcaps. For practical reasons, the readout planes are subdivided into individual modular readout chambers. There are a total of 18 trapezoidal sectors, each covering 20° in azimuth.

In one such sector there will be two different types of readout chambers - the inner (IROC) and outer (OROC) readout chamber. This was motivated by the fact that there is a radial dependence of the track density and by the ease of assembling and handling of such modules. Counting both endplates, there are a total of $2 \times 2 \times 18 = 72$ readout chambers, covering a total active area of $33.27\,\mathrm{m}^2$.

The readout itself is based on the conventional multi-wire proportional counters (MWPC) with a cathode pad readout. This implementation is needed because the total charge created by the primary ionization contains clusters of few electrons, which cannot be detected unless amplified above the mean electronics noise of around 0.7 ADC (700 e^-) [49]. Moreover, the MWPCs allow for fine segmentation of the pad plane, thus coping with the high track density expected in heavy ion collisions.

As such, the gas amplification mechanism is the key principle in gaseous detectors. The amplification region is defined by the pad plane and a scheme of wires a few mm above it (see Fig. 3.19). The wire configuration was chosen to shape the electric field lines and to minimize the ion back-flow (i.e., the amount of ions that stray back to the drift region after they are produced, thus distorting the electric field).

After the primary ionization has taken place in the active volume, the electrons will acquire high enough energy between two collisions to further ionize other gas molecules, whose liberated electrons, in turn, will gain energy to ionize more molecules, leading to an avalanche phenomenon.

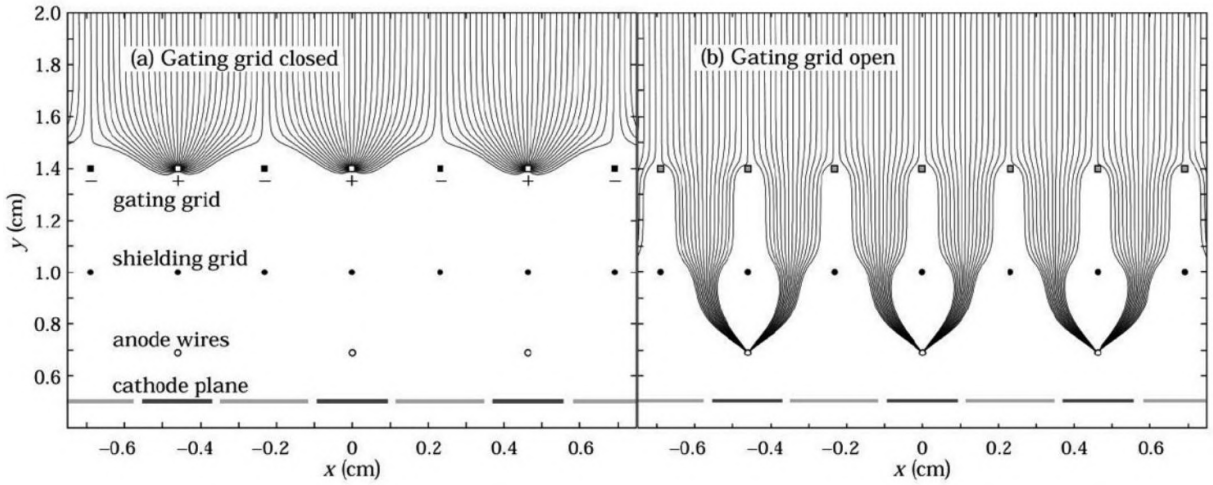

Figure 3.19: Example of electric field lines of a MWPC with gating mechanism [50].

Alongside the electrons, positive ions are generated, which drift very slowly towards the cathode, given their low mobility. At high rates, they accumulate in the drift volume and create clusters of positive charge that will alter the electric field lines, deviating the primary electron trajectories and resulting in distortions of the reconstructed tracks. The global effect is usually referred to as *space charge effect*.

To help combat this effect and to better shape the electric field, three wire grids running in the azimuthal direction were introduced at the readout of the ALICE TPC (similar to those depicted in Fig. 3.19, which belong to the DELPHI TPC at LEP). To prevent ions from drifting back, a gating grid is placed at the start of the amplification region, with alternating potential wires supplied with electricity.

The structure is switched on and off intermittently, according to a trigger. In the *open gate mode*, all wires are held at the same potential, providing full transparency to ionization electrons which enter the amplification region. The *closed gate mode* features an extra bipolar potential to the wires. Now, the gating grid prevents more electrons from entering the MWPC, thus protecting the amplification region against unwanted ionization, while also preventing the ions from going back in the drift region.

By default, the gating grid is closed and only opens when it receives a signal from the trigger, staying open for the duration of the electron drift time alongside the full length of the TPC. The resulting requirement was that the ion leakage has to be kept below 10^{-4}, setting a careful adjustment of the voltages.

Alongside the gating grid there is a cathode wire grid below that helps straighten the field near the amplification region, while also making sure to terminate the field in the avalanche area and provide additional radio-frequency shielding for the pads. The final plane is the anode plane where the electrons will end their journey.

Considering the effects of drift and velocity of the moving charges, the aforementioned avalanche will develop into a drop-like shape in the near vicinity of the anode wires (positive ions are left behind by the fast electron front) [51]. The electrons will quickly be

collected on the anode wires, while the ions, slower by about three orders of magnitude will drift towards the nearest cathode element.

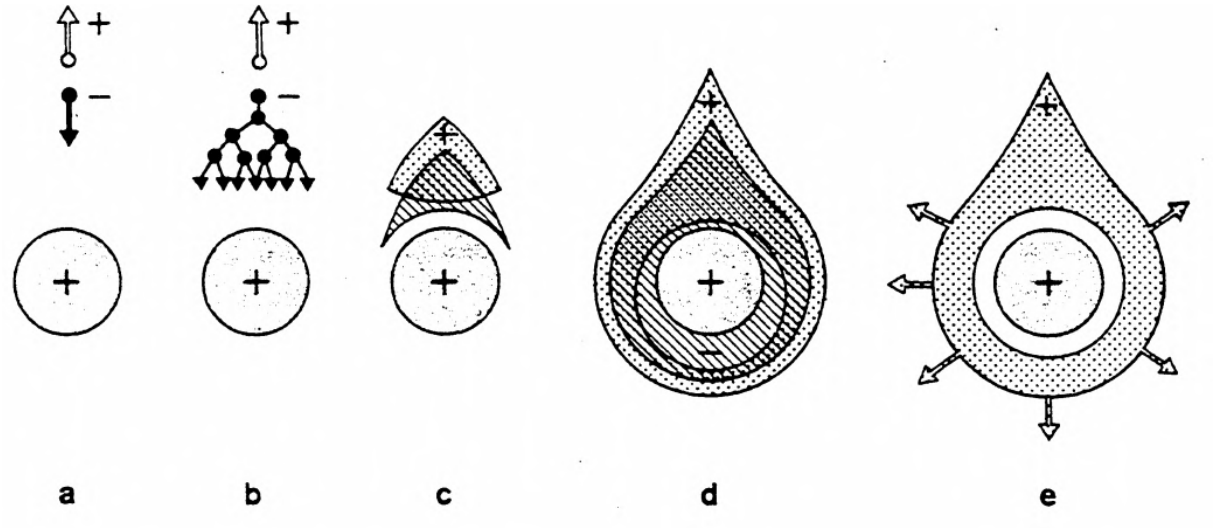

Figure 3.20: Development of the avalanche multiplication near an anode wire in a proportial chamber [52]. As a primary electron approaches the anode, it suffers ionizing collisions in the high field. Due to lateral diffusion, a drop-like avalanche will emerge, enveloping the wire [53]. Electrons are collected in times less than 1 ns, leaving behind a cloud of slowly moving ions, that will migrate toward the cathode.

Close to the anode wire (a few wire radii away, since at normal gas densities the mean free path between two collisions is of the order of microns) multiplication will start to take place. Considering that at constant potential the amplification increases with decreasing wire diameter [42], ALICE TPC showcases thin gold-plated tungsten wires that are only 20 µm thick.

Moreover, there is the risk of uncontrolled amplification by the ultraviolet photons created in the bulk of the avalanche that will escape the front and ionize further away.

The total number of charges created depends on the field strength, as well as the number and the distribution of the primary ionization electrons. The movement of these charges gives rise to electrical signals on the electrodes. The motion increases the surface charge on the electrodes and induces a contrariwise charge distribution at their surface. As such, if the cathode is connected to the voltage through a resistor, an increase of the negative charge on the electrode implies an inflow of electrons (that is, by definition, an outflow of positive charges) and the detected voltage difference will therefore be positive. The induced current will end when the charges will reach the electrodes and annihilate.

The electrons created in the avalanche will move to the wire surface within timescales of less than a nanosecond, resulting in a short but intense signal pulse. They will be absorbed by the anode wires and will not (only marginally [54]) participate in the signal creation. This is because the electron avalanche develops extremely fast and very close to the wire (few tens of µm); then the electrons traverse only a small potential difference.

On the other hand, the majority of the ions will be formed near the anode and will traverse almost all the potential difference. The positive ion sheath, will slowly drift toward surrounding electrodes (see Fig. 3.21), inducing an overall positive current signal on the pad plane.

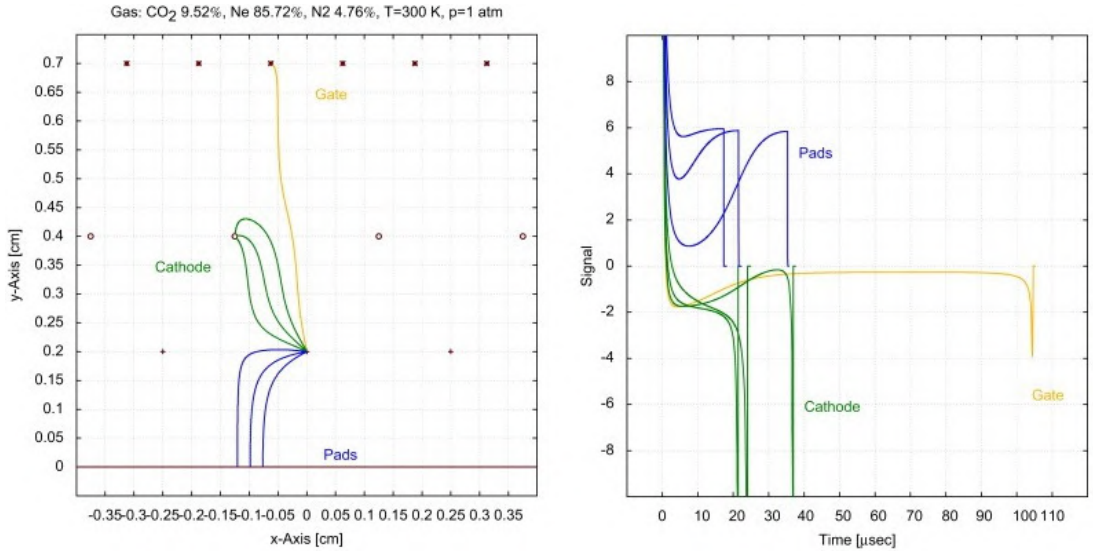

Figure 3.21: Simulations of ion tracks (left) and induced signals (right) from single ions of different angle to the multiplication wire [55]. If the ions reach the pads, the signal is positive. If the ions drift to a cathode wire or a gate wire, the signal is negative.

The signal delivered on the readout pads exhibits a fast rise-time of less than 1 ns, accompanied by a long tail (of the order of 50 µs) due to the motion of the positive ions [56]. The signal has a typical amplitude of 7 µA [57] and carries a charge that can be as low as a few fC [42].

The readout of the signal is done by 557 568 pads [42] that form the cathode pad planes of the readout chambers. The pad size is different in the inner and outer sectors to achieve the necessary spatial resolution near the center of the detector where the track density is bigger. The induced charge from the avalanche is shared over several adjacent pads. A pad response function (PRF) is defined that relates the signal induced on the pads to the position of the original track. The width of this PRF will be thus related to the position resolution of the TPC [58].

The signal from the pads is transferred via 6 flexible Kapton cables to the 4356 front-end cards (FECs) located some 7 cm away from the pad plane [42]. One FEC has 128 readout channels and does the actual signal processing. It contains eight Pre-Amplifier and Shaper chips (PASA) and eight Alice TPC Readout Chips (ALTRO).

The PASA makes use of a charge sensitive amplifier to boost the signal (conversion gain of 12 mV/fC) after which it transforms the charge induced on the pads into a differential semi-Gaussian voltage signal with the pulse shaper. The output will be a pulse with a rise time of 150 ns and a shaping time (FWHM[2]) of 190 ns [59].

[2]Full Width at Half Maximum

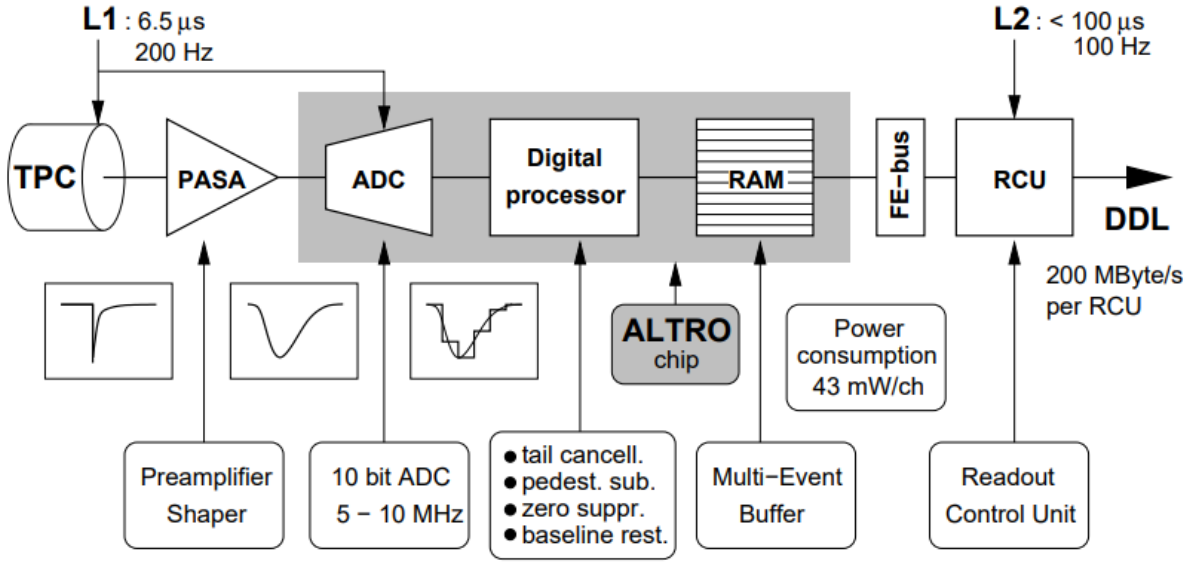

Figure 3.22: Schematic of the ALICE TPC front-end electronics [59]

The shaped signal is then fed into the digital ALTRO chip where it is digitized by a 10-bit 25 MSPS[3] low power analog-to-digital (ADC) converter operated at a sampling rate of 5-10 MHz [42]. The digitized signal is further processed by a set of circuits that condition and shape the signal [57].

The digital processing chain starts with a first baseline correction which removes perturbations like low-frequency spurious signals (e.g., temperature variation of the electronics) and signal distortions from systematic effects (e.g., triggering of the detector which can generate a superimposed noise pattern). After that, a tail cancellation is introduced to minimize the pile-up effect caused by the ion tail which overlap on subsequent pulses.

Next, a second baseline modification is needed to remove non-systematic perturbations of the baseline that are superimposed on the signal. The final step is a zero suppression correction which discards samples that do not carry information (e.g., values below a certain reference level called pedestal that are considered noise). This produces a limited number of non-zero data samples, thus reducing the overall data volume. Each data packet is formatted with its time-stamp and size information. The output is sent to a memory of 5 kB, which is able to store up to 8 acquisitions. [59].

Upon arrival of a first level trigger (L1) (about 6.5 µs after the interaction), the samples are temporarily stored in the multi-event buffer. When a second level trigger (L2) (accept/reject) is received (arrives after the full TPC drift time, in order to ensure the completion of the TPC readout), the data is either frozen in memory, until it is completely read out, else it is overwritten by the next event.

Data can be read-out from the ALTRO chip through a Front-End (FE) bus linking the FECs to the Readout Control Unit (RCU). The RCU is the interface with the ALICE Data Acquisition (DAQ) and the Detector Control System (DCS). Finally, the RCU transfers

[3]Mega Samples Per Second

data onto the Detector Data optical Link (DDL) and the DAQ system can perform event building.

The exact event size will depend on settings (trigger, interaction rat, event multiplicity), as well as the background. A major part of the data rate in ALICE comes from the TPC. The most central Pb–Pb collisions in the TPC generate up to 200 MB of data [60]. In Run 2, event rates of up to 2 kHz (pp and p–Pb) and 1 kHz (Pb–Pb) stem up to 40 GB/s from the TPC, with few more GB/s coming from other ALICE detectors [60].

3.2.4 TPC Upgrade

ALICE has a low interaction rate, which is crucial for the experiment, since it allows the use of slow, albeit high granularity detectors needed for rare events. Taking $\sigma^{\text{geo}}_{\text{PbPb}} = 7.8\,\text{b}$ [61] for the total (geometrical) cross-section, the event rate for Pb–Pb collisions at the LHC design luminosity of $10^{27}\,\text{cm}^{-2}\,\text{s}^{-1}$ will yield about 8000 collisions per second. Of these, a few percent correspond to the most central collisions, with maximum particle production.

The heavy ion program at LHC (see Fig. 3.23) takes roughly 10^6 s/yr (about 10% of the total year), which generates in excess of 10^7 central events for further offline analysis. Even for this small period of time, the 10 year Pb–Pb integrated luminosity goal of $1\,\text{nb}^{-1}$ has been achieved in the two LHC runs (in 2015 a total of $433\,\mu\text{b}^{-1}$, to which $606\,\mu\text{b}^{-1}$ [62] are added for the 2018 run), since it began data taking.

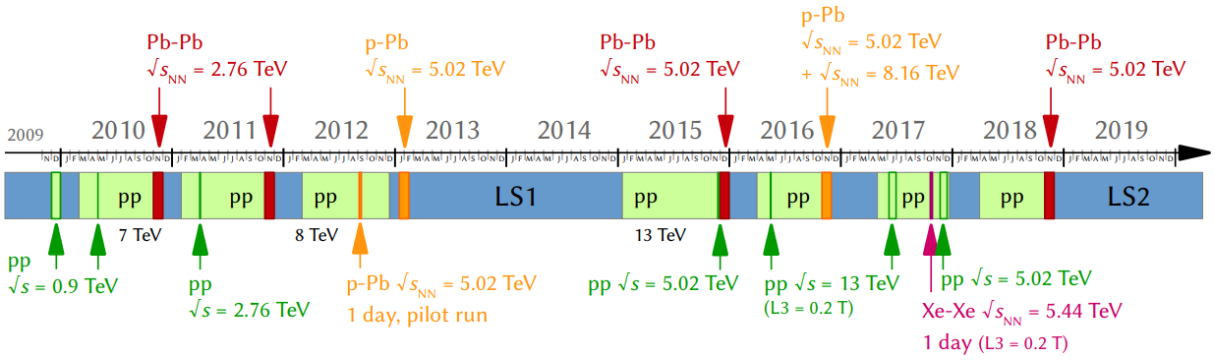

Figure 3.23: LHC data taking campaign (Run 1 and Run 2) [31].

For the TPC, the active bipolar gating grid placed in front of the MWPCs needs to stay closed in order to minimize the space charge due to positive ions from exiting the multiplication region. The maximal drift time of about 100 µs that electrons need from the central electrode to the readout stage, combined with the ion drift time of 180 µs from the anode wires to the different cathode elements, limits the readout rate of the present TPC to a maximum of 3.5 kHz. As such, the maximum design interaction rate provided by the accelerator system (8 kHz) cannot be fully exploited and a good number of events are lost.

On top, another limitation is the readout speed of the electronics, that are able to sustain a maximum minimum-bias[4] event rate in Pb–Pb of about 1 kHz for the whole ALICE detector (limited by the TPC and the ITS(SDD)) [63] and about 500 Hz for the TPC alone [64].

After the second technical shutdown of the LHC (LS2), the flagship machine of CERN will be revitalized, as the whole chain of the acceleration system will be upgraded.

Since ALICE is basing its physics objective on precision measurements of elusive observables of the exotic state of matter, the statistics have to be increased and so, more events captured and analyzed. In the third run of the accelerator complex and its subsequent detectors, the strategy of ALICE is to fully profit and utilize the higher luminosity ($6 \times 10^{27}\,\mathrm{cm}^{-2}\,\mathrm{s}^{-1}$) delivered by the LHC to collect $10\,\mathrm{nb}^{-1}$ of Pb–Pb collisions at 0.5 T, inspecting about 10^{11} interactions [65] at a designed center of mass energy per nucleon-nucleon pair of 5.5 TeV, alongside $3\,\mathrm{nb}^{-1}$ at a lower magnetic field of 0.2 T [64] [63]. This would mean an increase of 10 with respect to Run 2, but an actual increase of 100 in minimum-bias Pb-Pb collisions.

The foreseeable conditions at the LHC in the next rounds of operation correspond to a hadronic interaction rate of 50 kHz and this implies that TPC operation with a gating grid will be no longer possible, since considerable pile-up will occur.

Operating the MWPCs in an un-gated mode would result in massive space charge build-up. In view of their reduced mobility, ions would need 214 ms in Ne-CO_2-N_2 (90-10-5) ($K_0 = (2.92 \pm 0.04)\ \mathrm{cm}^2/\mathrm{V\,s}$ [46]) to reach the central electrode. An event rate of 50 kHz will result in a continued ion accumulation in the drift volume from several thousand collisions piling up. This mass will distort the electron drift paths in such a way that meaningful reconstruction of the particle trajectory would no longer be possible [64].

The solution to this stalemate comes in the form of gas electron multiplier (GEM) foils [66], a new type of gas amplification structure that is able to accommodate continuous readout, while preserving the current $\mathrm{d}E/\mathrm{d}x$ resolution, tracking and particle identification capabilities of the TPC. The main considerations for the upgrade are:

- A new GEM-based readout that is able to provide sufficient ion-blocking capabilities to minimize the drift field distortions at a tolerable level;
- An exhaustive overhaul of the electronics that must be able to accommodate the negative signal polarity of the GEM detectors;
- A new and improved data acquisition system that is capable of pushing the digitized and time stamped data to the online systems in a continuous, trigger-less mode and that can reduce data significantly in order to accommodate the limited bandwidth.

A GEM foil is a thin, self-supported polyimide sheet, sandwiched by two fine metal layers and pierced by a regular matrix of holes, where each hole is acting as a multiplication region; it is manufactured by conventional photo-lithographic methods commonly employed by the printed circuit board industry. It is among the most rate-capable gas detectors

[4] Most triggers introduce a bias by selecting only a certain class of events and rejecting the rest. In a minimum bias event, only the most interesting events are selected (trigger on minimum detector activity - for example, hits in specialized scintillation counters)

currently available, and is perfectly suited for tracking and triggering purposes, by virtue of the spatial and timing resolutions in the order of 50 µm and few ns, respectively [67].

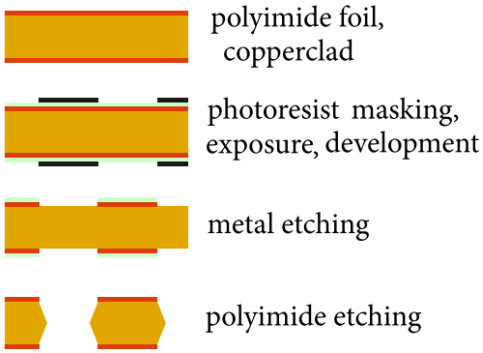

Figure 3.24: Steps for fabrication of a double-mask GEM foil [67].

In the standard *double-mask technique* (Fig. 3.24) detailed in [67], a photoresistive material is applied on both sides of the polyimide foil, on top of the metal layer and exposed to UV light. The resin includes the hole pattern. After development, the cladded foil is treated with a solvent, which removes copper from the holes, but not from the regions still masked by the photoresist. Next, the polyimide substrate is etched, the pierced metal grid acting as a mask. Finally, submerging the foil in another solvent bath, the Kapton is removed and a double-conical, hourglass-shaped hole structure is created.

The polyimide substrate, usually chosen to be Kapton [68], is 50 µm thick in the standard design. The metallized surface is usually made of 5 µm copper. The double conical surface, consequence of the manufacturing process, has an outer diameter of 70 µm and an inner one of 50 µm. The pitch, denoting the distance from center to center of two neighboring holes, is 140 µm. An electron microscope picture of such a standard design GEM foil is show in Fig. 3.25.

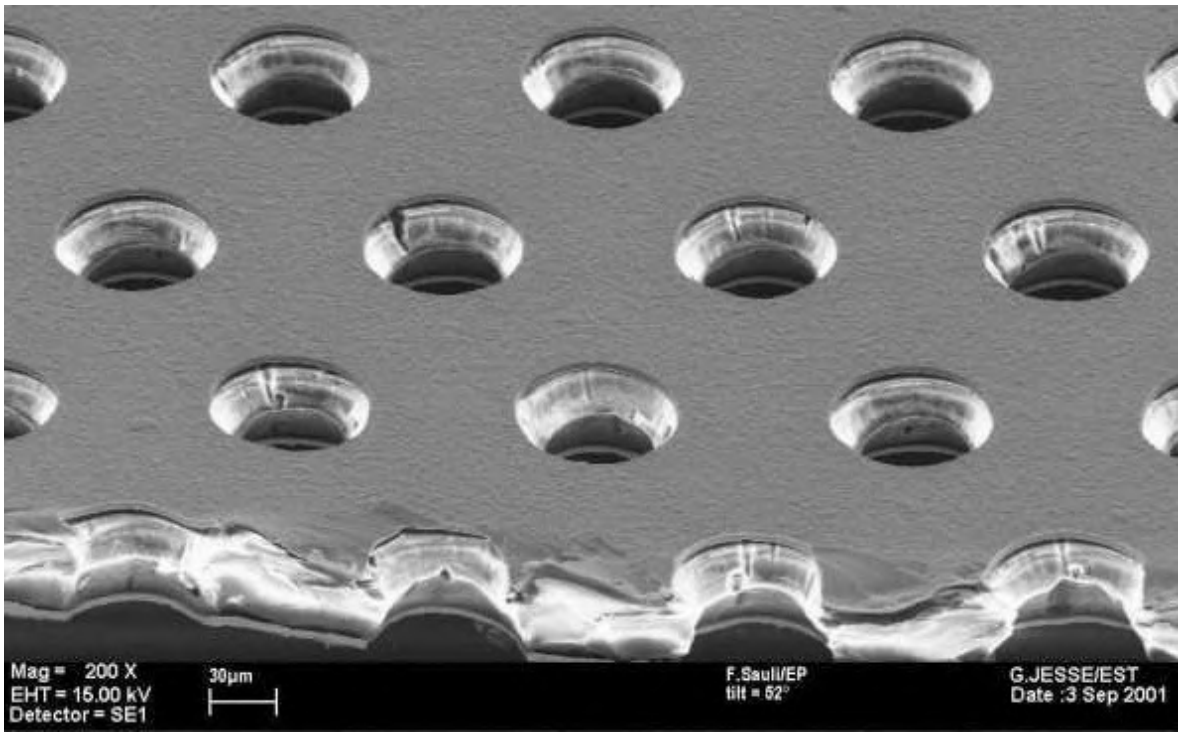

Figure 3.25: Electron microscope view of a GEM foil.
The hole diameter and pitch are 70 and 140 µm, respectively. Taken from [69].

The GEM structure is inserted between a drift and a charge collection electrode. Voltage is applied to the upper and lower metal electrodes of the GEM, resulting in a potential difference across the top and bottom side in the order of tyipically few hundred volts. The two surfaces form a parallel plate capacitor, since they are not electrically connected. The resulting electric field lines are shown in Fig. 3.26, with field strengths of up to several tens of kV/cm in the GEM hole [71], depending on the hole geometry and the applied voltages on the electrodes.

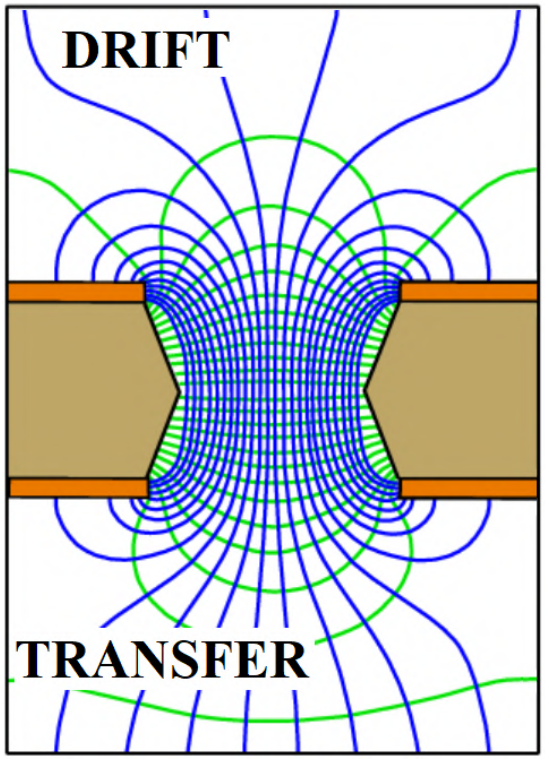

Figure 3.26: Simulated electric field and equipotential lines in a GEM hole [70].

Having suitable potentials applied, the whole structure acts as an amplifier for the electrons produced in the primary ionization in the drift region, located above the GEM. These electrons acquire sufficient energy by merit of the high field, and will ionize the atoms of gas that are filling the GEM holes. A considerable amount of electrons produced in the avalanche will be transferred into the lower part of the system, where they are collected by an electrode or further amplified by subsequent structures.

The GEM structure exhibits an exclusive feature, namely the electrical separation from the readout plane. As such, the readout can be grounded, and there is freedom in choosing the pattern, either as strips or pads. On the readout only the electron component is registered, allowing for a fast negative signal, without contribution from the slow ions.

Due to the nature of the surfaces involved, which are not perfect at a microscopic level, some of the electric field lines (and ultimately the charges trailing them) will inherently end up on the top and bottom side of the GEM. This implies that there are two effects to be considered when calculating the gain of such a structure, which can reduce the effective gas amplification — the collection efficiency ($\varepsilon_{\text{coll}}$), which gives the fraction of electrons collected into the GEM hole per number of electrons arriving and the extraction efficiency ($\varepsilon_{\text{extr}}$), which dictates the fraction of electrons that are able to exit the hole per electrons produced in the amplification (see Fig. 3.27).

The effective gain of a GEM foil is thus written as a product between the two efficiencies and the GEM intrinsic gain (i.e., the factor by which the number of electrons is increased by gas amplification inside the holes):

$$G_{\text{eff}} = \varepsilon_{\text{coll}} \cdot G \cdot \varepsilon_{\text{extr}}$$

The total amplification is exponentially dependent on the voltage applied across a GEM:

$$G_{\text{eff}} \sim \exp(k \cdot \Delta V)$$

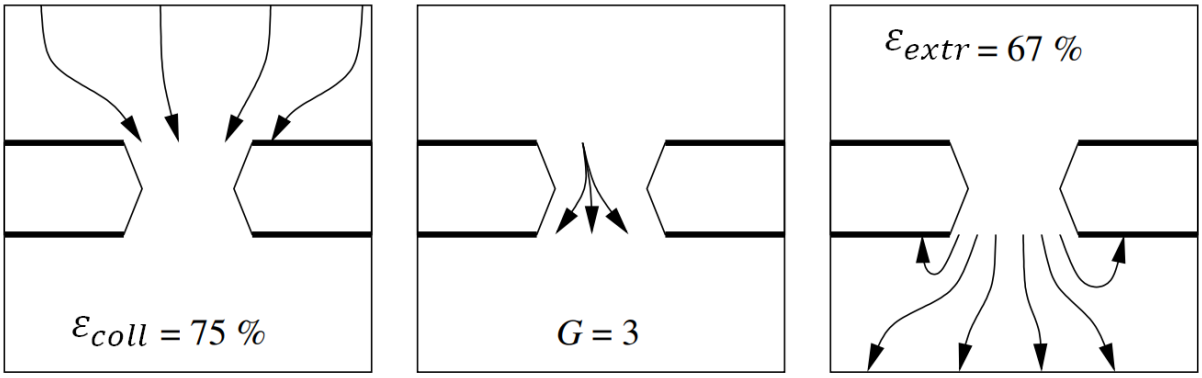

Figure 3.27: Illustration of the effective GEM gain factors for electrons (similar values can be defined for ions drifting in the opposite direction). The depicted values are chosen for informative purposes and are not related to physically relevant values. Adapted from [72].

where the coefficient k depends on the hole geometry. Amplification in excess of several 10^3 is possible for a wide range of operating gases and conditions, but at the cost of highly unstable operation.

Electrical fields are a critical component for the operation of GEMs. Collection requires a low drift field, while extraction demands a high transfer field. By conveniently choosing the potentials applied on the top and bottom side of the foil, almost full electron collection can be achieved.

Most electrons and ions will have been produced in the avalanche in the lower bottom of the GEM hole. Governed by similar efficiency values as for the electrons, the ions from the avalanche will drift back into the GEM hole. Since they are much heavier than their negatively charged counterpart, they will follow the field lines closer. Considering that the field inside the hole (of the order of 50 kV/cm) is much higher than the field above the hole (about 4 kV/cm), the ions will end up mostly on the top GEM electrode [73].

In this way, an important quantity can be defined for the GEM, which is the *ion backflow* (the flow of the positive ions resulting from the electron avalanches toward the direction of the drift region):

$$IBF = \frac{1+\epsilon}{G_{\text{eff}}}$$

where ϵ is the number of backdrifting ions per incoming electron coming from the multiplication region.

For the ion flow, the smallest possible value is preferred, to limit the distortions in the drift field and to leave the signal electrons unaltered. On the contrary, the biggest achievable transparency is desired for the electrons.

Overall, GEMs feature an intrinsic ion backflow suppression if an asymmetry of the drift and extraction fields ($E_{\text{drift}} < E_{\text{transfer}}$) with respect to the high field inside the GEM exists, which makes them extremely attractive for readout in high rate environments.

Last but not least, higher gain and enhanced operational stability is achieved by use of multi-stage GEM foils, subsequently stacked. In this way, the overall gain needed for

reliable detection can be attained with lower voltages on the electrodes of each individual GEM foil. Moreover, a significant decrease of the ion backflow can be achieved with such a towered structure, each layer acting as a filter for the ions drifting toward the drift volume from the previous element.

This has been the main motivation for the development of the GEM technology as a replacement for the MWPC chambers at the end-caps of the ALICE TPC.

In order to achieve all that, an extensive R&D effort has been undertaken - the ALICE TPC Upgrade (TPCU). The new TPC will have to include a quadruple GEM stack, since it was proven [63] that a conventional triple GEM bundle will be unable to provide sufficient ion blocking.

The requirement to keep the distortions minimal, while at the same time preserving the performance of the existing system in terms of momentum and energy loss per unit length resolution, leads to an upper limit of 1% for the ion backflow at a gas gain of 2000 in Ne-CO_2-N_2 (90-10-5 parts) (needed for a signal-to-noise ratio of 20) [63].

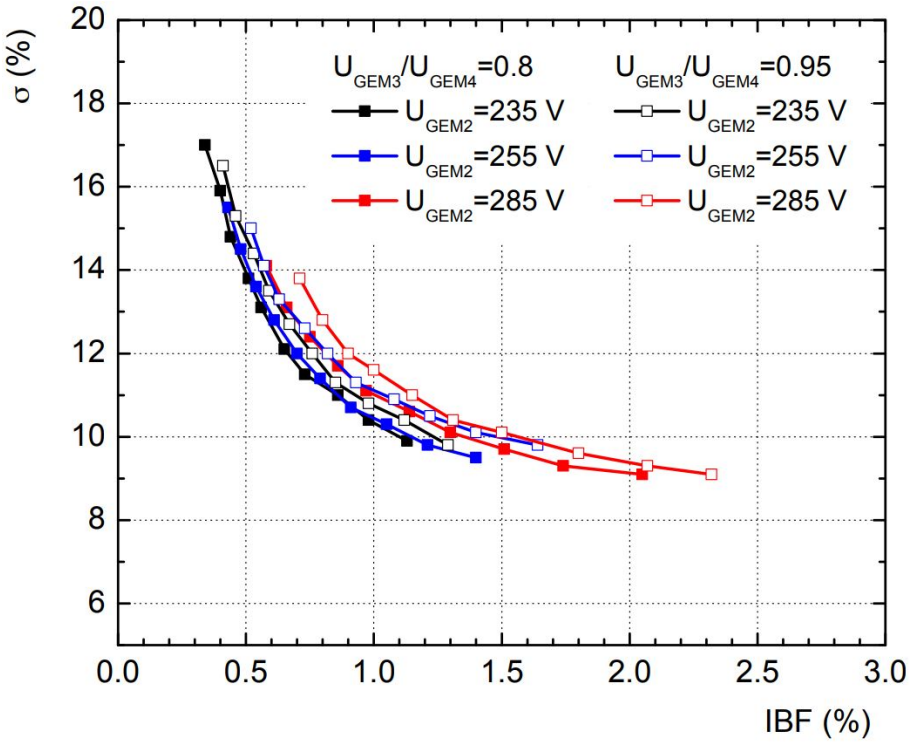

Figure 3.28: Ion backflow and energy resolution at 5.9 keV in a quadruple GEM stack for different values of ΔU_{GEM2} (GEM 1 faces the drift volume, GEM 4 faces the pad plane). The gain is kept at a value of 2000. Adapted from [63].

A prototype quadruple GEM stack system has been tested and was able to provide the previous requirements at an energy resolution of 12%(σ) of the ^{55}Fe photo-peak at 5.9 keV, sufficient for the TPCU prerequisite.

Simulation studies [63] have shown that optimal performance is reached in a setting where the hole pitch of the GEM foils differs among the layers.

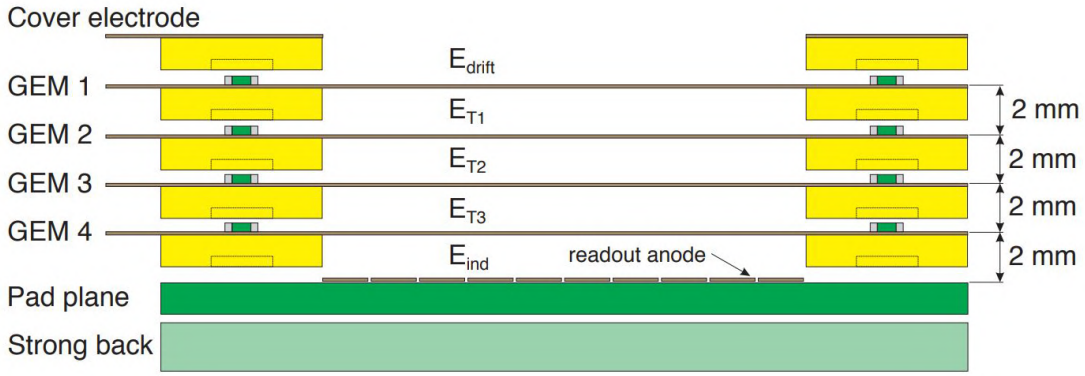

Figure 3.29: Schematic view of a GEM stack produced for the TPCU [74]. Each GEM foil is glued onto a 2 mm support frame, defining the gap.

To ensure consistency, a naming scheme has been defined. The numbering of the foils increases in order towards the pad plane (see Fig. 3.29). The space between the top side of the first GEM and the drift plane is called the drift gap, while the distance between the lower electrode of the last GEM in the stack and the readout plane is coined the induction gap. The slots between GEMs are called transfer gaps, following the same numbering scheme as for the GEMs.

For the TPCU a setting has been chosen where layers 1 and 4 feature a so-called standard(S) pitch (140 µm) and GEM foils 2 and 3 have a large pitch (LP) (280 µm). The hole pattern of each GEM is rotated by 90° with respect to the previous GEM arrangement. The HV configuration proposed for Run 3 in the technical design report can be found below.

E_{drift}	E_{T1}	E_{T2}	E_{T3}	E_{ind}	ΔU_{GEM1}	ΔU_{GEM2}	ΔU_{GEM3}	ΔU_{GEM4}
0.4	4	4	0.1	4 kV/cm	270	230	288	359 V

Table 3.2: Values for the GEM stacks from the Technical Design Report [63].

Considering that GEMs feature large high voltage values over small distances, there is a possibility for electrical breakdown to occur in the gas. This is to be avoided because high energetic gas discharges can lead to mechanical damage to the foil, possibly rendering the detector inoperative.

It was shown [75] that by reducing the capacitance between the electrodes of the GEM foil, electrical sparks are less likely to occur. Hence, a metallized side is segmented into sectors, each about 100 cm^2. Each sector is powered up separately through a high-ohmic loading resistor of the order of a few MΩ, soldered onto the foil and connected to a high voltage (HV) distribution line. The unsegmented side is supplied directly.

In case of a short circuit across one or several sectors, the resistor helps contain the event only in the affected sectors, leaving the rest of the foil fully operational. Moreover, by orienting the segmented side to face the drift zone helps prevent the propagation of the spark to other elements by making the voltage drop occur only there, leaving the

unsegmented side at its nominal potential.

The value for the loading resistor was motivated by dedicated discharge studies [75], as well as the expected densities in the Pb-Pb collisions amounting to roughly $5\,\mathrm{nA/cm^2}$ (500 nA per GEM foil sector); such a current can result in a considerable potential drop, thus reducing the gain.

The following chapter will detail the importance of mitigating gas discharges in MPGDs, alongside the physics that lay behind.

4 Playing with lightning

4.1 Requirements on GEM reliability in RUN 3

The plans of the ALICE collaboration to extend its heavy-ion programme, in order to exploit the scientific potential of the LHC after the upgrade for studies of the QCD and QGP, account for a timeline that stretches to about 10 years of operation after the LS2.

The essential objectives for a long-term operation of the enclosed detector systems, especially in the harsh environment of high-rate, high multiplicity that ALICE faces, are radiation hardness, ageing safeguard and stability against electrical discharges.

Deterioration of performance under irradiation remains one of the main limiting factors of gas detectors. This decline includes, among others, the loss of efficiency, gas gain, the worsening of energy resolution, excessive currents and changes in surface quality. Several years of intensive research aimed at matching the needs ALICE has in the upcoming physics runs of the LHC have proven that GEMs can be robust and stable in the presence of highly ionizing particles and high rates.

Furthermore, no decline in efficiency was observed for specific choices of aging-resistant gases. Ageing phenomena are the result of chemical reactions occurring in the presence of a gas mixture which lead to the formation of deposits on the electrode surfaces. They are a serious threat that can limit or severely impair the use of gaseous detectors. The biggest impact is the layering that develops on the surface of the cathode, which can become positively charged when the charges are unable to reach it. This, in turn, produces a large dipole electric field that can exceed the field emission threshold, triggering secondary electron emission from the cathode and producing new avalanches[1]. The consequences include a decrease of gain or a lack of its uniformity, the loss of energy resolution and dark currents. A detailed description of these efficiency degradation phenomena can be found in [77–83].

The biggest problem that these delicate structures face are electrical discharges. They will not only lead to degradation of performance or inefficiencies, but are a threat to the integrity of the GEM foils, as they can cause irreversible damage to the detector, leaving it blind and leading to a loss in acceptance. Their occurrence, response and mitigation are of utmost importance in systems where they are performing.

For the ALICE TPCU the optimization of the voltage settings, chosen to achieve minimal ion backflow (see Table 3.2), can facilitate the development of electrical discharges. The use of fragile electrodes, exposed to high electric fields which are needed to achieve the desired gains for the detection of small ionization yields, coupled with the microscopic distances involved, leave the GEM structures prone to electrical discharges.

[1] The Malter effect [76].

Intrinsically, elements like micro-particles or residual dust, highly ionizing particles or sharp edges, from which enhanced electric fields emerge, can contribute to an increased rate of discharges. Not only can the GEM foil be left impaired, but the impulse of this violent reaction can propagate to other foils and even reach the front-end electronics hardware, where it can pose a serious threat in the form of enhanced leakage currents and even permanent short-circuits.

Nevertheless, the enticing properties of the GEM detectors, such as intrinsic ion backflow, fast signal response, low radiation length, excellent spatial resolution and high rate capability, prompts their development and use in the new ALICE TPC.

This thesis aims at understanding the propagating nature of these discharges in the scope of the ALICE TPC upgrade, as well as proposing ways of mitigating them. This chapter will present in the first part the types and current knowledge of the discharge phenomena in MPGDs and in the last one studies done for preventing or minimizing such phenomena from occurring will be addressed.

The GEM foils that will be installed in the endcaps of the ALICE TPC have to pass several quality assurance steps, one of which is the leakage current measurement[2]. It is an electrical characterization that validates if the foils are stable under load by measuring the leakage current in each GEM sector in response to an applied high voltage (HV) across both electrodes (top and bottom side). It has been found [84] that the risk of a GEM discharge is sufficiently low for leakage currents below $I_{\text{limit}} = 0.5\,\text{nA}$ per segment, under a voltage difference of 500 V (which is slightly below the gas breakdown limit in N_2 [85][3] - the test environment chosen to minimize water and dust content).

Fig. 4.1 shows an example of one GEM sector experiencing several discharges before being recovered with N_2 cleaning and burning away of residue with instantly applied HV.

Once installed in the endcaps of the TPC, the readout chambers cannot be repaired in the span of the next physics runs at the LHC. It is imperative that they are not only behaving properly in the laboratory environment, but also under heavy irradiation at beam-tests. Moreover, dedicated *stress tests* with smaller prototypes are required, in which the limits of what a GEM foil can handle are pushed to extremes.

One of the first and most comprehensive reports of discharges in single and multi-GEM structures was detailed in [75]. The authors detailed that when operating the detectors at gains of several thousand (required for efficient detection of minimum ionizing particles), exposure to high radiation fluxes, or the release of a large amount of charge may induce a breakdown of the gas rigidity and trigger sparks.

Likewise, in Chapter 4 of [87], large-size prototypes were build and operated in test-beam campaigns at CERN's SPS in the fall of 2014. The discharge behavior under irradiation with high energy hadrons, similar to LHC operational conditions, was measured. A quadruple GEM IROC prototype with S-LP-LP-S configuration was used, featuring several HV settings to better suit the baseline settings for ion backflow and resolution.

[2] A leakage current is an electric current in an unwanted conductive path under normal operating conditions

[3] Breakdown occurring at 650 V $\quad (p_{\text{STP}}(760\,\text{torr}) \times d_{\text{GEMhole}}(50\,\mu\text{m}) = 3.8\,\text{torr/cm}$ in Fig. 4 [85])

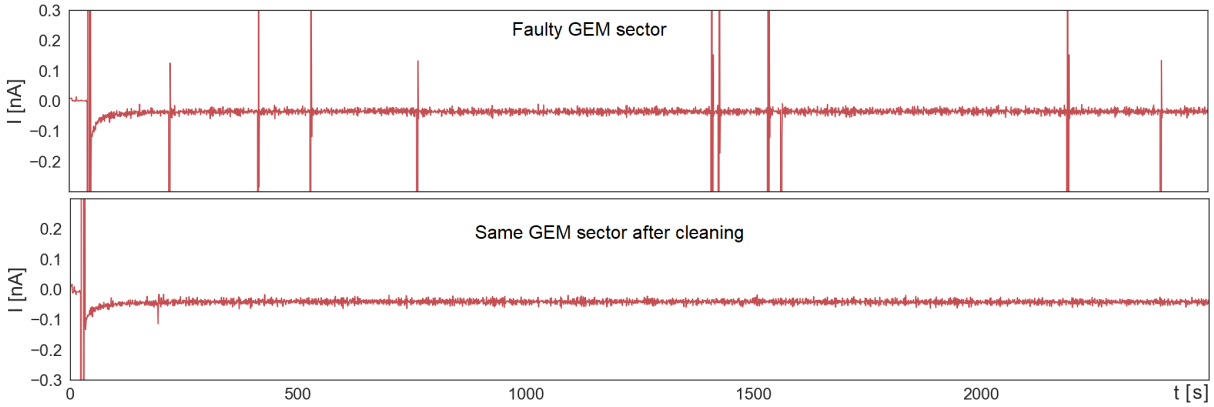

Figure 4.1: The leakage current measurement of one sector before and after cleaning. The GEM foil was successfully recovered after experiencing excessive sparking. Due to the fact that the GEM segments are connected to the HV bus via protection resistors (5 MΩ), the additional circuit introduces a lower practical limit of $I_{\text{limit}} = 160\,\text{pA}$, compared to the true current limit criteria of $I_{\text{limit}} = 0.5\,\text{nA}$ [86].

With the showers of highly energetic hadrons impinging perpendicular to the detector plane, a total number of accumulated particles of $N_{\text{tot}} = (4.7 \pm 0.2) \times 10^{11}$ was measured by integrating the chamber current over the beam time period. This number is consistent with the number of expected particles in the TPC for a run-time of $10^6\,\text{s}$ at a collision rate of 50 kHz. Assuming a charged particle yield $dN_{\text{ch}}/d\eta = 500$ [63] and a coverage of roughly one unit of η for each of the two readout planes, an estimate of $500 \times 2 \times 50000 \times 10^6 = 5 \times 10^{13}$ charged particles will be hitting the active readout area of the TPC per year of Pb-Pb. Splitting the amount among the 144 GEM stacks and including a factor of two on account of the background, will result in an accumulation of 7×10^{11} particles per GEM stack.

As such, a discharge probability of $(6.4 \pm 3.7) \times 10^{-12}$ per incoming hadron is estimated. This translates into between 2 and 5 discharges expected per GEM stack during the usual month of Pb-Pb. Based on the values, a maximum of 650 discharges for the whole TPC per month of Pb-Pb (there is at best one month of Pb-Pb data taking per year, as previously explained; see Fig. 3.23) at 50 kHz are to be expected. The number will be decrease for pp runs, where the $dN_{\text{ch}}/d\eta$ is smaller. These quantities are not believed to pose any serious risk to the TPC in the long run, ensuring an efficient and safe operation for the vessel in RUN 3 and beyond.

Nevertheless, understanding how a discharge affects the GEM foil, how long the detector is blind, how it is possible to recover the GEM if damage occurred and if there are means of mitigating their appearance is desired.

4.2 Transition from avalanche to streamer and breakdown of the gas rigidity

As detailed in Sec. 3.2.3, in high electric fields the electrons acquire sufficient energy between collisions to ionize the gas and release free charges, which, in turn, ionize further atoms. This triggered chain reaction, also called an avalanche, is responsible for the needed amplification of primary charge in gaseous detectors.

The developing number of electrons N can be calculated as:

$$N(x) = N_0 \exp(\alpha x)$$

and is related to the gain of the structure by:

$$G = \frac{N(x)}{N_0}$$

where α is the inverse of the mean free path, the so called Townsend coefficient. It depicts the probability per unit length of drift that a primary electron creates an additional electron. The exponential rise and the value of this coefficient are shown in Fig. 4.2.

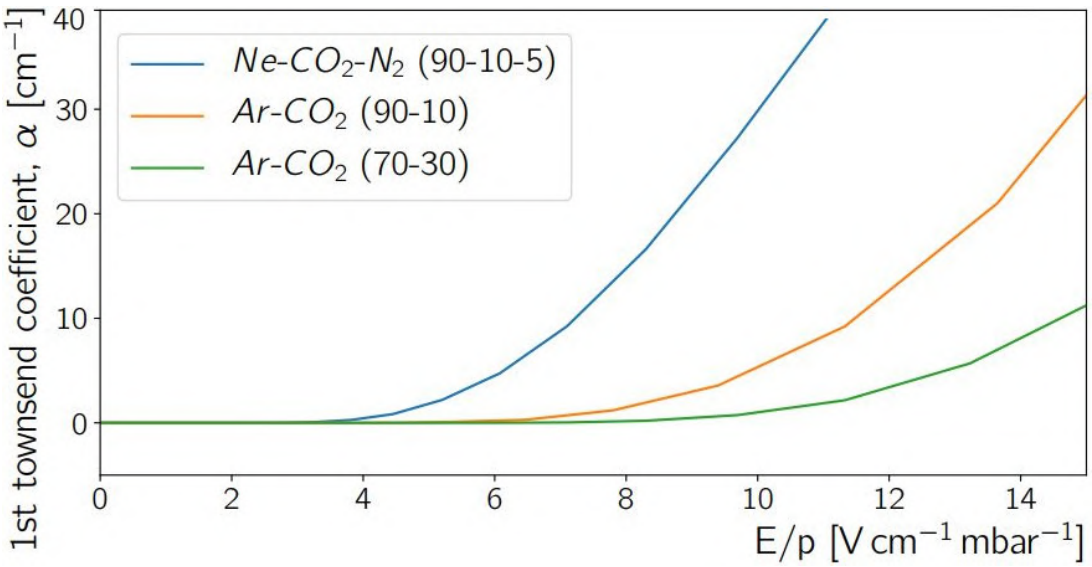

Figure 4.2: Magboltz [88] simulation of the Townsend coefficient for the gases used in the ALICE TPC [89]. The simulations were done for SATP[4]conditions.

Townsend's gaseous breakdown model accounts for electron impact ionization in the volume, as well as secondary electron emission from the cathode. Similar to the first ionization coefficient α, a secondary emission coefficient γ can be defined as a measure of the number of electrons ejected by secondary processes.

[4]Standard Ambient Temperature and Pressure (25 °C and 1 bar)

The process of secondary emission and multiplication will become self sustaining if the ions from the avalanche between $x = 0$ and $x = d$ meet the following criteria:

$$\alpha d = \ln\left(1 + \frac{1}{\gamma}\right)$$

At low gas pressures, this secondary ion and photon-induced feedback mechanism is dominant and can lead to a *slow breakdown* [90]. In the region of atmospheric pressure, the dominant mechanism of discharge is a fast, photon-mediated transition from proportional multiplication to a streamer, followed by a breakdown (see Fig. 4.3).

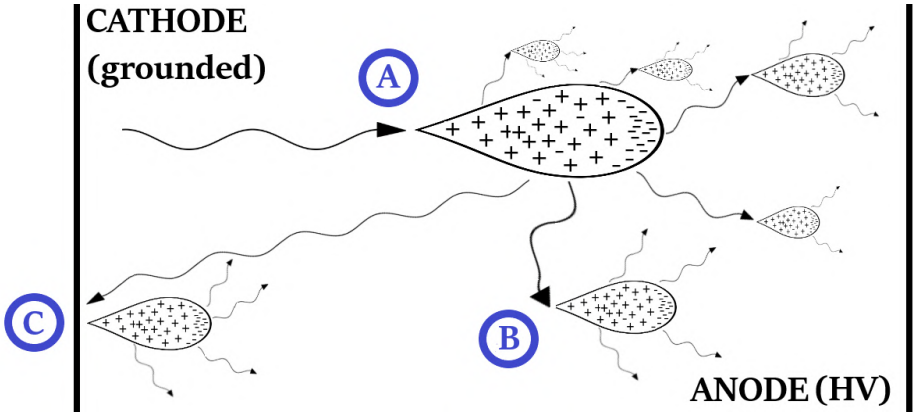

Figure 4.3: Schematic of charge generation by the Townsend breakdown theory. Ⓐ Radiation induced avalanche grows towards the anode. Ⓑ Photons are emitted from the main avalanche and can ionize gas atoms some distance away, starting a secondary avalanche. Ⓒ Photons can hit the cathode and liberate electrons.

Raether observed [91] the development of a pre-breakdown electron avalanche, whose spatial growth is described by the Townsend equation, into a current spark. He quoted development speeds of the electron avalanche from the cathode into the gas space in the order of $\sim 10^7$ cm/s. The development of an avalanche is shown both as a schematic and as a photograph in Fig. 4.4.

His results show that there is a critical point [93] in the amplification (around $\alpha x = 20$), also known as the *Raether limit*, corresponding to a several 10^7 electron-ion pairs ($\sim \exp(\alpha x)$), when the qualitative behavior of the avalanche changes.

The space charge build-up generates its own electric field E', which is added on top of the external (applied) field E_0. Because of the different charge mobility, charge separation occurs. Electrons will position themselves at the avalanche front, leaving ions behind (who can be assumed static for the timescales involved). This creates a dipole with the characteristic length λ, which describes the mean free path of electrons.

The ensuing local field modification is depicted in Fig. 4.5 (1). The avalanche head can be idealized to a negatively charged sphere (in truth it is spread as a crescent shape), behind which the positive space charge lies.

The external and intrinsic electric fields add up in front of the avalanche head, as well as between the positive head and the cathode, to make the whole ensuing field stronger, thus

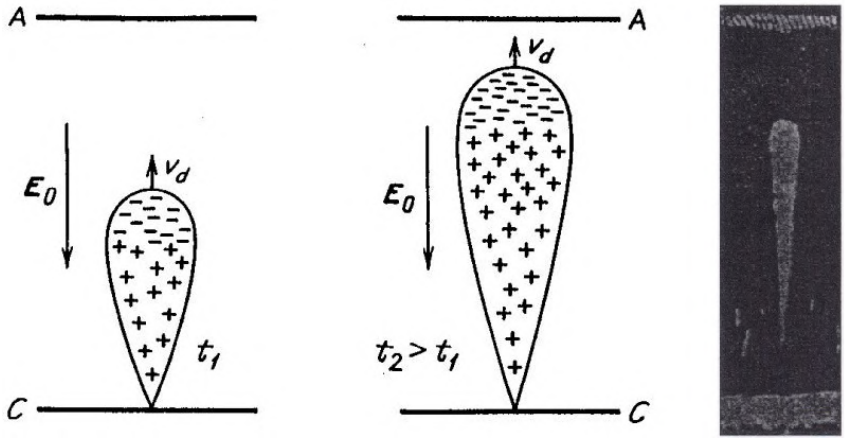

Figure 4.4: An electron avalanche at two consecutive moments of time. Arrows show the direction of external electric field E_0 and the velocity of the motion of the avalanche head v_D. On the right there is a photograph of an avalanche. Adapted from [92].

enhancing the ionization. Where the charge separation occurs, a radial electric field forms. Here, the resulting field is lower than the external one, slowing the ionization process, since the dipole field points against the applied external field.

The growth of the negative charge front during the development of the avalanche (and accordingly the intrinsic dipole field) will continue. At a distance of about an avalanche radius [94], the intrinsic electric field reaches the value of the applied external field, for the critical value of $\alpha x = 20$. At this point, the track will develop at a mean velocity of $(7 - 9) \cdot 10^7$ cm/s [91].

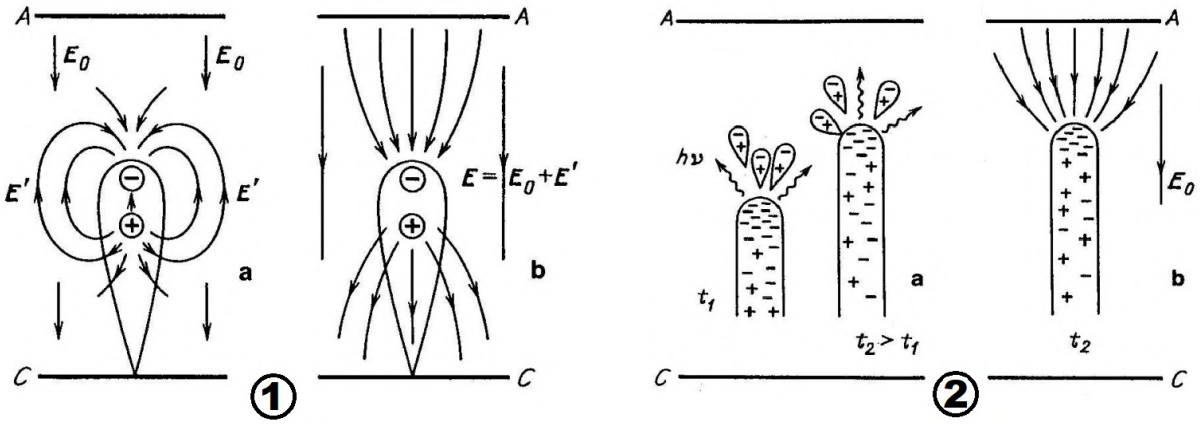

Figure 4.5: ① - Electric field distribution of a developing avalanche: (a) External and intrinsic fields depicted separately; (b) The combined outcome of the fields. ② - Anode-directed streamer at two consecutive moments in time: (a) Photons in front of the avalanche aid its development; (b) Field in the vicinity of the head. Adapted from [92].

When this *growing instability* is achieved and the Raether criterion is established, the transition from an avalanche to an anode-directed streamer takes place.

Concomitantly, four to ten times as many atoms and molecules are being excited alongside the ionization products. The excited species emit radiation of short wavelength within some 10^{-8} s [95], that is highly absorbed in the gas, leading to cumulative ionization in the whole gap.

These photons are emitted isotropically by de-exciting atoms. They create corresponding photo-electrons. Only the electrons produced ahead of the front tip are aiding the avalanche rate development. The ones produced on the side arise in a field only slightly distorted ($\ll E_0$), their ionization potential falls rapidly with the field [96] and their contribution is negligible (see Fig. 4.5 (2)).

The electrons will sink in the anode element as soon as the avalanche front reaches it. In their wake, only the ion trail with an apex of maximum density at the anode will remain, stretching as far as the initial primary electron, given the speeds involved in the development of the streamer and the low ion mobility (because of the larger mass ions have compared to electrons, they are slower by about a factor of 10^3). The streamlines for the electric field are depicted in Fig. 4.6 (1). The mirror charge in the anode, alongside the ion trail are combining to generate the total electric field. This field is modest near the anode, but grows further away toward the cathode, where it can exceed E_0, reaching a maximum at the characteristic ionization distance λ (the mean free path of electrons) [94].

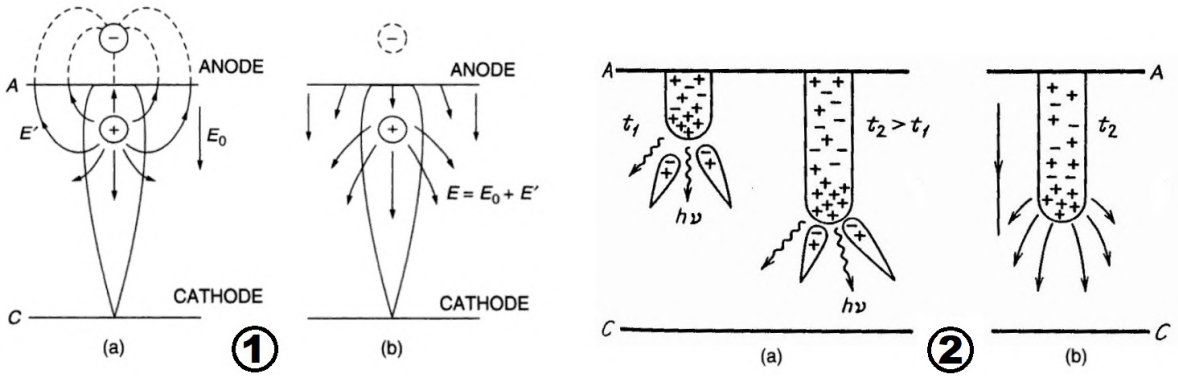

Figure 4.6: ① - Electric field distribution of an avalanche reaching the anode: (a) External and intrinsic fields depicted separately; (b) The combined outcome of the fields. ② - Cathode-directed streamer at two consecutive moments in time: (a) Photons seed electrons for avalanches towards the cathode ; (b) Field in the vicinity of the streamer head. Adapted from [92, 94].

Soon after reaching the anode, the streamer returns towards the cathode, further developing in the path of the original avalanche, at even higher speeds $(1-2)\cdot 10^8$ cm/s [91]. The emergent electric field is so high that it supplies the electron drift with velocities exceeding by a factor of 10 the typical electron drift velocities in gas (few cm/µs = few 10^6 cm/s).

Given the very high velocities involved, the return phenomenon cannot be explained by the movement of the positive charge. Only the photo-electrons seem to be liable for such a fast effect (see Fig. 4.6 (2)).

The density of the positive ion space charge (and hence the field distortion) is strong enough to attract photo-electrons produced near the positive charge channel, rendering it a conducting quasi-neutral plasma. The high fields also give rise to positive-ion induced secondary electron emission from the cathode [97], in addition to photo-electric emission. This way, a cathode spot is forming, which can become a source of visible light [95]. It also acts as a source of heat, releasing a substantial amount of electrons from the material, aiding the breakdown of the gap and the spark formation.

Considering this counter-growth, the two electrodes will be bridged by a conducting filament of plasma. If an efficient cathode spot has formed, a large return electron current travels the streamer channel toward the anode at speeds in the order of $10^9 - 10^{10}\,\mathrm{cm/s}$. The high velocity of this ionization wave is not the velocity of the electron motion, but rather the phase velocity of the ionization wave.

The high density current in the channel results in Joule heating, with temperatures as high as 20 000 K [94]. At the same time, electron concentration rises to about $10^{17}\,\mathrm{cm}^{-3}$, which is close to complete ionization. All the while, the channel grows in diameter.

The heated gas expands and creates a shock wave along the full spark channel, which can be heard. The intense ionization gives rise to many photons, so the spark is also visible. Finally, the breakdown is completed as a spark[5] [95].

For the fragile structure of the GEM detector, the heat and shock wave pose a serious risk. The high current and the ionization channel will extend until the energy stored in the system (the capacitance between the cathode and anode elements) is exhausted. Usually, the spark is quenched when the potential difference across the gap between the anode and cathode surfaces drops.

Nonetheless, a transition to permanent arc discharge can occur if the power supply can sustain the high currents in the spark channel for some amount of time. This is to be avoided by all means.

Therefore, studies of discharges in GEM detectors, similar to those implemented in the ALICE TPC, are a current topic of research. The following sub-chapters will detail the experimental setup used, the classification of discharges for the setup, as well as ways to mitigate the sparks.

[5] Spark - unstable discontinuous process marking the transition from one stable state of current in a gas to another stable state.

4.3 Experimental setup

4.3.1 Double-GEM detector

A detector vessel containing two $10 \times 10\,\mathrm{cm}^2$ GEM foils manufactured by CERN's micro pattern gas detector workshop are used to study discharges. Each of them consists of a sheet of 50 µm of Kapton, cladded on both sides with a thin layer of 5 µm copper. The GEM is perforated with a matrix of holes, each with an outer diameter of 70 µm, an inner diameter of 50 µm and a pitch (distance from the center of a hole to the center of an adjacent hole) of 140 µm.

The two GEM foils came in a kit, which further contained a readout board, a drift mesh electrode, a gas box cover and an epoxy gas box frame with O-ring grooves. The detector was assembled in a clean room in order to avoid any dust contamination. Each GEM foil was optically checked and cleaned with a nitrogen blower, making sure never to touch the sensitive surface.

Afterwards, a quick leakage test is performed at 600 V without any series protection resistors, at a 5 µA/100 cm current limitation for about a minute. This test is done to have comparable results to the ones obtained by the workshop before packing the GEMs. When the HV is turned on, the current stabilizes to the leakage current of the GEM foil after a few seconds, while the system charges all the capacitances.

It passes the test if the leakage current is less than 1 nA in a medium with less than 35% humidity. Sparks can occur for the first few seconds, as any dust residue that is present is burned. In addition, a capacitance test is done and its value is compared to the recorded value of 5.8 nF.

Having passed the necessary tests, the two GEMs are stacked on top of the sensitive area of the readout board. The desired spacing layout between foils is achieved using nylon screws of different sizes. On top of those elements, the drift plane is inserted. The GEMs and mesh electrode are soldered by a fanout onto the readout board featuring pads with a Panasonic connector. The gas box frame and a cover are fixed around the components. A picture taken during the assembly of the detector can be seen in Appendix E.

The leakage test is redone for each GEM, this time in a nitrogen environment with a controlled humidity level. Moreover, a gas tightness test using a sniffer is also performed, ensuring that the O-rings are well positioned.

The final detector ensemble used in the current study is sketched in Fig. 4.7.

There are several regions defined by the electrodes and further named and abbreviated in the thesis. The region from the mesh cathode and down to the uppermost GEM is called the *drift gap*. Following that comes the topmost GEM, called GEM 1. Of importance are the top and bottom electrodes, abbreviated **G1T** and **G1B**, respectively. In between the two GEMs is the *transfer gap*. Subsequently, comes the second GEM with its two electrodes **G2T** and **G2B**. The space between the lowermost GEM and the anode pad plane is the *induction gap*.

The detector container is flushed at a rate of 100 mL/min with Ar-CO_2 (80-20) at atmospheric pressure. The gases are supplied from a main line in the laboratory and are mixed using a Brooks® Mass Flow Controller 5850 TR Series.

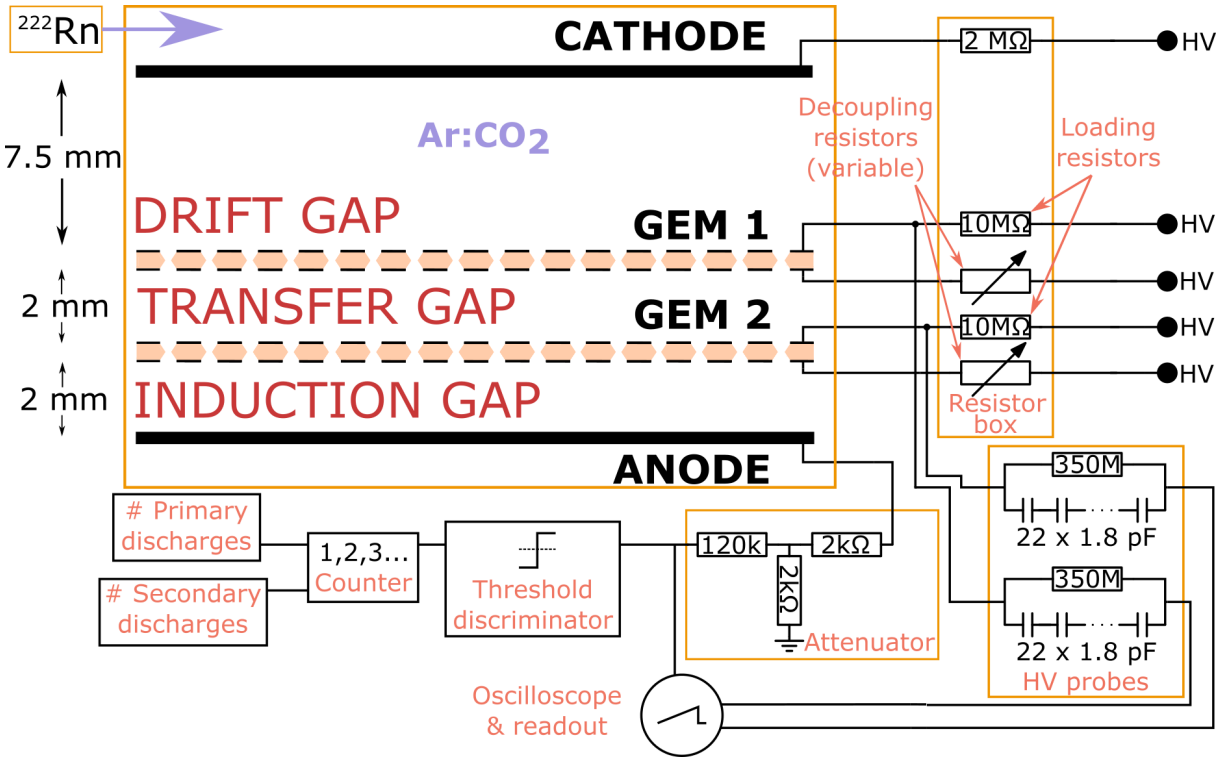

Figure 4.7: Sketch of the setup used for discharge measurements. Two GEMs are stacked and sandwiched by a readout anode and a cathode mesh. Discharges are generated by proper choice of voltages and a gaseous Rn alpha particle emitter. The induced signal is read by an oscilloscope and then processed offline. To infer the occurrence of a discharge on the various elements, two HV probes are used, monitoring the potential drop.

The effects of different gas mixtures were not studied in the present document. Their influence on the appearance and behavior of discharges is well known. It will be briefly discussed later and is detailed in [98–102].

The vessel is an open gas system, which means that the pressure in the detector follows the atmospheric pressure of the room. Ambient conditions, of which the most considerable being the pressure, have a big impact on the rate of discharges. This is because the properties of the gas, such as the gain or the drift velocity, depend on the gas pressure.

Therefore, pressure needs to be monitored and taken into account when explaining the different effects. To this end, a MSR 145 data logger is placed near the detector which simultaneously records a variety of parameters, such as temperature, humidity and pressure. The values are recorded once every 60 s and saved.

The readout plane of the setup features pads. The signal induced on the pads is outputted through a Panasonic connector to a 6-dB T-type attenuator[6] and further to a Tektronix® MDO3024 oscilloscope. The use of an attenuator is necessary to protect the electronics of the oscilloscope from the high currents during discharges in the detector and

[6]The input value is assigned the 0-dB reference value. The attenuation of 6-dB indicates that the output is below the reference value, with a radio between output/input corresponding to 1/2.

to match the signal amplitude of the events to the oscilloscope's dynamic range (±10 V). A zoomed-in example of a discharge on the pads can be seen in Fig. 4.9.

A photograph of the GEM detector and the hardware used for the setup is shown below.

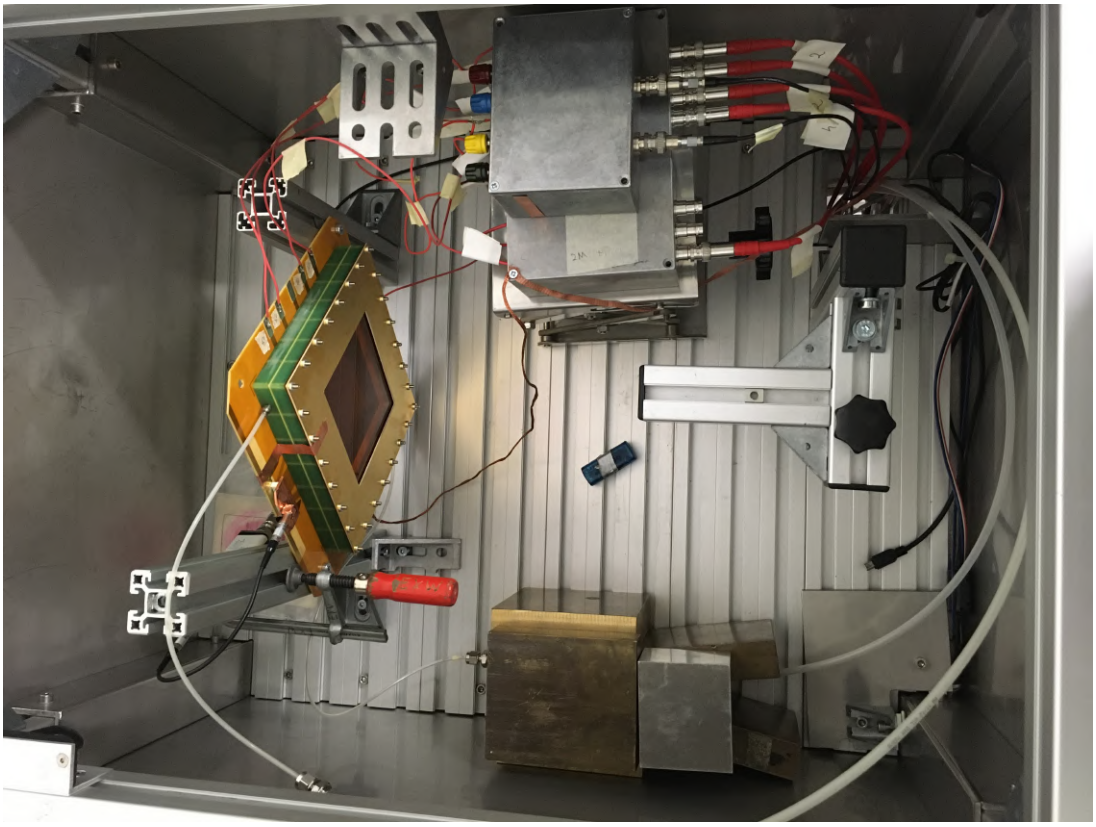

Figure 4.8: Top view of the box in which the detector operates, alongside some of the hardware used for this thesis.

The electrodes of the GEM setup are housed in the metallic structure on the left side of Fig. 4.8. The pad plane PCB, shown in yellow, has traces to which wires are connected to a resistor box. Moreover, it delivers the pad plane signal, which goes in the attenuator.

The resistor box houses the top and bottom electrode resistors needed to protect the GEM. The red HV wires come from the power supply. The box on the top houses the two HV probes. The input is represented by the respective electrode under test, while the output is sent to the oscilloscope, alongside the attenuated pad plane signal.

The small blue device is the MSR 145 sensor for reading the temperature and pressure of the chamber. The gas comes from a mixer, which operates at atmospheric pressure. It is fed through a container (hidden behind the lead bricks on the bottom side of Fig. 4.8) containing a gas mantle (Glühstrümpfe), acting as a Rn emitter, and finally introduced in the detector.

4.3.2 Generating and counting discharges

A counting scheme is employed to count the two types of discharges that can occur, either in the GEM hole or in the gap between the two GEMs (the events are detailed later on). The two events have different characteristics, which aid in constructing a rather simple counting logic using NIM modules. This logic is used in conjunction with software processing to count the different events. The flowchart of the logic is detailed in Fig. 4.9.

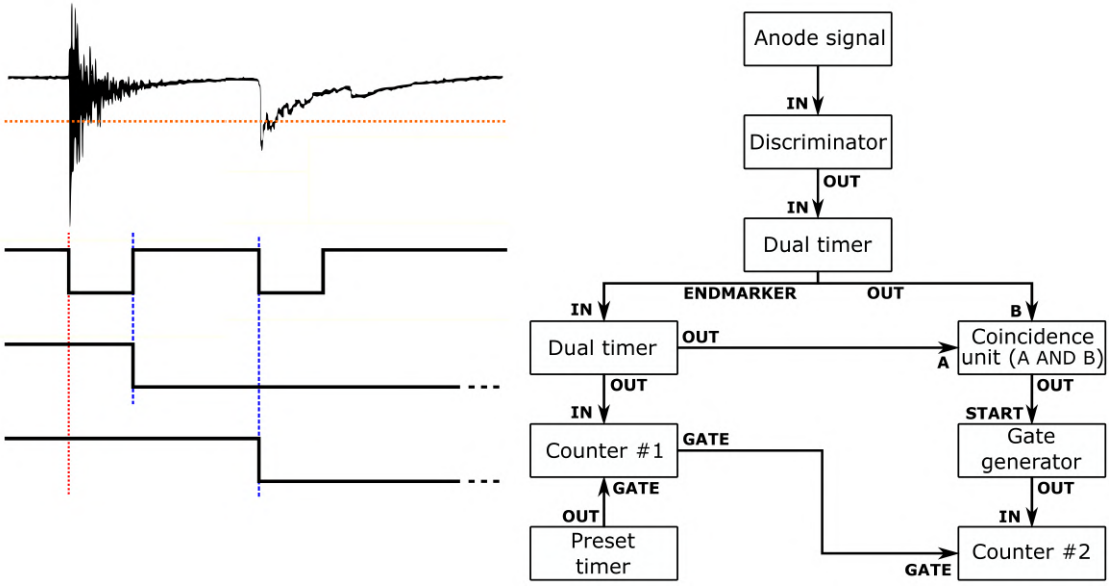

Figure 4.9: A typical anode signal and the NIM module counting logic used for distinguishing events.

The anode signal is used for the counting logic. It is first fed to a LeCroy 623B Octal Discriminator with a fixed threshold, way above the ground noise level. Oscillations are present for the discharges occurring inside a GEM hole (the first of the events in Fig. 4.9).

As such, the discriminator output (a short width signal, a few tens of ns) is stretched for about 0.5 µs (in all events the oscillations cease – drop below the discriminator threshold – after less than 500 ns), ensuring that the oscillations are well below the threshold level. This is done using a CAEN 2255B Dual Timer.

Later on, the endmarker signal (output pulse leading edge is coincident with the trailing edge of output signal) is stretched for about 100 µs and recorded in the first counter (CAEN N1145 Quad scaler and preset counter), denoting how many times the first event (discharges in a GEM hole) has occurred.

A splitter sends the signal from the Dual Timer into a CO4001 Quad Coincidence unit. A second wire carrying the information from the stretched primary signal arrives here and when the coincidence occurs, a secondary event is registered. This is also stretched over 100 µs to ensure proper counting and that no other events are misidentified (e.g. reignition of discharges, as explained later).

The counting logic is used in conjunction with an in-depth analysis done with offline waveforms saved from the oscilloscope.

To induce controlled discharges, an ^{220}Rn internal gaseous alpha particle emitter is added to the gas flow. When entering the detector, the Ar-CO_2 gas passes through a container with traces of ^{228}Th. This isotope will decay via ^{224}Ra to ^{220}Rn. While the thorium and radon have lifetimes of 1.9 years and 3.6 days, respectively, ^{220}Rn has a lifetime of just 55.6 seconds. The main decay mode happening in the detector will be the one where the Rn will emit an alpha particle with a decay energy of 6.405 MeV. Later in the chain, the end product will be ^{208}Pb which is stable. Part of the ^{220}Rn decay chain, relevant for the source used, alongside the half-lives and Q-values are shown in Fig. 4.10.

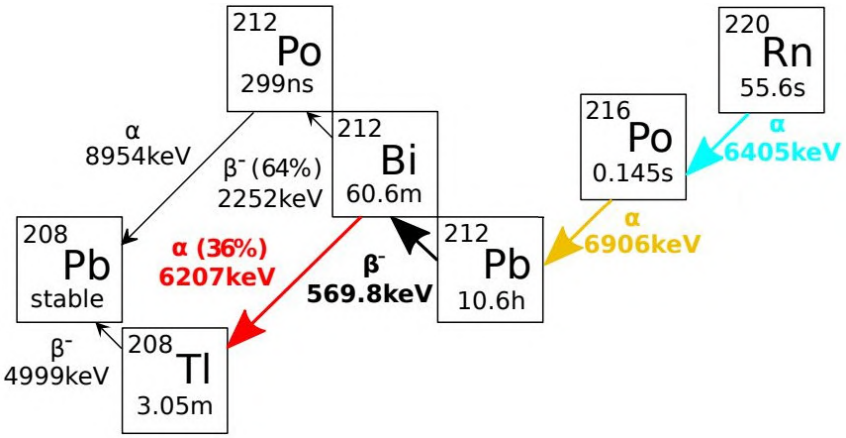

Figure 4.10: ^{220}Rn decay chain. Figure taken from [103]. Values taken from [104, 105].

Considering the amount of energy required to produce an electron-ion pair through ionization (W_i) in Ar-CO_2 mixture [106], a total of

$$\frac{E_\alpha}{W_i} = \frac{6.405\,\text{MeV}}{27.63\,\text{eV}} \approx 2.32 \times 10^5$$

electron-ion pairs will be created on average. Most of the energy loss of the alpha particles will occur when close to being stopped (near the Bragg peak) - see Fig. 4.11. Simulations and measurements [99] show that there is an enhanced discharge probability when an alpha radioactive source is placed at a distance from the GEM that corresponds to the track length (the distance at which the particle lost all its energy) for the Bragg peak. Consequently, it yields the highest local primary charge densities in the GEM holes.

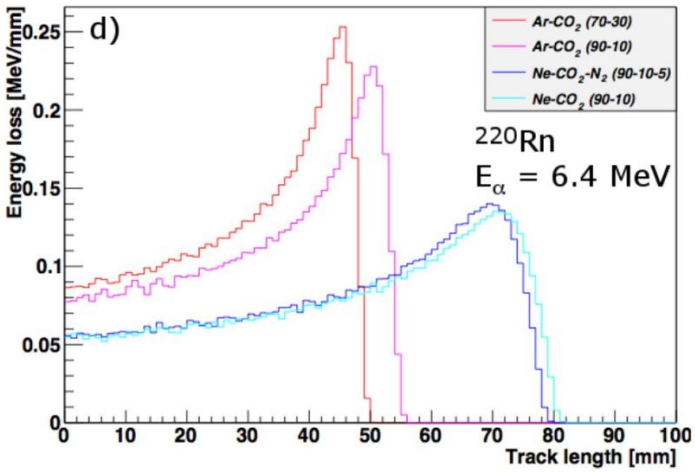

Figure 4.11: GEANT4 simulation of the range of alpha particles from a Rn source [87].

The advantage of using the Rn injection method is that the sensitive volume of the detector is uniformly exposed to the isotope. By having a bigger drift gap volume, most alpha decays will occur above the GEMs.

4.3.3 Powering a double-GEM setup

Regulated HV power supply units are routinely used to bias any kind of detector. Depending on the design, multi-channel power supplies are necessary for a single detector. They consist of a step-up transformer that generates the required high voltage the experiment needs. Different detector technologies require a range of biasing voltages, ranging from a few hundred volts to several kilo-volts.

Designs of HV systems for GEM detectors (see Fig. 4.12) have been typically realized by either using passive voltage divider or by employing independent HV channels referred to ground. The first scheme (B) has the disadvantage that the electrode voltages and fields are fixed by the choice of the resistor values; moreover, the magnitude of the current drawn is two orders of magnitude higher than needed for the chamber operation [107].

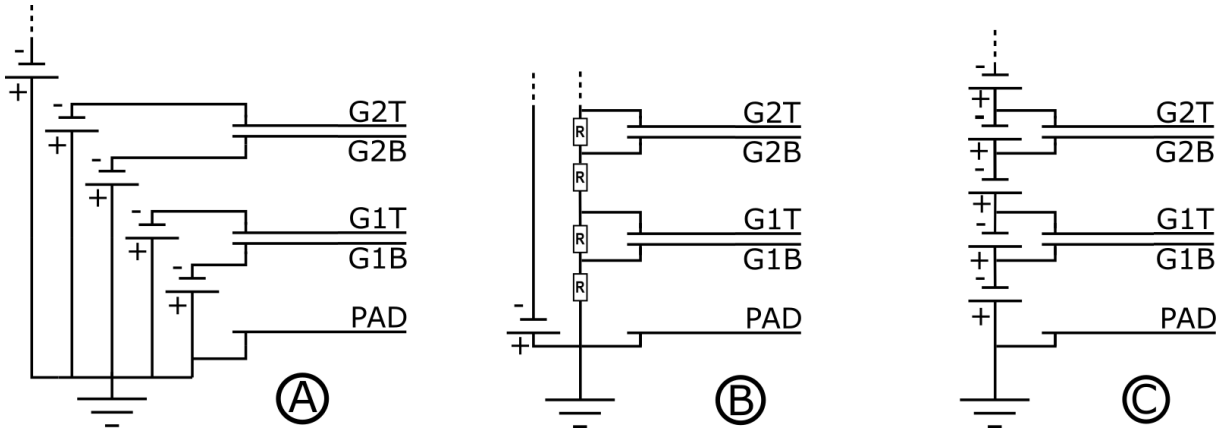

Figure 4.12: Different designs of power supplies. (A) Individual channel power supply. (B) Passive voltage divider with fixed value resistors. (C) Cascaded power supply.

As for the individual power supplies (A), great care has to be taken when powering on or off the detector, while also choosing suitable ramp settings to prevent any damage. The greatest problem such a system poses on GEM operation is that when a short-circuit occurs, the potential on the respective electrode supplied by one of the power supplies will drop to 0 and will therefore increase the fields of the neighboring metal plates, definitely triggering consequent sparking.

Cascaded power supplies (C) have the advantage of solving that problem. In case of a short-circuit across two electrodes, the higher potential will drop to the value of the lower one, essentially extinguishing the potential difference across them. This way, the elements below will be unaffected and stay at their nominal potential, while the ones above the affected two will drop their value by the same amount of the quenched potential difference.

The readout chambers in the new ALICE TPC will be powered by multi-channel A1515 floating channel CAEN power supplies, specifically designed for GEM detectors. Their configuration permits to avoid any possible issue related to the detector discharge and gives the possibility to fine tune the voltage on each detector layer easily.

Moreover, they are sensible down to 100 pA monitoring resolution to perform real-time detector diagnostics. Another attractive safety feature they have is a complex channel

for dealing with *trips* – permanent or momentary short-circuits – that can occur; this is usually accomplished with an overcurrent detection, detailed in the following paragraphs.

For powering the electrodes of the discharge setup, a HVG 210 module is used. It is a seven-channel cascaded power supply (PS) in the NIM standard format [108]. The seven independent HV channels provide each up to 700 V and are equipped with a high sensitivity current meter, as well as a current limiting option. The functional schema of one of the seven modules is presented in Fig. 4.13.

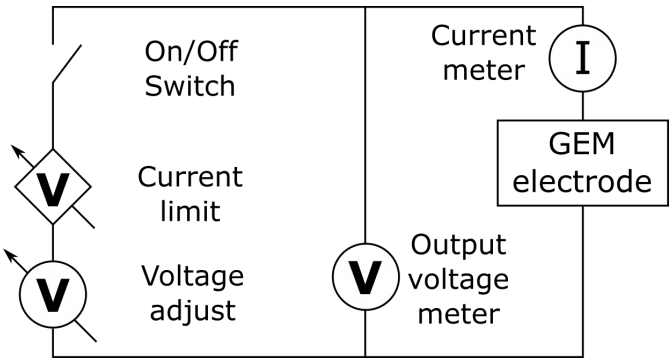

Figure 4.13: A HVG 210 channel.

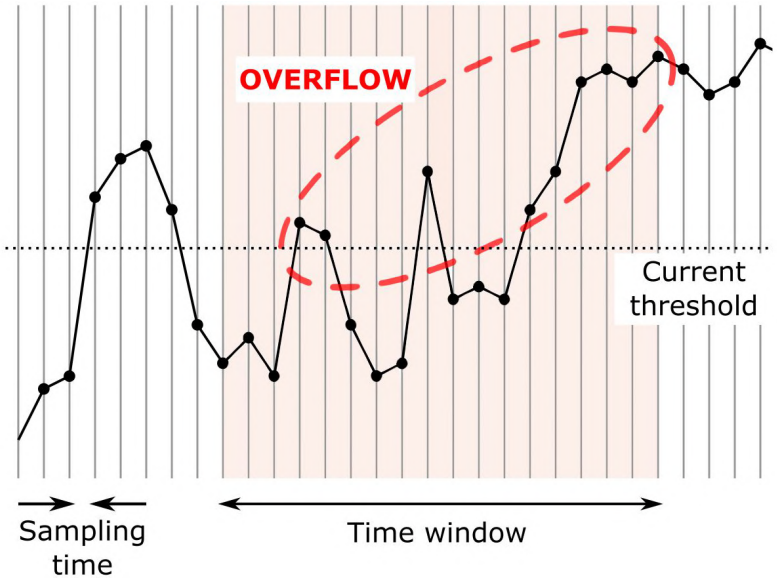

Figure 4.14: Trip control feature of cascaded power supplies designed for GEM operation.

The channels are built using a resonant switching sinusoidal wave mode [109], allowing for a very low common mode noise on the output channels. The power supply also features a mechanism to deal with trips. This is implemented via a firmware routine checking the current sourced by each channel.

With reference to a time window, the current in each channel is sampled (or averaged) at a rate given by the sampling time (the interval between two consecutive current readings). The number of times it goes beyond a user set current threshold is counted and saved in an overflow channel indicator. If any of the seven counters reaches the overflow threshold[7], a trip event is signaled implying the following:

- The overflows indicator retains the overflow counts and the channel, displaying a message for the user.
- A *trip check* flag is set to *trip detected* status.
- Output voltages will drop to zero following a preset ramp-down rate.

[7]The number of times the current reading has gone beyond the specified level; defined by the user.

The values for the time window and current threshold are carefully chosen for the studies done here, to only trigger a trip of the power supply if a violent, continuous discharge occurs. Almost all of the discharges induced in the double GEM setup are transient and therefore do not meet the requirements for a trip. The discharges will increase the current output of the higher potential element involved momentarily. The power supply will therefore be in a *constant current* mode, effectively behaving like a current generator. The output voltage is varied to keep the current below the programmed limit.

The effects of different power supplies on the occurrence of discharges have been thoroughly studied in [102, 110].

4.3.4 Protection resistors and high voltage probes

Another important aspect of the experimental setup is the use of resistors to control the response of the system when a discharge occurs. The top electrode of each GEM features a 10 MΩ **loading resistor** ($\mathbf{R_L}$) that decouples it from the HV power supply, similar to the ones used for the TPCU GEMs (5 MΩ). Their main role is to quench a spark, reduce the current and protect the GEM segment. In case of a discharge, the potential across the GEM (ΔV_{GEM}) will drop and will recover in hundreds of milliseconds.

The value is twice the one of the GEMs used for the TPCU. Extensive studies have been done with different values of $\mathrm{R_L}$ and showed that it plays no significant role in the occurrence and mitigation of discharges [102, 111, 112]. A relevant plot will be explained later on (Fig. 4.36).

The bottom electrodes can feature a **decoupling resistor** ($\mathbf{R_D}$). Contrary to their top electrode counterpart, slight value variations are shown to help mitigate discharges, as will be discussed in the following sections. As a result of the discharge studies, the ALICE TPCU will feature 100 kΩ decoupling resistors on each of the GEM bottom electrodes in a stack.

Similar discharge studies cited further on in the thesis can feature so-called *sink resistors*, which are added to each HV-powered channel to ground to help sink excess currents in case of a discharge. They are not employed in the current work.

The last elements of the experimental setup, of utmost importance to detect discharges, are the two custom made HV probes (see Fig. 4.15). Custom probes are preferred to commercially available probes, since the latter have much larger frequency response and as a consequence the signal is largely modified.

They are inserted in the path of one GEM electrode to the PS, at the GEM side, after the resistors, when looking from the PS side. As such, they are coupled with the response of the GEMs and do not see the circuit effects from the resistors and cables used.

In the event of a discharge, they have a fast response to potential changes on the GEM electrodes. The probes are read on two separate channels on the oscilloscope and form a voltage divider with its internal resistance.

For each probe, an equivalent resistance of 353 MΩ forms a voltage divider with the internal 1 MΩ resistance of the oscilloscope, allowing to measure high potentials of interest within the dynamic range of the oscilloscope (±10 V).

Fast probes are desired, to study effects of discharges which happen within time frames down to order of 100 ns. As a result, an attempt is made to match the impedance of the probes to that of the scope channels, ensuring proper signal transmission. The oscilloscope has 13 pF internal capacitance on each channel, an approximate value that is quoted in the manual. The equivalent RC constant will be 13 µs.

Therefore 22 capacitors, each 1.5 pF, are soldered in series and mounted in parallel to the resistors above mentioned. The resulting theoretical probe capacitance is 68 fF. In addition to this value, parasitic capacitances are expected, due to soldering connections, as well as shunt capacitances to ground. The resulting RC constant of the HV probe will be approximately 24 µs, comparable to the RC of the oscilloscope.

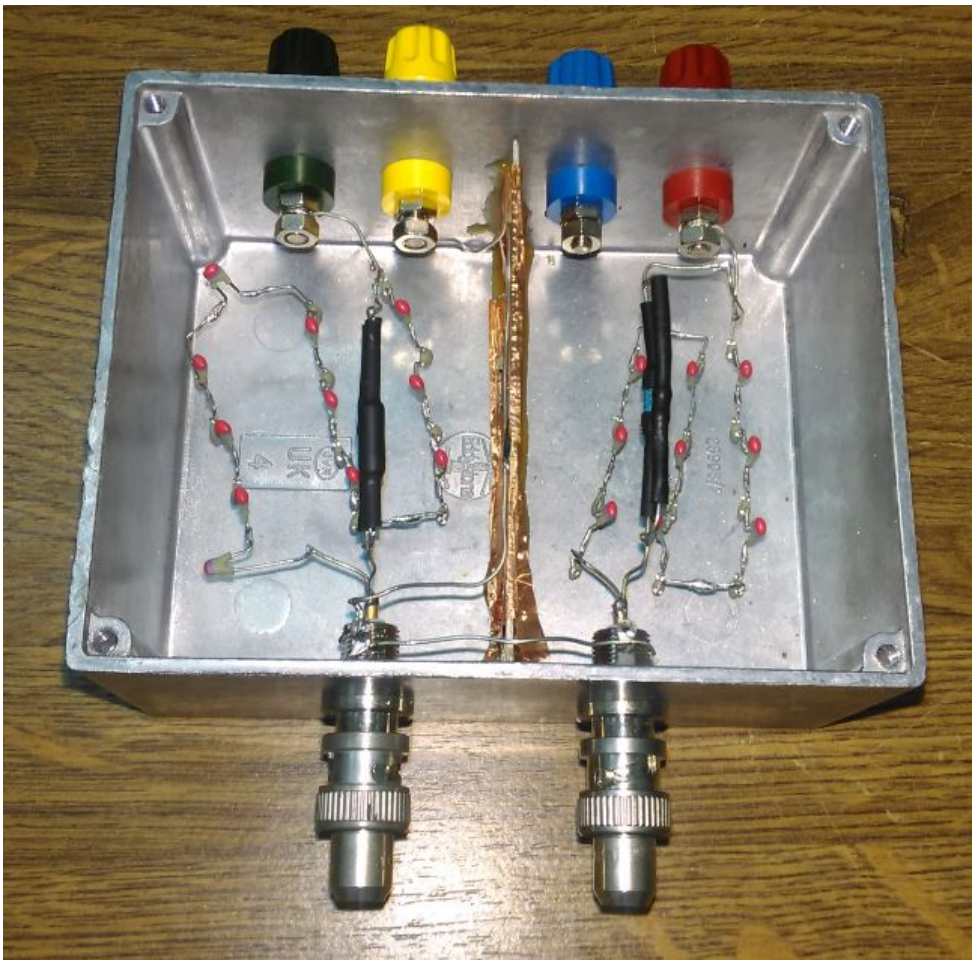

Figure 4.15: Custom made HV probes (2 channels). Wires linking the GEM electrodes are easily connected and interchanged in the banana connectors. After the RC circuit, a lemo connector ensures the transmission of the response to the oscilloscope. A plastic wall is added in between the two channels to avoid cross-talk. The metal housing is cushioned with Kapton tape to avoid leakage currents.

Consistency checks are done at several known voltage values returned by the PS and read by the probes. There will be a difference between the set voltage and the real voltage on the electrode, due to a voltage divider circuit between the probe and the loading/decoupling resistors, which creates a small discrepancy that is accounted for in the following way:

$$U_{\text{real}} = U_{\text{set}} \times \frac{R_{\text{probe}} + R_{\text{osc}}}{R_{\text{probe}} + R_{\text{osc}} + R_{\text{L/D}}}$$

In the path of the decoupling resistor, this effect can be neglected due to the use of kΩ resistors as compared to the hundreds of MΩ in the denominator, but for the loading resistors (top electrode of GEMs) the real voltage is 97.25% of the input value. In the rest of the thesis, if not otherwise stated, ΔV_{GEM} values are the real, corrected voltages across the specified GEM.

4.4 Measurement variables

Throughout the following chapter, results will be discussed based on different variables. These are defined in the following lines, considering previous works on the subject.

4.4.1 Primary discharges

A **primary discharge** is a full breakdown in the gas occurring inside a GEM hole. Consequently, as detailed in Sec. 4.2, a spark will bridge the gap between the top and bottom electrode of a GEM foil. Breakdown conditions are met when the total charge in an avalanche exceeds the Raether limit. Low rate MIP-like particles that cross the sensitive detector volume create on average few tens of electrons per cm^2. The resulting charge density, multiplied by typical gain values of the order of 10^4 is well below the stability threshold.

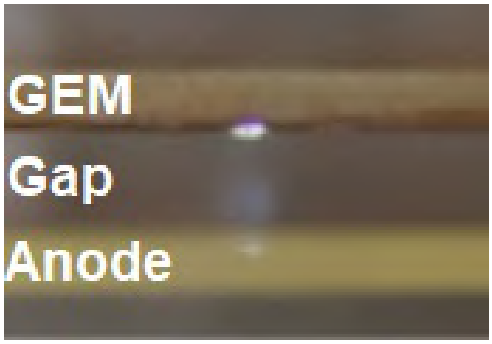

Figure 4.16: Photograph of a primary discharge in a single GEM setup placed in a transparent gas vessel and filmed with a CANON 5D Mark III camera [89].

However, the presence of alpha particles from Rn decay are able to produce upwards of 10^4 electrons per cm^2. The energy deposition of the alpha particles peaks toward the end of the trajectory, as shown previously. This gives rise to high charge densities in the vicinity of the GEM foil, if a source is placed at a proper distance.

To multiply the primary charge to sensible levels and to cope with the charge deposited by rare highly ionizing particles, the amplification is shared among successive GEMs, shifting the maximum sustainable gain upwards. Moreover, the charge is spread out during drift by diffusive processes, diluting the charge per GEM hole as it approaches the readout pads.

For the TPCU, the caveat is the way the GEMs are powered to achieve low levels for the ion feedback. One way of achieving good ion suppression is to gradually increase the gain of each GEM foil in the stack towards the pad readout. The larger amplification in the last stage, combined with the pre-amplified charge density from the previous GEMs can enhance the probability to create the critical amount of charge needed for an electrical discharge to occur.

The authors of [99] have shown that large clusters of primary charge are the main reason ultimately leading to the formation of a spark in a GEM hole. This number is in the order of 5×10^6 electrons after amplification for Ar-CO_2 (70-30) and 9×10^6 for Ne-CO_2-N_2 (90-10-5) – the mixture that will be used in the TPC in RUN 3 – a value highly dependent on the choice of gas mixture.

Given their effective ionization potentials (see Table 3.1), the number of primary electrons liberated in Ar is twice as large as the one in Ne. Therefore, higher local charge densities are expected in Ar-based mixtures. On top, drift times of charges are slower in Argon.

This would lead to an accumulation of space charge in the TPC volume, distorting the electric field. Moreover, as shown in the cited article, for a given gain, the probability to have a discharge occurring in Ar-CO_2 is higher by several orders of magnitude than in Ne-CO_2-N_2, this being one of the reasons for it being chosen as the default gas in the next studies. This is understood by the fact that the range of α-particles in Ar mixtures is 40% shorter compared to Ne.

To analytically estimate the charge needed for streamer conditions, a simple case can be considered, following the explanations in [92, 98, 102]. When the two electrodes of a GEM hole are biased across with a potential difference, a strong external electric field (denoted E_0) ensues in the hole, given the small distances involved. When the primary charge enters the hole from the drift area, it suffers avalanche multiplication. An amount of charge will be created, depending on the gain of the GEM foil (i.e. the potential difference applied across) and the primary charge density.

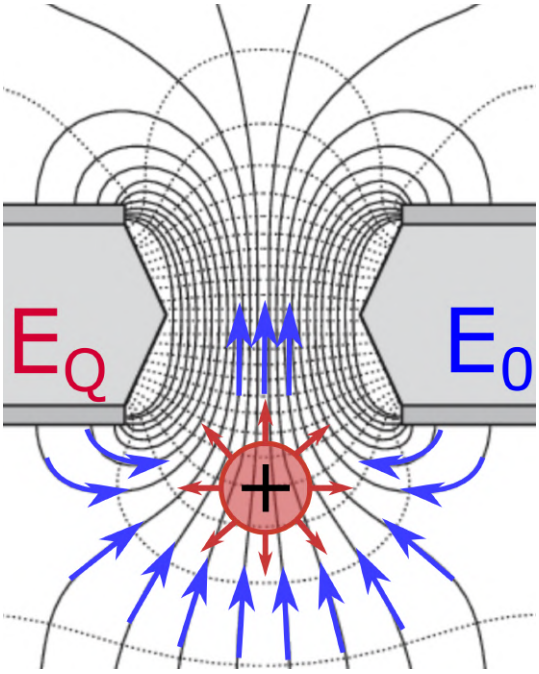

Figure 4.17: Ion cloud below GEM hole in the wake of the primary amplification distorts the external field. Adapted from [71]

The mean free path of electrons (the inverse of the Townsend α coefficient) decreases with increasing field (i.e. $\lambda = 1\,\text{cm}$ (10 kV/cm), $\lambda = 67\,\mu\text{m}$ (30 kV/cm), $\lambda = 20\,\mu\text{m}$ (50 kV/cm) [113]) , and thus only after sensing a high enough field will the electrons start multiplying exponentially. As such, the bulk of the charge will be located some very small distance below the GEM, in the last multiplication step.

Avalanche to streamer transition requires a combined electric field, given by the external field and the space charge (E_Q) created in the wake of the avalanche, to be strong enough for a self-sustained resulting process. The streamer is initiated by the positive ion cloud that is located below the GEM hole (see Fig. 4.17) after the electrons have been extracted.

A streamer starts to develop from an avalanche as soon as the field of its space charge reaches a value of the order of the external field ([92] pp. 336-337). Considering the positive charge below the GEM, the criterion for the streamer formation can be written as:

$$E_Q \approx E_0$$

The external applied electric field is estimated from simulations [114, 115] done in similar conditions to the ones used throughout the thesis. An example is shown in Fig. 4.18. A standard CERN GEM, similar to the ones used in the thesis, is simulated, featuring a potential difference of $\Delta V_{GEM} = 400\,\text{V}$. On top, a drift field of 1 kV/cm collects the

primary charge, while below an extraction field of 3 kV/cm releases it further into the system.

A value of $E_0 = 30\,\mathrm{kV/cm}$ is chosen, representing the mean at 30 µm below the GEM:

$$\frac{eN_{\mathrm{ions}}}{4\pi\epsilon_0\epsilon_r R_{\mathrm{Q}}^2} \approx 30\,\frac{\mathrm{kV}}{\mathrm{cm}}$$

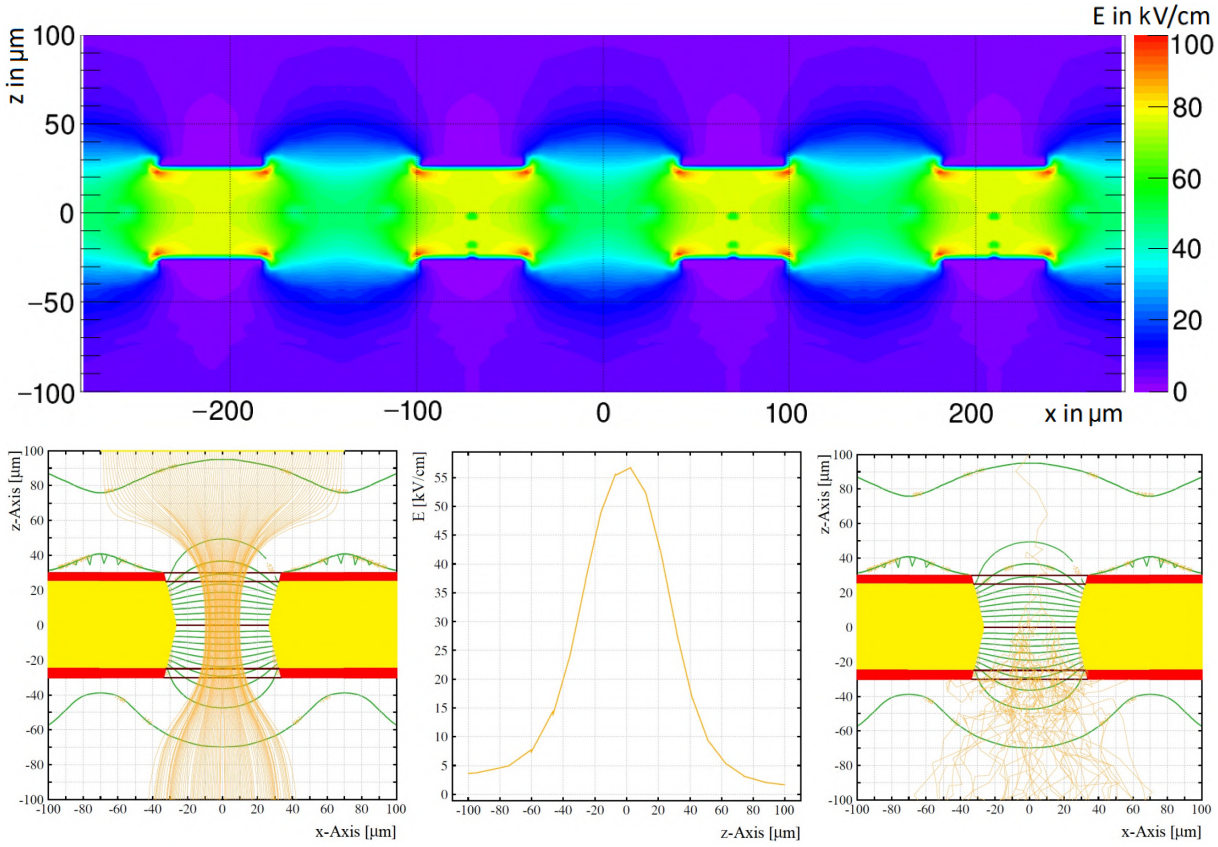

Figure 4.18: Top: Simulation of the electric field across a GEM foil. Adapted from [116]. Bottom: GEM hole simulation. Left: equipotential lines (green) and field lines (yellow). Center: corresponding electric field strength along the axial plane of the GEM hole. Right: Avalanche simulation. Taken from [114].

For simplicity, the positive space charge is assumed to be spherical. Its radius can be estimated from analytical calculations [92] (pp. 332 - 334), where the maximum transverse size of the avalanche head is said to be in the order of α^{-1}. Simulations, like the one in Fig. 4.18 (bottom right), support this idea.

The mean free path of electrons was shown before to decrease with increasing electric fields. At 30 kV/cm, the mean free path is $\lambda = 67\,\mu\mathrm{m}$, resulting in a spherical space charge radius of $R_{\mathrm{Q}} = 50\,\mu\mathrm{m}$, the size of the GEM hole diameter.

From this information, the number of ions N_{ions} necessary for streamer development is approximated as follows:

$$N_{\text{ions}} \approx 3\,\frac{\text{V}}{\mu\text{m}} \times \frac{4\pi\epsilon_0 \cdot 1 \cdot (50\,\mu\text{m})^2}{e} \approx 5.2 \times 10^6$$

This is a value similar to the one from [99] (5×10^6 for Ar-CO_2 (70-30) and 4.7×10^6 for Ar-CO_2 (90-10)). From this, an estimate on the number of electrons that need to enter the GEM hole to cause a discharge can be given, using GEM gain values from [99]. There, a single-GEM foil can be inferred to have a gas gain of $G \approx 1000$ at a value of $\Delta V_{GEM} = 480\,\text{V}$ in Ar-CO_2 (80-20). These gain values are very high for single GEMs because the detector was operated at high voltages. Using these values, a number of

$$N_{\text{e}} = \frac{N_{\text{ions}}}{G} \sim \frac{5.2 \times 10^6}{1000} = 5200$$

electrons need to enter the hole to initiate a streamer. This number is consistent with values of primary electrons liberated and collected in one GEM hole by the occurrence of an alpha particle from a Rn decay.

This description offers just the magnitude of the charge, consistent with other works explaining the primary discharge occurring in a GEM hole. Further effects must be considered for a more realistic description.

The charge density below the GEM was approximated as being spherical, when in fact it forms a drop-shape. Even so, the intrinsic electric field superimposes with the external one, enhancing the total field toward the GEM hole and giving probable cause to start a streamer, while weakening it underneath the space charge cloud, to the point of no further amplification (below $E_{\text{Townsend}} = 10\,\text{kV/cm}$).

Moreover, any fabrication imperfection influences the field inside the hole, resulting in different field lines the ions follow, having an influence on the occurrence of a streamer. In addition, effects like charge screening can also modify the resulting electric field experienced by the charges.

As the streamer starts, it grows into a weakly conducting path between bottom and top side of the GEM foil. Since such a process cannot be directly observed, the development of discharges in a GEM hole is inferred from simulations, as the one seen in Fig. 4.19.

The streamer evolution follows the cathode-directed behavior, as explained in Sec. 4.2. Occasional electrons entering from the drift region, alongside generated photoelectrons, aid the amplification process above the space-charge cloud. As soon as the streamer head connects to the top electrode, it will develop fully into a conducting channel, with a small resistance.

The large potential difference will, in turn, aid the electric field and will accelerate an anode-directed streamer. This is when the two sides are shortened and the spark is created, which can be seen and heard. The formation of the streamer is very fast, as can be inferred from the simulations.

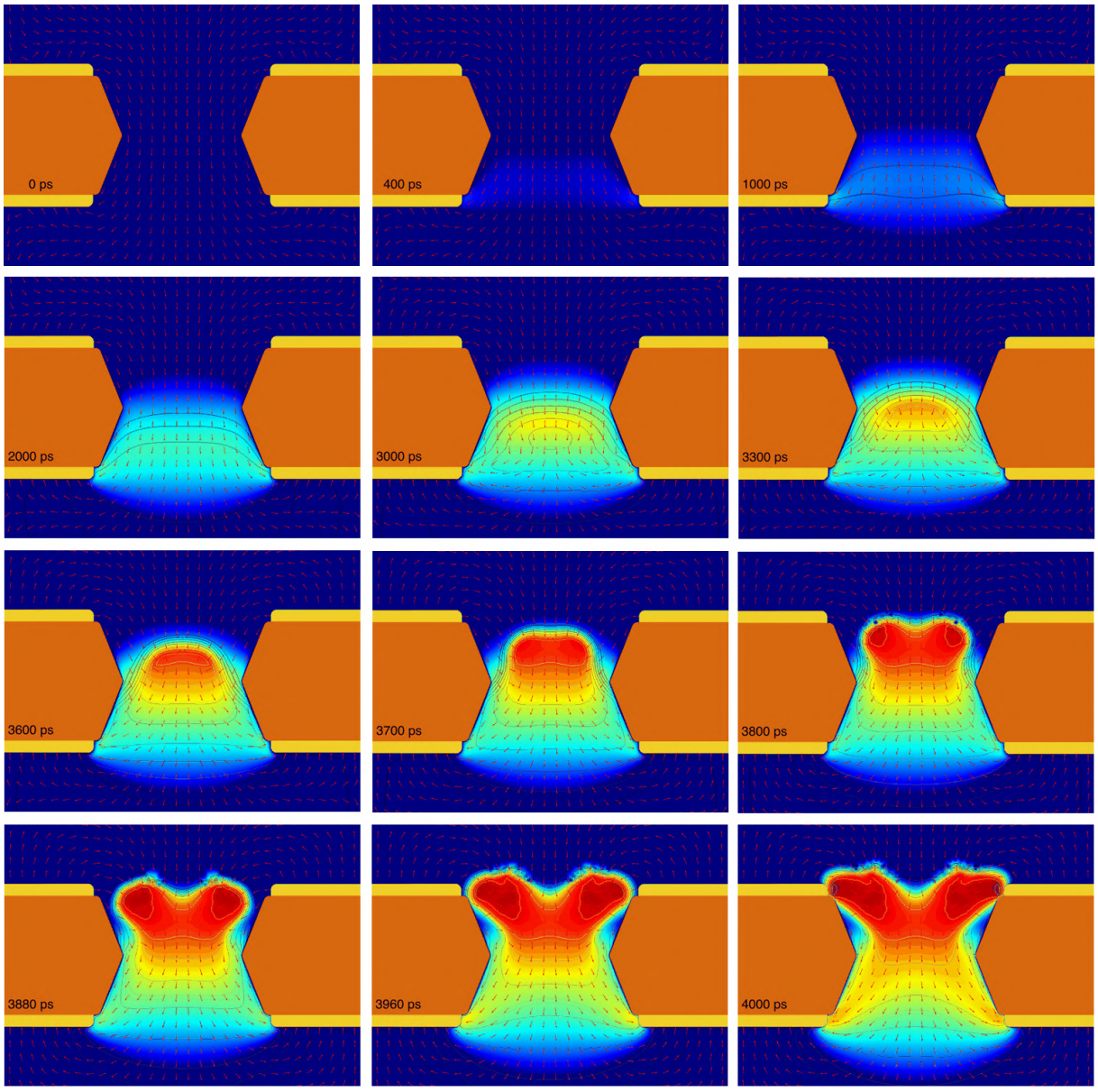

Figure 4.19: Simulation of the development of a discharge in a GEM hole. The arrows indicate the direction of electron motion (the electric field). The contour shows the electron density and the colours represent the ion density. Adapted from [117].

An example of a primary discharge seen with the HV probes is shown in Fig. 4.20 and 4.21 for different timescales.

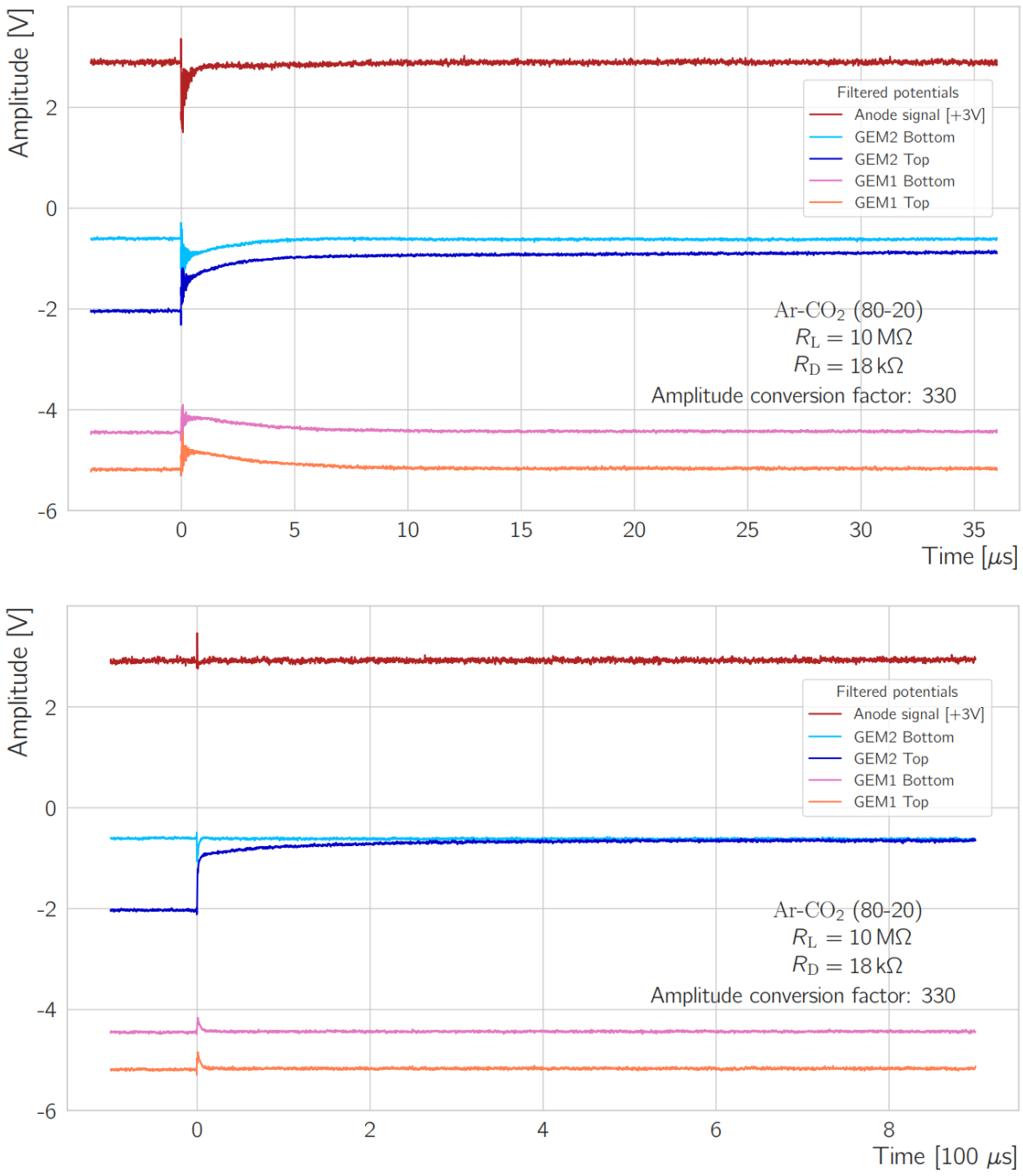

Figure 4.20: HV probes response during a primary discharge occurring in a GEM 2 hole. A discharge occurs at $t = 0$ in GEM2. The system response to the discharge is shown on two time-scales: few tens of microseconds and tenths of milliseconds. The top electrode potential drops and meets the value of the bottom one of GEM 2, signaling that the GEM discharged.

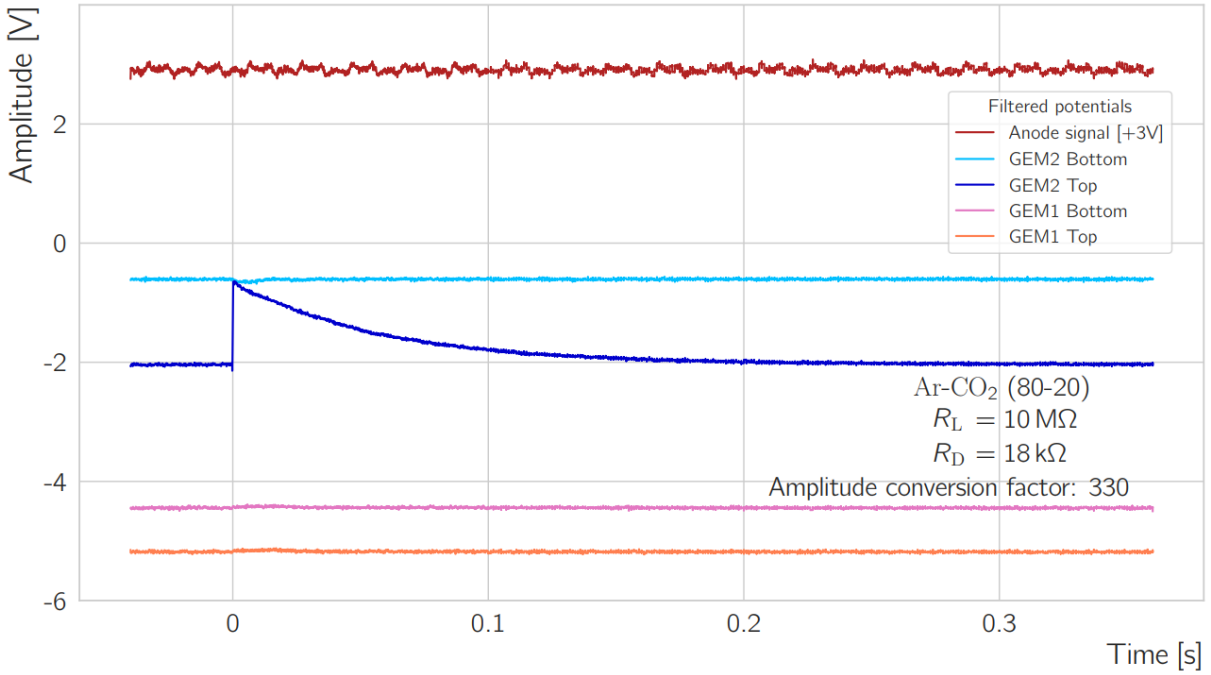

Figure 4.21: System response during a discharge in GEM 2. G2T potential recovers in approximately 150 ms. During most of this time, another discharge is improbable, given that the potential difference across GEM 2 is low.

The vertical axis shows the amplitude of the pulses, as seen through the HV probes. To get the corresponding true voltage on the respective element, the mean value of the amplitude before the discharge is multiplied by the conversion factor, given by the voltage divider formed by the resistors and the internal resistance of the oscilloscope. The HV probes exhibit a slight dynamic scaling for a range of voltages, but the value of 330 is a good approximation for the commonly used voltages.

The displayed anode signal is also scaled up by a factor of 50. Because of the attenuator the normal signal would be too small to be seen reliably on the oscilloscope. All the figures in this thesis featuring anode waveforms will feature the scaling factor, unless otherwise stated.

Since only two probes and the anode signal are recorded at the same time, the figures showing the behavior of potentials encompass two similar events which are superimposed. The potentials are smoothed by a software filter, as explained in Sec. 4.5. The anode signal baseline is at the ground level, but it is moved for better visualization at the value of +3 V.

A violent system response is visible at $t = 0$ when the discharge occurs. The anode quickly collects the electrons released and amplified just above it, exhibiting an uni-polar negative signal. A zoomed in pad plane response to a discharge occurring in the lowermost GEM, followed by a secondary discharge – which will be explained later on – is shown in Fig. 4.22.

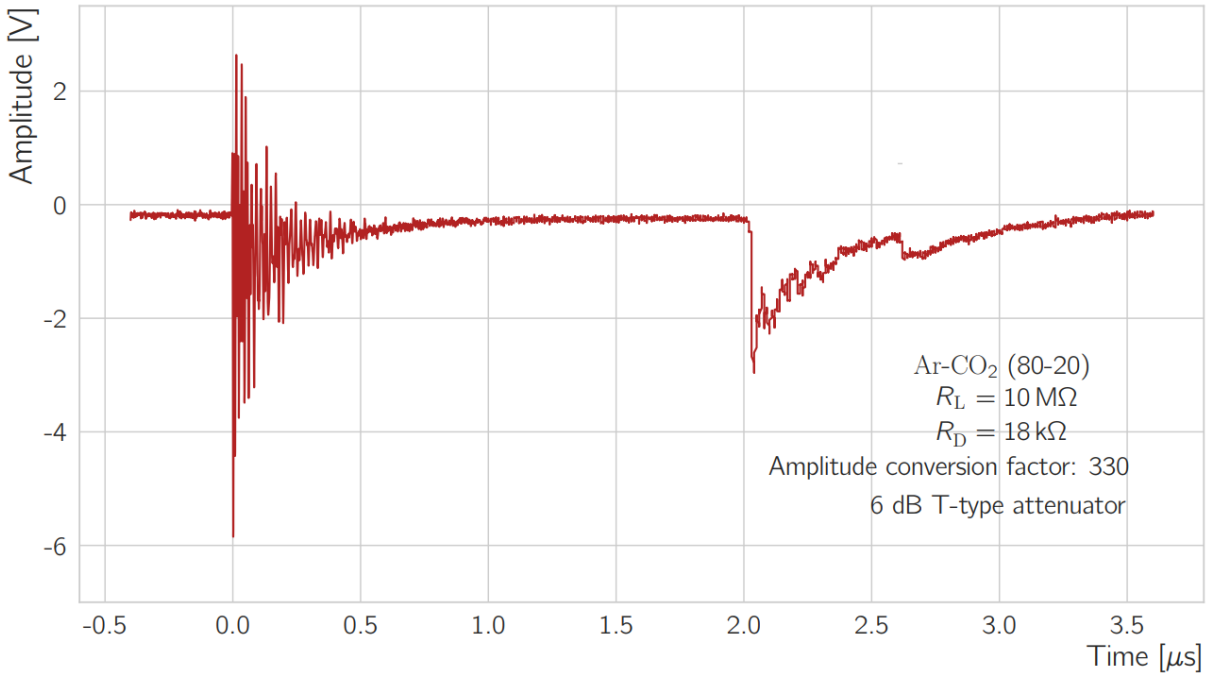

Figure 4.22: Microsecond scale behavior of a primary discharge in GEM2, followed by a secondary discharge in the gap between GEMs.

The signal has an oscillatory nature, given the impedance that is not exactly matched, the parasitic capacitances and spurious AC signals superimposed on the normal signal. Nonetheless, it is clearly a negative polarity signal, since the carriers are electrons. The signal recovers in less than 1 µs.

The shape of the primary discharge is dependent on the attenuating circuit used, as shown in [89]. For increasing resistance in the anode path, the signal is dominated more and more by the charge deposited and the time needed to discharge it again. Moreover, the oscillatory behavior and duration changes with the parasitic capacitances of the system and with the value of the anode resistive elements.

Given that the discharge event is induced in GEM 2, the G2T potential drops toward lower values, while G2B increases for a brief moment (depending on the value of R_D) – the two signals exhibiting opposite polarities, indicating that a discharge has occurred here. This happens because the top side features a loading resistor of 10 MΩ in the HV power supply path, while the bottom side has a resistance lower by three orders of magnitude. The voltage drop will occur across the loading resistor and will be registered as a drop of the top potential, while the bottom potential will stay constant. With higher decoupling resistors and similar loading resistor values, it was shown in [102] that both top and bottom potentials meet briefly at a value somewhere in between the two original potentials.

Looking at the microsecond behavior of the GEM electrodes, a visible effect is present on all electrodes (not just the affected GEM one), where a small, distinctive voltage change occurs at the time of the discharge. Contrary to the pulses seen on GEM2 electrodes, on GEM1 these have the same polarity indicating that they have pick-up (induced) origin.

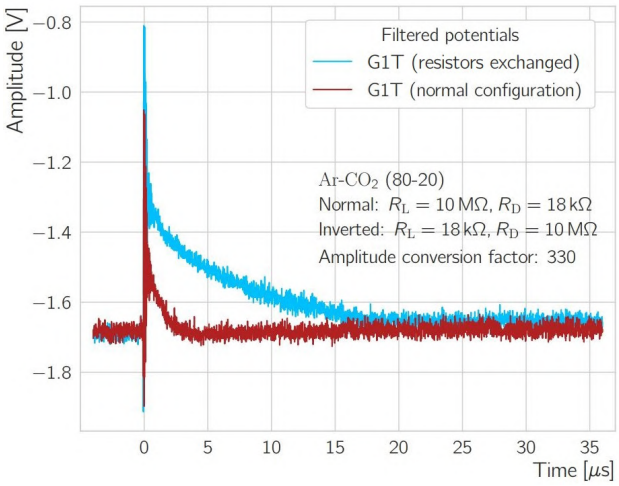

Figure 4.23: Capacitive coupling on G1T before and after switching resistors.

These simultaneous voltage drops are caused by the capacitive coupling between the different electrodes in the detector. The electrons generated in the discharge are collected at the anode, manifesting in a negative pulse, whereas a positive induced signal is seen on the GEM1 electrodes.

To prove that this effect is due to the capacitive coupling between the electrodes, a dedicated test where the top and bottom resistors have been interchanged is done (see Fig. 4.23). In this way, when a primary discharge occurs in GEM2, GEM1 will feel a slightly higher response, because the high resistor on G2T does not shield the lower GEM response anymore.

The potential difference across GEM1, the GEM that is not affected by the discharge, is constant throughout the event duration and thereafter, and is equal to the set potential difference across the two GEM sides.

In the case of GEM2, at the time of the discharge, both potentials meet in between, as explained earlier, but there is still some potential difference across remaining in the wake of the discharge that just occurred. This difference slowly extinguishes after about 200 µs. At the moment, this effect is attributed to the response of the PS to the discharge event and is not clearly understood.

After about 150 ms the potential on G2T recovers and the detector is operating once more at the nominal set values. The shape of the anode signal in Fig. 4.21 is an artifact of the smoothing procedure used, as well as AC noise with a larger frequency.

Primary discharges - damages and mitigation

The two sides of the GEM foil can be treated as the electrodes of a capacitor. During a discharge, the stored energy (of the capacitor) is released. It can be approximated by the formula:

$$E_{\text{discharge}} = \frac{1}{2} \cdot C_{\text{GEM}} \cdot (\Delta V_{\text{GEM}})^2$$

The capacitance of a 10×10 cm^2 GEM foil is about $5 - 6$ nF, and the potential difference range needed to induce a discharge is between $450 - 500$ V (for commonly used gas mixtures). Therefore, the stored energy is anywhere between $500 - 750$ µJ. This amount can be influenced by improper decoupling from the power supply, cable and parasitic capacitances.

This energy is released all at once during the discharge, leading to a substantial heating of the gas. While heating, the gas expands and produces a localized short, accompanied by a powerful cracking noise, which can be easily heard, caused by the shock wave (sharp rise in pressure due to an intensive release of Joule heating in the spark channel when the high discharge current passes through it). Electron microscope pictures of GEM foils after such an event can be seen in Fig. 4.24.

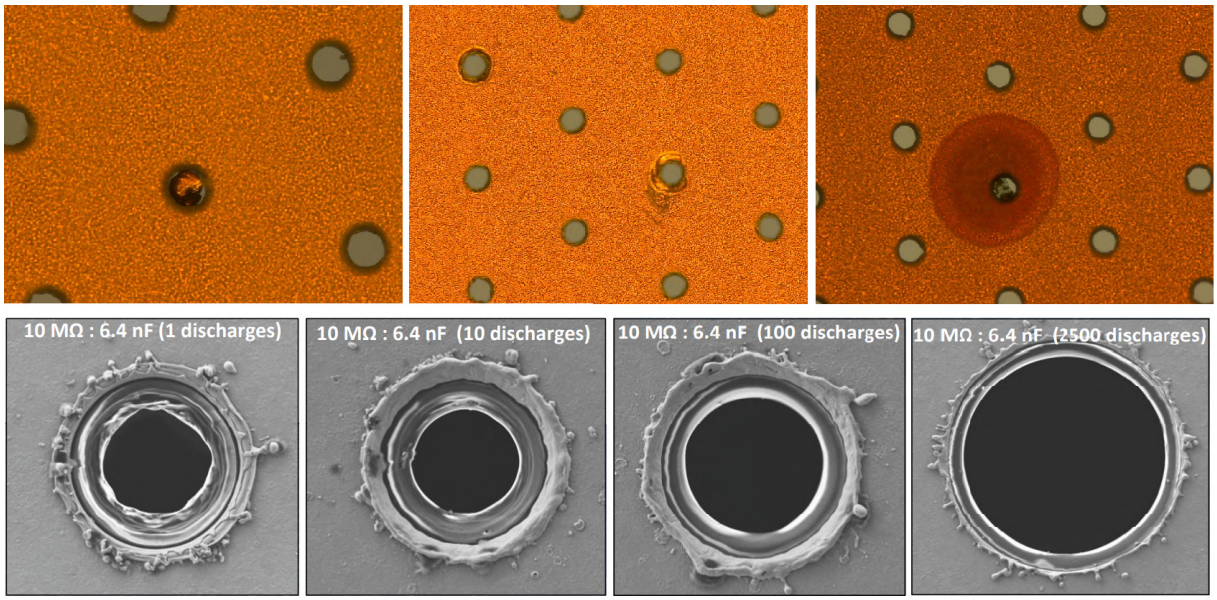

Figure 4.24: Upper row: Microscope pictures taken by the author of faulty GEM foils tested for the ALICE TPCU. From left to right: metallic dust stuck inside a hole; GEM holes that suffered discharges near unaffected ones; a dust particle in one GEM hole causes a continuous discharge and burning of the nearby area.
Bottom row: Electron microscope picture from [118] of a single GEM hole after a different number of discharges. A 10 MΩ loading resistor is used. The study was done on a different setup than the one used in the ALICE TPCU or throughout the thesis. Nevertheless, the deformation is clearly visible. The polyimide layer is enlarged and melted copper is splashed around the hole.

Causes for the discharge range from dust particles, that can be removed with ease by using an air gun on the GEM foils, to the most problematic permanent shorts that basically render the GEM foil unusable.

It was recently reported in [118] that GEMs are sturdy structures that can withstand a lot of sparking. A GEM foil prototype with one hole and 5.7 nF capacitance, similar to the ones used throughout the thesis, was shown to withstand between 1000 and 2000 radiation-induced discharges before a short-circuit rendered it inoperable. They noticed a strong correlation between capacitance (energy) and the hole longevity, with smaller capacities being favored.

Furthermore, they found that having a protection resistance plays a role in the damages caused by discharges. A number as low as 10 discharges is indicated before the hole fails

for resistances up to $\sim 300\,\mathrm{k}\Omega$. Higher values result in a big increase in the discharge rate.

The choice for employing a loading resistor on the top side of the GEM foil is now obvious. This resistor helps minimize the energy and duration of the primary discharge. After the top potential drops in value to the bottom one, several hundred milliseconds are needed to recharge the top side. This timescale ensures the discharge has been properly quenched.

The loading resistor also ensures proper decoupling from the cables and PS, which can add extra capacitance, as detailed in [119]. Furthermore, the segmentation on the top side ensures that less capacitance and therefore less energy is available for the discharge. Moreover, in case a permanent short develops, only one small area of the GEM is affected.

On par, the decoupling resistor featured on the bottom side of the GEM foil helps decouple the power supply scheme and cable capacitance from the sensible structure. Its role will further be discussed in the next section.

Both R_{D} and R_{L} are placed as close to the GEM as possible. In similar works about discharge studies [98, 102], extra protection resistors (R_{sink}) are used in the path of the PS to the GEM electrode, before the loading/decoupling resistors, to sink excess currents during discharges. Commissioning tests have shown that with the type of power supply used here, these resistors are not necessary and are not used in the current thesis.

Clearly, the bottom line is that there is a maximum number of discharges a GEM hole can withstand. With every discharge, the probability to render a foil ineffective by encountering a permanent short increases. It must therefore be imperative to minimize the occurrence of discharges in localized places on the GEM foil.

Knowing that a primary discharge is caused by the charge density buildup in a GEM hole exceeding a threshold, it is clear that minimizing the accumulation of large amounts of charge is important.

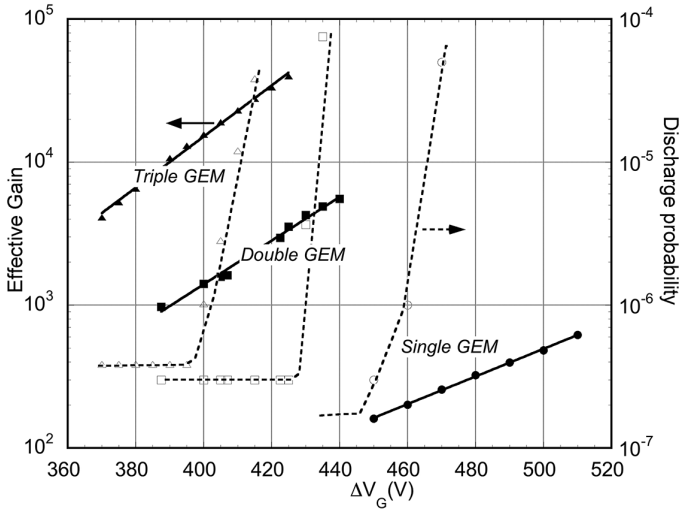

Figure 4.25: Effective gain, discharge rates and onset curves as a function of ΔV_{GEM} in multi-GEM detectors in Ar-CO_2 (70-30) [120].

Stacking GEMs is a safe and easy way of achieving a set nominal gain using lower voltages per foil than in the case of a single GEM. Combining lower voltages per foil for the same gain with the charge diffusion (charges will spread over several holes before reaching the next layer, causing lower charge density per hole) in a combined electric and magnetic field leads to a reduced chance to experience a transition from avalanche multiplication to streamer.

Recent works [120] have shown that the primary discharge probability is reduced by more than an

order of magnitude for each additional GEM added to the detector (also depending on the voltage settings and gas mixture used).

In Fig. 4.25 it can be seen that at the same effective gain (calculated as the amount of charge collected by the pad plane divided by the primary charge), a lower operating voltage per foil is needed for multi-GEM structures. Also shown (dotted lines) are the kickoff curves[8] for the single, double and triple GEM detector. Considering the kickoff of discharges as the operating limit, it is obvious that in order to attain the nominal gain of 2000 needed for the ALICE TPC in Run 3, a triple GEM setup is not enough, since it has some probability to discharge.

4.4.2 Secondary discharges

Another variable of interest is the **secondary discharge**. In addition to the discharge occurring in the high field of the GEM hole, caused by charge buildup exceeding a threshold value, it was observed that under certain conditions a primary discharge is followed by a subsequent breakdown of the gas rigidity between two adjacent GEM foils, or between the GEM facing the pads – the last in the stack – and the anode plane.

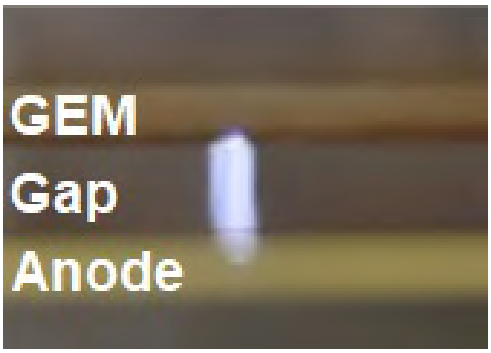

Figure 4.26: Photograph of a secondary discharge in a single GEM setup placed in a transparent gas vessel and filmed with a CANON 5D Mark III camera [89].

The phenomenon was first reported by authors of [121] under the name of *delayed breakdown*. Other studies [75, 122] have encountered this effect aswell. Recent studies [98, 101, 102] have extended this knowledge and aimed to better understand this behavior. Finally, an effort was undertaken to propose a mechanism for the production of secondary discharges in [89], to which the author participated.

The secondary discharge is a powerful event, releasing a great amount of energy when forming the streamer in between the different electrodes, given the large distances involved (compared to the GEM hole distances). They pose a significant threat to the amplification structure and to the readout electronics.

So far, they have been observed to occur only after primary discharges, never alone. This indicates that some charge buildup is needed to start the streamer in this case. This secondary discharge probability was seen to have a sharp onset, from 0 to 100%, around the threshold value of the electric field involved (either transfer or induction field).

The secondary discharge probability (indicated in the thesis as P_2) is defined as the ratio of the observed secondary discharge events to the total primary GEM primary discharges. This probability increases with the strength of the electric field in the gap and is noticeable already at fields lower than necessary for amplification in gas (e.g., via Townsend amplification - see Fig. 4.2).

[8] The kickoff value is the value at which the effect starts to be visible.

The time between the occurrence of the primary discharge and the secondary discharge (denoted in the following as t_{12}) can be as short as a few microseconds to almost 100 µs, highly dependent on the external applied electric field in the concerned gap.

An example of a primary discharge induced in GEM 2 by choice of potentials, followed shortly by a secondary in the transfer gap is shown in Figs. 4.27 and 4.28.

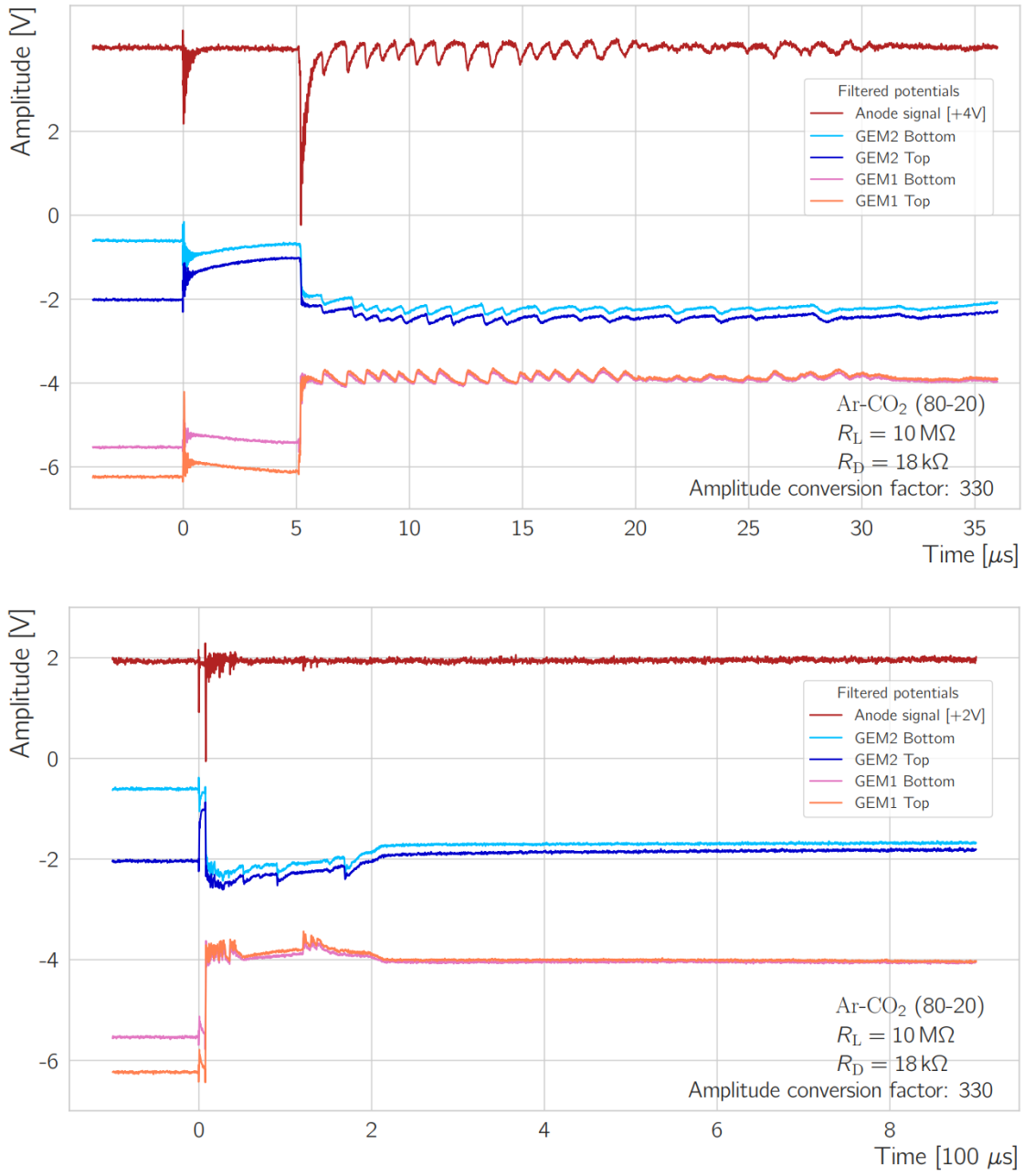

Figure 4.27: HV probes response during a primary discharge induced across GEM 2, followed by a secondary discharge in the transfer gap between the two GEMs. An initial discharge occurs at $t = 0$ in GEM 2. The system response to the discharge is shown on two time-scales: few tens of microseconds and tenths of milliseconds.

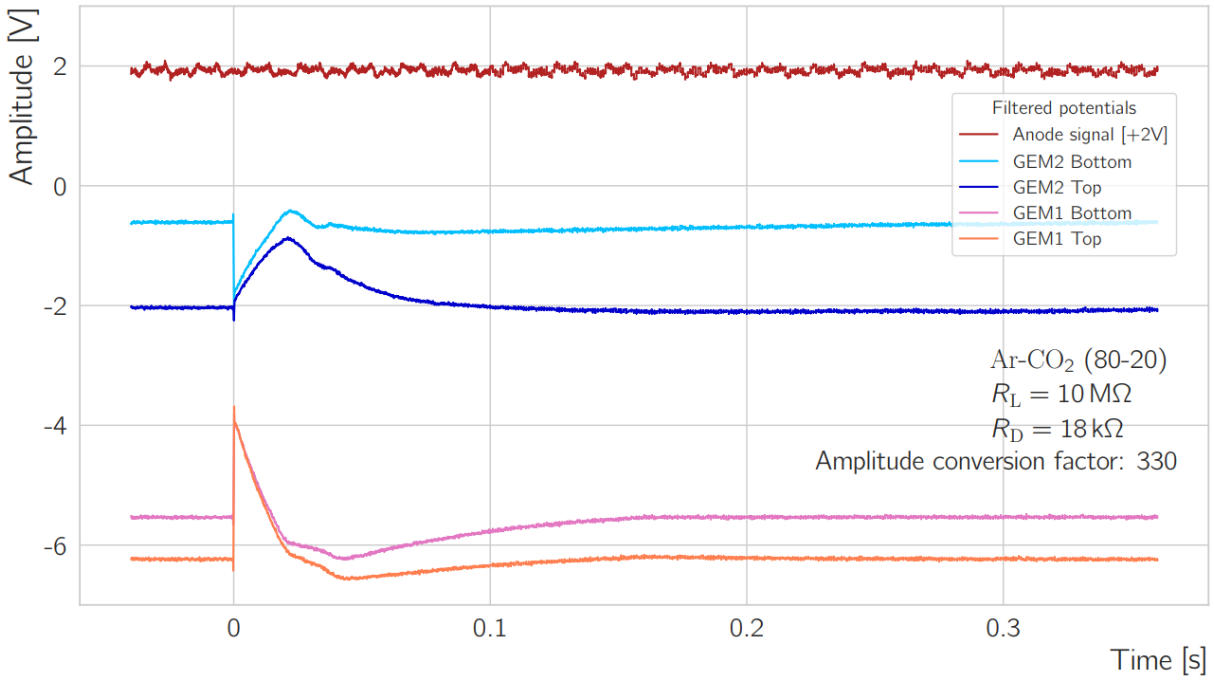

Figure 4.28: System response during a discharge in GEM 2. GEM potentials recover in approximately 150 ms. During most of this time, another discharge is improbable, given that the potential difference across GEM2 is low.

The anode signal is shifted again by a certain amount to disentangle waveform features. The vertical axis shows the scaled voltage as a result of the voltage divider in the HV probes. The scaling is indicated on the plot. Since only two probes are recorded at the same time, each plot has two separate, but similar types of events superimposed. The potentials are smoothed by a software filter, detailed in Sec. 4.5.

At $t = 0$ a discharge is induced in GEM 2, by convenient choice of HV values and the charge released by the Rn decay. The G2T potential approaches the G2B one, signaling that breakdown occurred in this respective GEM. After 5 µs, a large negative pulse on the anode signal, indicates the appearance of a secondary discharge in the transfer gap. The shape of the secondary on the pad plane depends on the value of the various anodic circuit elements (for example the attenuator).

At the time of the secondary, the transfer field value was close to a critical discharging threshold. Given that the G2T potential drops (towards G2B, therefore towards lower values) at the time of the primary, the electric field in between the GEMs is modified. It increases by approximately the same amount extinguished by the primary discharge ($\Delta V_{\mathrm{GEM2}}/d_{\mathrm{t}}$), managing to exceed the discharge threshold and triggering the secondary.

When the secondary discharge happens, a spark channel will link G2T with G1B in the transfer gap. As such, E_{transf} is reduced, and the corresponding potentials approach each other. Contrary to what is expected, the two potentials do not meet, signaling that perhaps there is still a potential difference present in the gap. This effect is so far not completely understood and further investigations are done.

One probable cause is related to the complicated circuitry in the power supply and its response, when coupled with the RC circuit of the HV probes. Another speculation would be that the plasma channel in the transfer gap might not be fully conductive and some resistance might be present, keeping the potentials from fully meeting, but only dousing the potential difference. Since the capacitance in the gap is smaller (given the large distance between the electrodes), compared to the capacitance of a GEM, there is less energy stored in the transfer gap. As such, it might be harder to create a fully conductive plasma. Moreover, the power supply is combating this effect, when it senses the reduced potential.

The G1T potential starts dropping toward the G2T potential value, i.e. toward lower negative voltage values. While this happens, ΔV_{GEM1} increases and immediately triggers a primary discharge across GEM1, quelling the potential difference across GEM1. Now, both GEM1 potentials share same value and will continue to drop towards GEM2.

Meanwhile, GEM2 potentials start increasing, as the power supply tries to keep the voltages constant. Electrons are flowing from GEM1 to GEM2 (GEM1 has a more negative potential), because they are connected through a conductive path, as a consequence of the plasma channel formed in the wake of the secondary discharge. This increase in the number of electrons pushes GEM2 towards more negative potentials. Meanwhile, GEM1 supplies the electrons and therefore goes to less negative potentials. The resistors slow down the evacuation of electrons, which in turn causes the ms recovery times.

After the secondary discharge, a large number of oscillating signals are present in all electrodes. A high-speed camera investigation of this behavior [123] showed that the additional potential drops are caused by reignitions of the secondary discharge, at the same position as the original one.

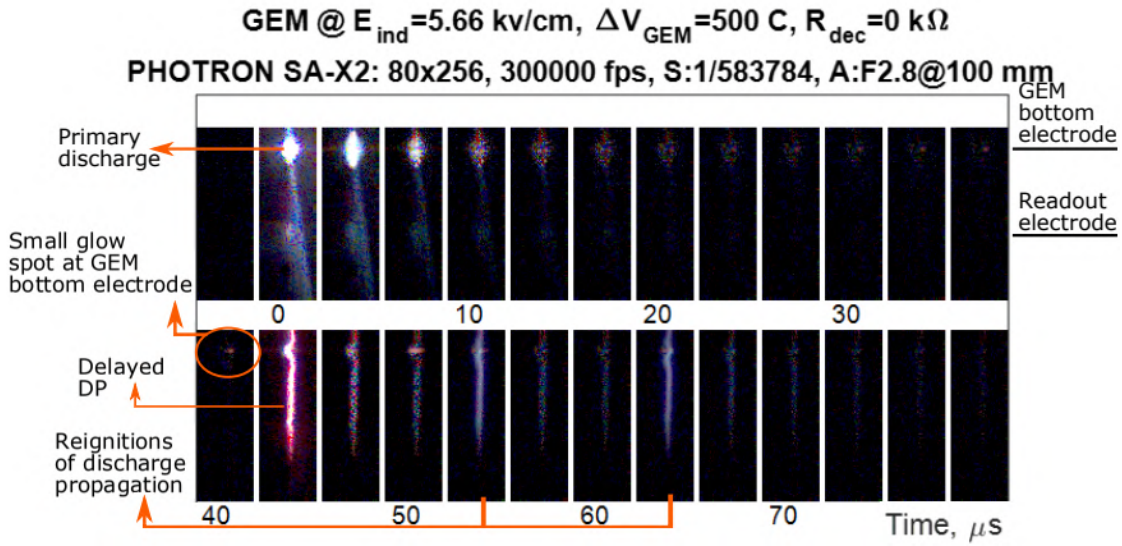

Figure 4.29: High speed camera image of a discharge in a GEM detector. The primary discharge occurs in a GEM hole at $t = 0$, followed by a secondary discharge at $t = 43\,\mu\mathrm{s}$. Two reignitions of the secondary discharge occur at $t = 53\,\mu\mathrm{s}$ and $t = 63\,\mu\mathrm{s}$. Note: The authors refer to secondary discharges as delayed/propagated discharges. Taken from [123].

After some 100 µs (see Fig. 4.27) the potentials will level. The long term behavior shows that after 150 ms all the electrodes have recovered.

As detailed in [89], the most probable cause for the appearance of secondaries is an interplay between the charge resulting from a primary discharge, photon feedback and thermionic emission, all of which contribute to the final discharge. The study shows that, for a given gas mixture, there seems to be a certain amount of charge produced in the primary discharge that is needed to trigger a secondary. The effective measured charge aiding in its development has a value of about 10^{10} electrons for Ar-CO_2 (80-20).

The electrons produced after the primary can ionize and excite the gas in the concerned gap. From the 10^{10} electrons, about 10^9 are found in [89] to have energies larger than 7.9 eV (the first excited state of CO_2), about 2×10^8 are found to have energies larger than 10.5 eV (the second excited state of CO_2) and about 5×10^6 are found to have energies bigger than 13.7 eV (where the first and second excited states of Ar are 11.3 eV and 11.6 eV, while the ionization potentials of CO_2 and Ar are 13.7 eV and 11.8 eV, respectively). Values for excitation and ionization are taken from [88]. Since there are many charge carriers above the excitation/ionization level, they can increase the "charge load" even further.

Alongside electrons, the ions can also play an important role in the formation of the secondary discharge. In [89], the idea that that secondary discharges are caused by ions that cross the induction or transfer gaps is discussed. The drift field above a GEM was varied over a wide range of values (negative to positive). No effect of this variation on the probability to observe a secondary discharge was observed. The time between primary and secondary was also not affected. As such, the ion extraction from the GEM hole was shown to not play any role in the creation of the secondary discharge, being unlikely that the secondary discharges are caused by ion bombardment of the top GEM electrode.

On the other hand, the ions hitting the GEM bottom can be accounted for aiding the secondary development, since they can cause extraction of secondary electrons from the GEM surface or from the GEM electrode acting as cathode. An indication for this was given in [89], where it was shown that in higher CO_2 concentrations less electrons are involved in a secondary discharge, whereas ions have a higher energy.

Furthermore, a primary discharge produces a large heat load on the concerned GEM electrodes (recount Fig. 4.24). This, in turn, facilitates thermionic emission of extra electrons upon ion bombardment and infra-red radiation. This process is self-sustained until massive electron emission ultimately results in the gap breakdown. The high-speed camera footage shown in Fig. 4.29 supports this idea. A small orange glow is visible near the GEM bottom electrode, localized around the area where the primary discharge just occurred. This hints at a possible charge source in the gap below the GEM. Just before the secondary occurs, the glow is more intense, supporting the idea of a gradually increasing intensity up to a massive charge emission pre-breakdown.

Nonetheless, the bottom line is that the charge created in the wake of the primary discharge decides whether or not a secondary can occur. A characteristic charge in the order of 10^{10} electrons seems to be the threshold. As more effects come into play, it is not a hard border, leading to cases where secondaries can either occur or not at fixed values of voltages on the GEM electrodes.

Secondary discharges - damages and mitigation

The damage caused by a secondary discharge is of far more concern to the GEM detector than the primary discharge. For the ALICE GEM foils, when a secondary occurs, the large, unsegmented area of the bottom GEM electrode will be involved, allowing for a far greater energy release.

One could consider an OROC 3, in a simplified, ideal case. It features 24 segments, each about $100\,\mathrm{cm}^2$ with approximately 5 nF capacitance. Using nominal voltage values, at the time a secondary discharge happens, the transfer field is about $\Delta V_{\mathrm{transfer}} = 800\,\mathrm{V}$. This field is enhanced by about $\Delta V_{\mathrm{GEM}} \simeq 288\,\mathrm{V}$ from the discharging GEM. Hence, a secondary in the first or second transfer gap results in an energy release of 71 mJ, an increase of about two orders of magnitude from the normal GEM primary discharge.

Moreover, secondary occurrence in the last gap, the induction region, allows for large currents associated with such a violent event to sink into the anode path, reaching the readout electronics and possibly damaging them.

From dedicated studies using a single GEM with Ne-CO_2-N_2 (90-10-5), the gas choice of the ALICE TPC in RUN 3, with nominal HV settings, the onset [9] of secondary discharges in the induction gap is found to be around the value of 4.3 kV/cm.

Using the nominal voltage values, the most dangerous gap for a secondary to occur would be the second transfer gap. The field here is set to 4 kV/cm. If a primary discharge is to occur in GEM3 ($\Delta V_{\mathrm{GEM3}} = 288\,\mathrm{V}$), the second transfer field will increase by the amount G3T has dropped. The highest possible value (if no bottom resistor would be considered, or if its effect on the potential drop is negligible) the field would attain is 5.44 kV/cm. This exceeds the onset of secondaries and will trigger a discharge in the second transfer gap. The use of the decoupling resistor is mandatory.

4.4.3 Propagation of discharges

Another peculiar feature of discharges has been observed in [101, 102] when operating GEMs in a stack. Under certain conditions it can happen that a primary discharge in one GEM can lead to a primary discharge in another GEM almost instantly.

This phenomenon is termed **discharge propagation** throughout this thesis. The same term is often used in other publications, prior to finding this new aspect, for describing the secondary discharge occurring in the gaps between electrodes in the detector, and is not to be confused.

The following lines will detail how a propagated discharge behaves and what its response on the GEM electrodes looks like, alongside ways of mitigating it.

An example of an event where a primary discharge was induced in GEM2 and quickly propagated to GEM1 is shown in Fig. 4.30.

[9] The onset field is defined as the electric field at which $P_2 = 0.5$, i.e. the probability for a secondary discharge to occur after a primary discharge is 50%.

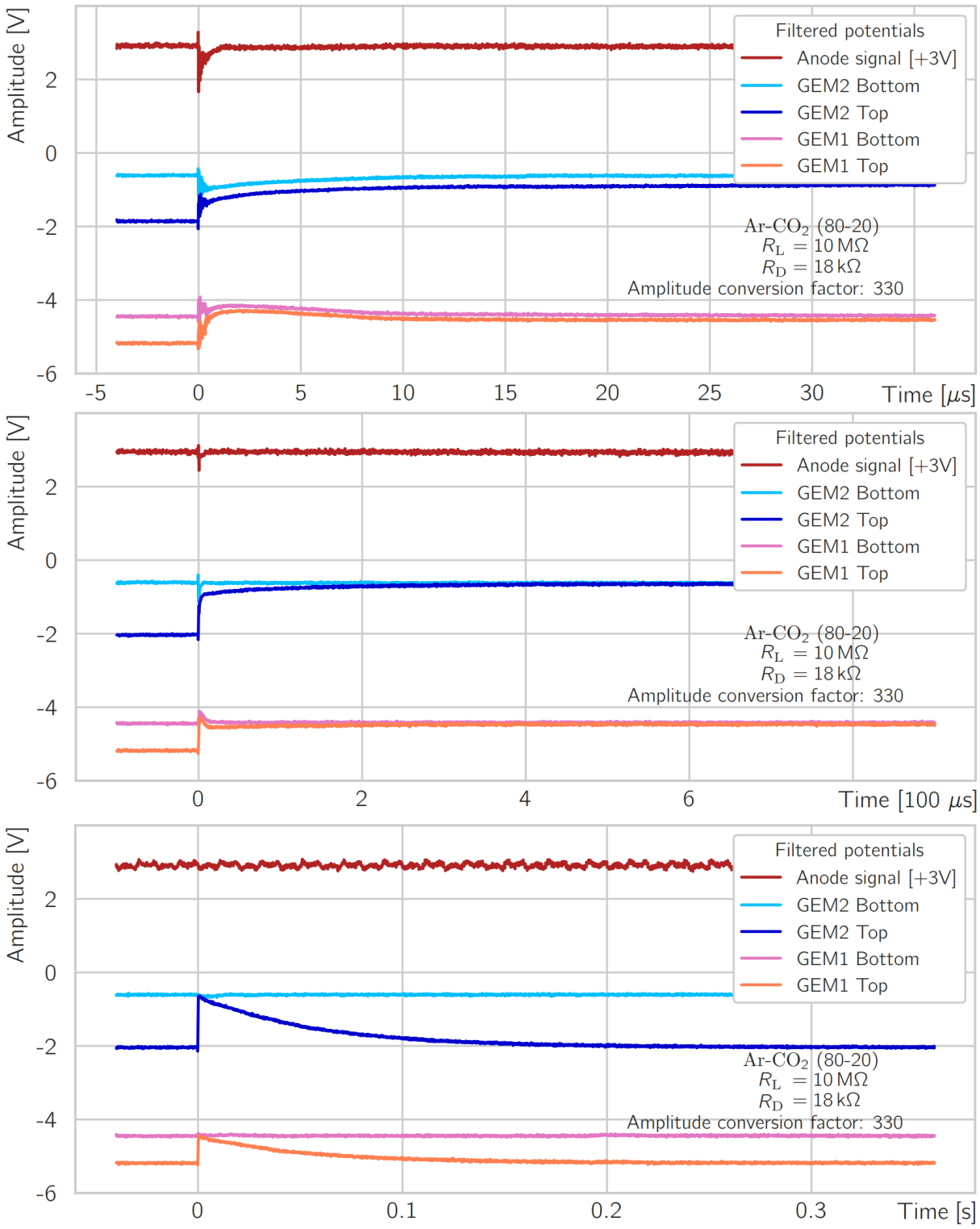

Figure 4.30: GEM discharge propagation. At $t = 0$ a discharge was induced in GEM2, which propagates quickly to GEM1. It manages to trigger a breakdown across its electrodes, even though the potential difference across GEM1 is smaller than across GEM2, and insufficient to start a discharge on its own. No secondary discharge occurs.

At $t = 0$ a primary discharge event occurs across GEM2 electrodes. This discharge almost instantly propagates to GEM1 and triggers a breakdown of the gas inside one of its holes, even though the potential difference across it is insufficient to discharge on its own ($\Delta V_{\mathrm{GEM1}} \sim 250\,\mathrm{V}$).

Both top potentials approach their corresponding bottom electrode potential value, quenching the two discharges. It seems that the electric circuit and the PS have a big role in the evolution of potential difference across the GEM electrodes after discharges. In the case of GEM2, the higher potential difference across its sides results in a somewhat larger remaining potential difference in the first few tens of µs after the discharge, compared to GEM1, where the difference is barely visible.

A secondary discharge did not occur. The transfer field before the discharge was set to 4.6 kV/cm and after the discharge it increased to 7 kV/cm, because of G2T potential drop. Following the explanations in Sec. 4.6, this value has a very low probability to trigger a secondary in the transfer gap.

The capacitive coupling is visible on all electrodes. Also, in both GEMs the recovery of potentials takes approximately 150 ms.

The final type of event that can occur in the detector is the occurrence of a primary discharge, which is able to propagate and trigger a discharge in the other GEM, followed by a secondary in the transfer gap. An example of such an event is shown in Fig. 4.31.

At $t = 0$ a discharge is induced in GEM2. The top electrode potential drops toward the bottom one, given the choice of resistors.

The discharge is propagated to GEM1 and triggers a breakdown in one of its holes, similarly dropping the top potential. About 2.5 µs after the primary, a secondary discharge occurs in the transfer gap. The transfer field before the discharge was set to 5.7 kV/cm, but is increased by the G2T potential drop. The field after the primary was calculated to be 8.16 kV/cm, enough to trigger the secondary (the following chapter will show that the P_2 at 8 kV/cm has a very high value, so we are almost always guaranteed that if GEM2 discharges, a secondary will follow).

The discharges are quenched by the two potentials approaching each other. The two GEMs recover, as in the previous examples, in about 150 ms.

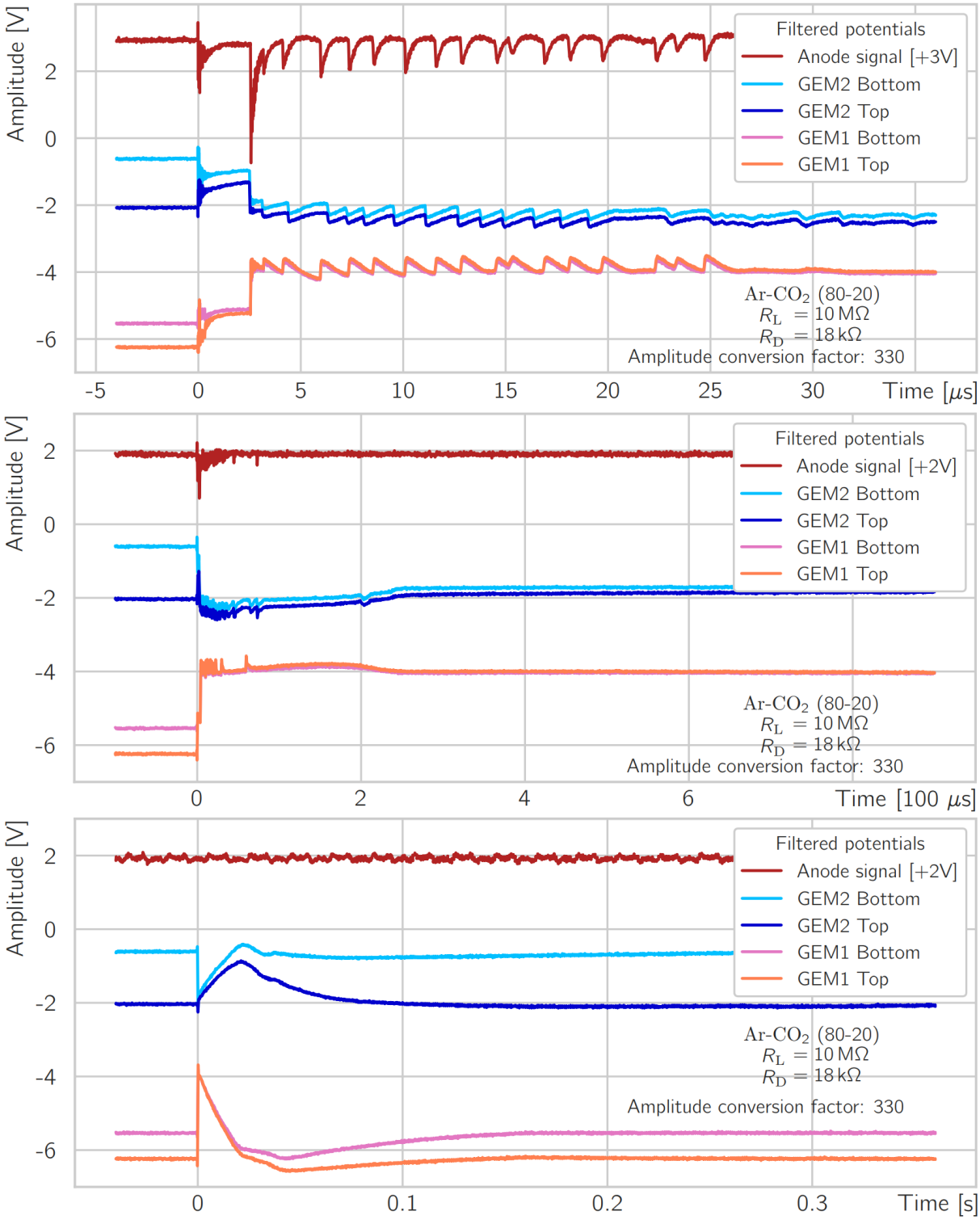

Figure 4.31: Both GEMs discharging, followed by a secondary in the transfer gap. A discharge is induced in GEM2. The discharge propagates to GEM1 and triggers a discharge across its two electrodes. Given the drop of G2T, the transfer field is increased and a secondary discharge occurs here.

4.5 Measurement procedure

The current research picks up on several curious features hinted in previous works on the topic of discharges in GEM detectors. The secondary and propagating discharges are the focus of this thesis. The aim is to propose means to mitigate their occurrence, providing feedback to the ALICE TPCU community for hardware choices prior to operating the TPC in RUN 3.

Extensive work has been done with single or double-GEM setups on the secondary discharge mechanism in the induction gap. Electrode potential behaviors have been monitored. The gas mixture's influence was studied. The effects of different power supply configurations has also been addressed. Finally, the GEM material and its influence on discharges has been checked. Further in-depth explanations are given in the publications: [98, 101, 102]. The essence of those publications, alongside results from this work are presented in [89].

The focus of this work is on understanding the phenomenon of discharge propagation from one GEM to another, alongside secondary development in the transfer gap between two GEMs. A cascaded power supply, similar to the ones that will be used in the upgraded ALICE TPC, is employed.

By convenient choice of the operating voltages, primary discharges are induced in GEM2 (the lower GEM in the stack). The operating range of voltages for the occurrence of discharges is addressed in other works (e.g. [75]). In Ar-CO_2 (80-20), primary discharges are induced by having ΔV_{GEM2} in the range of $440 - 500\,\mathrm{V}$, with higher values resulting in a higher rate of discharges. The bigger the potential difference, the bigger the amplitude of the primary discharge on the anode plane, alongside more energy and charge released.

GEM1 is used as a pre-amplification structure and cannot normally initiate a discharge on its own (the maximum value at which GEM1 was operated for some dedicated measurements was 300 V, insufficient for streamer development).

The gas dependency was approached in previous works on discharges and will not be studied in this document (e.g. [98, 102]). Alongside the gas mixture calibration, the pressure is recorded throughout the span of each measurement to be able to compare results.

The discharge rate is primarily dictated by the potential difference, alongside pressure variations. To ensure good statistics, a discharge count larger than 500 for any working point is recorded with an oscilloscope.

A working point is defined as a state of fixed set of voltage values for each electrode in the system. For a specific measurement, a number of working points are identified and for each the waveforms are recorded and analyzed.

The high number of recorded events is necessary, since one of four different events are present at one time in the detector:

- A primary discharge occurring only in GEM2.
- A primary discharge in GEM2, followed almost instantly by a propagated primary discharge in GEM1.

- A primary discharge in GEM2, followed after some µs by a secondary discharge in the transfer gap. At the time of the secondary, the discharge of GEM1 is expected, given that G1B potential drops when the secondary occurs, instantly engaging the top potential as well.
- A primary discharge in GEM2, with propagation to GEM1 almost instantly, where it triggers a discharge, followed some µs later by a secondary in the transfer gap.

The events are summarized in Table 4.1 for future reference:

	Discharge across		
	GEM2	Transfer gap	GEM1
Primary, no propagation	X		
Primary, with propagation	X		X
Secondary, no propagation	X	X	
Secondary, with propagation	X	X	X

Table 4.1: The four types of discharges occurring in the detector. An X marks the gap concerned in the respective discharge.

To have consistency throughout the span of the measurements (drift velocity and energy loss are dependent on the medium density) and to be able to compare to similar works, the values of the electric fields are normalized to the ambient pressure. Alongside the E/p normalized field, a correction is needed when referring to the electric field in the transfer gap.

Because of the fact that GEM2 discharges, it enhances the field in the transfer gap by an amount equal to $\Delta V_{\mathrm{GEM2}}/d_{\mathrm{t}}$, where $d_{\mathrm{t}} = 2\,\mathrm{mm}$ is the transfer gap width. As such, a corrected transfer field is consequently mentioned in the measurements, as $E_{\mathrm{tr}} = E_{\mathrm{tr}_{\mathrm{nominal}}} + \Delta V_{\mathrm{GEM2}}/d_{\mathrm{t}}$.

This correction is not necessarily perfect. It assumes an immediate and constant field modification, which might not be necessarily true. Nonetheless, this modified quantity allows to relate all the relevant set voltages to the measured parameters (like the secondary discharge probability, or the propagation probability). Furthermore, the modified field is a better approximation of the true field before the secondary, than the nominal field (calculated with set voltages).

Discharges are recorded on the oscilloscope and the waveforms are further processed by MATLAB [124] and Python [125] scripts on a personal computer.

The waveforms are recorded in the oscilloscope's internal .isf file format. Since it is a binary format, the file size is small and the file transfer is fast. A first script converts the format into a human readable comma-separated-value table and removes any entries with incompatible NaN or Inf values (in the case a value is bigger than the dynamic oscilloscope range, the values are outputted as Inf).

The next step is to apply a smoothing filter to all the waveforms. This is desirable to easily spot signal features, remove noise and oscillations, which aids as well applying further software. An example of how the result of the smoothing mechanism works is shown in Fig. 4.32, when applied on a pad plane waveform.

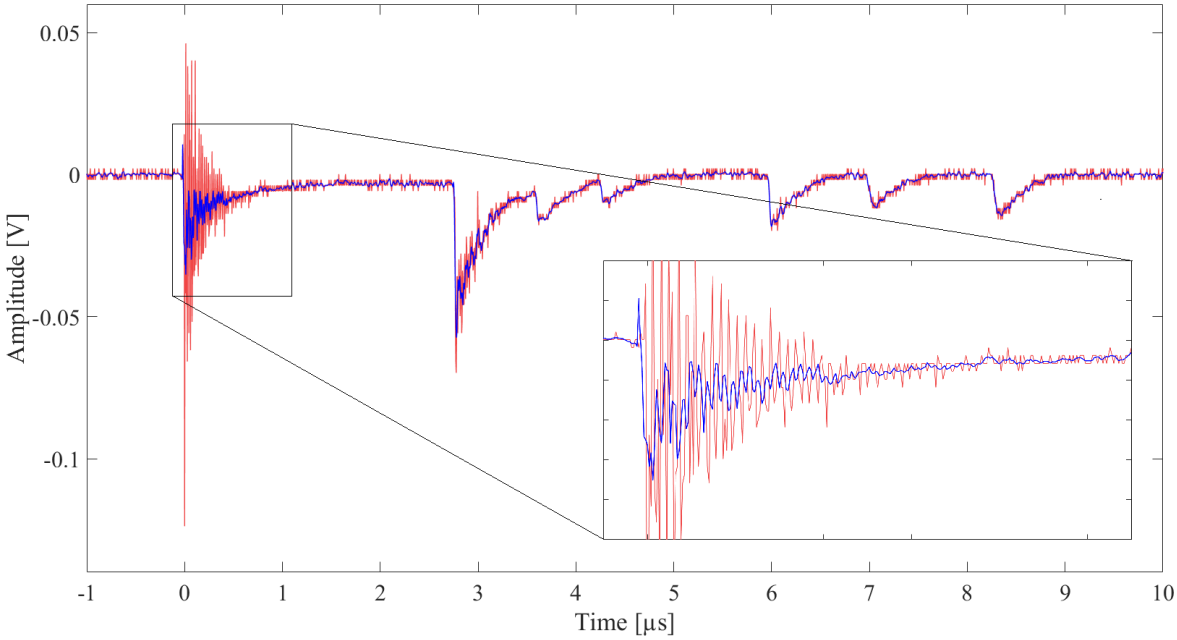

Figure 4.32: Savitzky-Golay digital filtering of waveforms read from the oscilloscope. Red: original, unfiltered signal. Blue: Filtering with a 3^{rd} order polynomial.

In red the original signal from the oscilloscope is shown and in blue the smoothed signal is superimposed. The smoothing is done using a Savitzky-Golay filter [126], a type of finite impulse response (FIR) digital filter applied on the waveform points. It increases the precision of the data in a process known as convolution, by fitting successive subsets of adjacent data points with a low polynomial (of 3^{rd} order in this case) by the method of linear least squares, without distorting the signal tendency.

It was found to perform better than other standard averaging FIR filters. While there is less smoothing of the broad features, the narrower features in the signal have their heights and widths preserved. Even though the amplitude does not look conserved in Fig. 4.32, a higher order polynomial can be successfully applied to accurately reproduce the amplitude of signals if that information is needed.

Given that the AC response of a first version of HV probes used in the measurements were not fast enough to disentangle potential drops happening in microseconds, a decision was made to use the anode signal as the basis for deciding if an event was a primary only, or if it also features a secondary. The analysis code was modified to include a decision for propagated events after a new and final version of HV probes were tested, which have a faster response. Since the scripts are working with extremely good efficiency on both data sets, it was opted to continue using them. Further information about the "fast" probes' response can be found in [89].

After the smoothing, the anode signal is used on one side to determine the time when a primary and a secondary occurred. Even after the smoothing is done some oscillations are present. The amplitudes for the primary and secondary can vary, as well as the time after which the secondary occurs. This time can be tens or hundreds of µs long or shorter than a µs, possibly sitting in the oscillatory region of the primary.

Therefore, further software processing must be done to ensure proper detection of the time at which the primary and the secondary discharges occurred. To this end, a minimum peak prominence quantity is defined and used to disentangle primary and secondary peaks from normal AC oscillations, noise and secondary re-ignitions.

The prominence is a measure of how much the peak in question stands out from the surrounding baseline of the signal, due to its amplitude and location relative to other peaks. So, a low amplitude isolated peak is more prominent than a high amplitude one located near similarly high peaks.

The peak-finder function takes the one-dimensional array of waveform voltage values provided by the oscilloscope and finds all the local maxima by comparison of neighboring values. From each of the peaks a horizontal line is extended to the left and to the right until it reaches either the start or end of the signal, or it intersects the signal at the slope of a higher peak. In each of these intervals, the minimum of the signal is recorded and it defines the peak's base (on the respective side of the peak). The higher of the two defines the peak's lowest contour line. Finally, the prominence is calculated as the vertical difference between the peak height and the lowest contour line. An example of signal with several peaks and the decision tree is shown in Fig. 4.33.

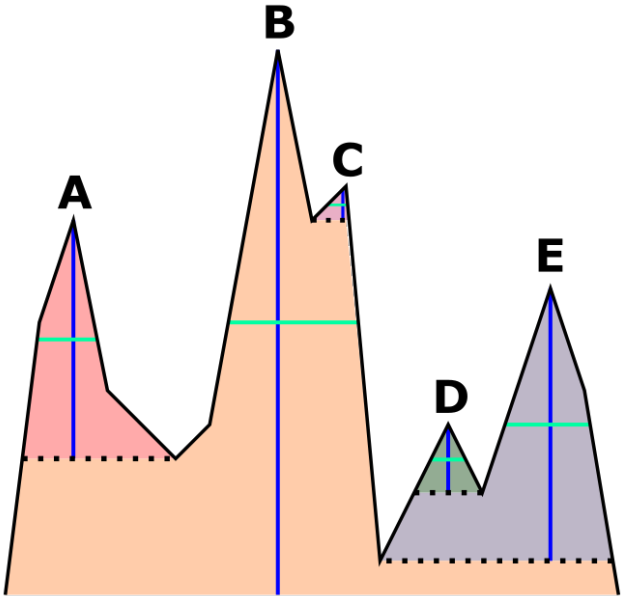

Figure 4.33: Peak prominence decision making. Peaks are identified and the algorithm calculates the prominence (vertical blue line) and from it the peak width (at half prominence shown in green). Based on the two variables, the most prominent peaks are selected. As such, peaks C and D are discarded, while the rest are retained.

For the smoothed pad plane signal from Fig. 4.32, the peak finding algorithm is applied and shown in Fig. 4.34.

Only the most prominent peaks are selected. For the example in Fig. 4.34, a selection criterion is set for peaks that have an amplitude of at least 0.015 V and are separated by at least 0.8 µs. The occurrence of the primary and secondary discharges will always be the first and second of these peaks, so their location is stored and will be used in calculating t_{12}, the time until the secondary occurs.

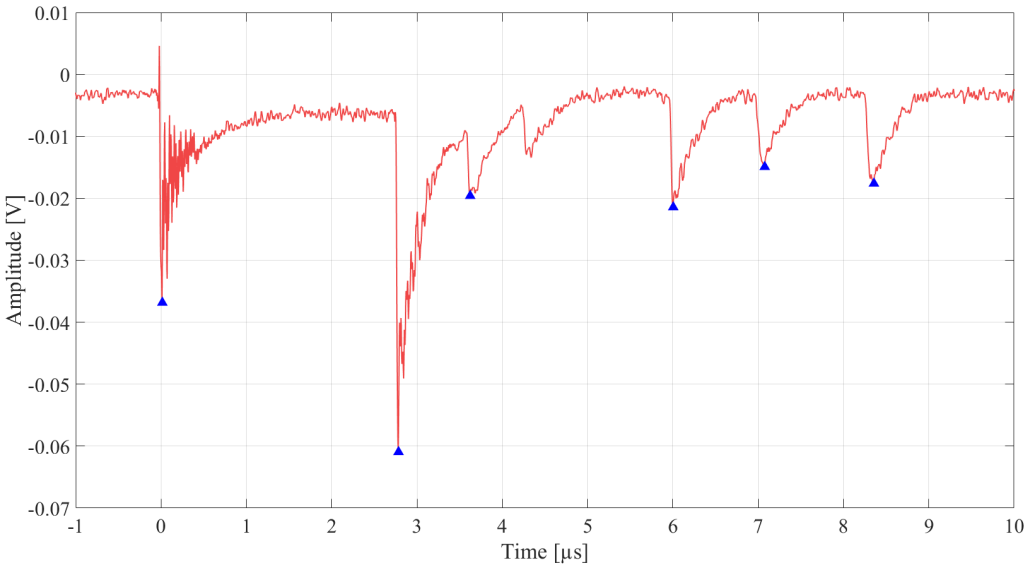

Figure 4.34: Peak-finding algorithm applied to a smoothed anode signal. Several prominent peaks are found.

Once primary and secondary events are identified, it still needs to be analyzed if the primary discharge was propagated to the other GEM. To ascertain when a GEM discharges and if the event has propagated to the other GEM, a projection of the GEM top electrodes on the vertical axis is used (see Fig. 4.35), corroborated by a second script using threshold values (explained below).

After the projection, the number of isolated peaks is calculated. This contains a good estimate on what kind of event happened in the detector. For the G1T electrode, just one isolated peak near the mean amplitude value before $t = 0$ means that no propagation or secondary occurred; two peaks separated by less than 1.5 V indicate that the primary discharge has propagated to GEM1; two peaks separated by more than 1.5 V indicate that a primary discharge, followed by a secondary just took place; three peaks show that alongside a primary and a secondary, GEM1 discharged, so propagation occurred.

A second script is also used, in case the secondary occurs extremely fast after the propagation and/or a middle peak used for distinguishing propagation is not well represented in the projection script (when the secondary happens quickly after the propagation, a peak for the propagation does not have time to develop). The second script calculates a mean value of the first hundred ns after $t = 0$ of the G1T potential (the only one used to ascertain if GEM1 discharged), removing the first few points to make sure the smoothing function is not misbehaving. If this mean is above twice the threshold of the capacitive coupling, the event is a propagated one.

Based on these scripts, all the samples taken at a working point are subdivided into four categories mentioned before, with 100% efficiency (large waveform sets were manually verified).

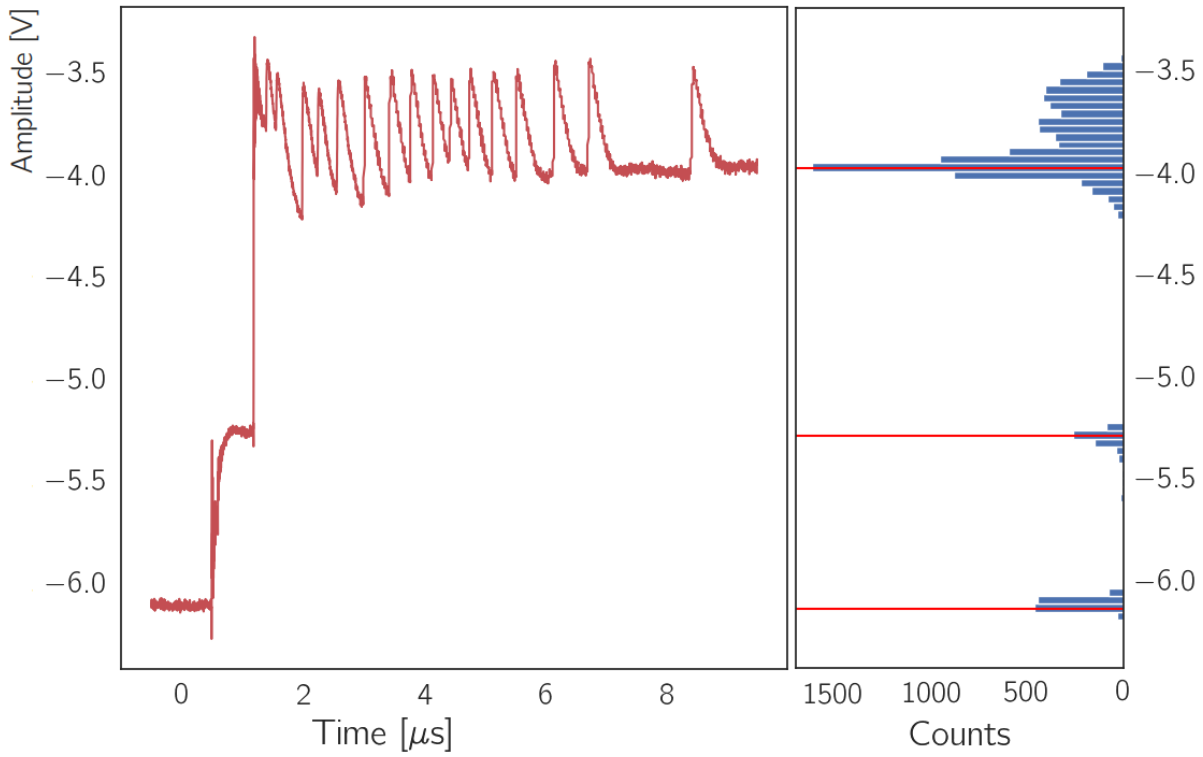

Figure 4.35: G1T HV probe response is projected on the vertical axis.

1.) One peak around the baseline (the mean value of the waveform before $t = 0$, the set voltage) means no event occurred (just capacitive coupling).
2.) Two peaks, one around the baseline and one less than 1.5 V away (~ 330 V on the GEM, taking into account the amplitude conversion factor) would indicate that the primary discharge has propagated to GEM1, trigger a discharge across it.
3.) Two peaks, one around the baseline and one further than 1.5 V away would indicate a secondary that occurred in the transfer gap, without any prior propagation and subsequent discharge in GEM1 (biggest potential value set across GEM1 was 250 V).
4.) Three distinct peaks indicate that the primary from GEM2 has propagated and triggered a discharge across GEM1, followed shortly by a secondary discharge in the transfer gap.

4.6 Mitigation of discharges with resistors

Loading resistors

The effect of the loading resistors on the occurrence of discharges has been studied in-depth in other works and it is not further discussed here, but merely mentioned.

In a one-GEM setup [119] in Ar-CO_2 (90-10), the secondary discharge probability was measured in the induction gap below the GEM as a function of the loading resistor. The result is shown in Fig. 4.36.

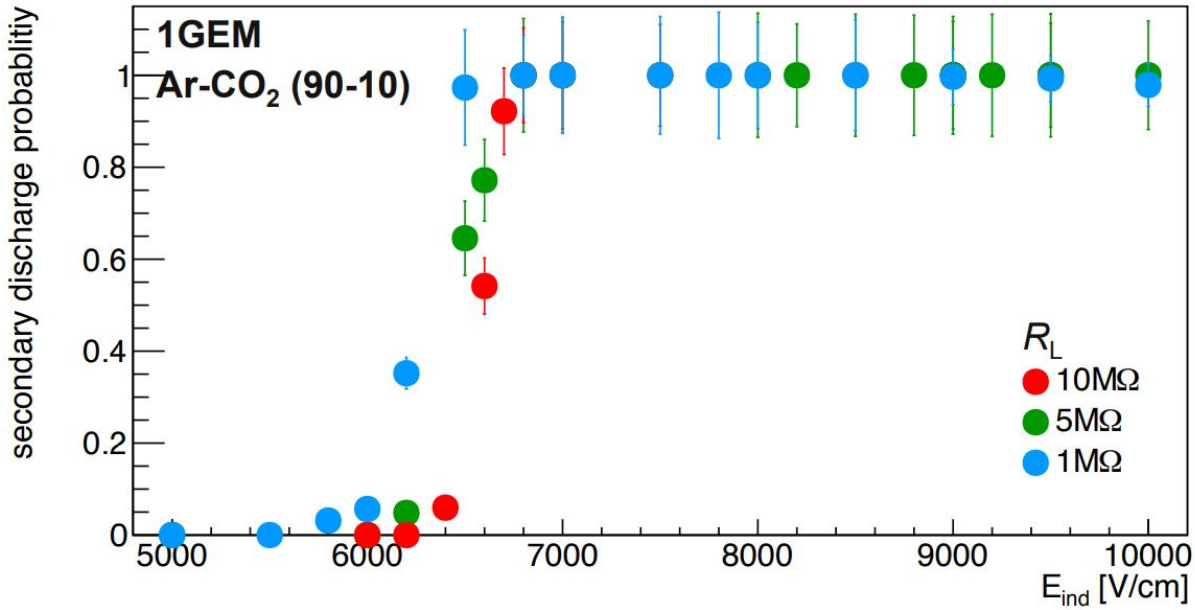

Figure 4.36: P_2 as a function of the E_{ind} for different loading resistors. Taken from [119].

It can be clearly seen that in the MΩ range the secondary probability does not strongly depend on the loading resistor value. A nominal value of 5 MΩ has been chosen for the TPCU GEMs. For the thesis, given the vastly higher number of discharges expected for the detector, a conservative value of 10 MΩ was chosen.

Decoupling resistors

Previous studies have already proven that secondary discharges are mitigated in the transfer field by having a bigger decoupling resistor (R_D) on the bottom GEM elements. The most relevant examples are Fig. 7.8 (b) in [102] and Fig. 14 (a) in [89]. To have a good comparison with previous works, those results have been reproduced.

There are a few differences nonetheless. Here, a cascaded power supply has been used, similar to the final design of the powering scheme of the ALICE TPC. Moreover, the gas composition used here is Ar-CO_2 (80-20) and no extra sinking resistors are used.

4.6.1 The effect of the decoupling resistor on the secondary discharge probability

Fig. 4.37 shows the influence of the decoupling resistors on the occurrence of secondary discharges between the GEMs. Both GEM bottom resistors have the same value when the measurement is recorded.

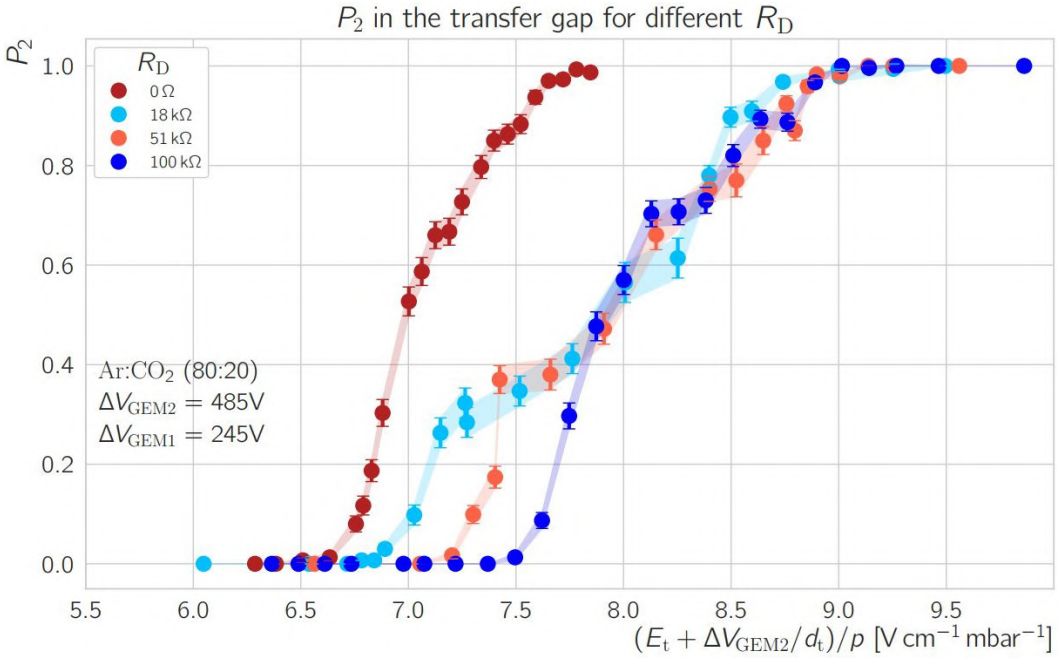

Figure 4.37: Secondary discharge probability in the transfer gap for different decoupling resistors (all events included).

The measurements have been performed with Ar-CO_2 (80-20), with discharges initiated in the lower GEM.

The secondary discharge probability (P_2) has been calculated by dividing events where a secondary occurred alongside the primary in GEM2 by all events at each working point:

$$P_2 = \frac{\text{recorded events with a secondary in the transfer gap}}{\text{all events recorded}}$$

The shaded area encloses the uncertainty for each case (see Appendix D for explanations). A secondary discharge is a binary event (it can either occur after a primary or not). The probability to observe such an event can be described by a binominal distribution. With a large enough number of waveforms, the uncertainty will be in the percent level (see Appendix D).

From Fig. 4.37 it is clear that the onset of secondary discharges is influenced by the decoupling resistor. Here, the four S-curves (described by the error function) are separated by about 0.25 V cm^{-1} mbar^{-1}. The higher the choice of the resistor in the path from the power supply to the GEM bottom electrode, the higher the electric field necessary for secondary discharges to occur in the transfer gap. The trend appears linear.

At about 40% P_2, the curves for the cases where a resistor is present seem to collapse to the same values until they reach 100%. The case without resistor increases rather quickly and until it reaches the region where all primaries have a secondary in the transfer gap, its S-curve remains independent from the trend of the others at higher values of P_2.

This behavior hints at some underlying mechanism responsible for changes at high P_2 for runs with decoupling resistors. This mechanism does not seem to affect the coupling of the GEM bottoms to the power supply in the case where no ohmic resistance is inserted in between.

These results do not seem to reproduce previous findings on this subject. A representing result from similar investigations can be seen in Fig. 4.38. The outcome, even though done in a slightly different gas mixture and featuring current-sinking resistors, shows that the four resistor curves are clearly separate. The onset field for secondary discharges (taken as the value where P_2 is 50%) increases with increasing R_D.

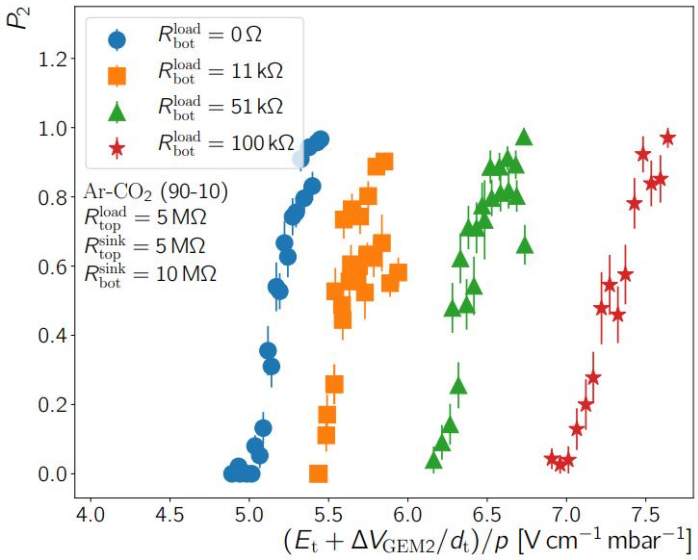

Figure 4.38: Secondary discharge probability as a function of the modified transfer field for different decoupling resistors [89]; work done before this thesis.

At a careful inspection, it was found that all previous works have not treated the aspect of propagated discharges. Previous measurements for secondary events in the transfer gap have been done in conditions where the propagation of discharges is always 100%, or with a single GEM.

To understand why this difference appears, the events with propagation and without propagation to GEM1 have been treated differently. Two new quantities are defined in the following way:

$$P_{2w} = \frac{\text{recorded events with propagation and a secondary in the transfer gap}}{\text{all propagated events}}$$

$$P_{2w/o} = \frac{\text{recorded events with no propagation, but with a secondary in the transfer gap}}{\text{all propagated events}}$$

In the first case, all events where the primary discharge has propagated from GEM2 to GEM1, followed by a secondary in the transfer gap are divided by all events with propagation - that is primary discharges in GEM2 with propagation but no secondary, and primary discharges with propagation and a secondary in the gap. The result is shown in Fig. 4.39.

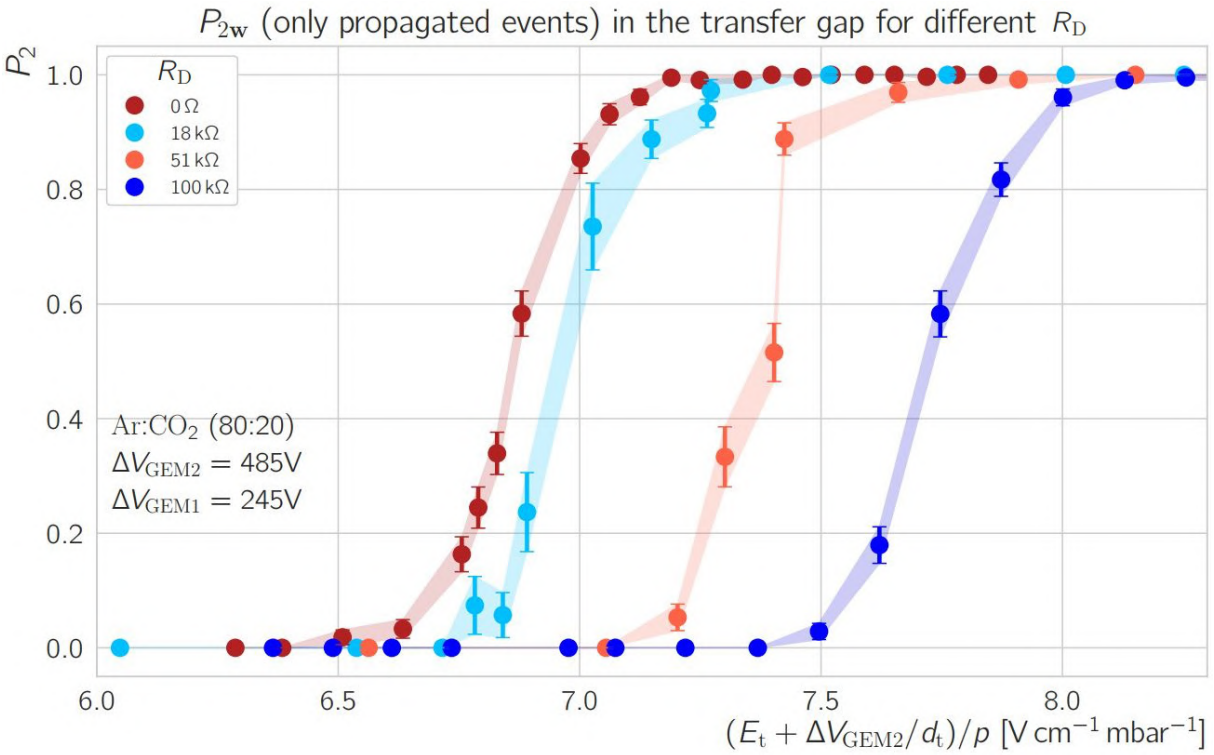

Figure 4.39: Secondary discharge probability in the transfer gap for different decoupling resistors. Only for events with propagation.

It was expected that taking only those events where propagation occurred, would mean basically operating in a region with 100% propagation. As such, previous results from [89] and other papers on the secondary probability in the transfer gap are reproduced.

The onset at 50% P_2 for any of the S-curves is clearly independent from the others. The onset follows a linear trend as a function of the decoupling resistors, as expected from the other investigations and plotted in Fig. 4.40.

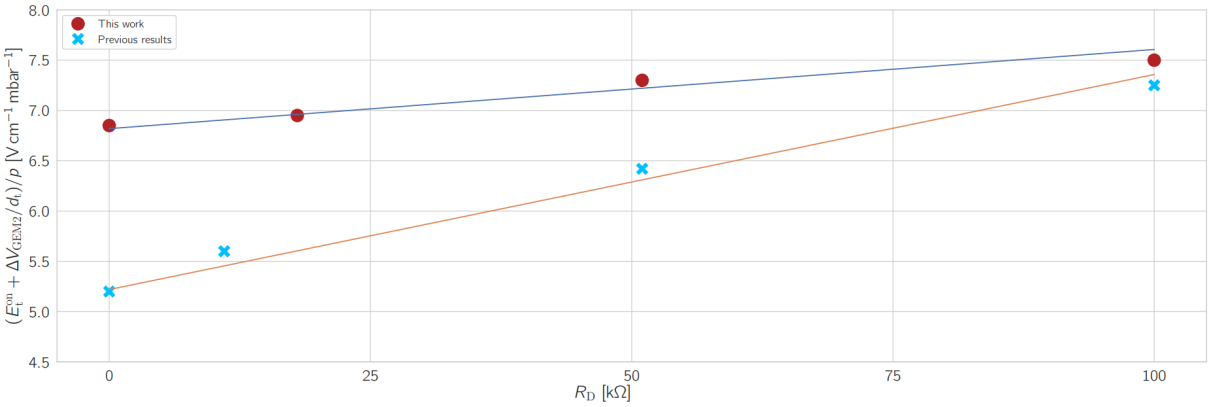

Figure 4.40: Both this work and previous results [89] agree on the linearity of the secondary discharge onset field as a function of the decoupling resistor.

The difference between the slope and values are due to a difference in the gas mixture: here, Ar-CO_2 (80-20) was used, whereas in [89] the detector was flushed with Ar-CO_2 (90-10). With more CO_2 content, the onset for the Townsend coefficient occurs at lower fields (see Fig. 4.2). Furthermore, an independent channel PS, as well as current sinking resistors are used in [89] to help dissipate excess currents coming from the discharge.

The other kind of events are those where a secondary occurs, but the gas rigidity in the upper GEM is not broken, so no propagation is achieved. Plotting those kind of events against all non propagated events at each working point, yields Fig. 4.41.

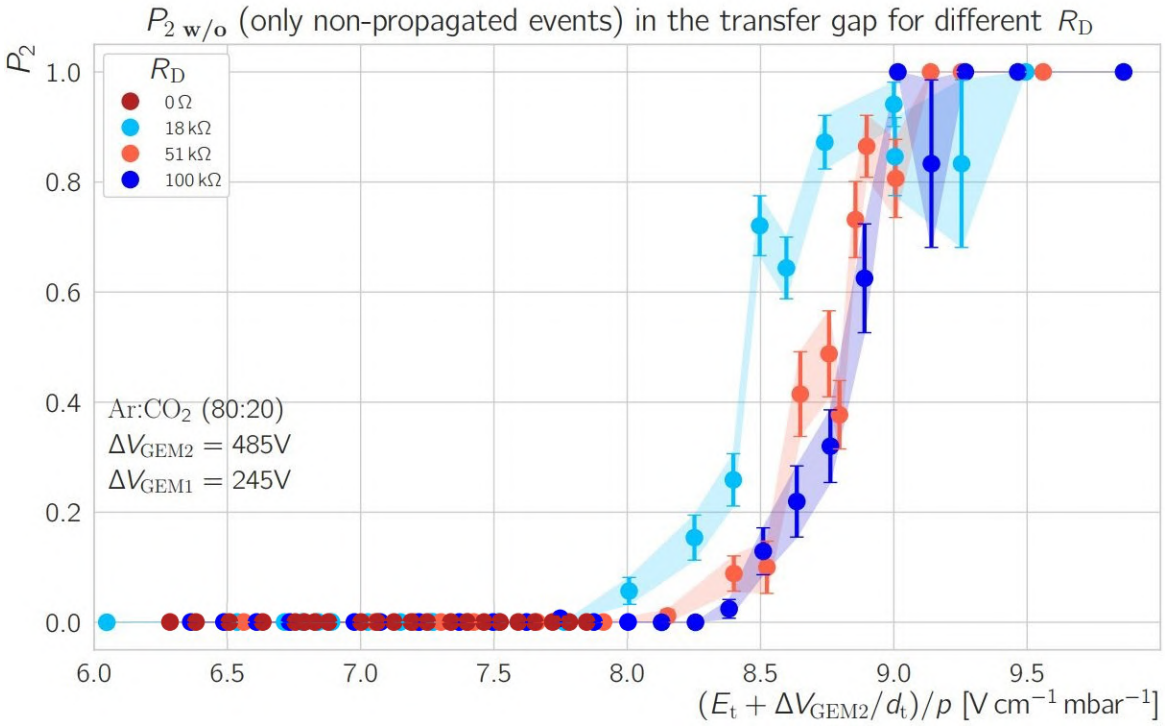

Figure 4.41: Secondary discharge probability in the transfer gap for different decoupling resistors. Excluding all events with propagation. For $R_D = 0\,\Omega$ there are no secondary events without a propagated discharge.

In this plot, it can be seen that when a decoupling resistor is present, a secondary discharge occurs roughly at the same values of the transfer field. This means that if no propagation occurs, the mechanism responsible for the production of secondary discharge in the gap allows for such events in a narrow region of values of the transfer field, irregardless of the value of the decoupling resistor. The secondary is thus achieved if the field is higher than $\sim 8.4\,\mathrm{V\,cm^{-1}\,mbar^{-1}}$.

One consequence of this is the fact that secondary discharge probability seems to be driven by propagation probability. In this case the secondary occurrence in the transfer gap seems to not care about the value of the decoupling resistor. The propagation behavior, on the other hand, is very sensible to changes in the value of the decoupling resistor, as will be later showed.

As a side note, mitigation of the secondary discharge with decoupling resistors has been observed (e.g. [98]). The difference between the conclusions from this thesis and the ones done in the single GEM case are referring to the direction the secondary streamer takes. For the single-GEM, the secondary can occur only in the induction gap. The anode-directed streamer can *only* be initiated from the discharging GEM and will propagate downward, in the direction of the electric field. In case two GEMs are present, the secondary in the transfer gap can go with the field, if the initial discharge happens in the top GEM. Alternatively, if the initial discharge took occurred in the lower GEM, the secondary discharge can develop against the electric field direction, if no propagation took place, or it can start from *both* GEMs, if the initial discharge occurred in the lower GEM and propagation to the top GEM took place prior to the secondary discharge.

Another conclusion drawn from the plot is that in the case where no decoupling resistor is present, there are no secondaries happening if propagation does not occur prior. This can be understood by the fact that if no decoupling resistor is used, the GEM bottoms are capacitively coupled to the power supply unit, and therefore sensible to any parasitic or extra capacitance on the line.

4.6.2 Consequences of parasitic capacitances

Previous works have shown that extra capacitance pushes the occurrence of secondary discharges at lower fields. A longer cable will introduce more capacitance in the system. This has to be properly decoupled from the sensible GEM, by use of a R_{D} (the top side always features the R_{L}).

If this extra capacitance is situated between the GEM bottom and R_{D} (Fig. 4.42, top), the effect is the onset of secondaries shifts toward lower values, as the capacitance increases.

This is because at the time of a discharge, not only the capacitor formed by the two sides of the GEM discharges, but also the extra reservoir given by the cables and other parasitic capacitances in the RC system. This motivated the need to install decoupling resistors close to the readout chambers of the upgraded ALICE TPC.

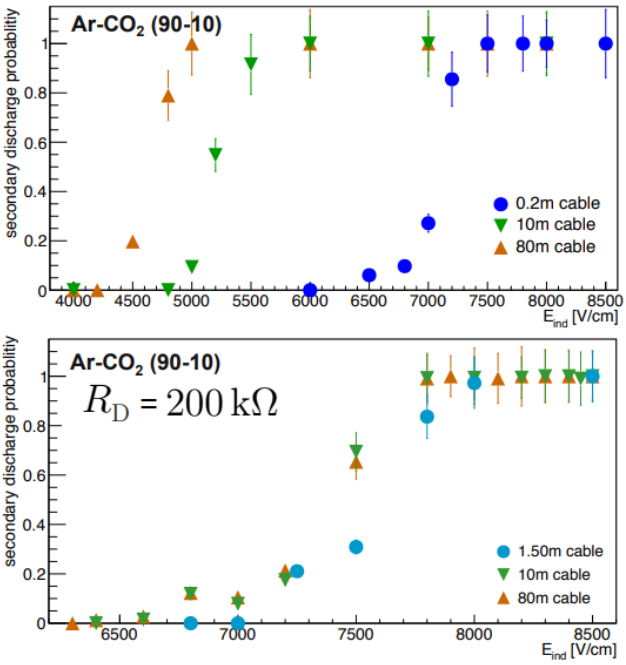

Figure 4.42: Top: Extra capacitance (cable length) between GEM bottom and R_{D} (induction gap studied with a one GEM setup). Bottom: capacitance between R_{D} and the PS [119].

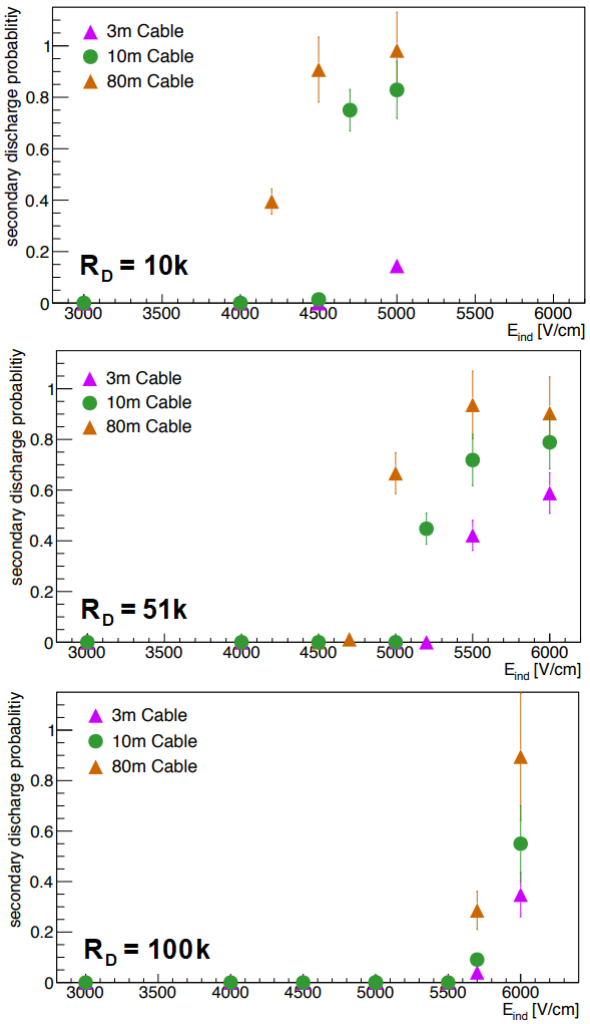

Figure 4.43: A high enough ohmic path ensures that extra capacitance does not influence the secondary discharge probability [119, 127].

If extra capacitance is located between the R_{D} and the power supply, there appears to be no effect on the secondary onset, but this might change with the value of R_{D}.

If low R_{D} are used, the dependence on the cable length is visible (see Fig. 4.43). The *decoupling power* increases with a bigger value R_{D}, showing that higher resistance is preferred on the bottom side.

Returning to Fig. 4.41, the lack of secondaries without propagation for the case where no R_{D} exists is understood in the following way: the bottom GEM has extra capacitance, since it is not decoupled from the PS and the cables.

When the primary discharge occurs in GEM2, the reaction is more violent, releasing more charge, more photons, which trigger a discharge in GEM1 shortly after in all cases. The probability to have GEM1 trigger when GEM2 discharges is thus increased. A secondary can follow only after both GEMs discharged.

4.6.3 The effect of the decoupling resistors on the propagation probability

To further validate this claim, the propagation probability is analyzed in the transfer gap, for the four different resistor choices. The P_{prop} quantity is calculated at each working point by dividing all events where propagation to GEM1 occurred by all events recorded at said specific parameters:

$$P_{\mathrm{prop}} = \frac{\text{recorded events featuring propagation to GEM1}}{\text{all recorded events}}$$

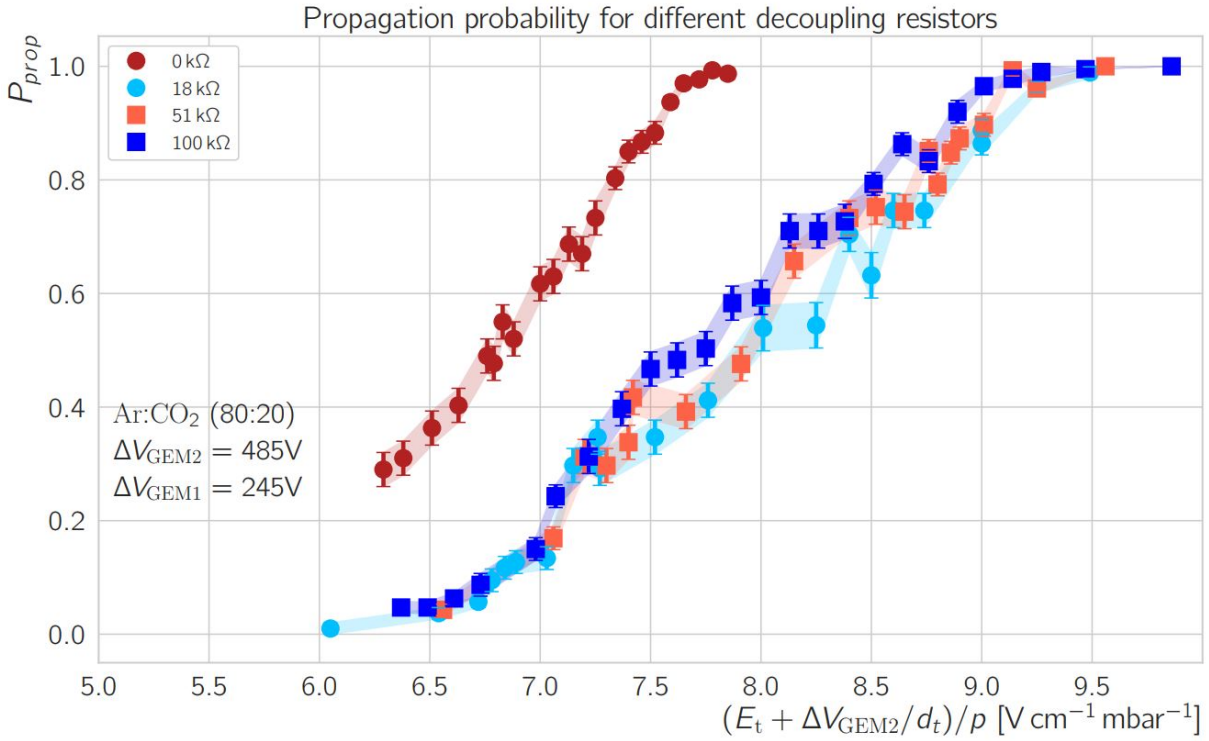

Figure 4.44: Propagation probability as a function of the modified transfer field for increasing decoupling resistor values.

In Fig. 4.44 it is immediately obvious that the propagation probability does not depend on the value of the decoupling resistor, but on its physical presence in the path from the power supply to the GEM bottom electrodes.

Propagation probability increases linearly with the transfer field for all decoupling resistors. The non-zero decoupling resistor curves all lie within the same region and share a common starting point, ending point and slope for the linear increase.

The 0 Ω decoupling resistor curve has a similar slope, but is offset toward lower values. That is, at a certain value of the transfer field between the two GEMs, there is a higher propagation (and therefore secondary) probability for the $R_D = 0$ case than there is for the non-zero components.

This behavior supports the earlier claim that, if uncoupled from the power supply and cables, the GEMs have some extra capacitance and are more prone to discharge at lower fields if the mechanism for propagation is fulfilled.

4.6.4 Consequences of parasitic capacitances

Another confirmation comes with adding a capacitor of 1 nF between the electrodes of GEM1 when no R_D is present. This increases the GEM capacitance (mimicking the cables in the previous discussion) by 20% and consequently its proneness to experience a discharge (see Fig. 4.45).

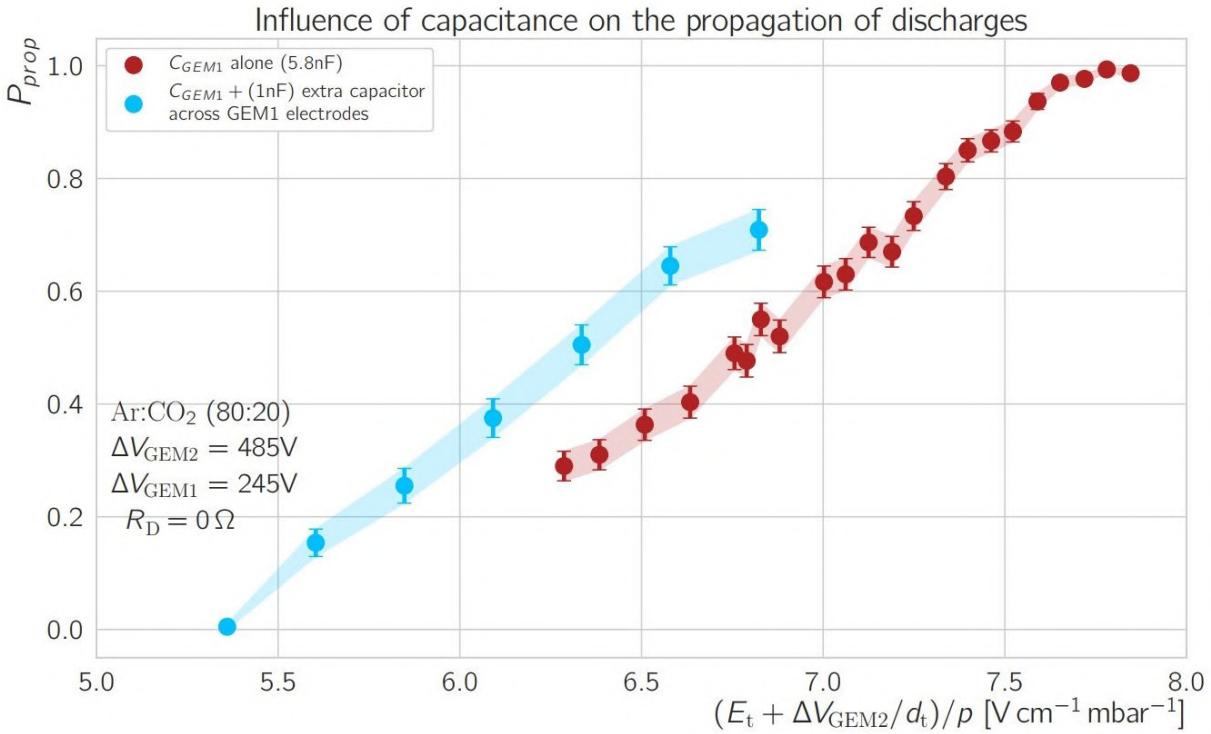

Figure 4.45: Extra capacitance (e.g., cable length) has a big influence on the propagation probability when no R_D is used.

The GEMs alone have each about 5.8 nF across the electrodes. Adding the 1 nF in parallel to the GEM electrodes increases the overall GEM capacitance, and therefore the available energy reservoir. When the discharge occurs, the capacitor formed by the GEM capacitance releases the energy. Having the extra energy, it will discharge at lower electric fields.

Before going further with the measurements, the bottom GEM malfunctioned. A very high current appeared in the control software, indicating that a short-circuit occurred, linking the top and bottom electrode. Moreover, the capacitance across the two electrodes dropped to 0 and a high resistance was present in the path from top to bottom (an infinite resistance should be present in normal conditions).

Probable causes for the failure of a foil are many. In this care some ejected material (after a primary discharge) might have got stuck in one of the holes or, more probably, the GEM might have experienced a very large number of discharges. In [102] the usual number of discharges recorded by a GEM before it fails lies in the few tens of thousands. Taking into account the commissioning of the setup, alongside the number of files recorded and processed, an estimated number upwards of 60000 discharges were recorded and stored. The real number is several times higher, since not all events are recorded (dead time induced by the oscilloscope when the speed of writing to file is larger than the rate of discharges, calibration runs, test runs, etc.).

The recovery requires instantaneous connection to high voltage ($500 - 600\,\mathrm{V}$) in air. If present in a stack, there is a risk that the recovery discharge might damage the other GEMs. As such, the detector had to be opened and the GEM removed. It was recovered separately in a clean room environment.

The recovery was successful and a couple of tests were done to observe any changes in behavior. A slight shift of the onset curves for all the events has been observed, as further detailed in Appendix A. Since all the curves are shifted by the same amount, this is an indication that mechanical distances between the GEMs and thus the inter-electrode fields have been slightly altered. Previous works [98] have shown that a shift is expected. Nonetheless, the same effects are observed and data can be related by adding the necessary offset.

4.6.5 The influence of GEM1 potential difference on the secondary and propagation probabilities across the transfer gap

It seems that GEM1 has a big influence on the appearance of secondary discharges if the propagation mechanism manages to induce a discharge across its electrodes. In order to better understand how propagation influences the behavior of secondaries, the voltage across GEM1 is varied. The transfer field is scanned and the previous measurement variables are checked.

To ensure good statistics and consistency across the measurements, for each working point 300 waveforms are recorded in a time ranging from 30 to 45 minutes. To have a sufficient rate of primary discharges, the potential difference across GEM2 is set between $490 - 500\,\mathrm{V}$. The uncertainties are in the percent level ($\leqslant 2\%$) at each working point and are not shown in the plots.

The induction field is kept constant at $1\,\mathrm{kV/cm}$ and the drift field is kept at $0.6\,\mathrm{kV/cm}$. Both GEMs feature the $10\,\mathrm{M\Omega}$ loading resistor on the top electrode and $18\,\mathrm{k\Omega}$ decoupling resistor on the bottom side.

The recorded values for the transfer field start where other events apart from just GEM2 sparks happen and stop at $9.5\,\mathrm{V\,cm^{-1}\,mbar^{-1}}$ where there is a risk of seriously damaging the GEM foil. By this time, the propagation has well reached 100% and this is the region where secondaries have a 100% chance to occur and will dominate everything else.

Fig. 4.46 shows how the propagation and secondary discharge probabilities change with the modified transfer field and the potential difference across GEM1.

At $0\,\mathrm{V}$ across GEM1, this GEM allows charge flowing unhindered, but does not amplify it. The field lines above and below it will leak into the GEM1 holes and form a very small, but non-zero field inside. If some charge deposition occurs above the GEM, a large part of the electrons will be guided through the GEM holes. Analogously, if some charge is created below the GEM, most ions will go through the holes and further up, while some will be collected on the GEM electrode on the side of the charge deposit.

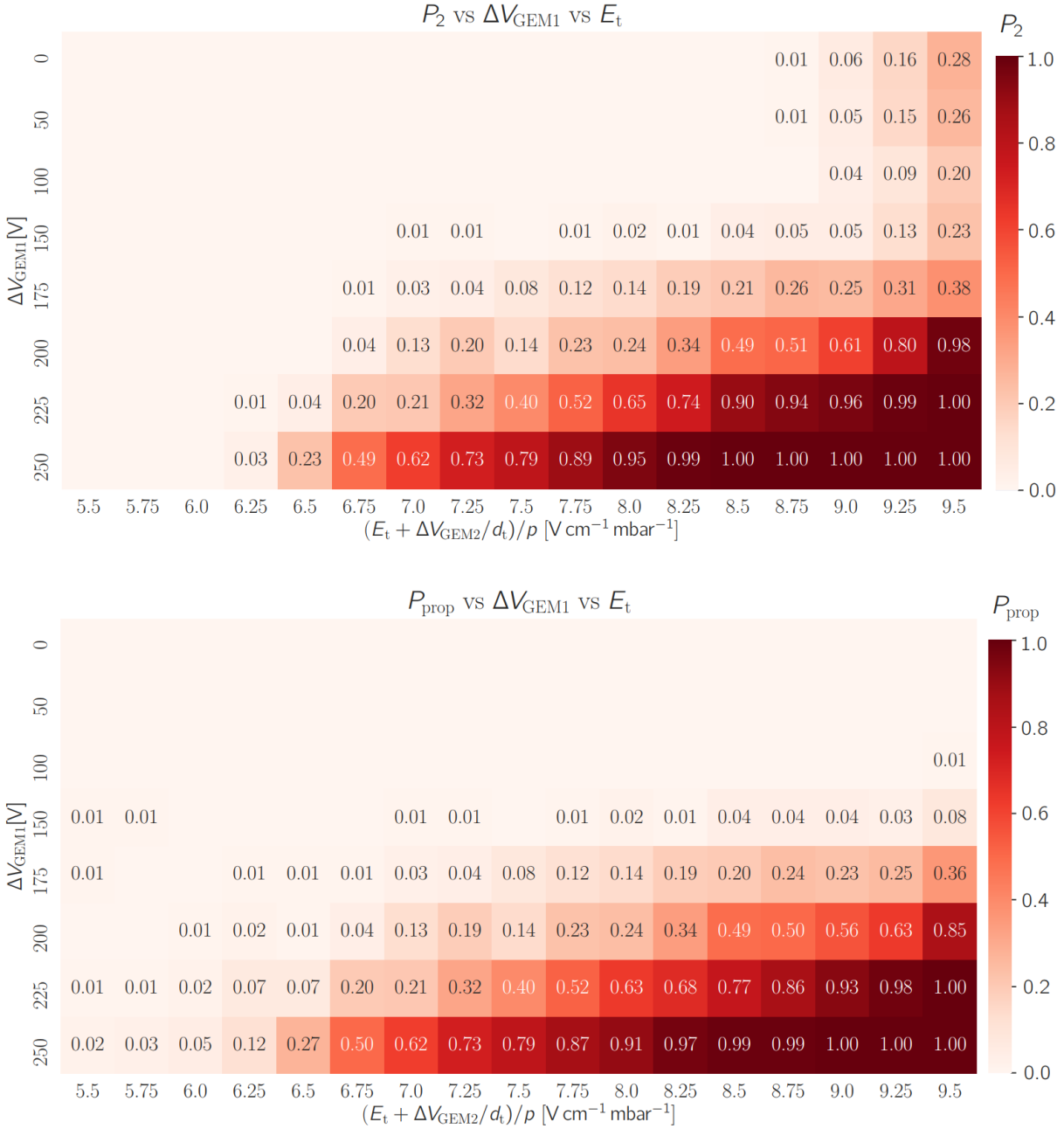

Figure 4.46: Heatmap of the secondary and propagation discharge probabilities as a function of the potential difference across GEM1 and the modified transfer field.

There is zero probability to have any discharge occurring across GEM1 in these conditions, because the fields are too weak to create the critical amount of charge. Any secondary discharges occurring in the transfer gap will be *pure* (i.e., not influenced by the propagation probability). This means that the extreme conditions present during a discharge in GEM1 are missing and will not interfere with (or support) the development of a secondary discharge starting from GEM2. As can be seen, there is a ridge forming at high transfer field values where the mechanism producing secondary discharges becomes significant.

Further details about these pure propagated events, as well as an explanatory plot, are given in Appendix F.

Any secondaries forming in this low ΔV_{GEM1} regime are starting from GEM2 and develop upwards, unaided by any charge amplification in GEM1 (or only marginally).

The onset where P_2 will be at 50% will most likely be very close above $9.5\,\mathrm{V\,cm^{-1}\,mbar^{-1}}$. The values of P_2 here seem to lie in the same range for up to 150 V across GEM1, after which the propagation probability starts to be visible. This extra charge from the GEM1 discharge aids the secondary discharge formation, resulting in a reduced threshold/onset field, their occurrence being more probable.

At $\Delta V_{\mathrm{GEM1}} = 150\,\mathrm{V}$, infrequent secondaries start occurring at lower transfer fields. This is a clear indication that the potential difference across GEM1 is high enough that secondaries are created with the help of the charge left in the wake of the sparse GEM1 discharges.

Further increasing the voltage across GEM1 shows a very large increase of the secondary probability at high transfer fields ($> 7\,\mathrm{V\,cm^{-1}\,mbar^{-1}}$). Here, when GEM1 discharges, the critical charge needed to create a secondary can be attained at lower transfer fields than in the case of a pure secondary (no propagation). At this point, the interference of the propagation in the appearance of secondaries starts becoming obvious.

This is also confirmed when looking at the propagation probability counterpart. As expected, the propagation probability is non-existent for low ΔV_{GEM1} voltages, even at high transfer fields. This is an indication that the mechanism responsible for inducing a primary discharge in here has to do with a certain amount of charge created before the GEM discharges, in the presence of high electric fields inside the holes. At low potential difference across the GEM1 electrodes, the field is insufficient to created the threshold charge to induce a discharge.

For medium values of the transfer field ($6.5 - 8\,\mathrm{V\,cm^{-1}\,mbar^{-1}}$), the propagation probability is almost identical to the secondary probability (see Fig. 4.46). This shows that even when changing the GEM1 potential difference starting with mild fields, the secondary and propagation probability are linked and an interplay is present between their effects. This implies that the propagation is dictating if and how many secondaries can happen at these transfer field values.

This similarity between the two probabilities fades towards high transfer field values where the mechanism for the secondary becomes important and the high values of the electric field ensure that a secondary discharge will always follow the primary one. Here, the propagation probability is slightly smaller than the secondary probability, but nonetheless is the driving factor.

For smaller transfer fields, the values shown represent primary discharges with propagation, but no secondaries, due to low field.

To better emphasize the regions where the secondary and propagated discharges do not influence one another, their difference is computed. The results are shown in Fig. 4.47.

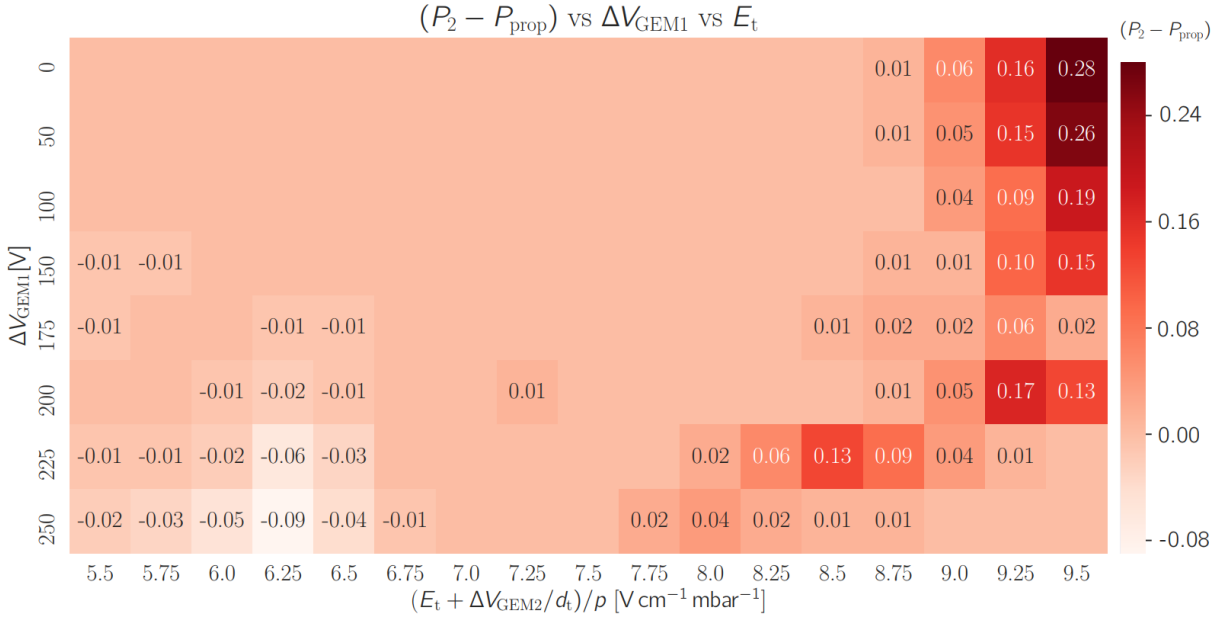

Figure 4.47: Heatmap of the difference between the secondary and propagation probability as a function of the potential difference across GEM1 and modified transfer field.

Two regions appear accentuated. The first is a region of high secondary probability, with very little propagation. This happens at low values of ΔV_{GEM1}, where propagation is unlikely to manifest and trigger a discharge in GEM1. These events are mostly pure secondaries. Toward higher GEM1 voltages, this ridge starts veering toward lower transfer field values, indicating that propagation starts to be the dominant effect by increasing the voltage values and with it, more and more charge is being produced, enough to initiate the secondary discharge. This happens, because with each increase of potential difference across GEM1, more energy is available and more charge is created.

Another region is visible at high ΔV_{GEM1} values, but low transfer fields. This is the opposite of what was explained before. Here, due to the high potential difference across GEM1 electrodes, the pre-amplification is more powerful, the GEM has a higher gain and a higher amount of charge is created. Thus, it is more likely that discharges in GEM2 are able to push GEM1 beyond the discharging limit already at low transfer fields. Due to the low transfer field, secondaries are unlikely to emerge.

In terms of the difference between secondary and propagation probabilities, in the region of medium transfer fields ($\sim 6.75 - 7.75\,\text{V cm}^{-1}\,\text{mbar}^{-1}$) and for all values of ΔV_{GEM1}, the secondary and propagation probabilities are equal. Here, the propagation and secondary mechanisms are in an interplay. That is, a primary in GEM2 will release some amount of charge and photons, which can with some probability cause a discharge in GEM1. The release of the charge in GEM1 will in all cases, in this intermediate regime, trigger a secondary discharge. If no propagation proceeds, the secondary will not materialize.

4.6.6 The influence of the decoupling resistors on the time between primary and secondary discharges

An essential peculiarity of secondary discharges is their relatively long incidence time of up to several tens of microseconds.

Therefore, the following measurement was done toward understanding the time between primary and secondary discharges and how it is influenced by the decoupling resistors. This could convey information about the secondary discharge preparatory mechanism and the influence it feels when discharges are propagated through the gap.

Using the peak-finder algorithm the time between the occurrence of the primary discharge and the secondary discharge, abbreviated in the thesis as t_{12} is calculated with high precision.

The results for the four decoupling resistor cases are shown in Fig. 4.48.

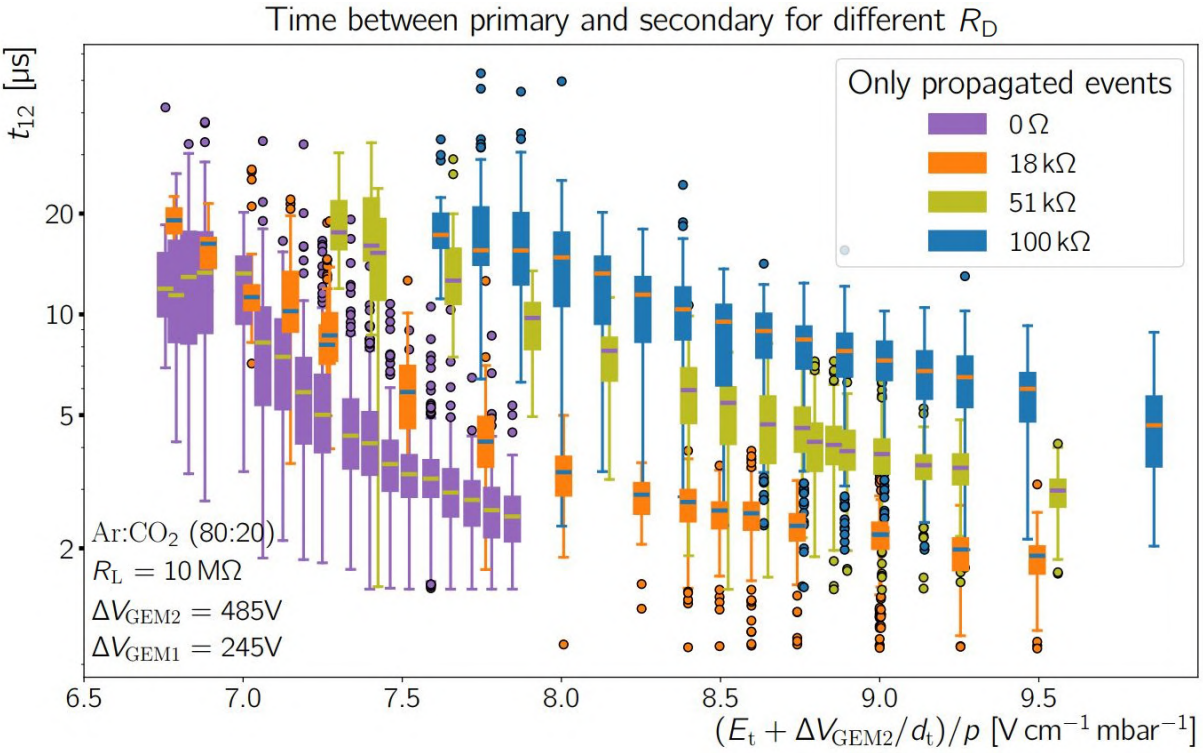

Figure 4.48: The time between primary and secondary discharges as a function of the transfer field for different decoupling resistor values. Only events where propagation occurred are shown, due to higher statistics. Taken before GEM malfunction.

The distributions of t_{12} for each transfer field value do not feature a prominent peak, but a smeared one, with a tail towards larger or smaller values. Therefore, to the normal mean value with standard deviation is not chosen, but instead a boxplot distribution is calculated to include all events at any given working point. On top, information on the variability or dispersion of data is kept and the representation takes less space, which is useful when comparing the four data sets.

Each colored box contains the t_{12} values between the 25th and 75th percentiles (denoting the likely range of variation; also called the interquartile range - IQR). Also featured inside each box is a central mark which indicates the median. The box therefore contains 50% of all the data.

The whiskers extend to the most extreme data points that are not considered outliers. The whiskers contain points that lie within 1.5× IQR range. For a large dataset, they add the other 24.64% on either side of the 50% of data.

The outliers fall outside the 1.5× IQR range and are plotted individually using small circles at their respective values. For a big set of data, they represent in total 0.7% of all data (0.35% on each side of the whiskers).

Fig. 4.48 shows that the mean t_{12} decreases exponentially with the increasing electric field in the transfer gap. This is valid irregardless of the presence or value of R_{D}.

A horizontal shift is present for increasing R_{D} value. At a given transfer field value, it is clear that a higher decoupling resistor hinders the mechanism that produces the secondary discharge in the gap, increasing the time it takes for the secondary to form.

Similar measurements done in [89] show that the median t_{12} decreases in a similar manner for inverted induction fields (i.e., the direction of the electric field is reversed; the charge carriers travel the opposite ways), indicating that to a first order only the strength of the electric field influences the secondary discharges and not the field direction. Even though these results were obtained in a one-GEM configuration, studying the induction field, a comparison can be made.

For the normal case studied here, the known carriers are studied. The electron drift velocity in the known mixtures used for the TPC is plotted in Fig. 4.49.

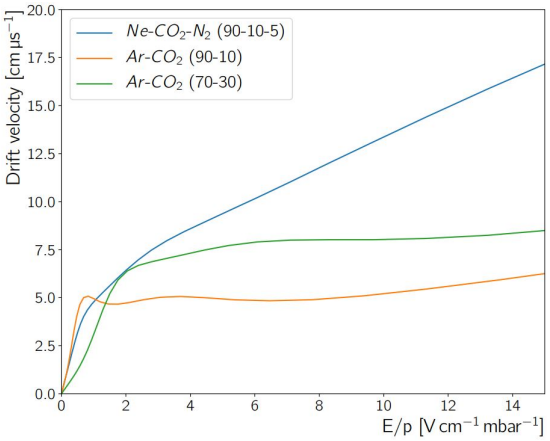

Figure 4.49: Magboltz [88] simulation of the electron drift velocity (done for SATP conditions) [89].

The electrons need about 0.03 µs to traverse the 2 mm transfer gap under the fields and gas conditions employed for this work. The times seen in Fig. 4.48 are very long compared to this. As such, the electrons from the initial discharge are not prone to cross the gap and start the discharge. On top, the potential configuration does not allow them to travel upward, since the field forces them to move towards the readout anode.

Ions on the other hand would be compatible with this scenario. Using the ion mobility values in [46] and for observed transfer field values where secondaries occur ($6-10\,\mathrm{V\,cm^{-1}\,mbar^{-1}}$), the time it would take ions to cross the 2 mm gap would be in the range of 10 and 20 µs.

However, the abrupt t_{12} decrease for relatively small E_t changes is larger (exponential) than the expected corresponding change of the ion drift time (linear). Moreover, previous results [89], [98] have shown that secondary discharges are observed for inverse fields as well, where ions would travel in the opposite direction of a secondary discharge. Similar

times were recorded. This rules out ions from the initial discharge crossing the gap as the cause for the formation of secondary discharges, leaving only a photon-mechanism accountable.

A further step was taken towards understanding if there is a difference between t_{12} for events with only propagation against events where no propagation occurred beforehand.

For this, large enough statistics are needed. Data was recorded using only one resistor $R_D = 18\,k\Omega$ on each GEM bottom electrode. For each working point 10 000 events were recorded and split into subsets with only propagation and without propagation before the secondary. The boxplot for this study is shown in Fig. 4.50.

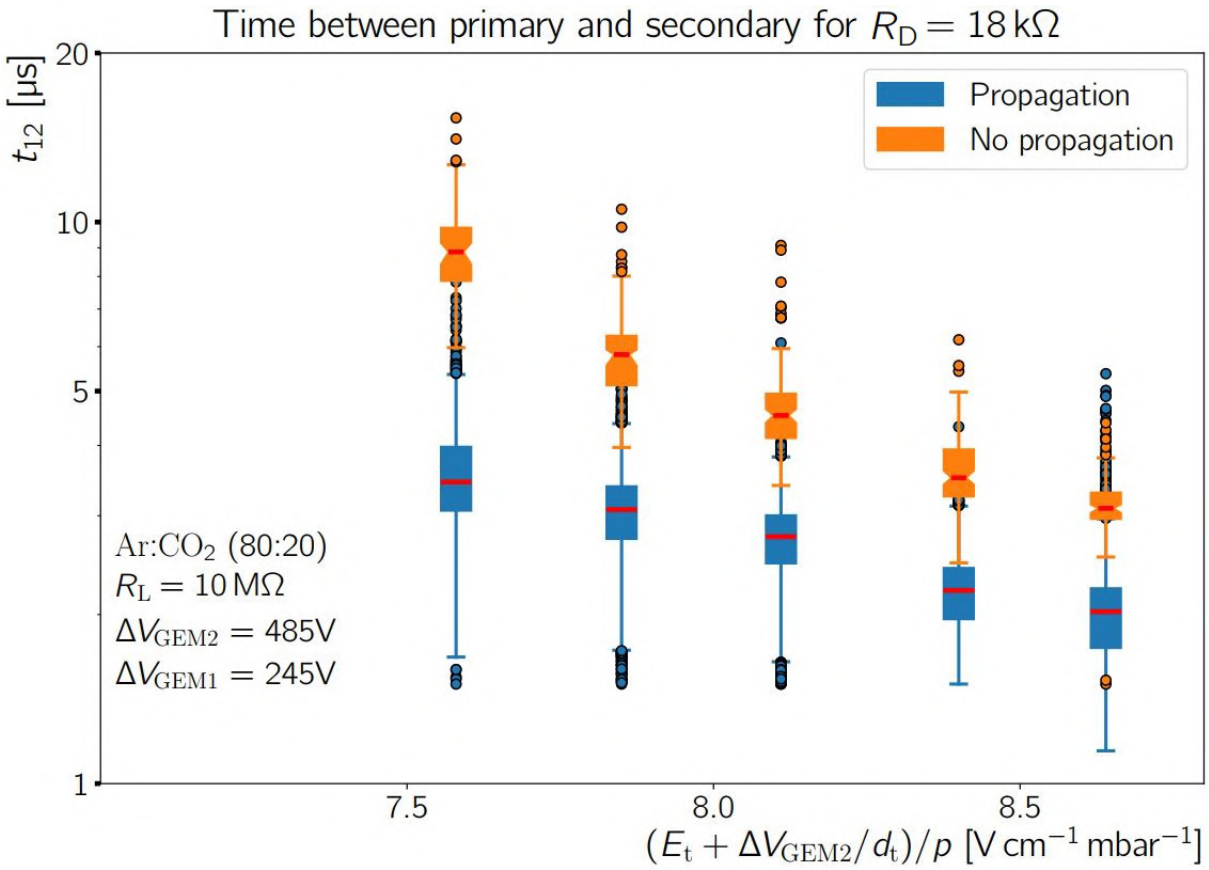

Figure 4.50: Time between primary and secondary discharges as a function of the modified transfer field, using a 18 kΩ decoupling resistor. Split into subevents with only propagation and without propagation to GEM1 before the occurrence of the secondary.

As seen before, the tendency of exponential decrease of t_{12} with increasing E_t is kept. The striking feature however is that propagated and non-propagated events are clearly separated.

When no propagation occurs, the secondary discharge can only be initiated from GEM2 and is evolving against the field direction. The preparatory mechanism for the ignition of secondary takes some few microseconds until it is able to produce the spark across the gap.

When propagation happens prior to the secondary, there is one additional source of charges and photons, which aid in generating the secondary discharge, namely GEM1. This secondary discharge can evolve in both directions. As such, the secondary develops faster than in the case where the primary did not propagate. Of most help here are the fast electrons produced in GEM1 after the induced discharge, which cross the gap. Even though they cross the gap fast and are collected at the electrodes, G1B also acts now (alongside G2T for the primary) as a thermionic source for charges crossing the gap and producing ionization and excitation.

4.7 Peculiar uncommon events. Late propagation?

Benefiting from the powerful smoothing algorithms MATLAB offers in its Signal Processing Toolbox, particular features may surface from the noisy signal. Throughout careful observation it was seen that the potential of G1T, in cases where propagation occurs from GEM2, does not immediately drop and that is suffers some delay, inconsistent with the theory of photons mediating the propagation, in which case a prompt discharge should be measured in both GEMs if propagation proceeds.

Thus far, to the best of author's knowledge, this type of behavior has not been reported elsewhere in the literature or in similar studies done with discharging GEMs.

There are two brief mentions of this delay not being observed. First one is in [128] using X-rays, where the authors conclude that no time delay was found with the accuracy of $\sim 10\,\text{ns}$. The other is in [102], with the same time resolution, states the discharges are simultaneous. The following results will disprove this claim.

The configuration for the detector operation was chosen with the aim of studying the propagation of discharges and understanding what causes it. The voltages increase toward more negative values with each electrode encountered going from the anode to the cathode. As such, the electric field points everywhere upward (i.e. from pad plane to the cathode).

In this field configuration electrons and ions follow the field lines. Electrons travel in the opposite direction the electric field points and ions will go along the direction of the electric field.

Electrons always travel downward, toward the pad, and are unable to go against the transfer field. Ions are able, but given their velocity, they require several microseconds to reach the upper GEM. Propagation has been seen to occur almost instantly, so they are also unable to help discharge the other GEM.

When propagation occurs, the only possible culprits are the photons released when the spark develops, which are released isotropically. Some will be able to travel to the upper GEM.

In about half of the cases for most of the the working points encountered in these studies, the propagation seems to occur after few hundred of nanoseconds.

A compilation of five superimposed events recorded on G1T potential that are encountered is shown in Fig. 4.51. The five events have been taken at very similar working points, so they can easily be compared.

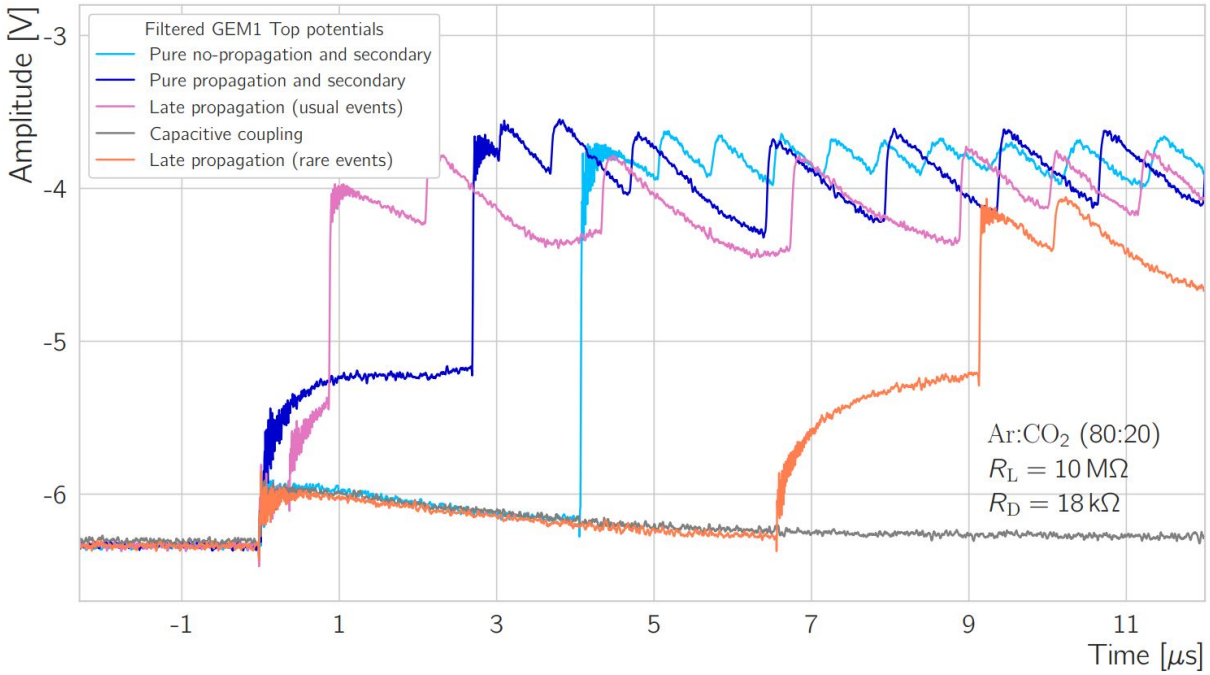

Figure 4.51: Five superimposed waveforms showing the peculiar behavior of late propagation. The orange curve was taken with different voltage settings.

The gray signal shows how G1T potential responds to a discharge in GEM2. The small jolt at $t = 0$ is due to GEM1 being capacitively coupled to the discharging GEM. The G1T potential drops slightly towards the ground value and regenerates rather quickly in about 7 µs.

The bright blue signal shows G1T potential during a GEM2 discharge, followed by a secondary discharge in the transfer gap at $t = 4$ µs. As previously explained, the capacitive coupling is present, in the form of the small jolt at $t = 0$. On the recovery path, the conditions to form a secondary discharge are met and the potential drops toward G2T.

The dark blue signal shows G1T potential during a discharge that propagated, quickly followed by a secondary event in the transfer gap. A discharge is induced in GEM2 and it instantly propagates and triggers a spark in GEM1. The G1T potential starts dropping toward G1B potential, following a curve dictated by the RC constant in the detector and probe circuits (see Appendix C). In ~ 1 µs it reaches a common plateau value it shares with G1B. After about 2.6 µs a secondary discharge occurs in the transfer gap, entailing the potential of G1T toward the lower GEM potential values.

These were the results one would expect from the behavior of discharges explained so far. The following two events show a new type of event, in which the propagation is delayed.

Depending on the working point, up to half of all events where propagation to GEM1 is achieved exhibit a slight delay, as can be seen in Fig. 4.51 (pink waveform) and further discussed in Fig. 4.52. For these events, the G1T filtered signal is used. The binning window is kept below 0.6 µs to accurately reproduce the two peaks with a relatively small bin count. The parameters used are the following: $\Delta V_{\text{ind}} = 200$ V, $\Delta V_{\text{GEM2}} = 480$ V, $\Delta V_{\text{transfer}} =$ variable, notation on the figure, $\Delta V_{\text{GEM1}} = 250$ V, $\Delta V_{\text{drift}} = 450$ V, pressure $\simeq 1000$ mbar.

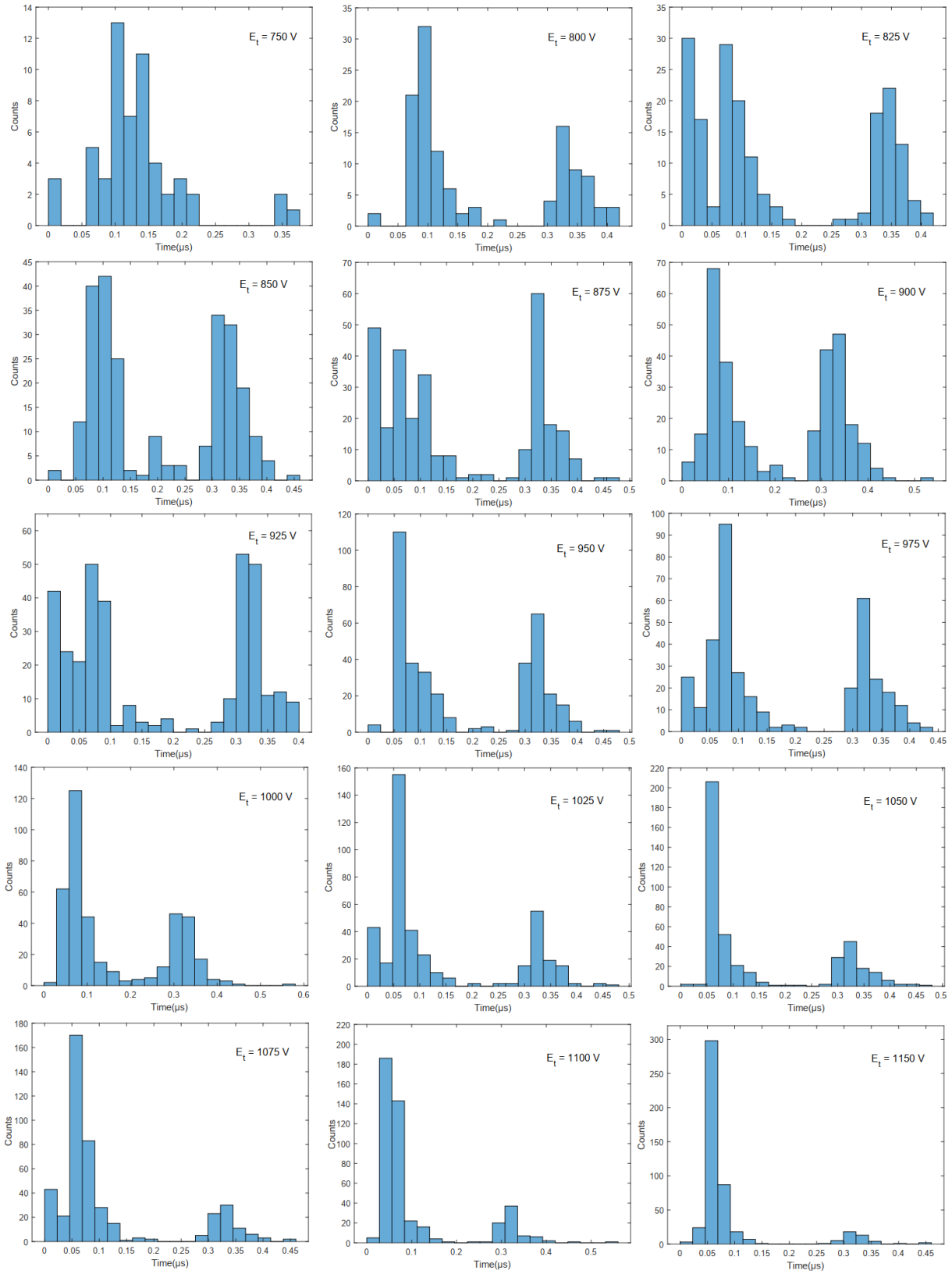

Figure 4.52: Time between the occurrence of the primary discharge and the discharging of GEM2, to which the discharge has propagated to.

The counts that form the peak around $t = 0.1\,\mu s$ come from pure, instant formation of the propagated discharge in GEM1. These 100 ns come from the trigger settings, i.e. from the threshold introduced to limit the noise when executing the peak detection scripts, alongside the RC nature of the probe's response (see Appendix C for an explanation). The events which form this peak are identical to the dark blue G1T signal shown in Fig. 4.51.

Starting with 750 V potential difference across the transfer gap (roughly corresponding to $6.15\,V\,cm^{-1}\,mbar^{-1}$ at normal temperature and pressure values), a second peak starts forming at later times. Employing a Gaussian mixture model on the histograms, reveals that this time is always around the value of ~ 330 ns and does not appear to be influenced by the transfer field.

It appears that in some cases there is a preparatory mechanism for the discharging of the upper GEM or that the propagation mechanism takes longer. This would exclude the direct ionization by photons in the GEM holes, which would occur instantaneously.

Sporadic events occur at later times (up to several µs), but they are rather rare.

The most striking of these late propagation events manifested after 6.6 µs and its G1T signal is also pictured in Fig. 4.51 (orange waveform). Since it so clearly shows the late propagation it is worth taking a look at and inspecting its features. The three channels, G1T, G2T and the pad plane probes responses are shown in Fig. 4.53.

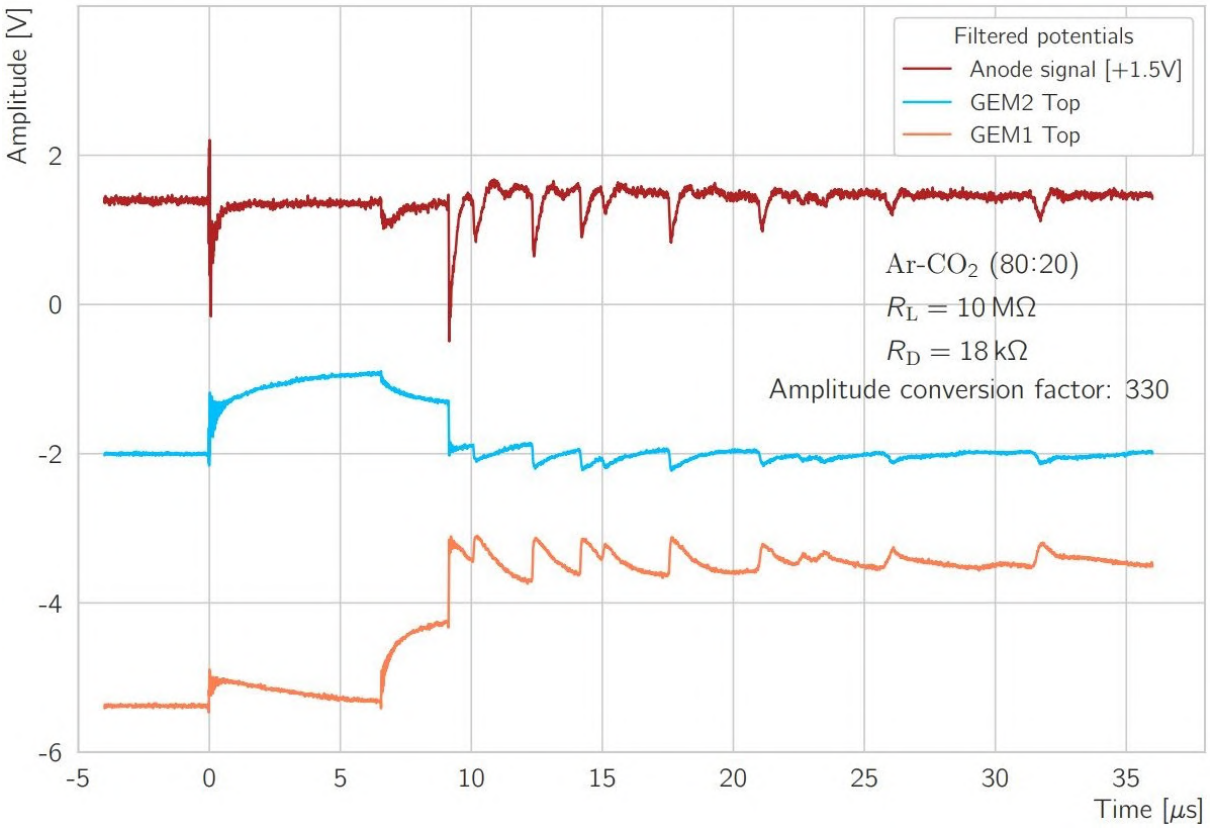

Figure 4.53: Delayed propagation event. GEM1 discharges due to propagation after 6.6 µs, followed by a secondary discharge in the transfer gap $\sim 2.6\,\mu s$.

After the induced discharge in GEM2 at $t = 0$, it can be seen that G2T potential drops toward lower negative potential, toward G2B value. At the same time, G1T potential *feels* the violent event and exhibits just the usual capacitive coupling, the signal recovering in about 5 µs.

At $t = 6.6$ µs, the drop of potential on the G1T electrode signals a discharge in the upper GEM. This occurs while GEM2 potential is quenched due to the previous discharge and the insufficient time to recover (in the order of µs $\ll 150$ µs). Looking at similar events at the same working point (see Fig. 4.51 dark blue signals), it is concluded that the GEM reached the plateau, indicating that G1T reached the common value it shares with G1B after the discharge.

The nature of the slow curve on G1T which occurs after propagation induces a discharge in the upper GEM is investigated with a signal generator and detailed in Appendix C. It was found out that it is due to the RC circuit and it has no gas physics nature.

The potential on G2T has a pick-up nature, since it increases toward higher negative high voltages, also supporting the idea of GEM1 discharging.

At about $t = 9.2$ µs after the original discharge, a secondary event follows because of the increased transfer field in the wake of the original primary discharge in GEM2, which shared its potential difference to the transfer field. Moreover, the extra charge produced in GEM1 when it discharged aids the development of the secondary. Consequently, several reignitions of the secondary are observed , probably due to a hot spot close to the discharging GEMs, which generates electrons from thermionic emission.

The anode signal shows the existence of charge carriers following the discharge in GEM1. The electrons induce a negative signal on the pad plane, clearly visible at $t \sim 6.6$ µs.

4.7.1 Mechanism proposed for delayed propagation of discharges

These results are the aim of further investigation. The results are unexpected and contradict brief mentions of this propagating behavior of discharges in [128] and [102].

If charges traversing the gap cannot be accounted for this behavior, due to either the wrong field direction (electrons) or due to slow drift velocity (ions), and photons ionizing the gas in the upper GEM holes due to their immediate reaction, the only possible explanation might be an interplay of these effects. An explanation is attempted using current knowledge.

At the time of the GEM2 initial primary discharge, the transition from avalanche to streamer and ultimately a spark generates a good amount of photons (the discharge is clearly visible). They travel instantly towards the upper GEM.

Once there, they will either enter the upper GEM holes and pass through, or undergo photoelectric effect at the interface with the metal side near the bottom GEM hole or with the kapton inside the GEM hole.

If the photons entered a GEM hole, they can either travel unhindered into the upper part (in the drift region) and ionize the atoms there, producing electrons, which then enter the holes and produce an avalanche or they can produce photoelectric effect with the kapton foil inside the GEM hole.

Either way, the resulting electrons will be funneled into the GEM hole almost instantly and find themselves into the high field region where they will be amplified. Combined with the already existent charge from the pre-amplification, a streamer can be produced with a certain probability. This mechanism is fast and can account for the events where the propagation happens instantly.

Another possibility is that these photons create photoelectrons at the interface with the metal surface, close to the GEM hole. The electrons that are produced close to the GEM hole on the bottom side, will follow the electric field lines, traveling out of the GEM.

Quickly (since they are created close to the GEM hole, the very high field of the GEM hole leaks to this regions) enough they gather enough energy to ionize. Once they attain a sufficient amount of energy, they ionize and produce ions.

The produced ions will feel the strong field of the nearby GEM hole, where they have been produced and will follow the field lines toward the GEM hole.

Using electric field simulations of the field present in the GEM holes, an estimation can be made about its intensity at the interface with the metal surface, close to the hole. Looking at the values shown in Fig. 4.18, at a distance of $\sim 40\,\mu\text{m}$ from the center of the GEM, and toward the metallic surface, a conservative value of the electric field is about $10\,\text{kV/cm}$ (the value is lower than the corresponding $20\,\text{kV/cm}$ shown in the plot, because the simulation shown there was done for a potential difference across the GEM of $\Delta V_{\text{GEM}} = 400\,\text{V}$, but in the case of propagation to the upper GEM under discussion here, GEM1 has a potential difference of $250\,\text{V}$).

The drift velocity of ions in gases as a function of the electric field is taken from [129] (see Appendix B). In the region of low to mild electric fields, the drift velocity is tangent to a line of slope 1, indicating a direct proportionality: $v \propto E/p$. At a value of $10\,\text{kV/cm}$ for IUPAC (SATP) conditions, the drift velocity of Ar ions is approximately $0.17\,\mu\text{m/ns}$.

The ions would need to travel from the metal surface, into the GEM hole, a few tens of µm until they are able to ionize the gas and produce the discharge. A conservative value of $50\,\mu\text{m}$ can be taken, from a point on the metal surface, close to a GEM hole, up to the high electric field region, where they create enough ionization to start the streamer.

It was proven in [99] and explained in Sec. 4.4 that the mechanism by which a GEM discharges is the fulfillment of a critical charge density inside one of the holes.

In order to traverse the $50\,\mu\text{m}$ at these speeds, the ions would need about $300\,\text{ns}$. This value is consistent with the delay seen in events where propagation is achieved.

Once the streamer is started, the speeds involved in its development are orders of magnitude higher, so for the purpose of this explanation, the spark will occur instantly once the charge threshold is achieved.

The value is consistent with very recent results in [46] of ion mobilities done at low electric fields with a similar two-GEM setup, where the authors state that *The time it takes one ion to cross GEM1 can be estimated to be lower than* $1\,\mu\text{s}$*, using conservative values for the mobility and the electric field inside the GEM hole (*$K = 1\,\text{cm}^2\,\text{V}^{-1}\,\text{s}^{-1}$*,* $E_{\text{GEM}} = 10\,\text{kV/cm}$*).*

If one would consider the mechanism of photoelectron production at the interface with the kapton or the metal to be accountable for the delayed propagation, there would be a probability at each point of these surfaces for an avalanche to be created. This probability

will start at the tip of the kapton foil, in the middle of the GEM hole, will continue until the bottom part, at the interface with the metal and start decreasing once we go far away on the surface of the metal from the GEM hole, since the field starts decreasing rapidly away from the rim.

Contrary to this belief, the histograms in Fig. 4.52 show that there is a *valley* separating the two peaks, where no or very little events are possible. There seems to be a physical region where photoelectons cannot start a discharge.

An explanation for the clear valley between the peaks can be the different mechanisms at play. The photons incident on the kapton extract an electron and this is immediately accelerated in the very high field of the hole, producing the avalanche and the discharge. The photons incident on the interface with the metal surface around the rim extract electrons from the metal, which need to gain some energy before ionization can occur. After that, the ion, in turn, needs to travel backwards, toward increasing electric field, gaining energy for ionization and ultimately initiating the avalanche and discharge.

In order to test these hypothesis, further tests need to be done.

5 Conclusion

The world's most powerful particle accelerator has gone quiet since the end of last year. The complex machine will be shut down for two years, in which a series of upgrades are envisioned.

After this LS, the second in the history of the Large Hadron Collider, an improved, more powerful instrument will emerge, by virtue of a range of enhancements. The energy will finally reach the 14 TeV regime the initial design promised.

To cope with the upgraded accelerator complex, its detectors will require a series of maintenance and upgrade activities. For some of the detection systems a complete overhaul is foreseen. New and improved detection technologies are available and are embraced.

The ALICE detector, one of the four detection giants at the LHC, houses a unique network of hardware, particularly built to study the conditions of matter moments after the Big Bang. For ALICE, the technical break is an occasion to upgrade or replace subdetectors, as well as systems used for triggering and data-acquisition.

The goal for ALICE in the next physics run is to accumulate, for Pb-Pb collisions at $\sqrt{s_{\mathrm{NN}}} = 5.5\,\mathrm{TeV}$, an integrated luminosity exceeding $10\,\mathrm{nb}^{-1}$. The upgrade of the detector readout systems will allow to record the interactions with a minimum bias trigger, up to a rate of 50 kHz, representing an increase in the data sample by two orders of magnitude. ALICE benefits from such a statistics increase to study rare phenomena of the Quark Gluon Plasma, the peculiar state of matter prevailing in the first moments the Universe came to life.

At the heart of ALICE lies the TPC – a $88\,\mathrm{m}^3$ gas giant, providing the needed tracking and identification of charge particles passing its sensitive volume. These particles emanate from the interaction point, ionizing the gas atoms and leaving a trace of electrons behind as an indication of their passing.

As a consequence of electric field present, mixed with a strong magnetic field throughout the detector volume, these electrons will drift towards the two endcaps of the TPC cylinder. Although they contain the necessary information about the nature of the particles that have just flown, they are too few to be properly recorded. They are multiplied by wire chambers, read-out and their signal is processed.

To be able to exploit the increased interaction rate in the next runs of data taking, the wire chambers need replacing. The most suitable candidate for this task was found to be the Gas Electron Multiplier (GEM) technology. A GEM is a thin foil of polyimide interposed between two metal layes connected to high voltage and pierced by a regular matrix of holes, where each hole acts as a multiplication region for the incoming electrons.

The final readout design of the ALICE TPC will feature a quadruple GEM stack to gradually increase the resulting charge and ensure a proper signal.

To safeguard a long-term operation of the detector system in the environment of high-

rate, high-multiplicity that ALICE faces, it is imperative to ensure proper functioning of the enclosed detectors. GEMs in particular are sensitive structures, prone to damage.

One of the biggest threats they face comes in the form of electrical discharges that can not only degrade performance and cause inefficiencies, but can affect the integrity of the GEMs themselves. They can prompt irreversible damage to the readout electronics and the detector, leaving it blind and therefore losing acceptance.

Once operation starts, it will be impossible to undertake any repairs for the entire span of the next physics timeline, stretching about 10 years after the LS 2. Therefore it is essential to understand the occurrence of discharges and find ways of mitigating them.

This work was focused on understanding the nature of these discharges and how to limit their damage.

To achieve this, a small prototype setup featuring two $10 \times 10\,\mathrm{cm}^2$ GEM foils, similar to the ones used for the TPC upgrade, is used to shed light into the peculiar nature of GEM discharges by inducing sparks into the detector structures by proper choice of high voltage settings.

Two different types of discharges were studied. A so called *primary* discharge can occur inside the holes of a GEM, across its two electrodes, if a certain amount of charge is created upon amplification. The second type is the *secondary* discharge, a rupture of gas rigidity developing in the gaps between GEMs or between the last GEM in the stack and the pad plane.

So far, the secondary discharges were studied carefully and thought to have been independent on any other physical mechanism, apart from the primary discharge which must occur before. This was found to not be entirely true.

A discharge materializing in one GEM can propagate to other GEMs by means of photons resulting in the wake of the initial discharge. They are able to ionize the gas around the holes of other GEMs and quickly trigger a spark in the hole, if the potential difference across the two electrodes of the GEM is close to the primary discharge threshold value.

This discharge propagation was found to heavily influence the secondary discharge probability. There is an interplay between the effects of the two reactions and it was shown that the mitigation of the propagation probability can help reduce the occurrence of the secondary discharges.

The propagation (and therefore the secondary) probability was demonstrated to be reduced and pushed to lower electric fields by the use of *decoupling resistors* on the bottom GEM electrode, alongside the normal loading resistors used on the top side.

Moreover, additional capacitive load on the GEM (parasitic capacitances, cable length, etc.) was found to influence the propagation probability.

Throughout the research done on the propagating nature of discharges, it was discovered that the propagation cannot be due to photons alone, since uncommon events exhibiting delayed propagation in the order of hundreds of nanoseconds were encountered.

These recent findings have not been observed in similar works and are the subject of intense research.

In the long run, the occurrence of discharges cannot be avoided. Previous works have found that an estimated number of around 650 discharges for the whole TPC per month of Pb-Pb at 50 kHz are to be expected, with smaller numbers for p-p runs.

Nevertheless, this and similar studies have helped in gaining a better understanding on the occurrence and consequences of electrical discharges in GEM detectors. Using this knowledge, safeguards can be implemented and the settings can be tuned in order to limit the damages envisioned.

Appendices

Appendix A : GEM recovery

After the first four resistor runs, GEM2 malfunctioned, showing a permanent high current from one channel to another, indicative of a short-circuit across its two sides.

The GEM was recovered successfully by instantaneously applying 600 V in air, in a clean room. It had to be taken out of the stack, to avoid short-circuiting the other elements when recovering. When installing back, a dedicated test was done to check if it is behaving as expected.

The same quantities as described in the thesis were checked and plotted.

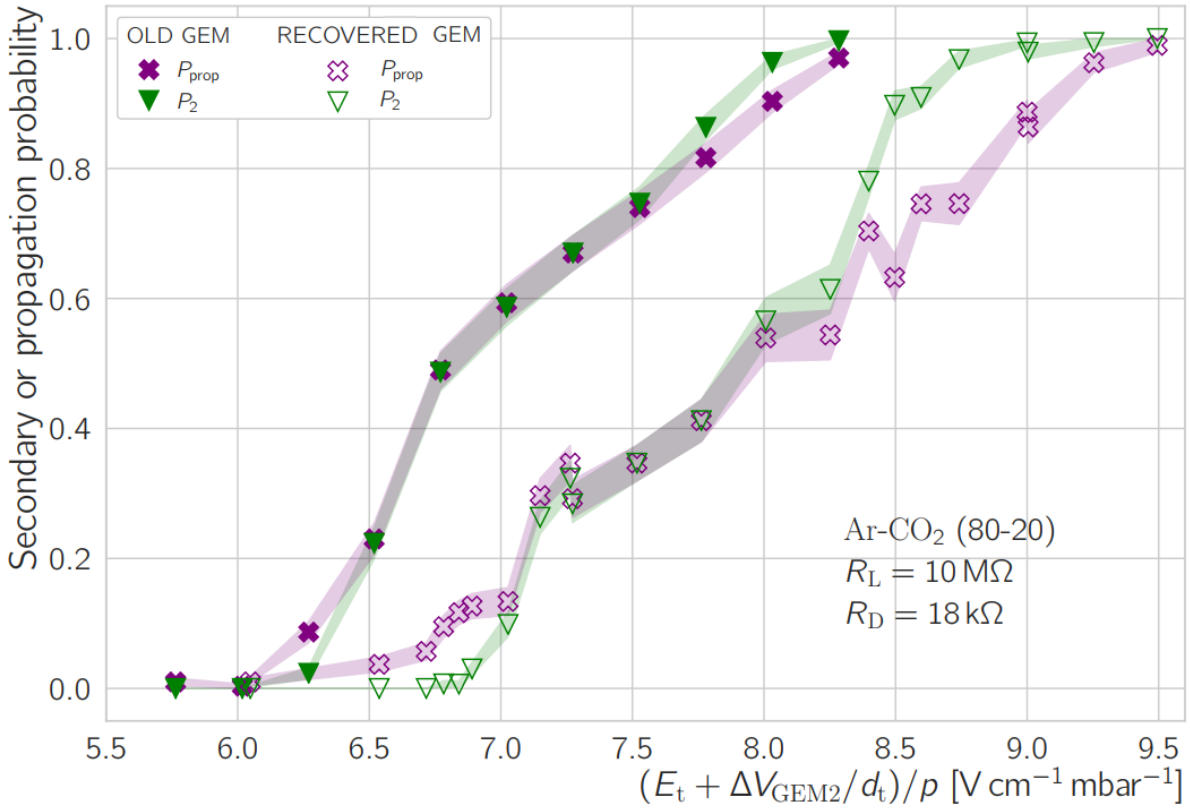

Figure A.1: P_2 and P_{prop} before and after recovering GEM2.

In Fig. A.1 the first two quantities under investigation in the thesis, P_2 and P_{prop}, are plotted both before (full symbols) and after (empty symbols) recovering the GEM. The shaded area represents a fill between the top and bottom of the error bar on each point, chosen not to load the figure too much (details in Appendix D).

It can be seen that a shift is present in between the old and new results. The features are still present. The curves show the same linear behavior, and an interplay between the two is seen in the interesting regime of medium transfer field strengths. The P_2 does a slight undershoot at low transfer fields and a slight overshoot close to 100% in both cases.

The offset is toward lower transfer fields. A mean shift was calculated to be about $0.7\,\mathrm{V\,cm^{-1}\,mbar^{-1}}$. The shift appears to be due to physical displacement of the GEM foil closer to the other one.

The second quantity to check was the secondary events with and without propagation to GEM1. They are shown in Fig. A.2.

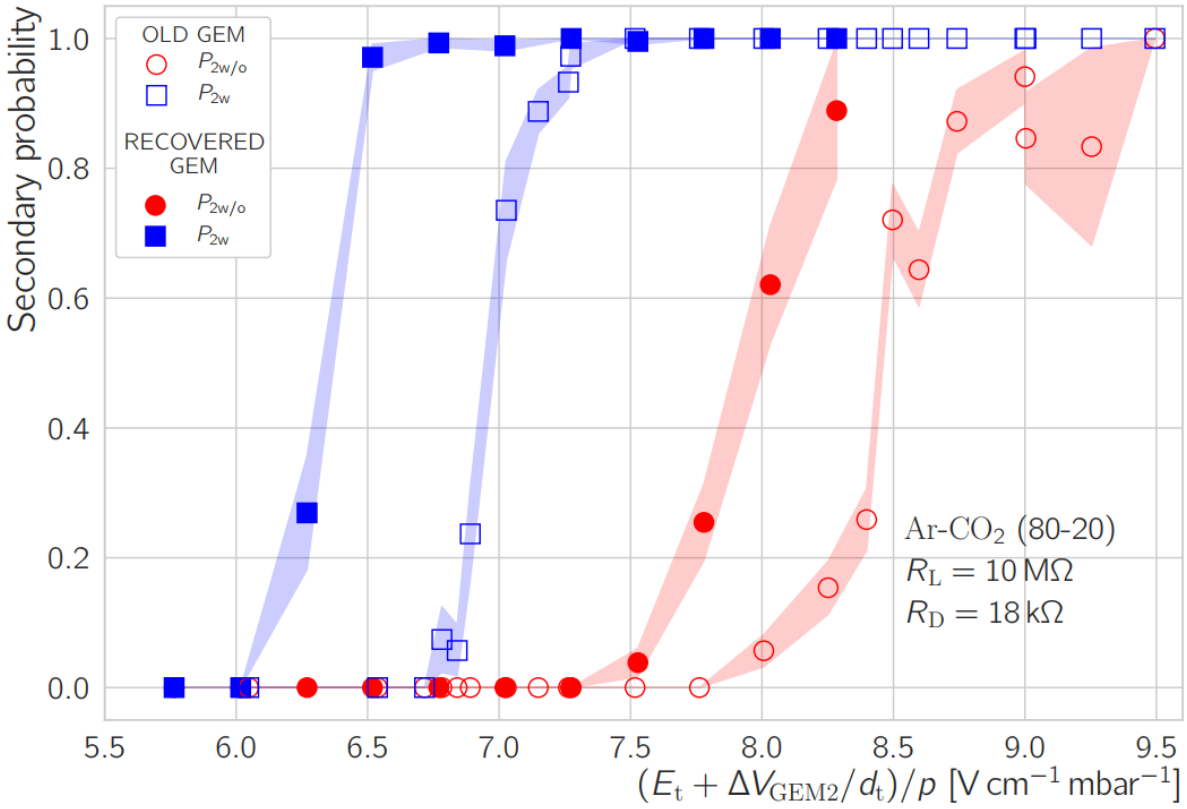

Figure A.2: Secondary probability for events with and without propagation to GEM1. Events recorded before and after recovering GEM2.

The same shift toward lower transfer field is also present here, confirming that the shift is physical in nature and that the distances have been very slightly changed. Such shifts were expected from previous works, as explained in the text.

The shift is also approximated within the errorbars to be close to $0.7\,\mathrm{V\,cm^{-1}\,mbar^{-1}}$ for both cases.

Appendix B : Drift velocity of ions

Ion mobilities for low electric fields for TPC mixtures are detailed in [46]. For high electric fields, further explanations are given in [129].

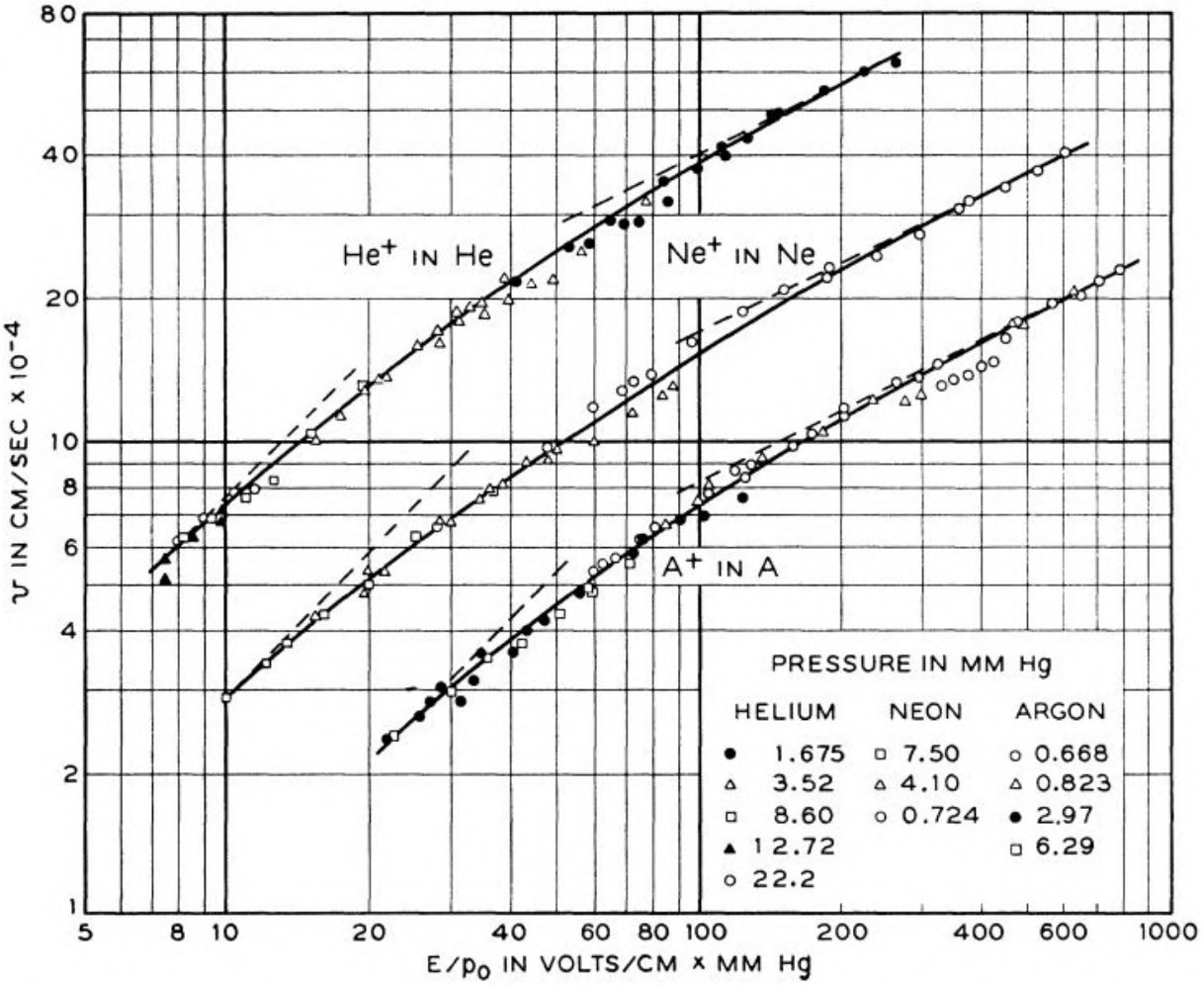

Figure B.1: The drift velocity of atomic ions as a function of E/p. Taken from [129].

Appendix C : Charging curve

Waveforms of events with a discharge exhibit a slow rise time (see Fig. C.1). In case of the upper GEM top electrode, after an event occurred and the propagation induced a discharge in one of GEM1 holes, it takes about 1 µs for the G1T potential to drop to a plateau it shares with G1B, signaling the discharge of the GEM.

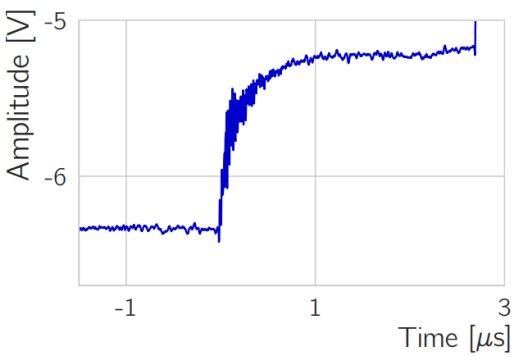

Figure C.1: Typical G1T signal after discharging due to propagation.

To ascertain whether a physical mechanism is behind the slow increase of the signal, as seen by G1T probe (see Fig. 4.51), the probes are fed a square wave by a signal generator. The frequency of the wave is set to 200 kHz, the amplitude is set to 4 Vpp (volt-peak-to-peak).

The probe response is scaled to the generated signal and the two are superimposed. The result is shown in Fig. C.2.

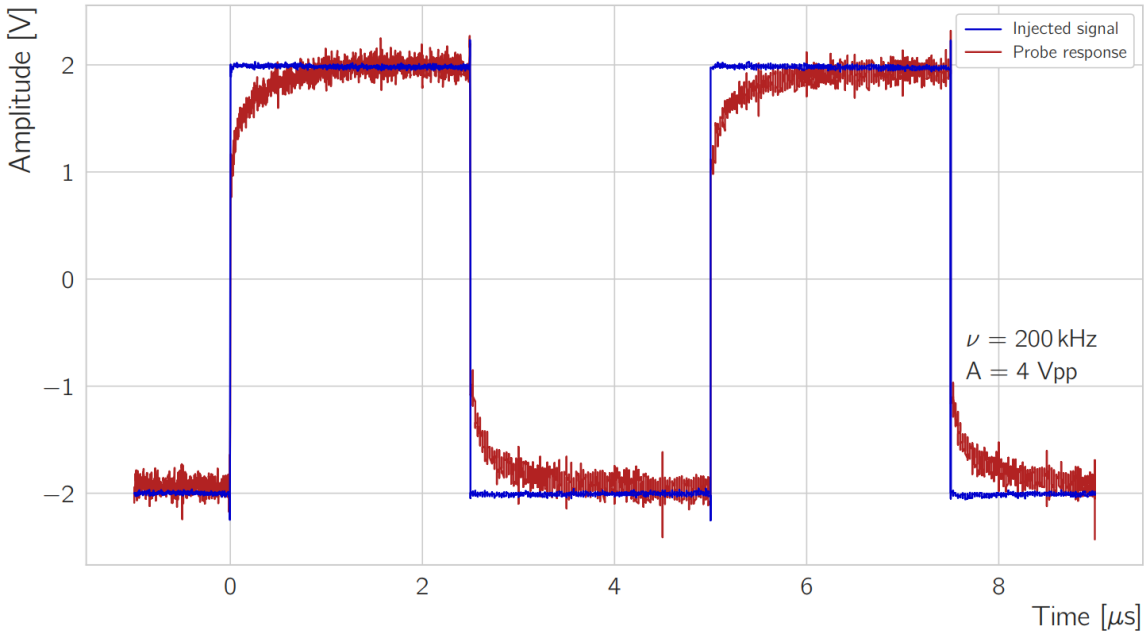

Figure C.2: HV probe response (scaled) to a generated square wave.

It can be easily seen that the response time of the probe has some delay. Both the rise and fall time reach the desired level in ~ 1 µs. This shows that the probe response is an artifact of the probe's construction and the RC circuit therein.

Appendix D : Binomial distribution

Since a secondary discharge is a binary event (it can either occur after a primary or not), the probability to observe such an event, given the prior occurrence of a primary discharge, can be described by a binominal distribution.

The variance of such a distribution is of interest. Its value can be found in the literature [130]. Applied to the events of interest, it can be written as:

$$\mathrm{var(X)} = \frac{P_2(1-P_2)}{N_{\mathrm{events}}}$$

where P_2 is the secondary probability and N_{events} is the total number of events at the working point under discussion. The standard error is nothing more than the square root of the variance:

$$\sigma = \sqrt{\frac{P_2(1-P_2)}{N_{\mathrm{events}}}}$$

With a large enough number of waveforms, the error will be in the percent level.

Shaded region representation

The shaded area for most of the plots in Sec. 4.6 is an visual guide for the uncertainties contained within the figure.

For each point in the graph, the standard error is calculated with the formulas above. The upper limits (the value of each of the points + their respective error) are linked with a line. The same is done with the lower limits (the value of each of the points - their respective error). The area between the two lines is shaded with the same color the points have, but with a lower saturation.

Appendix E : Commissioning of the GEM detector

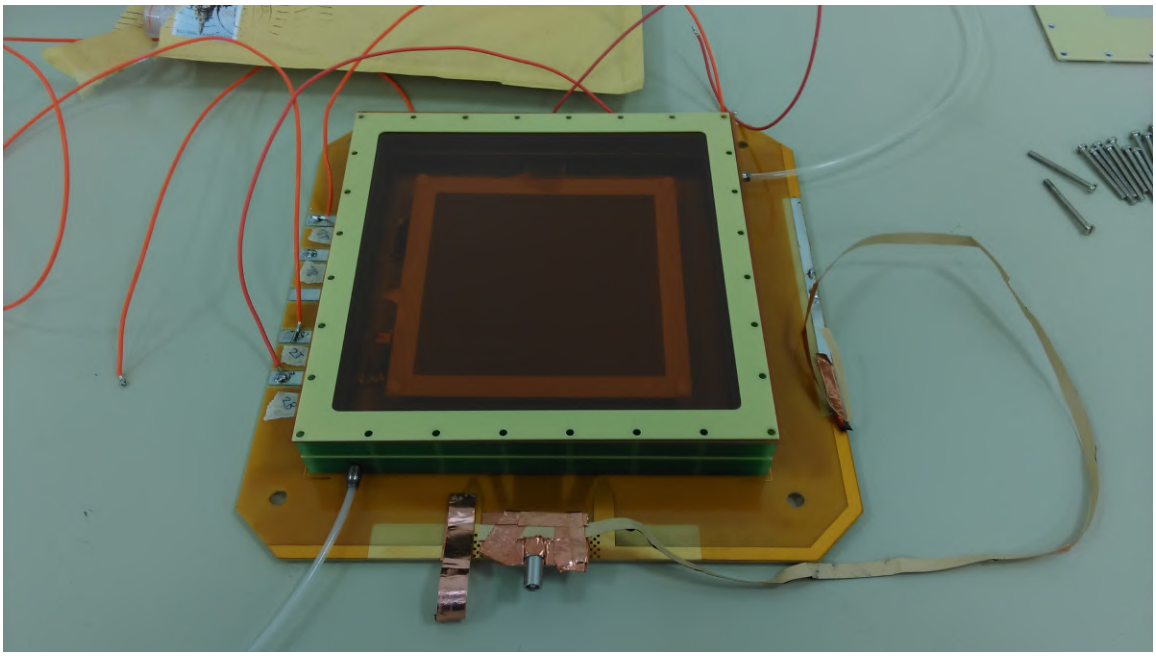

Figure E.1: Picture taken during the commissioning of the GEM detector. Here, the two GEMs have been stacked on top of the readout pads. The gas box frame can be seen surrounding the detector. The Panasonic connector and the connections to the GEM electrodes were installed for testing purposes.

Appendix F : Heatmap of pure secondaries (no propagated events)

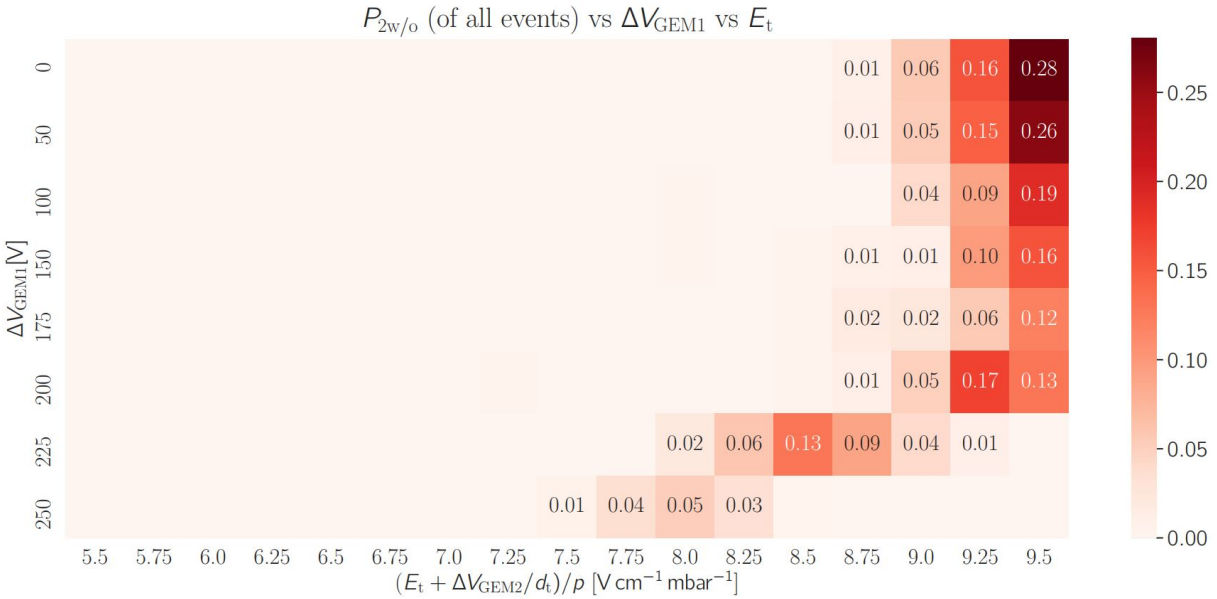

Figure F.1: Heatmap of events containing a secondary discharge, but no propagation.

It can be seen that a ridge forms at high transfer field field values, where the secondary probability dominates. It is more pronounced at low ΔV_{GEM1} values, where propagation is highly unlikely. Here, the onset of secondaries is around $9.75\,\mathrm{V\,cm^{-1}\,mbar^{-1}}$. Measurements were not performed here, since operating the detector at these high potential differences could result in serious damage to the GEM structure.

The ridge veers toward lower transfer field values when the potential difference across GEM1 increases, signaling that the secondary can start from both the upper and the lower GEM. Here, ions from the primary discharge, as well as electrons from the propagated discharge in GEM1, start creating both an anode-directed and a cathode-directed streamer.

A proof toward this claim is shown in Fig. 4.50, with explanations therein.

Bibliography

[1] Zachary Weinersmith. *Science: Abridged Beyond the Point of Usefulness*. 2017. URL: http://theweinerworks.com/.

[2] Mark Thomson. *Modern particle physics*. New York: Cambridge University Press, 2013. URL: http://www-spires.fnal.gov/spires/find/books/www?cl=QC793.2.T46::2013.

[3] Wikimedia Commons. *Elementary particle interactions*. 2007. URL: https://en.wikipedia.org/wiki/File:Elementary_particle_interactions.svg.

[4] M. Tanabashi et al. "Review of Particle Physics". In: *Phys. Rev. D* 98 (3 2018), p. 030001. DOI: 10.1103/PhysRevD.98.030001. URL: https://link.aps.org/doi/10.1103/PhysRevD.98.030001.

[5] Lawrence Lee et al. "Collider searches for long-lived particles beyond the Standard Model". In: *Progress in Particle and Nuclear Physics* 106 (2019), pp. 210 –255. DOI: https://doi.org/10.1016/j.ppnp.2019.02.006. URL: http://www.sciencedirect.com/science/article/pii/S0146641019300109.

[6] "Bubble chamber: colour enhanced tracks". 1998. URL: https://cds.cern.ch/record/39312.

[7] Chris Baraniuk. "How do we know that things are really made of atoms?" In: *BBC story* (20 Nov 2015). URL: http://www.bbc.com/earth/story/20151120-how-do-we-know-that-things-are-really-made-of-atoms.

[8] Sergio Cittolin. "Drawings of the elements of CMS detector, in the style of Leonardo da Vinci. Dessins des éléments de CMS détecteur, dans le style de Leonardo da Vinci". CMS Collection. 2014. URL: https://cds.cern.ch/record/1157741.

[9] Matt Strassler. *Of Particular Significance — Conversations About Science with Theoretical Physicist Matt Strassler*. personal blog, 2011. URL: https://profmattstrassler.com/.

[10] Collier Paul. "The technical challenges of the Large Hadron Collider". In: *Phil. Trans. R. Soc. A* 373 (2015). DOI: http://doi.org/10.1098/rsta.2014.0044.

[11] Julie Haffner. "The CERN accelerator complex. Complexe des accélérateurs du CERN". In: (2013). General Photo. URL: https://cds.cern.ch/record/1621894.

[12] Jordi Boixader et al. "ALICE and the Soup of Quarks and Gluons : cartoon on the ALICE experiment, the detector and the physics". 2004. URL: https://cds.cern.ch/record/1456256.

[13] A. Pich. "Quantum chromodynamics". In: *High energy physics. Proceedings, 2nd European School, Sorrento, Italy, August 29-September 1, 1994. Vol. 1, 2*. 1995, pp. 157–207. arXiv: hep-ph/9505231 [hep-ph].

[14] K. Nishijima. "BRS invariance, asymptotic freedom and color confinement (a review)". In: *Czechoslovak Journal of Physics* 46.1 (1996), pp. 1–40. DOI: 10.1007/BF01692238. URL: https://doi.org/10.1007/BF01692238.

[15] Tristan Hübsch. *Advanced Concepts in Particle and Field Theory*. Cambridge University Press, 2015. DOI: 10.1017/CBO9781316160725.

[16] Christian Klein-Bösing. *Study of the Quark-Gluon Plasma with Hard and Electromagnetic Probes*. 2013. URL: https://www.uni-muenster.de/imperia/md/content/physik_kp/agwessels/thesis_db/ag_wessels/klein-boesing_c_2013_habilitation.pdf.

[17] Alexandre Deur, Stanley J. Brodsky, and Guy F. de Teramond. "The QCD Running Coupling". In: *Prog. Part. Nucl. Phys.* 90 (2016), pp. 1–74. DOI: 10.1016/j.ppnp.2016.04.003. arXiv: 1604.08082 [hep-ph].

[18] A. Blumenfeld and M. Moshe. "Renormalization-scheme dependence of the strong coupling constant in quantum chromodynamics". In: *Phys. Rev. D* 26 (3 1982), pp. 648–657. DOI: 10.1103/PhysRevD.26.648. URL: https://link.aps.org/doi/10.1103/PhysRevD.26.648.

[19] Frank Wilczek. "Asymptotic freedom". In: 1996. arXiv: hep-th/9609099 [hep-th].

[20] Rajan Gupta. "Introduction to lattice QCD: Course". In: *Probing the standard model of particle interactions. Proceedings, Summer School in Theoretical Physics, NATO Advanced Study Institute, 68th session, Les Houches, France, July 28-September 5, 1997. Pt. 1, 2*. 1997, pp. 83–219. arXiv: hep-lat/9807028 [hep-lat].

[21] Peter Braun-Munzinger and Johanna Stachel. "The quest for the quark-gluon plasma". In: *Nature* 448 (2007), pp. 302–309. DOI: 10.1038/nature06080.

[22] Gordon Baym et al. "From hadrons to quarks in neutron stars: a review". In: *Rept. Prog. Phys.* 81.5 (2018), p. 056902. DOI: 10.1088/1361-6633/aaae14. arXiv: 1707.04966 [astro-ph.HE].

[23] A. Bazavov et al. "Chiral and deconfinement aspects of the QCD transition". In: *Phys. Rev. D* 85 (5 2012), p. 054503. DOI: 10.1103/PhysRevD.85.054503. URL: https://link.aps.org/doi/10.1103/PhysRevD.85.054503.

[24] Christopher J. Plumberg, Thomas Welle, and Joseph I. Kapusta. "QCD matter with a crossover and a first-order phase transition". In: *18th Hellenic School and Workshops on Elementary Particle Physics and Gravity (CORFU2018) Corfu, Corfu, Greece, August 31-September 28, 2018*. 2018. arXiv: 1812.01684 [nucl-th].

[25] Anton Andronic et al. "Decoding the phase structure of QCD via particle production at high energy". In: *Nature* 561.7723 (2018), pp. 321–330. DOI: 10.1038/s41586-018-0491-6. arXiv: 1710.09425 [nucl-th].

[26] Mateusz Ploskon. "Heavy-ion collisions - hot QCD in a lab". In: *14th International Workshop on Hadron Physics (Hadron Physics 2018) Florianopolis, Santa Catarina, Brazil, March 18-23, 2018*. 2018. arXiv: 1808.01411 [hep-ex].

[27] Tapan K Nayak. "Heavy Ions: Results from the Large Hadron Collider". In: *Pramana* 79.arXiv:1201.4264 (2012). Comments: Proceedings of Lepton-Photon 2011 Conference, to be published in Pramana, Journal of Physics. 15 pages, 719–735. 15 p. URL: https://cds.cern.ch/record/1418314.

[28] Fu-Ming Liu and Sheng-Xu Liu. "Quark-gluon plasma formation time and direct photons from heavy ion collisions". In: *Phys. Rev. C* 89 (3 2014), p. 034906. DOI: 10.1103/PhysRevC.89.034906. URL: https://link.aps.org/doi/10.1103/PhysRevC.89.034906.

[29] Edmond Iancu. "QCD in heavy ion collisions". In: *Proceedings, 2011 European School of High-Energy Physics (ESHEP 2011): Cheile Gradistei, Romania, September 7-20, 2011*. 2014, pp. 197–266. DOI: 10.5170/CERN-2014-003.197. arXiv: 1205.0579 [hep-ph].

[30] P. Braun-Munzinger, J. Stachel, and Christof Wetterich. "Chemical freeze-out and the QCD phase transition temperature". In: *Physics Letters B* 596.1 (2004), pp. 61 –69. DOI: https://doi.org/10.1016/j.physletb.2004.05.081. URL: http://www.sciencedirect.com/science/article/pii/S0370269304008822.

[31] Antonin MAIRE. "ALICE et la physique des ions lourds Conseil Scientifique In2p3 2018". 2018. URL: http://old.in2p3.fr/actions/conseils_scientifiques/media/2018_fevrier/Presentations/3_Conf-2018-ConseilSciIn2p3-PhysHad_ronique-ALICE-Presentation-8fev2018_new.pdf.

[32] Panagiota Foka and Małgorzata Anna Janik. "An overview of experimental results from ultra-relativistic heavy-ion collisions at the CERN LHC: Hard probes. An overview of experimental results from ultra-relativistic heavy-ion collisions at the CERN LHC: hard probes". In: *Rev. Phys.* 1.arXiv:1702.07231 (2017). Invited review paper, 18 pages, 172–194. 23 p. URL: https://cds.cern.ch/record/2271314.

[33] K. Reygers. "Hard Scattering, Jets and Jet Quenching". 2017. URL: https://www.physi.uni-heidelberg.de/~reygers/lectures/2017/qgp/qgp_ss17_08_jet_quenching.pdf.

[34] K Aamodt et al. "The ALICE experiment at the CERN LHC. A Large Ion Collider Experiment". In: *JINST* 3 (2008). Also published by CERN Geneva in 2010, S08002. 259 p. DOI: 10.1088/1748-0221/3/08/S08002. URL: http://cds.cern.ch/record/1129812.

[35] Steffen Georg Weber and Anton Andronic. "ALICE event display of a Pb-Pb collision at 2.76A TeV". General Photo. 2015. URL: https://cds.cern.ch/record/2032743.

[36] B Alessandro et al. *ALICE: Physics Performance Report. ALICE physics performance : Technical Design Report*. Ed. by B Alessandro. Vol. 32. Technical Design Report ALICE. revised version submitted on 2006-05-29 15:15:40. Geneva: CERN, 2005. DOI: 10.1088/0954-3899/32/10/001. URL: https://cds.cern.ch/record/879894.

[37] Elena Botta. "Particle identification performance at ALICE". In: *5th Large Hadron Collider Physics Conference (LHCP 2017) Shanghai, China, May 15-20, 2017*. 2017. arXiv: 1709.00288 [nucl-ex].

[38] Arturo Tauro. "ALICE Schematics". General Photo. 2017. URL: http://cds.cern.ch/record/2263642.

[39] Friederike Bock. *Neutral Pion and Eta Meson Production in pp and Pb–Pb Collisions at the LHC with the ALICE Detector*. Master Thesis, Physikalisches Institut at the University of Heidelberg. An optional note. 2012.

[40] Harald Appelshauser et al. "Space-charge distortion measurements and their calibration in the ALICE TPC". 2016. URL: https://indico.cern.ch/event/587756/attachments/1370525/2078384/TPC_distortions_summary_Nov_11.pdf.

[41] G Dellacasa et al. *ALICE time projection chamber: Technical Design Report*. Technical Design Report ALICE. Geneva: CERN, 2000. URL: http://cds.cern.ch/record/451098.

[42] J. Alme et al. "The ALICE TPC, a large 3-dimensional tracking device with fast readout for ultra-high multiplicity events". In: *Nuclear Instruments and Methods in Physics Research Section A: Accelerators, Spectrometers, Detectors and Associated Equipment* 622.1 (2010), pp. 316 –367. DOI: https://doi.org/10.1016/j.nima.2010.04.042. URL: http://www.sciencedirect.com/science/article/pii/S0168900210008910.

[43] "First results of the ALICE detector performance at 13 TeV". In: (2015). URL: https://cds.cern.ch/record/2047855.

[44] Claus Grupen and Boris Shwartz. *Particle Detectors*. Cambridge Monographs on Particle Physics, Nuclear Physics and Cosmology. Cambridge University Press, 2008.

[45] Rob Veenhof. "Choosing a gas mixture for the ALICE TPC". In: (2003).

[46] Alexander Deisting, Chilo Garabatos, and Alexander Szabo. "Ion mobility measurements in $Ar - CO_2$, $Ne - CO_2$, and $Ne - CO_2 - N_2$ mixtures, and the effect of water contents". In: *Nucl. Instrum. Meth.* A904 (2018), pp. 1–8. DOI: 10.1016/j.nima.2018.07.008. arXiv: 1804.10288 [physics.ins-det].

[47] Ernst Hellbar. "Ion Movement and Space-Charge Distortions in the ALICE TPC". In: (2015). URL: https://www.uni-frankfurt.de/59428504/Hellbaer-Masterarbeit.pdf.

[48] Erika Garutti. "Particle detector lectures". In: (2012). URL: http://www.desy.de/~garutti/LECTURES/ParticleDetectorSS12/L4_gasDetectors.pdf.

[49] Christian Lippmann. "Performance of the ALICE Time Projection Chamber". In: *Physics Procedia* 37 (2012). Proceedings of the 2nd International Conference on Technology and Instrumentation in Particle Physics (TIPP 2011), pp. 434 –441. DOI: https://doi.org/10.1016/j.phpro.2012.02.390. URL: http://www.sciencedirect.com/science/article/pii/S187538921201721X.

[50] J. Wiechula. "ALICE-TPC upgrade with GEMs". In: *5th HIC for FAIR Physics* (2015). URL: https://indico.gsi.de/event/3472/.

[51] Fabio Sauli. "Principles of operation of multiwire proportional and drift chambers". In: CERN, Geneva, 1975 - 1976. CERN. Geneva: CERN, 1977, 92 p. DOI: 10.5170/CERN-1977-009. URL: https://cds.cern.ch/record/117989.

[52] Fabio Sauli. "Principles of operation of multiwire proportional and drift chambers". In: CERN, Geneva, 1975 - 1976. CERN. Geneva: CERN, 1977, 92 p. DOI: 10.5170/CERN-1977-009. URL: https://cds.cern.ch/record/117989.

[53] Andreas Gareis. "Studies of Electron Avalanches in the Vicinity of an Anode Wire with Pad- and Pixel-Readout". PhD thesis. Universität Bonn, Physikalisches Institut, 2012. URL: https://www.lhc-ilc.physik.uni-bonn.de/ergebnisse/dateien/t00000031.pdf.

[54] J Wiechula and for the ALICE TPC Collaboration. "Commissioning and Calibration of the ALICE TPC". In: *Nuclear Physics A* 830 (July 2009). DOI: 10.1016/j.nuclphysa.2009.10.046.

[55] S. Rossegger and W. Riegler. "Signal shapes in a TPC wire chamber". In: *Nuclear Instruments and Methods in Physics Research Section A: Accelerators, Spectrometers, Detectors and Associated Equipment* 623.3 (2010), pp. 927 –930. DOI: https://doi.org/10.1016/j.nima.2010.07.061. URL: http://www.sciencedirect.com/science/article/pii/S016890021001675X.

[56] Bernardo Mota et al. "Performance of the ALTRO chip on data acquired on an ALICE TPC prototype". In: *Nuclear Instruments and Methods in Physics Research Section A: Accelerators, Spectrometers, Detectors and Associated Equipment* 535.1 (2004). Proceedings of the 10th International Vienna Conference on Instrumentation, pp. 500 –505. DOI: https://doi.org/10.1016/j.nima.2004.07.179. URL: http://www.sciencedirect.com/science/article/pii/S0168900204017164.

[57] Jorgen A. Lien. "The readout control unit of the ALICE TPC". PhD thesis. Bergen U., 2004. URL: http://weblib.cern.ch/abstract?CERN-THESIS-2005-013.

[58] Luigi Rolandi, Werner Riegler, and Walter Blum. *Particle Detection with Drift Chambers*. Vol. -1. Jan. 2008. DOI: 10.1007/978-3-540-76684-1.

[59] K Aamodt et al. "The ALICE experiment at the CERN LHC. A Large Ion Collider Experiment". In: *JINST* 3 (2008). Also published by CERN Geneva in 2010, S08002. 259 p. DOI: 10.1088/1748-0221/3/08/S08002. URL: https://cds.cern.ch/record/1129812.

[60] Shreyasi Acharya et al. "Real-time data processing in the ALICE High Level Trigger at the LHC". In: *Comput. Phys. Commun.* 242.arXiv:1812.08036 (2018). 43 pages, 21 captioned figures, 3 tables, authors from page 38, submitted to Computer physics communications, figures at http://alice-publications.web.cern.ch/node/4791, 25–48. 24 p. DOI: 10.1016/j.cpc.2019.04.011. URL: https://cds.cern.ch/record/2651166.

[61] Constantinos A. Loizides. "Jet physics in ALICE". PhD thesis. Frankfurt U., 2005. arXiv: nucl-ex/0501017 [nucl-ex].

[62] Michaela Schaumann. "LHC Machine Status report. 136 LHCC Meeting". In: (2018). URL: https://indico.cern.ch/event/771106.

[63] *Upgrade of the ALICE Time Projection Chamber*. Tech. rep. CERN-LHCC-2013-020. ALICE-TDR-016. 2013. URL: http://cds.cern.ch/record/1622286.

[64] B Abelev et al. *Upgrade of the ALICE Experiment: Letter of Intent*. Tech. rep. CERN-LHCC-2012-012. LHCC-I-022. ALICE-UG-002. Geneva: CERN, 2012. DOI: 10.1088/0954-3899/41/8/087001. URL: https://cds.cern.ch/record/1475243.

[65] Edmundo Garcia-Solis. "Perspectives of the ALICE Experiment and Detector Upgrade". In: *Nuclear and Particle Physics Proceedings* 267-269 (2015). X Latin American Symposium of High Energy Physics, pp. 382 –391. DOI: https://doi.org/10.1016/j.nuclphysbps.2015.10.134. URL: http://www.sciencedirect.com/science/article/pii/S2405601415010937.

[66] F. Sauli. "GEM: A new concept for electron amplification in gas detectors". In: *Nuclear Instruments and Methods in Physics Research Section A: Accelerators, Spectrometers, Detectors and Associated Equipment* 386.2 (1997), pp. 531 –534. DOI: https://doi.org/10.1016/S0168-9002(96)01172-2. URL: http://www.sciencedirect.com/science/article/pii/S0168900296011722.

[67] Marco Villa et al. "Progress on large area GEMs". In: *Nuclear Instruments and Methods in Physics Research Section A: Accelerators, Spectrometers, Detectors and Associated Equipment* 628.1 (2011). VCI 2010, pp. 182 –186. DOI: https://doi.org/10.1016/j.nima.2010.06.312. URL: http://www.sciencedirect.com/science/article/pii/S0168900210015020.

[68] DUPONT. *DUPONT KAPTON SUMMARY OF PROPERTIES*. 2017. URL: https://www.dupont.com/content/dam/dupont/products-and-services/membranes-and-films/polyimde-films/documents/DEC-Kapton-summary-of-properties.pdf (visited on 07/07/2019).

[69] Fabio Sauli. "Development and applications of gas electron multiplier detectors". In: *Nuclear Instruments and Methods in Physics Research Section A: Accelerators, Spectrometers, Detectors and Associated Equipment* 505.1 (2003). Proceedings of the tenth Symposium on Radiation Measurements and Applications, pp. 195 –198. DOI: https://doi.org/10.1016/S0168-9002(03)01050-7. URL: http://www.sciencedirect.com/science/article/pii/S0168900203010507.

[70] A. Pezzotta et al. "A CMOS 0.13um read-out front-end for Triple-Gas-Electron-Multiplier detectors". In: *5th IEEE International Workshop on Advances in Sensors and Interfaces IWASI*. 2013, pp. 65–70. DOI: 10.1109/IWASI.2013.6576054.

[71] S. Bachmann et al. "Charge amplification and transfer processes in the gas electron multiplier". In: *Nuclear Instruments and Methods in Physics Research Section A: Accelerators, Spectrometers, Detectors and Associated Equipment* 438.2 (1999), pp. 376 –408. DOI: https://doi.org/10.1016/S0168-9002(99)00820-7. URL: http://www.sciencedirect.com/science/article/pii/S0168900299008207.

[72] Adrian Vogel. "Beam-induced backgrounds in detectors at the ILC". PhD thesis. Hamburg U., 2008. DOI: 10.3204/DESY-THESIS-2008-036.

[73] M Killenberg et al. "Modelling and Measurement of Charge Transfer in Multiple GEM Structures". In: *Nuclear Instruments and Methods in Physics Research Section A: Accelerators, Spectrometers, Detectors and Associated Equipment* 498 (Feb. 2003), pp. 369–383. DOI: 10.1016/S0168-9002(02)02079-X.

[74] CERN COURIER. *ALICE selects gas electron multipliers for its new TPC*. 2016. URL: https://cerncourier.com/a/alice-selects-gas-electron-multipliers-for-its-new-tpc/ (visited on 05/18/2019).

[75] S. Bachmann et al. "Discharge studies and prevention in the gas electron multiplier (GEM)". In: *Nuclear Instruments and Methods in Physics Research Section A: Accelerators, Spectrometers, Detectors and Associated Equipment* 479.2 (2002), pp. 294 –308. DOI: https://doi.org/10.1016/S0168-9002(01)00931-7. URL: http://www.sciencedirect.com/science/article/pii/S0168900201009317.

[76] Louis Malter. "Thin Film Field Emission". In: *Phys. Rev.* 50 (1 1936), pp. 48–58. DOI: 10.1103/PhysRev.50.48. URL: https://link.aps.org/doi/10.1103/PhysRev.50.48.

[77] *International Workshop on Aging Phenomena in Gaseous Detectors*. 2003. URL: https://cds.cern.ch/record/490181.

[78] M Capeans. "Aging and materials: lessons for detectors and gas systems". In: *Computer Physics Communications* 1 (Dec. 2003). DOI: 10.1016/j.nima.2003.08.134.

[79] Maxim Titov. "New developments and future perspectives of gaseous detectors". In: *Nuclear Instruments and Methods in Physics Research Section A: Accelerators, Spectrometers, Detectors and Associated Equipment* 581.1 (2007). VCI 2007, pp. 25 –37. DOI: https://doi.org/10.1016/j.nima.2007.07.022. URL: http://www.sciencedirect.com/science/article/pii/S0168900207014441.

[80] M.C. Altunbas et al. "Aging measurements with the Gas Electron Multiplier (GEM)". In: *Nuclear Instruments and Methods in Physics Research Section A: Accelerators, Spectrometers, Detectors and Associated Equipment* 515.1 (2003). Proceedings of the International Workshop on Aging Phenomena in Gaseous Detectors, pp. 249 –254. DOI: https://doi.org/10.1016/j.nima.2003.09.006. URL: http://www.sciencedirect.com/science/article/pii/S016890020302477X.

[81] M. Hildebrandt. "Aging tests with GEM-MSGCs". In: *Nuclear Instruments and Methods in Physics Research Section A: Accelerators, Spectrometers, Detectors and Associated Equipment* 515.1 (2003). Proceedings of the International Workshop on Aging Phenomena in Gaseous Detectors, pp. 255 –260. DOI: https://doi.org/10.1016/j.nima.2003.09.007. URL: http://www.sciencedirect.com/science/article/pii/S0168900203024781.

[82] Maxim Titov. "Radiation Damage and Long-Term Aging in Gas Detectors". In: (Mar. 2004). DOI: 10.1142/9789812702951_0014.

[83] F. Sauli. *Gaseous Radiation Detectors: Fundamentals and Applications*. Cambridge Monographs on Particle Physics, Nuclear Physics and Cosmology. Cambridge University Press, 2014. URL: https://books.google.de/books?id=ToaYAwAAQBAJ.

[84] P. Gasik. "Building a large-area GEM-based readout chamber for the upgrade of the ALICE TPC". In: *Nuclear Instruments and Methods in Physics Research Section A: Accelerators, Spectrometers, Detectors and Associated Equipment* 845 (2017). Proceedings of the Vienna Conference on Instrumentation 2016, pp. 222 –225. DOI: https://doi.org/10.1016/j.nima.2016.06.070. URL: http://www.sciencedirect.com/science/article/pii/S0168900216306143.

[85] R. Massarczyk et al. "Paschen law studies in cold gases". In: *Journal of Instrumentation* 12.06 (2017), P06019–P06019. DOI: 10.1088/1748-0221/12/06/p06019. URL: https://doi.org/10.1088%2F1748-0221%2F12%2F06%2Fp06019.

[86] Jens Erik Brucken and Timo Eero Hilden. "The GEM QA Protocol of the ALICE TPC Upgrade Project". In: *5th International Conference on Micro Pattern Gas Detectors (MPGD2017) Temple University, Philadelphia, USA, May 22-26, 2017*. 2018. arXiv: 1811.07043 [physics.ins-det].

[87] *Addendum to the Technical Design Report for the Upgrade of the ALICE Time Projection Chamber*. Tech. rep. CERN-LHCC-2015-002. ALICE-TDR-016-ADD-1. 2015. URL: https://cds.cern.ch/record/1984329.

[88] Stephen Biagi. "Magboltz 2". In: (2000). URL: http://cds.cern.ch/record/1018382.

[89] A. Deisting et al. "Secondary discharge studies in single- and multi-GEM structures". In: *Nuclear Instruments and Methods in Physics Research Section A: Accelerators, Spectrometers, Detectors and Associated Equipment* 937 (2019), pp. 168 –180. DOI: https://doi.org/10.1016/j.nima.2019.05.057. URL: http://www.sciencedirect.com/science/article/pii/S0168900219307132.

[90] A.N. Lagarkov and I.M. Rutkevich. *Ionization Waves in Electrical Breakdown of Gases*. Springer New York, 2012. URL: https://books.google.de/books?id=3nDjBwAAQBAJ.

[91] H. Raether. "Die Entwicklung der Elektronenlawine in den Funkenkanal". In: *Zeitschrift für Physik* 112.7 (1939), pp. 464–489. DOI: 10.1007/BF01340229. URL: https://doi.org/10.1007/BF01340229.

[92] Y.P. Raizer, V.I. Kisin, and J.E. Allen. *Gas Discharge Physics*. Springer Berlin Heidelberg, 2011. URL: https://books.google.de/books?id=zd-KMAEACAAJ.

[93] H Raether. "The electron avalanche and its development". In: *Applied Scientific Research, Section B* 5.1 (1956), pp. 23–33.

[94] A. Fridman and L.A. Kennedy. *Plasma Physics and Engineering*. Taylor & Francis, 2004. URL: https://books.google.de/books?id=9wqtYiy_gloC.

[95] Leonard B. Loeb and John M. Meek. "The Mechanism of Spark Discharge in Air at Atmospheric Pressure. I". In: *Journal of Applied Physics* 11.6 (1940), pp. 438–447. DOI: 10.1063/1.1712792.

[96] H Raether. "The development of kanal discharges". In: *Electrical Breakdown in Gases* (Jan. 1973), pp. 28–41.

[97] D B Go and A Venkattraman. "Microscale gas breakdown: ion-enhanced field emission and the modified Paschen's curve". In: *Journal of Physics D: Applied Physics* 47.50 (2014), p. 503001. DOI: 10.1088/0022-3727/47/50/503001. URL: https://doi.org/10.1088%2F0022-3727%2F47%2F50%2F503001.

[98] Daniel Baitinger. "Secondary discharge studies in a single-GEM detector in the scope of the ALICE TPC upgrade". MA thesis. Physikalisches Institut - University of Heidelberg, GSI Helmholtzzentrum für Schwerionenforschung, 2019.

[99] P. Gasik et al. "Charge density as a driving factor of discharge formation in GEM-based detectors". In: *Nuclear Instruments and Methods in Physics Research Section A: Accelerators, Spectrometers, Detectors and Associated Equipment* 870 (2017), pp. 116 –122. DOI: https://doi.org/10.1016/j.nima.2017.07.042. URL: http://www.sciencedirect.com/science/article/pii/S0168900217307878.

[100] Gramos Qerimi. "Geant4 Simulation eines auf GEM basierten Detektors". Technische Universität München Fakultät für Physik, 2015. URL: https://www.das.ktas.ph.tum.de/DasDocs/Public/Bachelor_Theses/GramosQerimi_BachelorThesis.pdf.

[101] Alexandra Datz. "Studies on Secondary Discharges and their Mitigation with a two GEM Detector". Department of Physics and Astronomy, University of Heidelberg, 2017. URL: https://www.physi.uni-heidelberg.de//Publications/Datz_bachelor_thesis.pdf.

[102] Alexander Deisting. "Measurements of ion mobility and GEM discharge studies for the upgrade of the ALICE time projection chamber". English. PhD thesis. Ruprecht-Karls-Universitat Heidelberg, Heidelberg, Germany, Feb. 2018. DOI: 10.11588/heidok.00024133.

[103] Constanze Hasterok. "Gas Purity Analytics, Calibration Studies, and Background Predictions towards the First Results of XENON1T". English. PhD thesis. Ruprecht-Karls-Universitat Heidelberg, Heidelberg, Germany, Oct. 2017. DOI: 10.11588/heidok.00023693.

[104] S.-C. Wu. "Nuclear Data Sheets for A = 216". In: *Nuclear Data Sheets* 108.5 (2007), pp. 1057 –1092. DOI: https://doi.org/10.1016/j.nds.2007.04.001. URL: http://www.sciencedirect.com/science/article/pii/S0090375207000415.

[105] Brookhaven National Laboratory National Nuclear Data Center. *NuDat (Nuclear Structure and Decay Data)*. 2008. DOI: 10.1063/1.1945075.

[106] J. Weiss and W. Bernstein. "Energy Required to Produce One Ion Pair for Several Gases". In: *Phys. Rev.* 98 (6 1955), pp. 1828–1831. DOI: 10.1103/PhysRev.98.1828. URL: https://link.aps.org/doi/10.1103/PhysRev.98.1828.

[107] Vasilios Dimitris Karaventzas. "GEM voltage supply and real-time monitoring. GEM, Gaseous Electron Multiplier". In: (2015). URL: https://cds.cern.ch/record/2047018.

[108] G. Corradi, F. Murtas, and D. Tagnani. "A novel High-Voltage System for a triple GEM detector". In: *Nuclear Instruments and Methods in Physics Research Section A: Accelerators, Spectrometers, Detectors and Associated Equipment* 572.1 (2007). Frontier Detectors for Frontier Physics, pp. 96 –97. DOI: https://doi.org/10.1016/j.nima.2006.10.166. URL: http://www.sciencedirect.com/science/article/pii/S0168900206020146.

[109] G. Corradi et. al. "HVGEM 210 implementation guide and manual". In: (2011).

[110] Rainer Renfordt. *HV System Overview*. ALICE TPC upgrade HV EDR. 2017. URL: https://indico.cern.ch/event/677082/.

[111] Lukas Lautner. "Discharge propagation studies with a single GEM in Ar-CO2 (90-10)". Technische Universität München, Fakultät für Physik, 2017. URL: https://www.das.ktas.ph.tum.de/DasDocs/Public/Bachelor_Theses/LukasLautner_BachelorThesis.pdf.

[112] Piotr Gasik. *Discharge Studies With A Nominal HV Scheme*. TPC project review. 2016. URL: https://indico.cern.ch/event/563976/.

[113] F Archilli et al. *Technical Design Report of the Inner Tracker for the KLOE-2 experiment*. Tech. rep. arXiv:1002.2572. LNF-10-3(P). 2010. URL: http://cds.cern.ch/record/1240980.

[114] Marco Villa. "Developing and evaluating new micropattern gas detectors". PhD thesis. Mathematisch-Naturwissenschaftlichen Fakultat der Rheinischen Friedrich-Wilhelms-Universität Bonn, Nov. 2013. URL: http://hss.ulb.uni-bonn.de/2014/3552/3552.pdf.

[115] Sanghyo Han et al. "Operation of Single GEM, GEM + MWPC, and GEM + MSGC Detectors". In: *J. Korean Phy. Soc.* 41 (2002), pp. 674 –681. URL: http://www.jkps.or.kr/journal/view.html?uid=5124.

[116] Moritz Seidel. "Microscopic Simulation of GEM Signals". Fakultat fur Mathematik, Informatik und Naturwissenschaften der RWTH Aachen, 2018. URL: https://web.physik.rwth-aachen.de/~hebbeker/theses/seidel_bachelor.pdf.

[117] S. Franchino et al. “Effects of High Charge Densities in Multi-GEM Detectors”. In: arXiv:1512.04968 (2015), 7581778. 5 p. DOI: 10.1109/NSSMIC.2015.7581778. URL: https://cds.cern.ch/record/2115608.

[118] J. A. Merlin. *Effect of discharges on GEM detectors - Single hole setup*. RD51 Collaboration meeting and the MPGD stability workshop, Munich, 18-22 June. 2018. URL: https://indico.cern.ch/event/709670/.

[119] Lukas Lautner and Piotr Gasik. *Secondary discharge mitigation by HV scheme optimisation*. RD51 Collaboration meeting and the MPGD stability workshop, Munich, 18-22 June. 2018. URL: https://indico.cern.ch/event/709670/.

[120] Fabio Sauli. “The gas electron multiplier (GEM): Operating principles and applications”. In: *Nuclear Instruments and Methods in Physics Research Section A: Accelerators, Spectrometers, Detectors and Associated Equipment* 805 (2016). Special Issue in memory of Glenn F. Knoll, pp. 2 –24. DOI: https://doi.org/10.1016/j.nima.2015.07.060. URL: http://www.sciencedirect.com/science/article/pii/S0168900215008980.

[121] V. Peskov and P. Fonte. “Research on discharges in micropattern and small gap gaseous detectors”. In: (2009). arXiv: 0911.0463 [physics.ins-det].

[122] Piotr Gasik. *DISCHARGE STUDIES WITH SINGLE- AND MULTI-GEM STRUCTURES IN A SCOPE OF THE ALICE TPC UPGRADE*. RD51 Collaboration meeting, 8-11 February. 2016. URL: https://indico.cern.ch/event/496113/.

[123] A. Utrobicic et al. “Studies of the delayed discharge propagation in the Gas Electron Multiplier (GEM)”. In: *Nucl. Instrum. Meth.* A940 (2019), pp. 262–273. DOI: 10.1016/j.nima.2019.06.018. arXiv: 1902.10563 [physics.ins-det].

[124] MATLAB. *version 9.4.0.813654 (R2018a)*. Natick, Massachusetts: The MathWorks Inc., 2019.

[125] Python Core Team (2015). *Python: A dynamic, open source programming language*. Python Software Foundation. 2019. URL: https://www.python.org/.

[126] Abraham. Savitzky and M. J. E. Golay. “Smoothing and Differentiation of Data by Simplified Least Squares Procedures.” In: *Analytical Chemistry* 36.8 (1964), pp. 1627–1639. DOI: 10.1021/ac60214a047.

[127] Lukas Lautner et al. “High voltage scheme optimization for secondary discharge mitigation in GEM-based detectors”. In: *JINST* 14.08 (2019), P08024. DOI: 10.1088/1748-0221/14/08/P08024. arXiv: 1906.06721 [physics.ins-det].

[128] M Wallmark et al. “Operating range of a gas electron multiplier for portal imaging”. In: *Nuclear Instruments and Methods in Physics Research Section A: Accelerators, Spectrometers, Detectors and Associated Equipment* 471.1 (2001). Imaging 2000, pp. 151 –155. DOI: https://doi.org/10.1016/S0168-9002(01)00980-9. URL: http://www.sciencedirect.com/science/article/pii/S0168900201009809.

[129] John A. Hornbeck. "The Drift Velocities of Molecular and Atomic Ions in Helium, Neon, and Argon". In: *Phys. Rev.* 84 (4 1951), pp. 615–620. DOI: 10.1103/PhysRev.84.615. URL: https://link.aps.org/doi/10.1103/PhysRev.84.615.

[130] Athanasios Papoulis and S. Unnikrishna Pillai. *Probability, Random Variables, and Stochastic Processes, Fourth Edition*. 2002.

Erklärung:

Ich versichere, dass ich diese Arbeit selbstständig verfasst habe und keine anderen als die angegebenen Quellen und Hilfsmittel benutzt habe.

Heidelberg, den 16.12.2019 .....